New Physics with Nu Messengers

by

Thomas Schwemberger

A dissertation accepted and approved in partial fulfillment of the

requirements for the degree of

Doctor of Philosophy

in Physics

Dissertation Committee:

Timothy Cohen, Chair

Tien-Tien Yu, Advisor

Stephanie Majewski, Core Member

James Murray, Institutional Representative

University of Oregon

Summer 2025

DISSERTATION ABSTRACT

Thomas Schwemberger

Doctor of Philosophy in Physics

Title: New Physics with Nu Messengers

The particular properties of neutrinos provide a unique probe of physics beyond the standard model. In this thesis I explore how these properties in terrestrial and astrophysical environments can be used to test theories of new physics. These properties include their low mass and weak Standard Model interactions which I exploit to probe possible couplings to feebly coupled fields using neutrinos from the Sun in both low-threshold skipper CCD experiments and larger more conventional liquid noble element dark matter (DM) experiments.

We first consider a set of generalized interactions focussing on light mediators (scalar, pseudoscalar, vector, and axial vector), and consider coupling these mediators to either quarks or electrons. We find that such small low-threshold detectors can improve current constraints by up to two orders of magnitude for vector mediators and one order of magnitude for scalar mediators.

We then consider the case of much larger detectors which do not benefit from the low-energy enhancement provided by light mediators. In this case we enter a standardized regime in the literature where neutrino Non-Standard Interactions (NSI) are parameterized relative to the weak force. By mapping these parameters to the S_1 leptoquark, we set first limits on these models which result in sizable $\mu - d$ and $\tau - d$ sector neutrino NSI.

Due to their weak interactions, neutrinos propagate efficiently from the farthest reaches of the universe. We use this property to probe the annihilation

of DM during the formation of the first stars. Non-observation of such neutrinos in Super-Kamiokande is used to place constraints on Dark Stars, a non-standard cosmology which aims to explain the formation of supermassive black holes (SMBHs). We use the abundance of such SMBHs and JWST observations of high redshift galaxy-like objects to determine the population of such objects and set the redshift by which they must have collapsed to black holes.

Other neutrinos of astrophysical origin include some of the most energetic particles ever measured. We study a particular event, KM3-230213A, the highest energy neutrino ever recorded, to quantify the discrepancy between measurements of the two largest neutrino telescopes on Earth, KM3NeT and IceCube. We find that for most isotropic diffuse neutrino signals, this tensions falls in the region of $3.1 - 3.6\ \sigma$. while a transient reduces the tension to $2.0\ \sigma$

Through these studies, I demonstrate the utility of neutrinos as a complimentary probe of new physics in the era of multi-messenger astronomy.

This dissertation includes previously published and unpublished co-authored material

CURRICULUM VITAE

NAME OF AUTHOR: Thomas Schwemberger

GRADUATE AND UNDERGRADUATE SCHOOLS ATTENDED:

University of Oregon, Eugene, OR, USA
University of California Santa Cruz, Santa Cruz, CA, USA

DEGREES AWARDED:

Doctor of Philosophy, Psychology, 2016, University of Oregon
Bachelor of Science, Physics, 2018, University of California Santa Cruz

AREAS OF SPECIAL INTEREST:

Particle Physics
Astrophysics
Neutrino Physics

PROFESSIONAL EXPERIENCE:

DOE SCGSR Graduate Fellow, Fermi National Accelerator Laboratory, July 2024 - 2025
Graduate Research Assistant, University of Oregon, Sep. 2021 - June 2024
Graduate Teaching Assistant, University of Oregon, Sep. 2020 - June 2024

GRANTS, AWARDS AND HONORS:

DOE SCGSR International Research Collaboration Award, Fermilab/CERN, 2024
DOE SCGSR Graduate Research Fellowship Fermi National Accelerator Laboratory, 2024
QUP Internship Program (QUPIP), KEK Tsukuba, 2023
Weiser Teaching Award, University of Oregon, 2021

Thesis Honors, University of California Santa Cruz, 2018

PUBLICATIONS:

Thomas Schwemberger, Tien-Tien Yu, & Volodymyr Takhistov. (2024). Hunting Nonstandard Neutrino Interactions and Leptoquarks in Dark Matter Experiments. *JCAP*, 11, (2024) 068. Nov 28, 2024.

Thomas Schwemberger & Tien-Tien Yu. Detecting beyond the standard model interactions of solar neutrinos in low-threshold dark matter detectors. *Phys.Rev.D*, 106 (2022) 1, 015002. Feb 2, 2022

Benjamin V. Lehmann, Christian Johnson, Stefano Profumo, & Thomas Schwemberger. Direct detection of primordial black hole relics as dark matter. *JCAP*, 10 (2019) 046. Oct 17, 2019.

Thomas Schwemberger & Volodymyr Takhistov. First Neutrino Constraints on Dark Stars as Supermassive Black Hole Seeds. *Accepted in APJ-Letters* (2025)

Shirley Li, Pedro Machado, Daniel Naredo & Thomas Schwemberger. Clash of the Titans: ultra-high energy KM3NeT event versus IceCube data. *submitted to Physical Review Letters* (2025)

ACKNOWLEDGEMENTS

I thank all of the mentors who have guided and supported my academic career. Tien-Tien Yu for all of her support in both the science and professional development involved in this work. Volodymyr Takhistov for advocating for my work and merits to continue my research as a postdoctoral scholar in Japan. Pedro Machado for his guidance in my research at Fermilab.

Thank you to the rest of the theory group at Fermilab including Matheus Hostert, Asher Berlin, Roni Harnik, and Paddy Fox

Thank you to everyone in the Institute for Fundamental Science and the High Energy Theory group for countless discussions, academic and otherwise. Graham Kribs for giving me a hard time about riding my bike too much, Tom Bouley for always dropping whatever he's doing to explain something I'm stuck on. Thank you to Pouya Asadi, Ben Lillard, Tim Cohen, Spencer Chang, Dave Soper, Aria Radick, Haidar Esseili, Thomas Driscoll, Cristien Arzate, and Ivan Juarez-Reyes. Thank you all for keeping my ramblings mostly coherent and headed in the right directions.

Thank you to the physics graduate students as a whole. The memes, pizza lunches, onions, and general community were invaluable to maintaining sanity for the past five years.

Finally, a special thanks to Gilia, David, Becca, and Lena for reminding me to have fun and enjoy this incredible life we get to live. You kept me going through so much darkness in the past years. There's some famous quote about seeing far because I've stood on the shoulders of giants. Let it be known that I would have turned back long before reaching those shoulders without you.

Death will come

Then a cloud of love

There is nothing I can tell you now

To my father who did not live to see this work completed. You were always so proud of my more minor accomplishments. I wish you could see this one now.

TABLE OF CONTENTS

Chapter Page

Chapter Page

Chapter Page

LIST OF FIGURES

Figure Page

Figure Page

Figure Page

Figure Page

Figure Page

Figure Page

Figure Page

Figure Page

Figure Page

LIST OF TABLES

Table Page

CHAPTER I

INTRODUCTION

In the past century, the study of particle physics has build and refined one of the most successful models in science. Despite its great success and the discovery of the Higgs boson [2], this Standard Model of particle physics remains incomplete as it lacks the mechanisms to explain a handful of phenomena observed in the universe. Among the most prominent of these shortcomings are the inability to explain the nature and origin of neutrino masses and the elusive dark matter which is required to explain numerous astrophysical phenomena from the formation and speed of stars in galaxies and galaxy clusters [394, 375, 452] to the cosmic microwave background [415] and matter power spectrum [55] among others [402].

Multiple extensions to the standard model have been proposed to explain dark matter (DM) including its production and modern abundance, accounting for roughly five times as much mass as baryonic matter [55]. Many such extensions carry a common theme motivated by the freeze-out of thermal particles in the expanding universe [115]. In this paradigm, DM particles are in thermal equilibrium with the standard model in the early universe until Hubble expansion makes the bath too dilute for efficient annihilation. If one assumes a coupling similar to the weak force, the correct relic density for a DM is achieved by a mass at the weak scale in what is often called the "WIMP miracle" where WIMP stands for weakly interacting massive particle.

The pursuit of modern physics to fill in these gaps in the Standard Model has led to the construction of high energy particle accelerators [103, 205], detectors sensitive to the low energy recoil of particles from collisions with DM [87, 70, 428], and a suite of observatories [50, 67, 260, 197, 72] which scan the skies for the subtlest hints of the underlying nature of these gaps in the standard model.

Historically, astronomical observatories relied on the emission of electromagnetic radiation, first optical light [264], though they have now expanding to fill the entire electromagnetic spectrum from radio waves [72] to high energy gamma rays [197]. While this combined observation across multiple wavelengths of light has been a useful tool for astronomers for some time, recent observations of gravitational waves have heralded the era of "multi-messenger astronomy," particularly regarding observation of GW170817, a binary neutron star merger measured in both gravitational and electromagnetic radiation [31]. This is not the first multi-messenger observation however as cosmic rays and neutrinos had previously been observed in coincidence with electromagnetic radiation. The latter most famously in the case of supernova 1987A (SN1987A) [296, 153] in which several dozen neutrinos were observed in multiple experiments hours before the electromagnetic radiation reached Earth.

1.1 Neutrino Observatories

Neutrinos provide a unique prong in the fork of multi-messenger astronomy. Their low masses and weak couplings mean they travel in straight lines at the speed of light across cosmological distances. They are unaffected by the gas, dust, and magnetic field of galaxies and can escape the hottest and densest environments of the universe, only being briefly trapped within the cores of collapsing supernovae [177, 309]. These effects which trap or slow down light are responsible for the time delay between of the electromagnetic signal of SN1987A relative to the neutrino one. They also makes neutrinos a popular candidate to probe the most extreme cosmological environments [383] and can lead to the identification of ultra high energy cosmic ray sources as the highest energy photons are deflected by magnetic fields while neutrinos can be directly traced back to their origin [22, 419, 386].

Neutrino observatories take various forms depending on the energy of the neutrinos they aim to detect. The highest energy detectors look for the Cherenkov radiation produced by ultra-relativistic charged particles from the collision of neutrinos with standard model particles in or near the detector. The largest such detector, Pierre Auger, is built to detect primary charged particles at even higher energies and is thus only sensitive to 50 - 100 PeV neutrinos and has yet to observe any candidate events [275]. The largest dedicated neutrino observatories are cubic kilometer scale detectors such as IceCube [67] or KM3NeT [50] which leverage existing bodies of water (or ice) by adding strings of photomultiplier tubes (PMTs) to detect Cherenkov light. These experiments are built with PMTs spaced such that their lower energy thresholds range from 10 GeV to the TeV scale. Despite its smaller area and runtime and the non-observation in Pierre Auger or IceCube, KM3NeT has recorded the highest energy neutrino ever seen with an energy $\sim 72 - 2600$ PeV [69]. In Chapter 6 we discuss the tension this implies with other observations including possible explanations there-of.

Smaller experiments can provide better energy resolution and thresholds at the expense of reduced exposure. The largest detector in this category is Super-Kamiokande [260] which operates with a fiducial mass of 22.5 ktons of water and a threshold which varies based on neutrino flavor, but reaches a few MeV for electron neutrinos. For other flavors, the interaction cross section falls sharply at low energies since the dominant process (charged current scattering) has a kinematic limit to produce heavy charged leptons. Below $\sim$ 100 MeV, muon neutrinos can only scatter via neutral current interactions which has a smaller cross-section. The

Deep Underground Neutrino Experiment (DUNE) is under construction and will compliment the capabilities of Super-K with a similar scale detection volume and threshold while the liquid argon time projection chamber will provide additional information on the interaction and direction of the particles [41].

The lowest threshold detectors which are studied in this work for neutrino observation are not build with the intention of measuring neutrinos. Rather they are DM experiments in which neutrinos are considered an irreducible background [374]. This "neutrino fog" is regarded as a major limiting factor in the reach of such experiments as the signal is, event by event, indistinguishable from DM scattering. The first measurements of this solar neutrino background was recently reported by the XENON collaboration [90]. Efforts to mitigate this background include directionality and temporal variability in the scattering rate. A significant side effect of these efforts to distinguish a potential DM signal is an improved ability to measure the low energy neutrino scattering rate.

These DM experiments can broadly be grouped into two categories. First are nuclear recoil experiments. These are typically a ton-scale fiducial volume of a liquid noble element such as argon or xenon where recoiling nuclei emit photons measured in the detectors. Leading experiments include XENONnT [88] and LUX-ZEPLIN [6] which have thresholds of a few keV. Notably, the kinematics of imparting enough recoil energy to a heavy nucleus to be detected in such experiments poses a challenge for lighter DM or less energetic neutrinos.

This leads to the second broad class of DM direct detection experiments, those aimed at the detection of DM electron scattering. In this case, the lighter target allows for the detection of lighter (sub GeV) DM or lower energy neutrinos. While liquid noble element experiments are sensitive to electron recoils, dedicated experiments offer a number of advantages. Such experiments are usually based on semi-conductor targets where an electron is excited into the conduction band. This also reduces the threshold on recoil energy to the eV scale. The leading experiment in this category is SENSEI which uses a skipper CCD to probe recoil energies less than 10 eV [122].

1.2 Neutrino Non-Standard Interactions

In their own right, neutrinos constitute one focus of the 2023 Particle Physics Project Prioritization Panel (P5) guidance to "Decipher the Quantum Realm" due to their quantum oscillations [107]. As a probe of astrophysical environments, they are a powerful took for the second focus of the P5 report, to "Illuminate the Invisible Universe."

This dissertation follows these two foci in that order first exploiting the weak interactions of neutrinos to probe similarly weak couplings to potential new particles. These new theories are standardized in the literature as "generalized neutrino interactions" and "neutrino non-standard interactions" (NSI). The former retains the Lorentz structure and mass of the propagator while the latter simplifies the interaction as a four-point effective field theory (EFT) after integrating out the mediating field, requiring the field to be much heavier than the recoil energy of the target nucleus or electron. I study these two regimes in chapters 2 and 3 respectively.

These potential interactions of neutrinos beyond the standard model (BSM) arise in various well motivated theories which extend the underlying symmetries of the standard model to include features like gauged $B - L$ or $L_\mu - L_\tau$ symmetries or in grand unified theories which introduce leptoquarks, hypothetical particles with both baryon and lepton number. Such models have been proposed to provide a mechanism to generate DM or the baryon asymmetry of the universe. Modified neutrino scattering can then probe these models which evade constraints based on measurements of charged leptons [313].

Exploiting neutrino couplings induced by these models has a number of advantages over those induced in the charged leptons. Notably the kinematics and instabilities of the charged leptons. Since neutrinos don't decay and interact only weakly, modifications to the couplings of second and third generation fermions are more accessible.

Such couplings to standard model particles also modifies the matter potential experienced by neutrinos as they propagate through the Earth. This in turn modifies the oscillation probabilities providing another mechanism for their detection. This method is used in neutrino propagation experiments including Super-K measurement of atmospheric neutrinos [425] and planned work at DUNE [203, 225].

1.3 Searching for DM with Neutrinos

Considering the second focus of the P5 report, neutrinos provide a complimentary probe of the invisible universe. Just as they intertwine themselves in direct detection experiments, they are an integral part of indirect detection probes of DM. These indirect detection experiments search for the standard model products of DM annihilation or decay. In this work and most of the literature, the focus is on the former. In this case, the annihilation rate scales as the density squared along the line of sight of an observation. This is quantified by the J-factor:

$$J = \int\int \rho^2_{\mathrm{DM}}(x,\Omega) dx d\Omega \tag{1.1}$$

where x is the distance along the path and Ω is the angle over which the observation is performed. It is thus advantageous to search for DM in regions of high DM density while reducing the background from standard model processes. This often means searching in dwarf galaxies with low stellar luminosities [45].

Despite the high backgrounds, searches focused on the galactic center have also been promising with a confirmed excess of gamma rays, though it is unclear if the origin is DM since the background from unresolved point sources is not well understood [300, 202, 17, 329, 18, 299, 450]. While such studies are subject to larger theoretical uncertainties and must make certain simplifying assumptions [334], they often provide the most sensitive probes of new physics.

Using neutrino signals instead of gamma rays provides a complimentary probe of such signals [29] and allows for searches of different regions of space including those which are opaque to high energy photons or have different backgrounds of standard model processes. Typically the energy of neutrinos from DM annihilation is set by the DM mass, thus for canonical WIMPs experiments search for neutrinos with energies up to $\sim$ GeV $-$ TeV, and thus straddle the transition where large water Cherenkov detectors like Super-K or kilometer scale arrays like IceCube or KM3NeT are most effective.

One such scenario arises from DM annihilation in the first stars in the universe where photons would mostly be trapped within the star while neutrinos escape. These stars formed in an environment with a higher DM density than today due to Hubble expansion. As they formed in the centers of the first halos, it has been proposed that DM annihilation is actually the dominant source of energy for these stars. Such “dark stars” burn at much lower temperatures, allowing for continued accretion and fueling to sustain them at extremely large masses and luminosities on timescales similar to the age of the universe.

These objects are also proposed as explanations for the origin of supermassive black holes at the centers of galaxies which otherwise have no known production mechanism. In Chapter 4 we study the neutrino signal of such objects, finding they produce a detectable diffuse neutrino background, similar to the diffuse supernova neutrino background (DSNB) which arises from the cosmic history of supernovae. Using differences in their spectra, we place constraints on which DM models may produce such dark stars and seed supermassive black holes.

1.4 Outline

Chapter 2 studies the interaction of solar neutrinos in low threshold DM experiments to search for new light mediating particles and was co-authored with Tien-Tien Yu and published in Physical Review D [405]. These generalized neutrino interactions involve a new field which couples to both neutrinos and a nucleus or electron allowing scattering on target materials in DM experiments.

Chapter 3 represents a continuation of this work at higher energies to search for more massive mediators and leptoquarks in larger experiments. The work is co-authored with Tien-Tien Yu and Volodymyr Takhistov and published in the Journal of Cosmology and Astroparticle Physics [404].

Chapters 4 then turns to the second focus of the P5 report as I look at astrophysical neutrinos originating from beyond our solar system. These more exotic sources could reveal information about the nature of DM. This work is co-authored with Volodymyr Takhistov and has been accepted for publication in Astrophysical Journal Letters with a pre-print posted publicly [403].

Chapter 5 Continues the study of astrophysical neutrinos to evaluate a recent observation of an ultra high energy event in the context of data from competing experiments. This work is co-authored with Shirley Li, Pedro Machado, and Daniel Naredo-Tuero and is also under peer-review for publication in Physical Review Letters with a public pre-print [337].

CHAPTER II

DETECTING BEYOND THE STANDARD MODEL INTERACTIONS OF SOLAR NEUTRINOS IN LOW-THRESHOLD DARK MATTER DETECTORS

This work is co-authored with Tien-Tien Yu and is published in Physical Review D [405].

As low-threshold dark matter detectors advance in development, they will become sensitive to recoils from solar neutrinos which opens up the possibility to explore neutrino properties. We predict the enhancement of the event rate of solar neutrino scattering from Beyond the Standard Model interactions in low-threshold DM detectors, with a focus on silicon, germanium, gallium arsenide, xenon, and argon-based detectors. We consider a set of general neutrino interactions, which fall into five categories: the neutrino magnetic moment as well as interactions mediated by four types of mediators (scalar, pseudoscalar, vector, and axial vector), and consider coupling these mediators to either quarks or electrons. Using these predictions, we place constraints on the mass and couplings of each mediator and the neutrino magnetic moment from current low-threshold detectors like SENSEI, Edelweiss, and SuperCDMS, as well as projections relevant for future experiments such as DAMIC-M, Oscura, Darwin, and ARGO. We find that such low-threshold detectors can improve current constraints by up to two orders of magnitude for vector mediators and one order of magnitude for scalar mediators.

2.1 Dark Matter Experiments and Neutrino NSI

The WIMP paradigm has driven the landscape of DM research on both the experimental and theoretical fronts for the last several decades. The tightening of constraints in the WIMP parameter space has motivated the development of low-threshold detectors targeted at DM masses below those predicted by the canonical

WIMP models, which sit at the $\mathcal{O}(10-100\text{eV})$ mass scales. These low-threshold DM detectors are sensitive to $\mathcal{O}(\text{eV})$ energy depositions, opening up access to sub-GeV DM candidates. The DM detectors optimized for WIMP searches rely on the detection of DM-nuclear scattering, in which the recoiling nucleus imparts some detectable signature in the form of heat, light, or ionization. It has been long understood that neutrinos, specifically solar neutrinos, can mimic these same signatures through the coherent scattering of neutrinos on nuclei; this has been historically called the "neutrino floor" or "neutrino background" (see *e.g.* [150] and references therein). More recently, it was demonstrated that low-threshold detectors which observe ionization, *e.g.* electron, signatures are also subject to this neutrino background [235]. Although the background is due to neutrino-nuclear scattering, a fraction of the nuclear recoil energy can be converted into electron recoil energy, thus leading to an ionization signal.

The 2017 observation of coherent elastic neutrino-nucleus scattering (CEvNS) by COHERENT [71] motivates the discussion of the potential to unearth new BSM physics in the neutrino sector. This has led to a series of efforts to look for generalized BSM interactions of neutrinos with the SM in a variety of detectors. Previous work has focused on detectors with thresholds above $\mathcal{O}(100\text{ eV})$ [209, 350] or nucleon only interactions [339]. In this work, we make a systematic study of BSM neutrino interactions in low-threshold DM detectors, down to the bandgap energies of $\mathcal{O}(\text{eV})$, using a simplified models framework to encode the neutrino non-standard interactions (NSIs).[1] The advantage to using low-threshold DM detectors to study NSI is two-fold. Low-threshold ionization experiments, as discussed above, are sensitive to

[1]Note that we are using the terminology "NSI" for the simplified-models framework rather than the effective field theory style framework typically used to quantify new physics in the neutrino sector (see *e.g.* [214, 97, 154]). Thus, neutrino magnetic moments fall under our definition of NSI.

both electron and nuclear recoils, the latter as a result of the conversion of nuclear recoil energy into electron recoil energy. This makes these detectors sensitive to a wider range of models, some of which can evade the astrophysical constraints that rely primarily on electron interactions. We will calculate the sensitivity to both quark and electron couplings independently as well as a neutrino magnetic moment. Furthermore, there is an additional enhancement of the scattering rate which is inversely proportional to the nuclear recoil energy from which low-threshold detectors, with their sensitivity to small energy depositions, profit tremendously. We also calculate the sensitivities in noble liquid detectors using xenon and argon where the much larger exposures can overcome the relative inefficiency of converting nuclear recoil energy into an ionization signal.

The difficulty in detecting CEvNS and low-energy neutrino-electron scattering lies in running an experiment with both low detector noise and a low energy threshold. Recent technological advancements in semiconductor targets such as the use of Skipper CCDs [428] or high bias potential voltages [393, 102] have led to sensors with sub-electron noise and energy thresholds down to the band gap, $\mathcal{O}$(eV), of the semiconductor. Existing experiments to date have provided early data with an exposure of $\sim$ 10 g-days [406, 228, 79] which can place constraints on light vector boson-mediated models such as $U(1)_{B-L}$ comparable to those of Borexino [291, 263]. Similarly, noble liquid detectors such as XENON1T also set competitive constraints on such models [159]. These constraints will only strengthen with the next-generation of low-threshold detectors which will have increased exposure. With larger Skipper CCD experiments planned, it will be important to understand the signals they may be sensitive to both from neutrinos and dark matter.

The rest of this chapter is organized as follows. In Sec. 2.2 we present the expressions for the neutrino-nuclear and neutrino-electron scattering rates in both the SM and five NSI simplified models. In Sec. 2.3, we discuss the signatures of the scattering events in semiconductor (Si, Ge, and GaAs) and noble liquid (Xe and Ar) materials used in low-threshold detectors. Here, we include the discussion of ionization efficiencies and charge yields in each material. In Sec. 2.4 we discuss the effects of the simplified models on the event rates calculated in Sec. 2.3 and present our projected sensitivities to the NSI simplified model parameters. We discuss the interpretation of our results in relation to complete ultraviolet models in Sec. 2.5 and conclude in Sec. **??**.

2.2 Neutrino Scattering Rates

Neutrinos are produced in the sun via a series of nuclear processes, which are broadly categorized as *pp* or *CNO*, depending on the elements involved. These nuclear processes constitute the different components of the solar neutrino flux, as shown in Fig. 1. To determine the measured event rate from solar neutrino scattering in a detector, we follow the procedure outlined in [235], and sum the contributions from each component of the solar flux, themselves determined by integrating over their energy spectra. We use the fluxes given by the high-metallicity solar neutrino model BS05(OP) [117, 116]. Specifically, in order to produce a (kinetic) recoil energy E_R, the incident neutrino must have at least the energy given in Eq. (2.1) where m_T as the target mass (either electron or nucleus) and we have explicitly kept the neutrino mass (m_ν) to leave open the possibility of heavy sterile neutrinos. The minimum neutrino energy is therefore given by

$$E_\nu^{min} = \frac{1}{2}\left(E_R + \sqrt{E_R^2 + 2E_R m_T\left(\frac{m_\nu^2}{m_T^2}+1\right) + 4m_\nu^2}\right) . \tag{2.1}$$

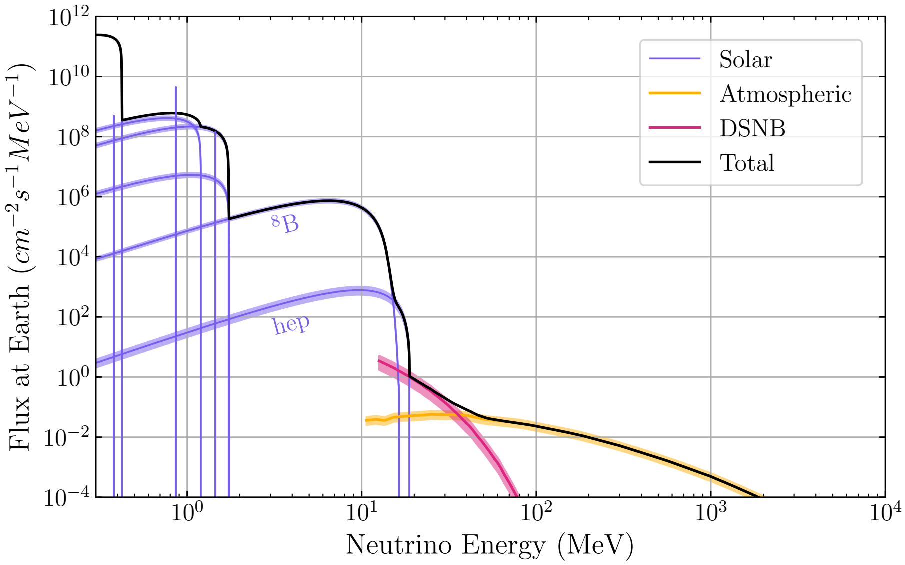

Figure 1. Differential neutrino flux components from the *pp* and *CNO* cycles using the high-metallicity solar neutrino model BS05(OP) [117, 116]. The black line does not include the monochromatic components which are included individually in the calculations which follow.

We integrate the differential neutrino flux, $\frac{dN_\nu}{dE_\nu}$, from this minimum energy to the highest energy neutrino in each solar component weighting by the differential cross-section for either nuclear or electron recoils and multiply by the number of targets per kg of detector material (N_T) to get the recoil rate in events per kg-yr,

$$\frac{dR}{dE_R} = N_T \int_{E_\nu^{min}} \frac{d\sigma}{dE_R}\frac{dN_\nu}{dE_\nu} dE_\nu \,, \tag{2.2}$$

where $\frac{d\sigma}{dE_R}$ is the differential cross-section of neutrino scattering. In what follows, we present the expressions for this differential cross-section in both the SM and in five representative NSI simplified models.

2.2.1 The Standard Model. The SM differential cross-sections for nuclear and electron recoils are

$$\frac{d\sigma}{dE_N} = \frac{G_F^2}{4\pi} Q_v^2 m_N \left(1 - \frac{m_N E_N}{2E_\nu^2}\right) F^2(E_N) \tag{2.3}$$

$$\frac{d\sigma}{dE_e} = \frac{G_F^2 m_e}{2\pi E_\nu^2}\left[4s_w^2(2E_\nu^2 + E_e^2 - E_e(2E_\nu + m_e)) \pm 2s_w^2(E_e m_e - 2E_\nu^2) + E_\nu^2\right] \,, \quad (2.4)$$

where G_F is the Fermi constant, s_w is the sine of the Weinberg angle, $Q_v = N - Z(1 - 4s_w^2)$ is the weak nuclear hypercharge (for N neutrons and Z protons), and the $\pm$ distinguishes electron neutrinos ($-$) from the other flavors ($+$). $F(E_N)$ is the Helm nuclear for factor as defined in [335], which is approximately unity at the energy scales we consider. We leave the discussion of our treatment of neutrino oscillation to Sec. 2.2.2.

2.2.2 Non-Standard Neutrino Interactions. Low-threshold detectors like SENSEI, Edelweiss and SuperCDMS, open up access to the lower range of recoil energies for which neutrino scattering produces a detectable signature. Therefore, we focus on a set of simplified infrared models for NSI which modify the differential cross-section at low energies. Arguably the simplest way to introduce a NSI is to give the neutrino a magnetic moment, μ_ν, via the interaction

$$\mathcal{L} \supset \mu_\nu \bar{\nu} \sigma^{\alpha\beta} \partial_\beta A_\alpha \nu \,. \quad (2.5)$$

As of 2022, the strongest constraint on the magnetic moment of $\mu_\nu < 2.8 \times 10^{-11} \mu_b$, where $\mu_b = \sqrt{4\pi\alpha}/2m_e$ is the Bohr magneton, is from Borexino [59]. Note the inclusion of this interaction provides an enhancement to both the CEvNS and electron recoil rates, though as we will see in Sec. 2.3 the former is suppressed by both the yield function and nuclear mass.

The enhancement of the neutrino-nucleus cross-section is given by

$$\frac{d\sigma_\mu}{dE_R} = \mu_\nu^2 \alpha Z^2 F^2(E_R)\left(\frac{1}{E_R} - \frac{1}{E_\nu}\right) \quad (2.6)$$

where $F(E_R)$ is, again, the Helm nuclear form factor as detailed in [335]. As before, $F(E_R) \sim 1$ for the recoil energies of interest. The neutrino electron cross-section is similar to Eq. 2.6 but without the nuclear charge number (Z) or form factor.

For full generality, we consider set of simplified models in which the couplings of the mediator to neutrinos and the target (nucleus, electron) along with the mass of the mediator are free parameters. This approach permits us to remain agnostic about the underlying theory and allows the reader the map our results onto a wide-range of UV-models. We calculate the enhancement (or suppression) to the scattering cross-section resulting from NSI mediated by scalar, pseudoscalar, vector, or axial vector propagators, as shown in Eq. (2.7). For scalars and pseudoscalars, we include line 1 of Eq. (2.7) while for vectors and axial vectors we use line 2. Line 3 denotes the operators $\mathcal{O}_i$ coupling the field (i) to fermions with the appropriate Lorentz structure as shown in Table 1.

$$\begin{aligned} \mathcal{L} \supset\; & (g_{\nu P}\phi\bar{\nu}_R\nu_L + h.c.) + (g_{\nu S}\phi\bar{\nu}_R\nu_L + h.c.) \\ & + g_{\nu V}\bar{\nu}_L\gamma^\mu\nu_L Z'_\mu + g_{\nu A}\bar{\nu}_L\gamma^\mu\nu_L Z'_\mu \\ & + g_{ei}\mathcal{O}_i(\bar{e},e) + g_{qi}\mathcal{O}_i(\bar{q},q) \end{aligned} \tag{2.7}$$

Mediator	Couplings	$\mathcal{O}_i(\bar{f},f)$
Scalar (S)	$g_{\nu S}, g_{eS}, g_{qS}$	$\phi\bar{f}f$
Pseudoscalar (P)	$g_{\nu P}, g_{eP}, g_{qP}$	$-i\gamma^5\phi\bar{f}f$
Vector (V)	$g_{\nu V}, g_{eV}, g_{qV}$	$Z'_\mu\bar{f}\gamma^\mu f$
Axial Vector (A)	$g_{\nu A}, g_{eA}, g_{qA}$	$-Z'_\mu\bar{f}\gamma^\mu\gamma^5 f$

Table 1. Couplings, and operators for the four (S, P, V, A) generalized mediator models. Note the relative minus-sign for the CP-odd interactions.

The electron recoil cross sections from the NSI contribution without the SM are given in Eq. (2.8). As in [175], we neglect terms which are higher order in E_R/E_ν since we focus on signals in low threshold detectors where $E_R/E_\nu \lesssim 10^{-2}$. The subscripts

(S, P, V, A) correspond to the scalar, pseudoscalar, vector, and axial vector mediated interactions. We consider NSIs where the neutrino coupling is generation independent, but the generalized case simply considers the recoil rate from each neutrino flavor weighted by their oscillation probability.

$$
\begin{aligned}
\left.\frac{d\sigma_e}{dE_R}\right|_S &= \frac{g_{\nu S}^2 g_{eS}^2 E_R m_e^2}{4\pi E_\nu^2 (2E_R m_e + m_S^2)^2} \\
\left.\frac{d\sigma_e}{dE_R}\right|_P &= \frac{g_{\nu P}^2 g_{eP}^2 E_R^2 m_e}{8\pi E_\nu^2 (2E_R m_e + m_P^2)^2} \\
\left.\frac{d\sigma_e}{dE_R}\right|_V &= \frac{\sqrt{2} G_F m_e g_v g_{\nu V} g_{eV}}{\pi (2E_R m_e + m_V^2)} + \frac{m_e g_{\nu V}^2 g_{eV}^2}{2\pi (2E_R m_e + m_V^2)^2} , \\
\left.\frac{d\sigma_e}{dE_R}\right|_A &= \frac{\sqrt{2} G_F m_e g_a g_{\nu A} g_{eA}}{\pi (2E_R m_e + m_A^2)} + \frac{m_e g_{\nu A}^2 g_{eA}^2}{2\pi (2E_R m_e + m_A^2)^2}
\end{aligned}
\tag{2.8}
$$

where g_v and g_a are the weak vector and axial couplings, and $m_{e,S,P,V,A}$ are the masses of the electron, scalar, pseudoscalar, vector, and axial vector respectively. Eq. (2.8) does not include the effects of electron binding energy which can have a measurable effect at low energies [181]. We will revisit this effect in Sec. 2.4 where its effect on sensitivities is relevant. Note however that they are coupling solar neutrinos to electrons, so we must consider a weighted average over the same-flavor and mixed-flavor couplings: $g_{v,e} = 2s_w^2 + 1/2$, $g_{a,e} = +1/2$ and $g_{v,\mu\tau} = 2s_w^2 - 1/2$, $g_{a,\mu\tau} = -1/2$. We do this with the typical 2-flavor neutrino mixing approximation in Eq. (2.9) where $\sin^2(\theta_{12}) = 0.31$ and $\Delta m_{12}^2 = 7.5 \times 10^{-5}\text{eV}^2$ are the mixing angle and mass splitting respectively. L is the Earth-Sun distance in km and $L_{osc} = 2.48\ \text{km} \times E_\nu/\Delta m_{12}^2$ with E_ν in GeV

$$
P(\nu_e \to \nu_\mu) = \sin^2(2\theta_{12}) \sin^2(\pi L/L_{osc}) \tag{2.9}
$$

For most solar neutrinos, $L \gg L_{osc}$ and $\sin^2(L/L_{osc}) \to \langle \sin^2(L/L_{osc}) \rangle = 1/2$ is a good approximation when we integrate over the neutrino energy spectrum. However, this is not true for monochromatic solar neutrino channels such as ^{7}Be and pep sources since we are effectively integrating a delta function and are sensitive to the exact value of Δm^2_{12}. Therefore, we use the full expression, Eq. 2.9, in our calculations.

The nuclear recoil cross-sections are given by

$$\begin{aligned}
\left.\frac{d\sigma_N}{dE_R}\right|_S &= \frac{F^2(E_R)Q'^2_s E_R m_N^2}{4\pi E_\nu^2(2E_R m_N + m_S^2)^2} \\
\left.\frac{d\sigma_N}{dE_R}\right|_P &= 0 \\
\left.\frac{d\sigma_N}{dE_R}\right|_V &= -\frac{F^2(E_R)G_F m_N Q_v Q'_v(2E_\nu^2 - E_R m_N)}{2\sqrt{2}\pi E_\nu^2(2E_R m_N + m_V^2)} + \frac{F^2(E_R)m_N Q'^2_v(2E_\nu^2 - E_R m_N)}{4\pi E_\nu^2(2E_R m_N + m_V^2)^2} \\
\left.\frac{d\sigma_N}{dE_R}\right|_A &= \frac{F^2(E_R)G_F m_N Q'_a[Q_a(2E_\nu^2 + E_R m_N) - Q_v E_R E_\nu]}{2\sqrt{2}\pi E_\nu^2(2E_R m_N + m_A^2)} + \frac{F^2(E_R)m_N Q'^2_a(2E_\nu^2 + E_R m_N)}{4\pi E_\nu^2(2E_R m_N + m_A^2)^2}
\end{aligned} , \tag{2.10}$$

where the effective nuclear couplings $Q'_{S,V,A}$ and $Q_{v,a}$ used in the CEvNS enhancement are listed in Eq. (2.11) and S_N is the nuclear spin weighted over the isotopes present in the detector.

$$\begin{aligned}
Q'_s &= g_{\nu S} g_{qS}(14A + 1.1Z) \\
Q'_v &= g_{\nu V} g_{qV}(3A) \\
Q'_a &= g_{\nu A} g_{qA}(0.3S_N) \\
Q_v &= A - (2 - 4s_w^2)Z \\
Q_a &= 1.3S_N
\end{aligned} . \tag{2.11}$$

In the above, A, Z correspond to the atomic mass and number, respectively.

The strengths of low-threshold detectors relative to traditional WIMP direct detection experiments is at low energies. To this end, we note the limiting behavior of each of these models, but also note that at such low energies the SM background is dominated by CEvNS which enhances both the signal and background. In the case of the neutrino magnetic moment, the recoil rate increases as $1/E_R$ without bound, though the neutrinos which produce such soft recoils also tend to be less energetic, so the $-1/E_\nu$ term reduces this gain. The scalar rate also scales as $1/E_R$ until $E_R \lesssim m_\phi^2/m_T$ where m_T is the target mass, below which the electron recoil rate falls proportional to E_R, however, below ~ 100 eV nuclear recoils dominate and the rates regain their power-law form. The pseudoscalar rate does not enjoy the same low energy enhancement so the detectors we discuss here will be less sensitive to it. Both vector and axial vector mediators produce a differential rate which scales as $1/E_R^2$ and plateaus at $E_R \sim m_\phi^2/m_T$ below which nuclear recoils dominate again. This makes vector and axial vector models particularly interesting for low threshold detectors. We plot the recoil rates for the magnetic moment as well as 1, 10, and 100 keV scalar and vector mediators in Fig. 2 to illustrate these behaviors.

2.3 Ionization Signals in Low Threshold Detectors

Once a neutrino has scattered off of a nucleus or electron, the recoil energy of the target must be translated into a detectable ionization signal. In this section, we summarize that process for both electron and nuclear recoils in semiconductors and noble liquid detectors. For scattering off of electrons, one must first translate the theoretical quantity of electron recoil energy into the experimentally measured number of electrons (or photoelectrons, for the case of noble liquid detectors). The exact procedure depends on the detector, which we will describe below.

For nuclear recoil, there is an additional step of converting the nuclear recoil energy into electron recoil energy. To determine the nuclear recoil rate, we consider the energy a nuclear recoil (E_R) must have to produce the same effect as an electron recoil with energy E_e. We use the convention $E_e = Y(E_R) \times E_R$ where $Y(E_R)$ is

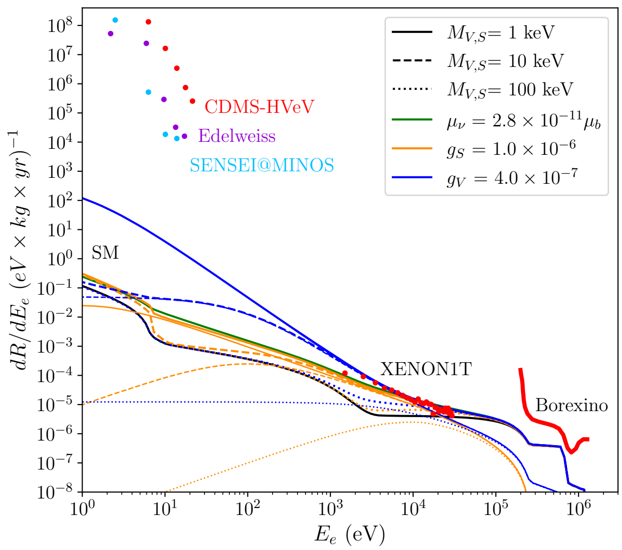

Figure 2. Combined electron and nuclear recoil rates in silicon from vector (blue) and scalar (gold) mediators and a neutrino magnetic moment (green). Nuclear rates are shifted to the rates at the equivalent electron energy to account for the yield function as discussed in Sec. 2.3. We plot the NSI electron recoil rates with thin lines to illustrate the limiting behavior at low-energies. The black line is the SM. Borexino data is from [139] and XENON1T from [86], while SENSEI@MINOS, Edelweiss, and CDMS-HVeV are from [406, 228, 79] respectively. The couplings are chosen to approximately saturate the XENON1T constraints.

the yield function which depends on nuclear recoil energy and the material of the detector. The electron ionization signal from a nuclear recoil is then calculated by binning the differential electron energies corresponding to a differential nuclear recoil element. This is calculated by differentiating the electron energy as a function of nuclear recoil energy.

$$\frac{dE_e}{dE_R} = Y(E_R) + E_R \frac{dY(E_R)}{dE_R} \tag{2.12}$$

Then by a change of variables

$$\frac{dR_e}{dE_e} = \frac{dR_N}{dE_R} \times \frac{1}{Y(E_R) + E_R \frac{dY(E_R)}{dE_R}} \tag{2.13}$$

where R_e and R_N are the effective electron ionization rate and nuclear scattering rates respectively. The rate in Eq. (2.13) is then binned like the direct electron recoils, noting that the right-hand side is a function of E_R so the bin boundaries must be adjusted to match using the inverse of the yield function.

At high energies, the quenching factor is well-approximated by the Lindhard model [344],

$$\begin{aligned} Y_{Lindhard}(E_R) &= \frac{kg(\epsilon)}{1+kg(\epsilon)} \\ g(\epsilon) &= 3\epsilon^{0.15} + 0.7\epsilon^{0.6} + \epsilon , \\ \epsilon &= 11.5 Z^{-7/3} E_R \end{aligned} \tag{2.14}$$

where Z is the atomic number of the recoiling nucleus and E_R is in keV. Although the original description set $k = 0.133 Z^{2/3} A^{-1/2}$, with A as the mass number of the nucleus, experimental data point to a range of values for k. Therefore, k is typically treated as a free-parameter.

However, the Lindhard model breaks down at the energies of interest to this work. Combined with the lack of experimental data at the lowest energies, we must extrapolate the yield function to a range of cut-off energies in an attempt to span all possible low-energy limits. To do this we define three yield functions (high, fiducial, low) which we set to vanish at three respective cut-off energies, E_c, and smoothly match them to the high-energy model with an analytic extrapolation. Where possible, we use more modern corrections to the Lindhard model which include the effects of binding energy to more closely match low-energy data from Refs. [179, 401, 195]. In the following sections we discuss these extrapolations and updates to the Lindhard model at low energies. Note that the sensitivity of the low threshold detectors is dependent both on the magnitude and slope of the yield function as seen in Eq. (2.13), and therefore has a strong dependence on the choice of extrapolation. We examine this dependence in detail in Sec. 2.3.3 and Appendix A.1.

2.3.1 Semiconductors. In low-threshold semiconductor experiments, such as those using Skipper CCDs, the ionization signal comes in the form of quantized electrons, n_e. The electron recoil energy, E_e, can be translated into quanta by binning the electron energies starting from the band gap energy with a bin width equal to the average electron-hole pair production energy. In other words, for a recoil with energy E_e, $n_e = 1 + \lfloor (E_e - E_{\text{gap}})/\varepsilon \rfloor$, where $\lfloor x \rfloor$ rounds x down to the nearest integer, E_{gap} is the bandgap energy of the material, and ε is the mean energy per electron-hole pair. This is a fairly good approximation, accurate to about $\sim 10\%$ [230] of more sophisticated models (see *e.g.* Refs. [384, 392] and references therein). The relevant energies are summarized for the three semiconductors of interest in Table 2. The procedure to convert nuclear recoil energy into quantized electrons is more complicated. First, the nuclear recoil energy is translated to electron energy with a yield efficiency (sometimes called quenching factor) which carries a large theoretical uncertainty and has not been measured at energies below several hundred eV.

The Lindhard model makes several approximations which begin to break down at the energies of interest, as discussed in Ref. [396]. For example, the Lindhard model neglects the binding energy of the electrons, assumes that the energy transferred to the electrons is significantly smaller than that transferred to the recoiling ion, and that the nuclear kinetic energy is small. Ref. [396] revisits the calculation of Lindhard in silicon and germanium using a first-principles approach and relaxing the above approximations. Note that this work assumes a constant binding energy. Near the transition region, there exists empirical measurements by DAMIC [179] for silicon and Ref. [401, 195] for germanium. We use an ionization model which combines the first-principles approach of Ref. [396] and the empirical measurements. For illustrative purposes, we adopt as our fiducial models an updated calculation from Ref. [363, 395], where they allow for the binding energy to vary. They also use an enhanced model of the electronic stopping power which takes into account Coulomb repulsion effects as well as high-energy effects from the Bohr stripping criterion. We extend this model to different cut-off energies to illustrate the sensitivity of the detectors to small changes in the yield function. The functions are plotted in Fig. 3. Our extrapolations are fit using a power law: $Y(E_R) = a(x - E_c)^b$ where E_c is the cut-off energy and a and b are chosen to match the high energy model at 600 eV in silicon and 100 eV in germanium (roughly 10 times the cut-off in the model developed by Ref. [363, 395]). In Si(Ge), our deviations extend the cut-off to 20(5) eV for the high-yield case and 200(20) eV in the conservative case.

In the absence analogous first-principles calculations for gallium arsenide, we extrapolate the Lindhard model, Eq. (2.14), below 254 eV to a choice of three cut-off energies (15, 40, and 90 eV), but use a different model for the extrapolation since the low energy behavior is smoother than the models of Ref. [363, 395]. Here we choose an exponential of the from $Y(E_R) = a(1 - e^{(E_c - E_R)/b})$ where a and b are again chosen to match the high energy model at the branching energy (254 eV). The lines in Fig. 3 are the average of the Ga and As yield function and our results are reported as a sum of the contributions from each component, but we keep the yield functions independent up to the final event rate calculations.

2.3.2 Noble Liquid Detectors. The Noble Liquid detectors, also known as Liquid Noble Gas detectors, used in many of the larger dark matter experiments such as XENON1T and DarkSide are primarily designed to look for nuclear recoils and treat electron recoil signals as background. The filtering of electron recoils

Material	E_g [eV]	ε [eV]
Si [432]	1.2	3.8
Ge [432]	0.7	3.0
GaAs [200]	1.52	4.2

Material	W [eV]	f_R	f_e
Xe [343]	13.8	0	0.83
Ar [218]	19.5	0	0.83

Table 2. Left: values used for the band gap energies (E_g) and the average energy needed to produce additional electron-holes (ε) in the three semiconductor materials considered. Right: values used for the Thomas-Imel model for electron recoil signals in xenon and argon

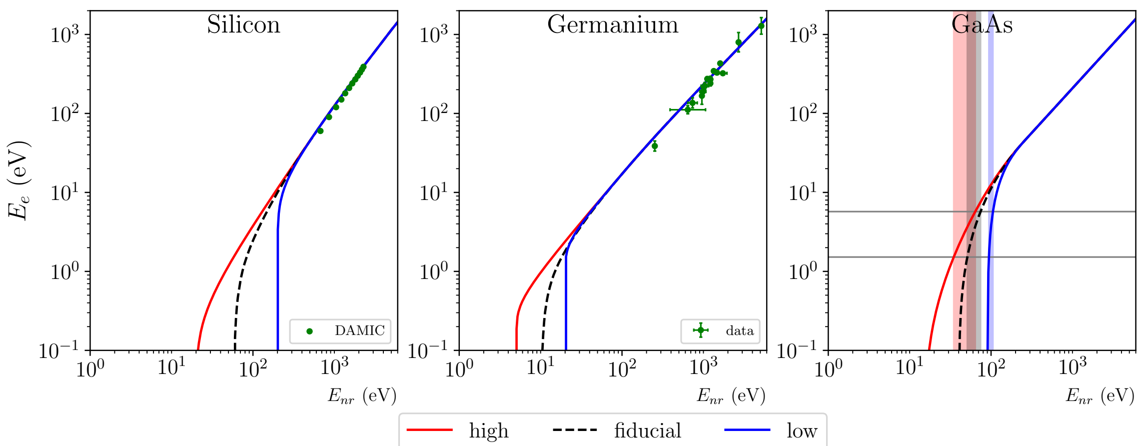

Figure 3. Yield functions in silicon, germanium, and gallium arsenide. Data points for silicon are from the DAMIC collaboration [179] while germanium is from [401, 195]. The vertical bands in the right frame illustrate the sensitivity of the recoil rate to the slope of the yield function. The wider bands imply that a larger range of recoil energies correspond to an event which produces the same number of electrons.

from nuclear recoils is based on the ratio of primary (S1) to secondary (S2) photons produced via scintillation (*i.e.* nuclear recoils) and ionization (*i.e.* electron recoils) respectively. Since the S2/S1 ratio is less effective below ~ 5 keV most analyses and experiments stop there. However, more recently these experiments have embarked on sub-GeV DM searches utilizing the S2-only data sets [85, 56, 183]. Here we argue that keeping these low energy events also allows for the detection of NSIs in a low noise noble liquid environment.

As with semiconductors, we must convert the electron recoil energy into the detectable signal; in this case, the photoelectrons which make up the S2 signal. We adopt the Thomas-Imel model [427] and sum the contributions from recoils of each orbital, of which the next-to-outer shells dominate. In this model, a recoiling electron with energy E_{er} produces both ions (N_i) and excited atoms (N_{ex}) with an average energy W, thus $E_{er} = (N_i + N_{ex})W$ since, at low energies, the fraction of ions which recombine is small ($f_R \sim 0$) and the fraction of observable quanta is $f_e = (1 - f_R)/(1 + N_{ex}/N_i) \approx 0.83$. The total number of observed electrons then follows a binomial distribution of n_1+n_2 with probability f_e where $n_1 = \lfloor E_{er}/W \rfloor$ is the number of quanta produced immediately and n_2 is the number of electrons produced when photons emitted from the excited states photoionize. For a more detailed discussion of this process, see [232]. We report the values used for W, f_R, and f_e in Table 2.

We follow an analogous procedure to the semiconductor case for converting nuclear recoil energy into quantized charges. For liquid xenon and argon detectors, the NEST collaboration [423, 422, 424] has provided excellent simulated models for $n_e(E_R)$ down to energies $\sim$ 200 eV for nuclear recoils which we use to predict the charge yield from nuclear interactions. Below this 200 eV limit, we again extrapolate as a power-law to a spectrum of cut-off energies for nuclear recoils and plot the results in Fig. 4. As can be seen in Fig. 5, the effect of this extrapolation in nuclear recoils is limited to the $1e^-$ and $2e^-$ bins. As with silicon and germanium, [396] provides an updated model for nuclear recoils in xenon, though we find that the choice of yield function has a much less significant effect in noble liquid detectors, and we use the NEST functions in this work.

Finally, to determine the event rate in each charge bin, we must consider the statistics which govern the binning of events so we use Poisson statistics to weight

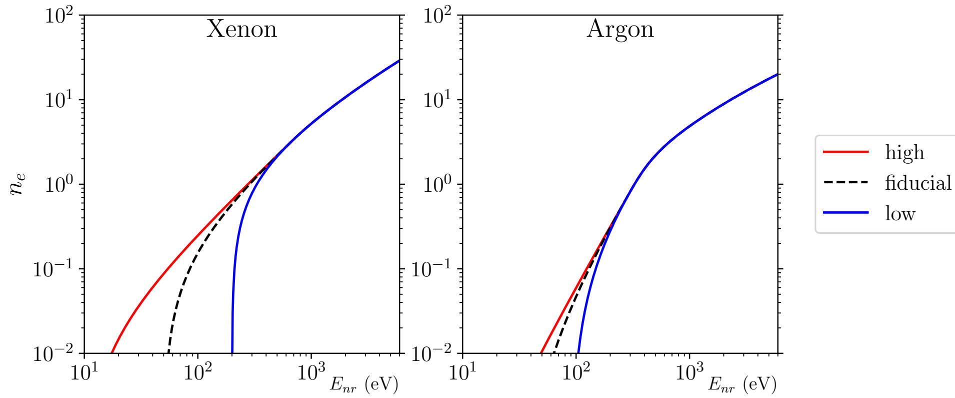

Figure 4. Charge yield of nuclear recoils in noble gases. The extrapolations to 10, 50, and 200 eV for xenon and 5, 30, and 90 eV for argon are fit to NEST simulations using a power-law

the recoil spectrum by its likelihood to be in each charge bin and integrate over all recoil energies to get n_i, the rate of observed events in the i-th electron bin.

$$n_i = \int_{E_R^{min}}^{E_R^{max}} \frac{dR}{dE_R} \frac{n_e^i(E_R)}{i!} e^{-n_e(E_R)} dE_R \tag{2.15}$$

2.3.3 Summary and Discussion on Ionization Signals. We provide a summary of the semiconductor and noble liquid parameters (Table 2) and a summary of the yield functions (Table 3) used in this work. The dependence of Eq. (2.13) on the derivative of the yield function as well at the shift of integration limits means that a more gradually changing yield function will significantly enhance the observed rate in the detector. We highlight the effect of the latter dependency on the $1e^-$ bin in GaAs with the shaded bars in Fig. 3. The width of these bars correspond to the range of nuclear recoil energies which contribute to each charge bin and their effect can be seen in our results that follow. Here, we see that the rates in the lowest charge bins can vary by orders of magnitude between yield functions highlighting the need for accurate, empirical measurements of the yield function at low energy. We investigate the effects of the choice of yield functions in more detail in Appendix A.1

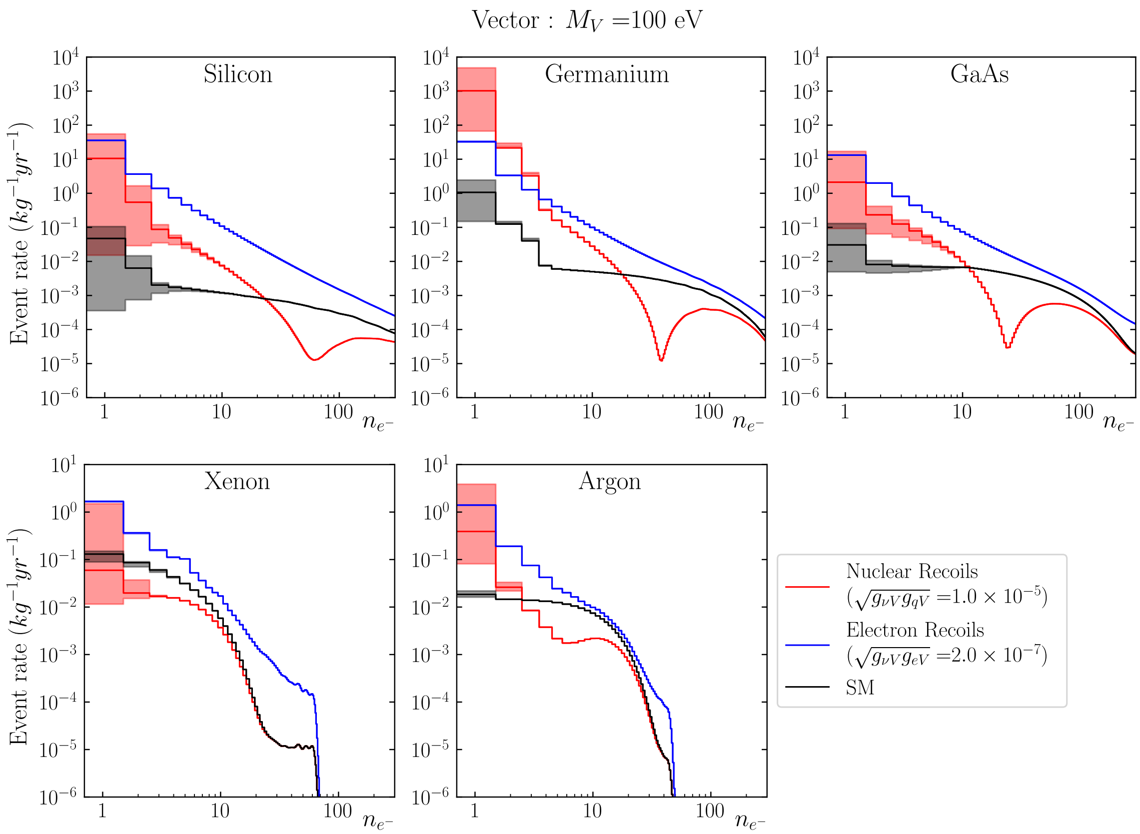

Figure 5. Event rates from nuclear (red) and electron (blue) recoil from a 100 eV vector mediator near the projected bound for vIOLETA [240]. The SM rate is given in black. The bands around the nuclear and SM rates come from varying the choice of ionization yield function.

2.4 Results

In this section, we present the results for the scattering rates as well as projections on the constraints of the NSI couplings. The simplified models – vector, scalar, axial vector, pseudoscalar – contain three free parameters: the mediator mass, the nuclear coupling, and the electron coupling. For the neutrino magnetic moment model, there is only one free parameter: the neutrino magnetic moment μ_ν. In what follows, we present our results in terms of the free parameters of the models under consideration. Note that for the simplified models, the nucleon and electron couplings are independent and must be constrained separately while the one parameter model for the magnetic moment allows for a more detailed analysis which we will discuss in Sec. 2.4.2. To generate constraints on each model from semiconductors and noble liquid detectors, we consider a detector which sees no events above the predicted background at 90%C.L., *e.g.* 3 events.

For the simplified models, we present the 90%C.L. projected constraints at exposures of 0.1, 1, and 30 kg-yrs in semiconductors which corresponds to the expected exposures of SENSEI, DAMIC-M, and OSCURA [131]. We consider exposures of 20, 200, and 1000 tonne-yrs in xenon, corresponding to XENONnT, Darwin [194], and a more far future detector and 50, 360, and 1000 tonne-yrs in argon, the first two being roughly the exposure of DarkSide-20k and ARGO [272], and the third is again a far future detector. Because of their larger exposures, the noble liquid detectors can place a tighter bound on the electron couplings, but the lower threshold of the semiconductors makes them more sensitive to CEvNS and hence improves the quark coupling sensitivity.

As mentioned in Sec. 2.2, we neglected the effects of binding energy in the electron scattering cross-sections. They restrict the available phase space for the interaction and reduce the cross-section at low energies by a factor ~ 3. We approximated this effect in xenon with a series of step functions as in [181] which led to a reduction in sensitivity of $\mathcal{O}(30\%)$ for vector models and $\mathcal{O}(20\%)$ in scalar models, both in the low mass limit. We expect the magnetic moment sensitivity to behave like the scalar under this correction due to its similar $\frac{1}{E_R}$ dependence at low energies and also expect a similar effect in other materials In what follows, we present the results without the effects of binding energy, leaving a more rigorous analysis for later work.

2.4.1 Simplified Models. Using the yield functions from Table 3, the methods described in Sec. 2.2, and the fluxes from Fig. 1 we are able to calculate the

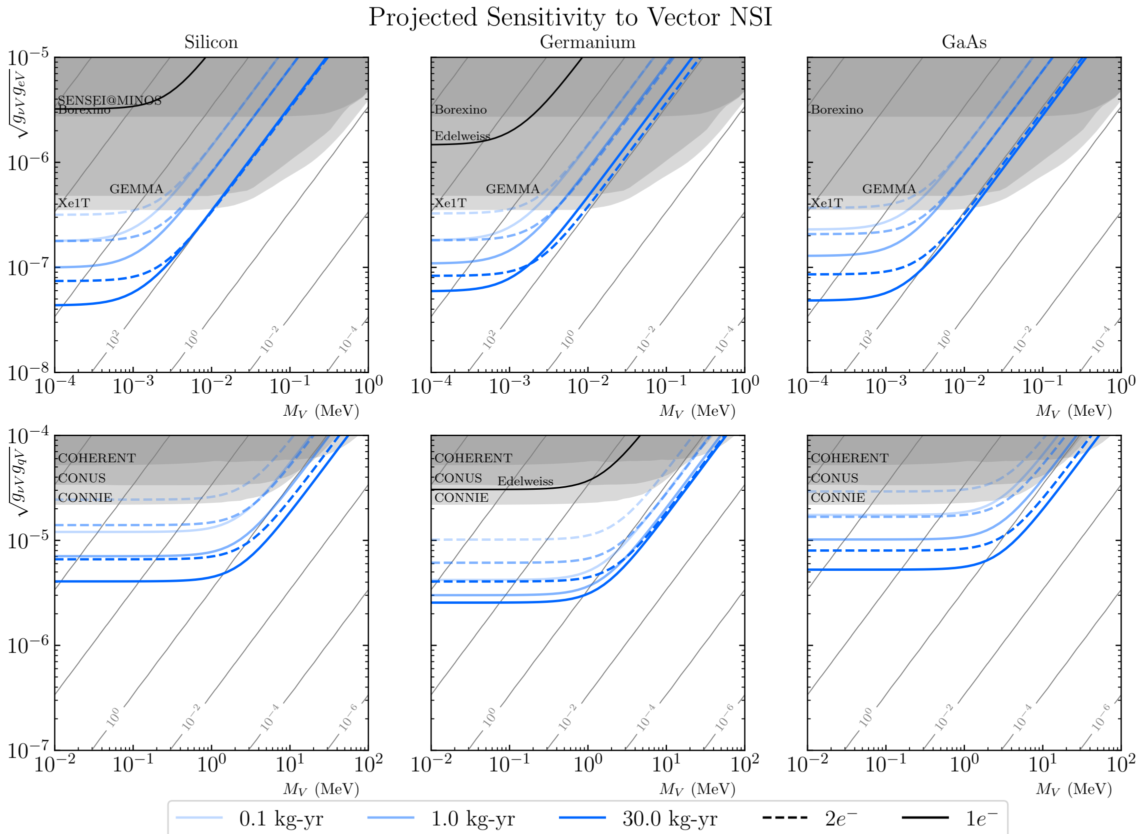

Figure 6. Sensitivity to NSIs mediated by a new vector in Si (left), Ge (middle), and GaAs (right) for electron (top) and nuclear (bottom) couplings. The line shading indicate the exposures of 0.1 (lightest), 1, and 30 (darkest) kg-years, while the solid (dashed) lines denote the one (two) electron bin. Also included are the current constraints from SENSEI@MINOS [406] in silicon and Edelweiss [228] in germanium. The shaded gray regions are the existing constraints on the parameter space and the grey contours are constant ϵ as defined in Eq. (2.16). See text for details.

event rate for an interaction mediated by either a scalar, pseudoscalar, vector, or axial vector coupling either to nucleons or electrons. In the following subsections, we plot illustrative examples of these rates for 100 eV mediators with generation independent couplings near the sensitivity projected for the vIOLETA experiment [240] for both electron (red) and nuclear (blue) recoils. Note that the NSI rates are the *combined* SM background (CEvNS and electron recoils) with the NSI contribution. As such, the region where the blue line is below the black in the vector model indicates destructive

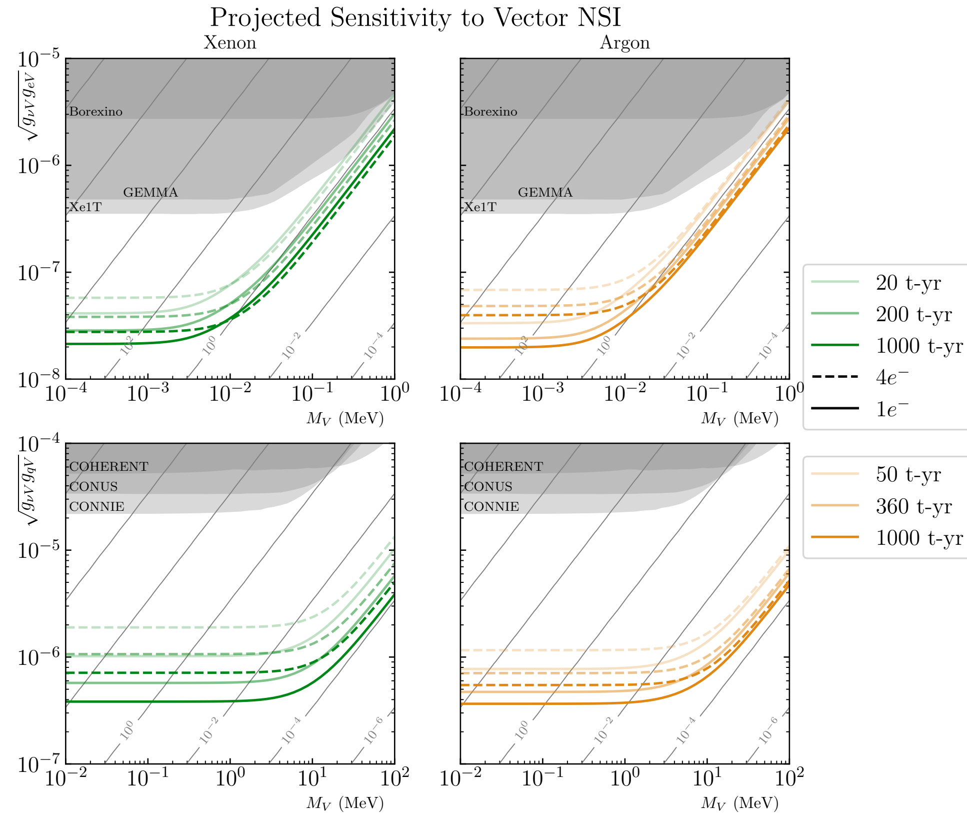

Figure 7. Sensitivity to NSIs mediated by a new vector in Xe (left) and Ar (right) for electron (top) and nuclear (bottom) couplings. The various shadings for the green (orange) lines denote the different exposures for xenon (argon), while the solid (dashed) lines denote the one (four) electron threshold. The shaded gray regions are the existing constraints on the parameter space and the grey contours represent constant ϵ as defined in Eq. (2.16). See text for details.

interference and a negative NSI contribution. The shading indicates the uncertainties resulting from the choice of yield function. Although these only effect the nuclear recoils, they are present in the background from SM CEvNS so we keep them for calculations of our sensitivity to electron couplings though they are too small to be visible in Fig. 5. Both the electron and nuclear rates are sensitive to uncertainties in the solar flux, but these uncertainties are subdominant to the choice of yields function. As such, the majority of the uncertainties in the event rate can be improved without changing the detectors, but rather improved measurement or modeling of the yield function.

Each of the bins in Figs. 5, 8, 11, and 14 can be used to place a constraint on the parameters of the model used to generate the NSI rate. At the exposures of interest in semiconductors, the background is essentially undetectable and any NSI signal will be dominated by the 1 and 2 e^- bins since they correspond to the lowest energy recoils, so we focus on those. The $1e^-$ bin will generally provide the stronger constraint at low exposures, but the $1e^-$ bin may still have too much noise in some experimental environments.

We consider two simplified cases in noble liquid detectors. The first is a sum of all events with four or greater electrons as such detectors are already sensitive to. The second is a sum of all events including those with less than four electrons. In each of these cases, the sensitivity could be improved by evaluating a likelihood function with a global fit to the entire set of event rates, but we take the simplified cases as conservative limits and simply note that qualitatively, the more robust analysis would have a larger improvement for the all-charges-included case since the low charge behavior has a stronger deviation from the SM and switches between constructive and destructive interference in the vector mediated case. In the vector case, we note that we do not consider the direction of the deviation from the SM, but rather consider the absolute value of this deviation and its ratio with the SM expectation.

In the subsections that follow, we overlay our projected sensitivity for the materials discussed in Sec. 2.3 on existing constraints. Existing nuclear coupling constraints come from CONUS [193], CONNIE [63], and COHERENT [341, 158, 277, 98, 96]. The latter is a collection of detectors using liquid argon, CsI(Na), and NaI(Tl) at the Spallation Neutron Source at Oakridge National Laboratory [71]

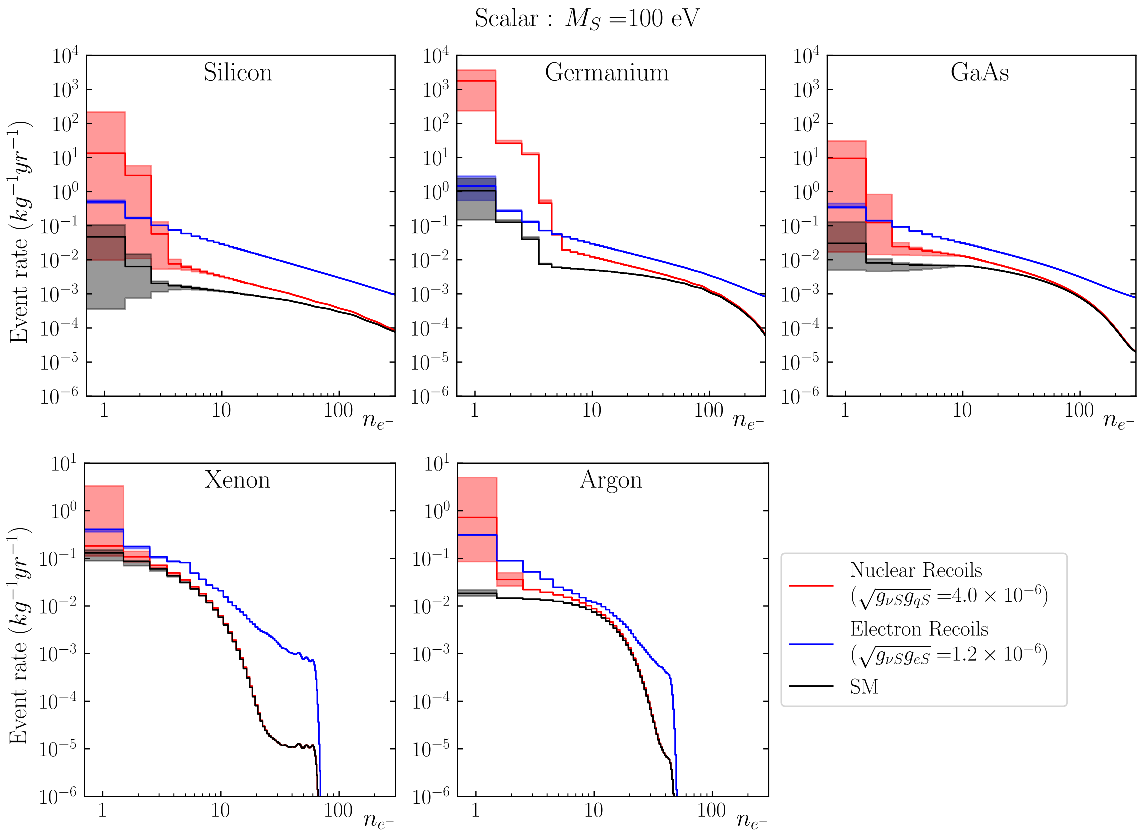

Figure 8. Event rates from nuclear (red) and electron (blue) recoil from a 100 eV scalar mediator near the projected bound for vIOLETA [240]. The SM rate is given in black. The bands around the nuclear and SM rates come from varying the choice of ionization yield function.

while the first two are germanium and silicon detectors at commercial nuclear power plants. As such, they are only sensitive to couplings to electron-neutrinos while COHERENT is sensitive to all flavors. Their constraints also depend on the particular properties of their detector materials. For instance, the argon detector subsystem of COHERENT cannot constrain axial vector mediators since argon nuclei have no spin. While CONUS and CONNIE can place constraints on the coupling to electrons, they are subdominant to some larger experiments. We focus instead on the results of XENON1T [160, 95, 101], Borexino [291], Texono [207], and GEMMA [240]. As a dark matter detector, XENON1T is designed to search for DM-nucleus recoils which are

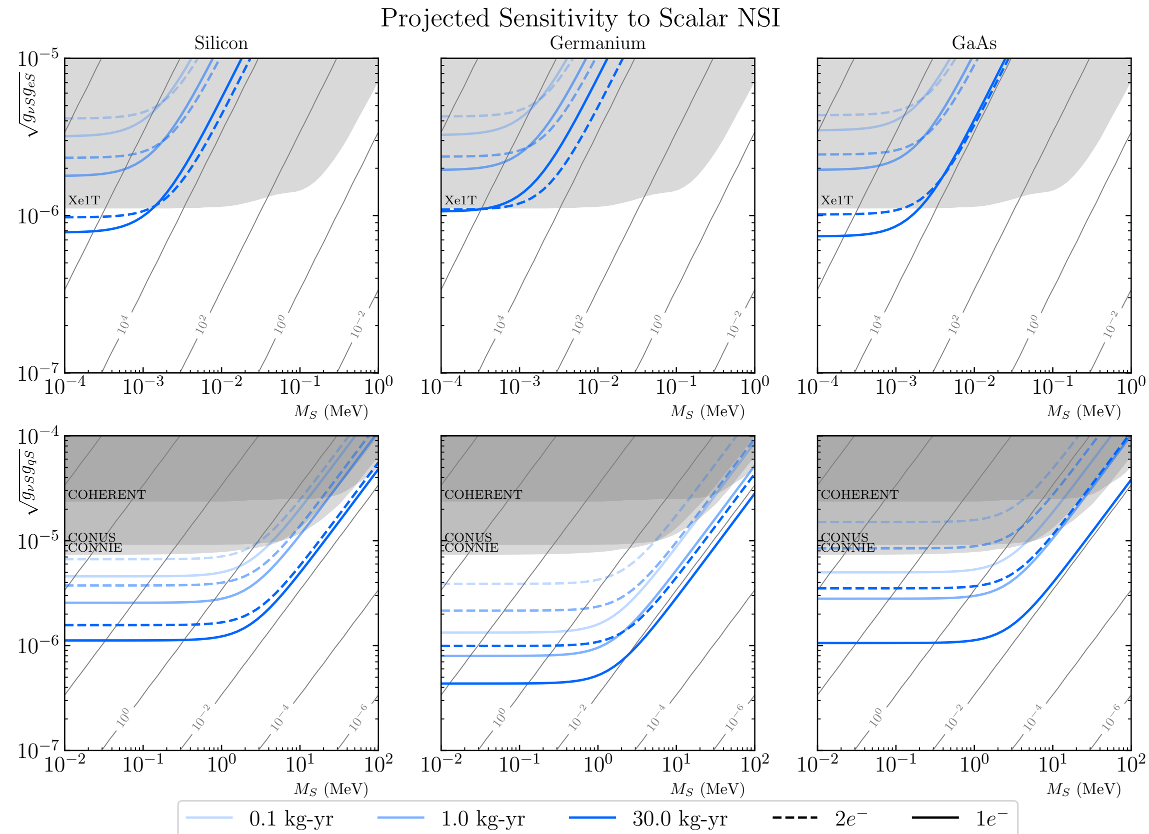

Figure 9. Sensitivity to NSIs mediated by a new scalar in Si (left), Ge (middle), and GaAs (right) for electron (top) and nuclear (bottom) couplings. The line shading indicates the exposures of 0.1 (lightest), 1, and 30 (darkest) kg-years, while the solid (dashed) lines denote the one (two) electron bin. The shaded gray regions are the existing constraints on the parameter space. The grey contours represent constant ϵ as defined in Eq. (2.16). See text for details.

individually indistinguishable from CEvNS. Such a distinction could only be made by the energy distribution of those recoils. The most distinct feature of that distribution is the much lower energy of CEvNS. Since DM recoils are at higher energy, XENON1T is not optimized to see CEvNS so we can only place competitive constraints on electron couplings since the lighter target recoils with higher energy. Borexino [106] uses a 5-ton liquid scintillator to detect scattering of solar neutrinos off of electrons. It is therefore sensitive to couplings with any neutrino flavor. Texono [207] and

GEMMA [133] are reactor experiments, with the former using a 187 kg CsI(Ti) scintillating crystal and the latter using a 1.5 kg germanium detector. As with other reactor experiments, they are only sensitive to electron-neutrinos.

$$\epsilon = \frac{g_{\nu i} g_{SMi}}{M_i^2 G_F} \tag{2.16}$$

As discussed in Sec. 2.1 we are using a different convention than much of the literature regarding NSIs. Elsewhere, the NSI strength is often given by ϵ (see *e.g.* [214]) which parameterizes the strength relative to the SM weak force and relates to our couplings by Eq. (2.16) where $g_{\nu i}$ and g_{SMi} are the couplings from Table 1 coupling the mediator (i) to neutrinos and quarks/electrons respectively. To visualize this relation, we include contours of constant ϵ in the figures covering the relevant parameter space.

2.4.1.1 Vector. We show the rates for neutrino-nucleus and neutrino-electron scattering in Fig. 5 for $m_V = 100$ eV and couplings near the projected bound for the vIOLETA experiment [240]. Here, we clearly see the enhancement in the rate at low-energies that result from the $\sim 1/E_R^2$ scaling for $E_R > m_V^2/m_T$, as discussed in Sec. 2.2.2. In addition, the new vector mediator leads to a unique feature in the recoil spectrum, which arises from the destructive interference between the new vector and the SM weak bosons. This destructive interference is visible at $n_e \sim 20 - 40$ in the semiconductor materials, where the nuclear recoil event rate drops below the SM rate in Fig. 5. Although not pertinent for our studies, which focus on the lowest charge bins, this unique feature could serve as a powerful means of discriminating between signal and background.

In Figs. 6 and 7, we plot the projected sensitivities to a vector mediator in semiconductor and noble liquid detectors, respectively. In Ar and Xe, the $1(4)e^-$

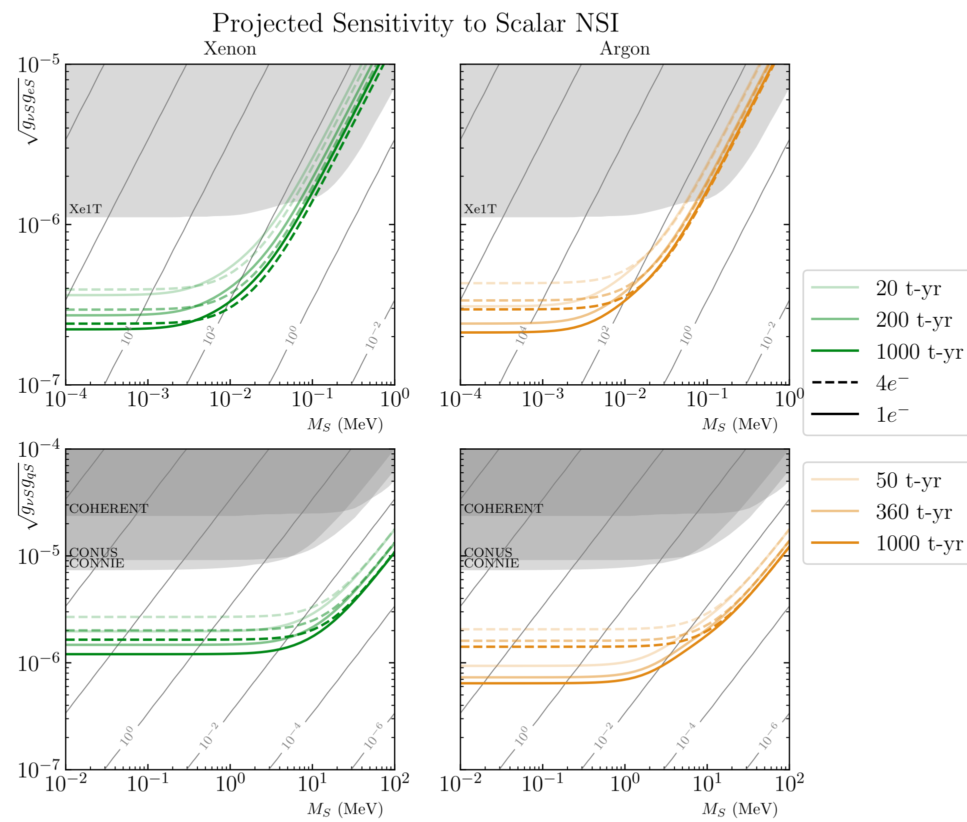

Figure 10. Sensitivity to NSIs mediated by a new scalar in Xe (left) and Ar (right) for electron (top) and nuclear (bottom) couplings. The various shadings for the green (orange) lines denote the different exposures for xenon (argon), while the solid (dashed) lines denote the one (four) electron threshold. The shaded gray regions are the existing constraints on the parameter space. The grey contours represent constant ϵ as defined in Eq. (2.16). See text for details.

refers to the lower bound of the summation of events while in the semiconductors, the $1(2)e^-$ refers explicitly to the charge bin used to derive the constraints. Electron-coupling constraints are plotted in the upper panels and nuclear ones on the lower. We see that, despite the destructive interference that appears at the high-electron bin, the low-thresholds of these experiments lead to an improvement of the sensitivity to both electron and nuclear couplings. In particular, the improvement from decreasing the threshold can, in some cases, be more significant than increasing the exposure. For comparison, we also calculate the constraints from SENSEI@MINOS [406] – the results from CDMS-HVeV [79] will be comparable – and Edelweiss [228] on the silicon and germanium panels, respectively, and show that they can be comparable to some of the existing constraints for low vector masses.

2.4.1.2 Scalar. We plot an example event rate for the scalar mediated interaction in Fig. 8. In contrast to the vector case discussed above, we see that the scalar recoil rate has a weaker enhancement at low E_R, as discussed in Sec. 2.2.2. Thus, we expect the sensitivity of semiconductor targets to be reduced as these targets have relatively small exposures and rely on the enhancement at low-energies to have competitive bounds. This reduced sensitivity is evident in Figs. 9 and 10 where even a 30 kg-yr semiconductor struggles to match the results of XENON1T. The new constraints from SENSEI@MINOS and Edelweiss are $4.0 \times 10^{-5}/1.3 \times 10^{-4}$ and $3.0 \times 10^{-5}/1.1 \times 10^{-4}$ respectively for the electron/quark couplings; these values are not competitive with existing constraints and thus do not appear in Fig. 9.

2.4.1.3 Axial vector. Like the vector model, the axial vector mediated cross-section has a $1/E_R^2$ enhancement for light mediators at low energies so semiconductors regain their advantage. However, there is an additional suppression due to the coupling of the axial vector to spin, which we can see explicitly in the

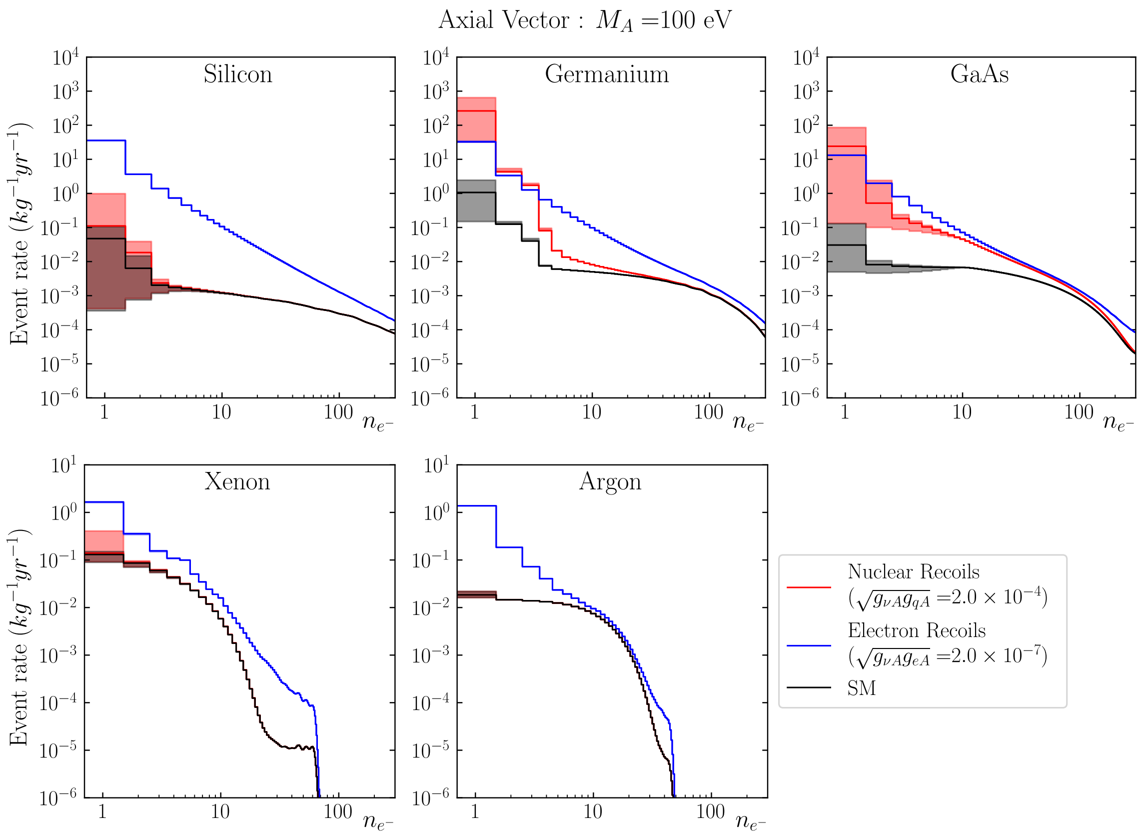

Figure 11. Event rates from nuclear (red) and electron (blue) recoil from a 100 eV axial vector mediator near the projected bound for vIOLETA [240]. The SM rate is given in black. The bands around the nuclear and SM rates come from varying the choice of ionization yield function.

lower panels of Figs. 12 and 13. Of particular note is argon and silicon; argon is not sensitive to axial vector mediated nuclear scattering since it has no nuclear spin (the same is true of ^{4}He although we do not include it in this work). This feature of argon, combined with its sensitivity to the other models, makes it a useful material to distinguish an axial vector mediator if a signal is seen in other materials. Similarly, the abundance-averaged spin of silicon is small, so the rate is also suppressed there.

2.4.1.4 Pseudoscalar. The pseudoscalar mediator case is notably distinct from the other three simplified models in that it does not couple to nuclei, resulting in no enhancement for nuclear scattering (see second line of Eq. (2.10)). Instead,

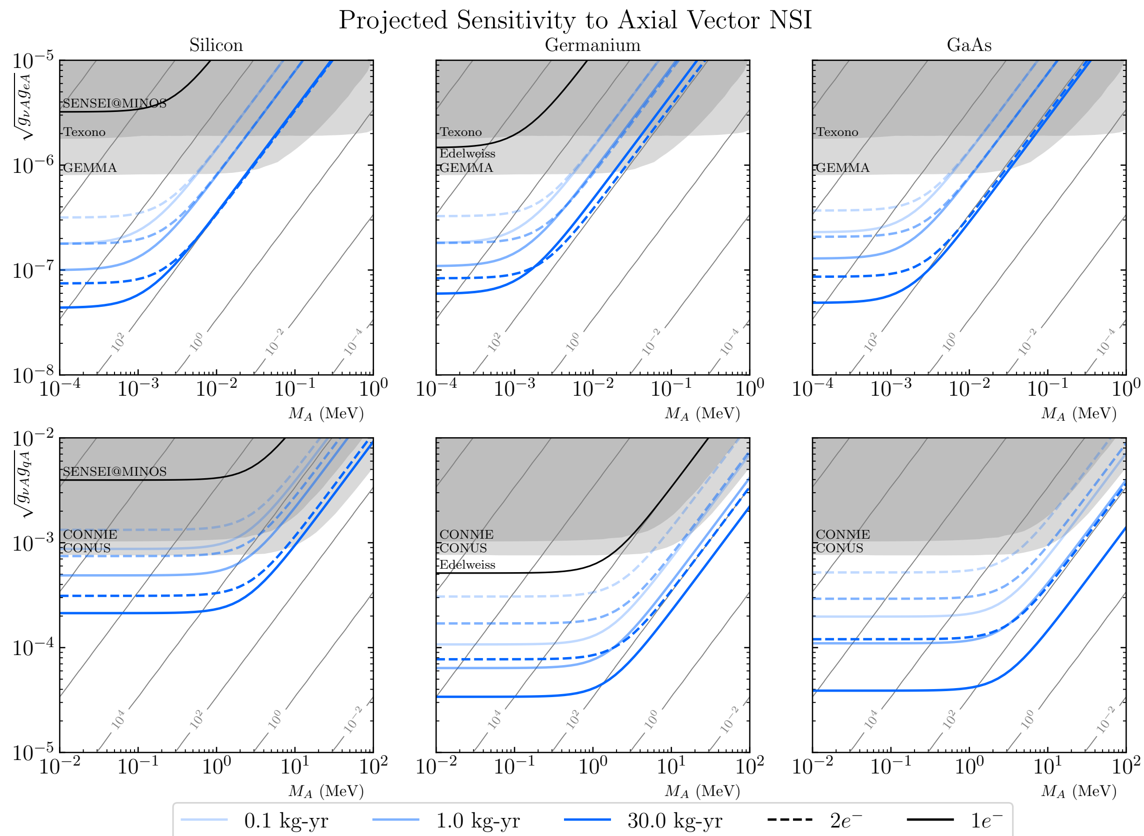

Figure 12. Sensitivity to NSIs mediated by a new axial vector in Si (left), Ge (middle), and GaAs (right) for electron (top) and nuclear (bottom) couplings. The line shading indicates the exposures of 0.1 (lightest), 1, and 30 (darkest) kg-years, while the solid (dashed) lines denote the one (two) electron bin. In the lower left panel, we see the effect from the suppression due to the small abundance-averaged spin in silicon. The shaded gray regions are the existing constraints on the parameter space. The grey contours represent constant ϵ as defined in Eq. (2.16). See text for details.

the NSI only appear in the electron-scattering rates, as shown in Fig. 14. Therefore, detectors that can distinguish between low-energy nuclear and electron recoils could be a promising way to test such a model. However, the recoil rate of a light pseudoscalar mediator is not enhanced at low energies, negating the advantages of low-threshold detectors. The top panels of Fig. 15 show that semiconductor targets require exposures well above the anticipated exposures of future experiments to probe

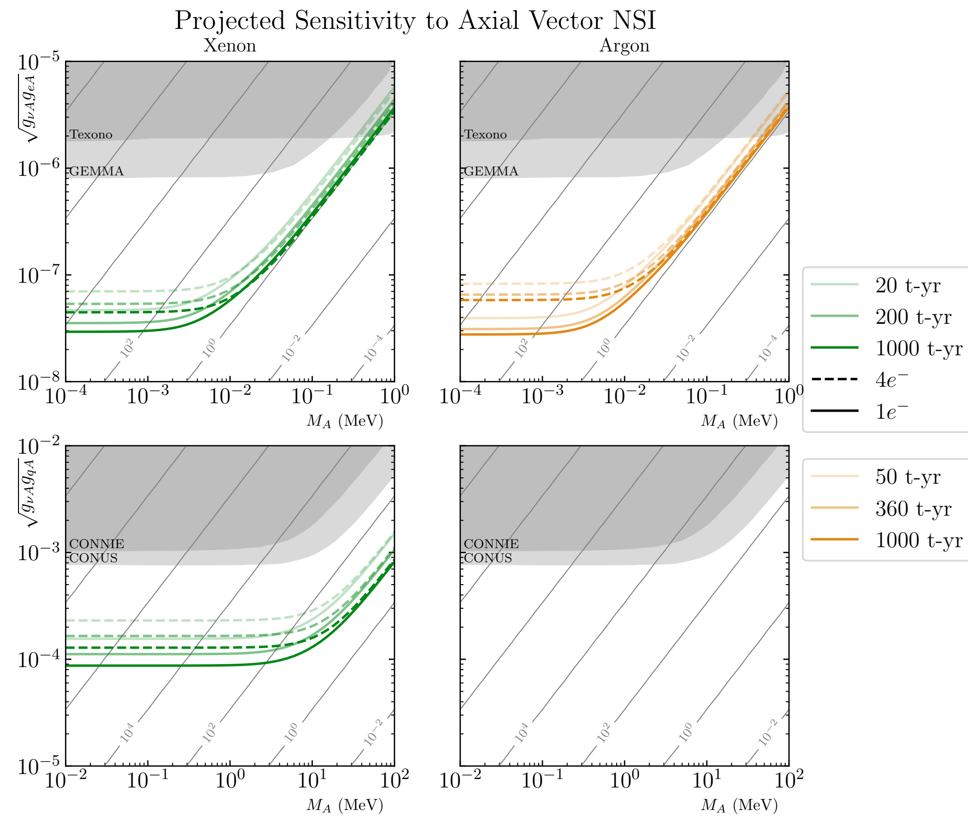

Figure 13. Sensitivity to NSIs mediated by a new axial vector in Xe (left) and Ar (right) for electron (top) and nuclear (bottom) couplings. The various shadings for the green (orange) lines denote the different exposures for xenon (argon), while the solid (dashed) lines denote the one (four) electron threshold. The lower right panel shows the effects of argon's lack of net nuclear spin. The shaded gray regions are the existing constraints on the parameter space. The grey contours represent constant ϵ as defined in Eq. (2.16). See text for details.

open parameter space. The noble liquid detectors are more promising and can probe new parameter space for pseudoscalar masses below ~ 50 keV.

2.4.2 Magnetic moment. We plot the event rate for the magnetic moment in Fig. 16 for a magnetic moment at the Borexino bound.

To predict the sensitivity of a detector to the neutrino magnetic moment, we use a more robust analysis because the model is fully determined by a single parameter. We define the likelihood that a particular distribution of events in an observing run

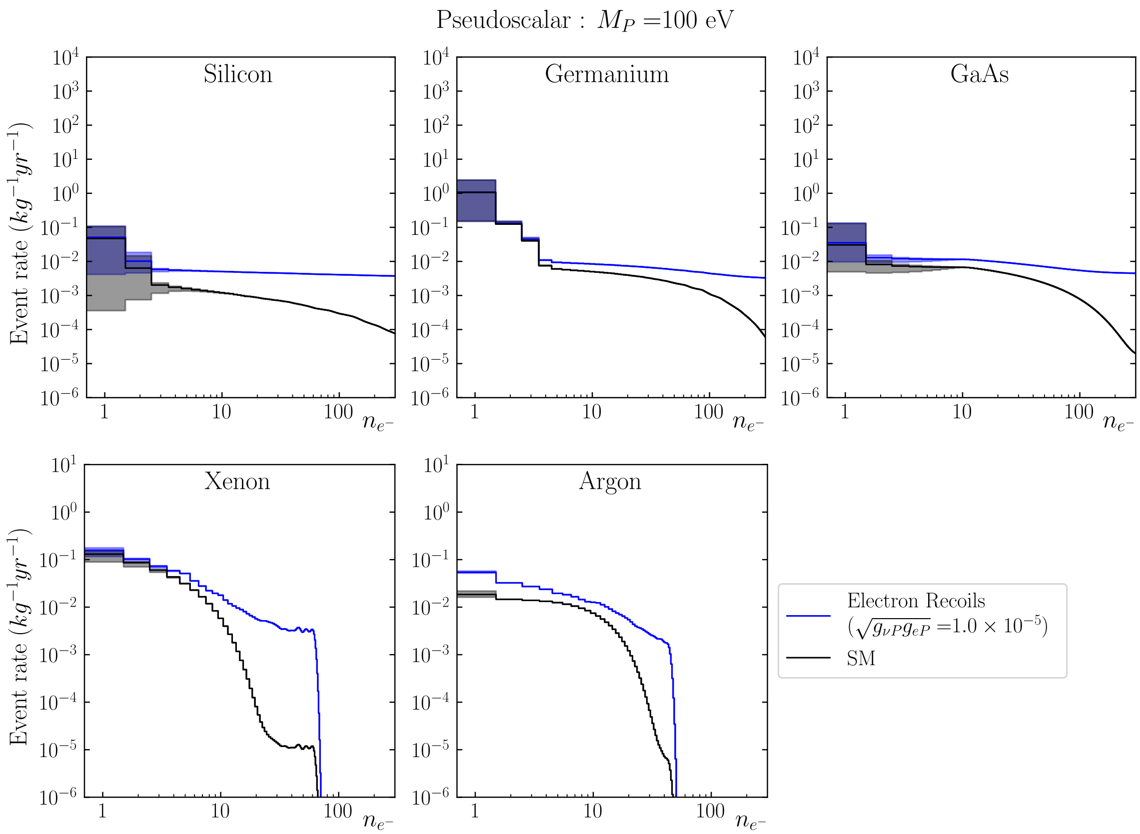

Figure 14. Event rates from electron (blue) recoil from a 100 eV pseudoscalar near the projected bound for vIOLETA [240].

is the result of our signal model (the magnetic moment) or the background (SM),

$$\mathcal{L}(\mu_\nu, \vec{\phi}) = \frac{e^{-(\eta_\mu + \Sigma_{j=1}^{n_\nu} \eta_j)}}{N!} \times \prod_{j=1}^{n_\nu} \mathcal{L}(\phi_j) \times \prod_{i=1}^{N} \left(\eta_\mu f_\mu(n_i) + \sum_{j=1}^{n_\nu} \eta_j f_j(n_i) \right) . \tag{2.17}$$

In so doing, we consider both the total rate of events as well as their distribution in the charge bins. This approach includes the effect of the uncertainties in the solar neutrino fluxes and can be generalized to determine the significance between multiple BSM models.

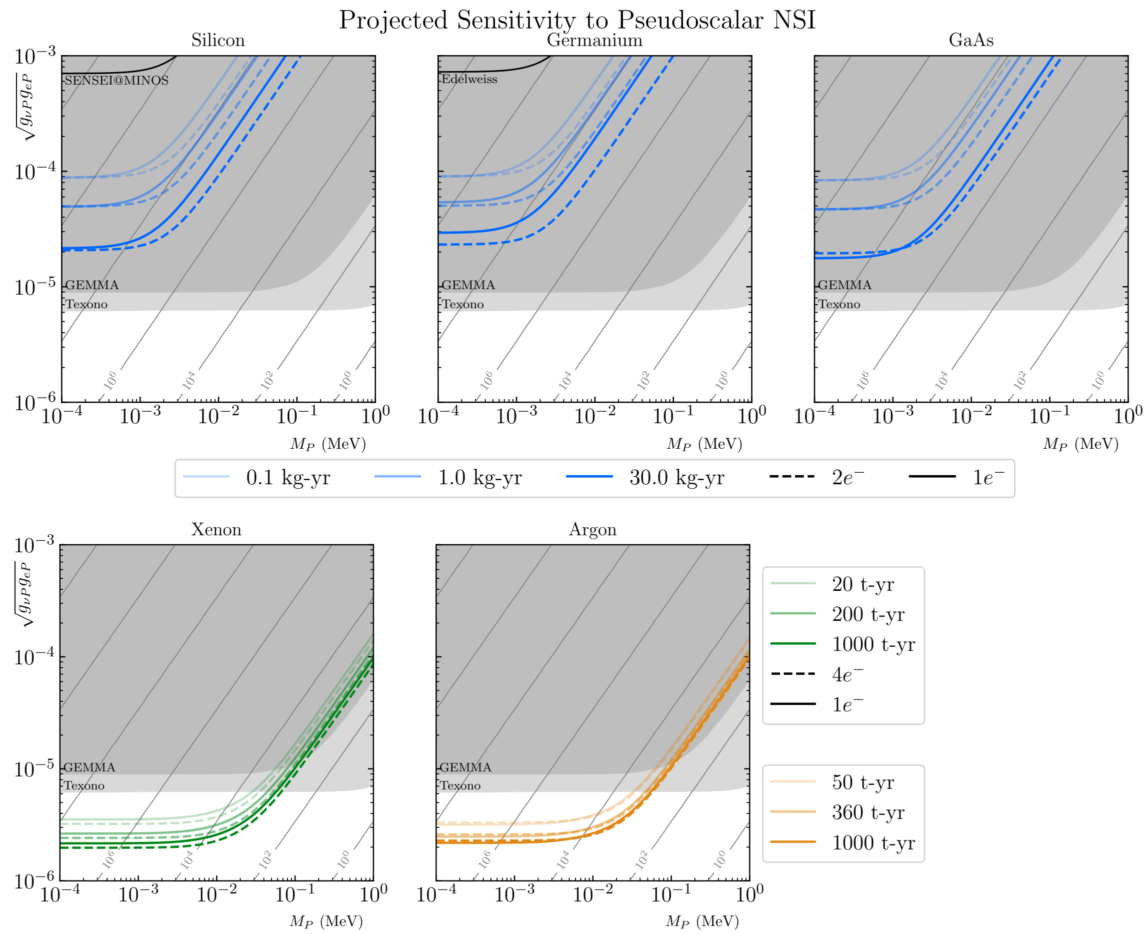

Figure 15. Sensitivity to NSIs mediated by a new pseudoscalar in semiconductor (top) and noble liquid (bottom) targets. The colored lines correspond to the varying exposures, while the solid (dashed) lines correspond to the detector thresholds. Note that, in contrast with the other simplified models, the pseudoscalar only couples to **electrons**. The grey contours represent constant ϵ as defined in Eq. (2.16).

Our approach follows the analysis in Ref. [235] and uses the likelihood function Eq. (2.17) where μ_ν and $\vec{\phi}$ are nuisance parameters corresponding to the magnetic moment and neutrino fluxes respectively. η_μ and η_j are the number of events resulting from the magnetic moment and j-th component of the solar flux respectively, and $f_\mu(n_i)$ and $f_j(n_i)$ are the (normalized) distributions of events in the n_i bin from the magnetic moment and solar flux components. We then vary the nuisance parameters to maximize the likelihood functions both with $\mu_\nu = 0$ fixed and with μ_ν as a free nuisance parameter. The statistical penalty associated with these variations of the fluxes is captured by

$$\mathcal{L}(\phi_j) = \frac{1}{\sigma_j\sqrt{2\pi}} e^{-\frac{1}{2}\left(\frac{\phi_j - \phi_{0,j}}{\sigma_j}\right)^2} . \tag{2.18}$$

The ratio of these two minima

$$\lambda = \frac{\mathcal{L}_{max}(\mu_\nu = 0, \vec{\phi})}{\mathcal{L}_{max}(\mu_\nu \neq 0, \vec{\phi})} , \tag{2.19}$$

is used to determine the test statistic: $t = -2\log(\lambda)$ if the magnetic moment which maximizes $\mathcal{L}$ is positive and zero otherwise.

This process gives the significance $\sigma = \sqrt{t}$ of a single data set containing the number of observations in each charge bin. To project a discovery reach, we assume the NSI exists, generate 1000 sets of Poisson fluctuated pseudodata around the rates predicted by the NSI at each exposure or magnetic moment and average the significance.

For the neutrino magnetic moment, we plot the results of our more rigorous analysis and show the projected reach of a 100 kg-yr detector as a function of the magnetic moment and the discovery reach for a fixed magnetic moment ($\mu_\nu = 2.8 \times 10^{-11}\mu_b$) at the Borexino bound as a function of the exposure.

2.5 Interpreting Simplified Models

We have presented our results in the language of simplified models, which focuses on the low-energy Lagrangian without specifying the gauge-invariant models at high-energies. However, one can map our results to motivated UV-completions to compare the constraints from low-threshold direct-detection experiments and with other model-specific probes.

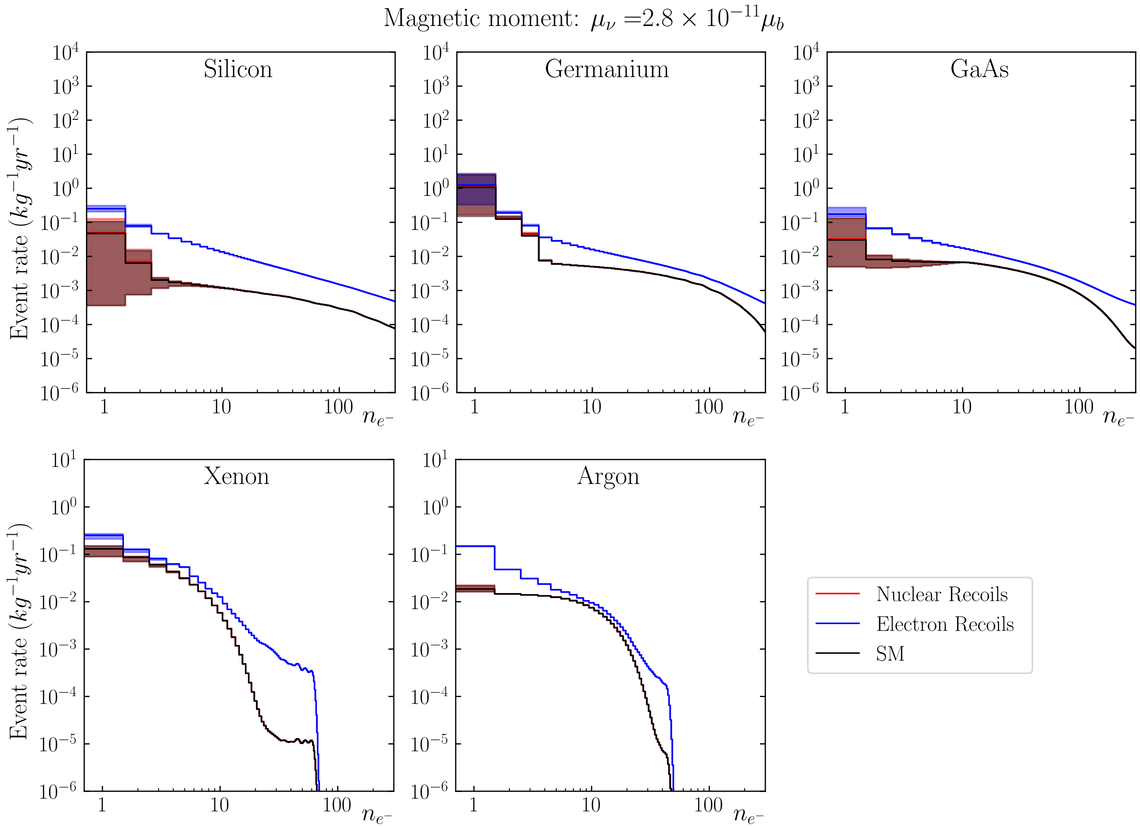

Figure 16. Recoil rates from a neutrino magnetic moment at the Borexino bound. Note that given one free parameter, the nuclear recoil rate (blue) is indistinguishable from the SM rate (black) while the electron rate (red) has a different spectral shape. The uncertainties, denoted by the bands, are dominated by the yield function's effect on the SM nuclear recoils.

As an illustrative example, one can map the vector-mediated model to the well-studied gauged $U(1)_{B-L}$. The Lagrangian for such a model is given by

$$\mathcal{L}_{B-L} \supset -g_{B-L}\bar{e}\gamma^\alpha A'_\alpha e + \frac{1}{3}g_{B-L}\bar{q}\gamma^\alpha A'_\alpha q - g_{B-L}\bar{\nu}\gamma^\alpha A'_\alpha \nu - \frac{1}{2}\epsilon F'_{\mu\nu}F^{\mu\nu}\,, \quad (2.20)$$

where A' is the new vector boson, g_{B-L} as the gauge coupling and ϵ is the kinetic mixing of the SM photon A and A'. In addition to the direct-detection constraints presented in this work, the $B-L$ model has constraints from both terrestrial experiments [140, 378, 156, 128, 234, 231, 127, 65, 164, 48] and astrophysical observables [199, 208, 385, 94, 361, 242, 106, 134, 290]. In Fig. 18, we show these

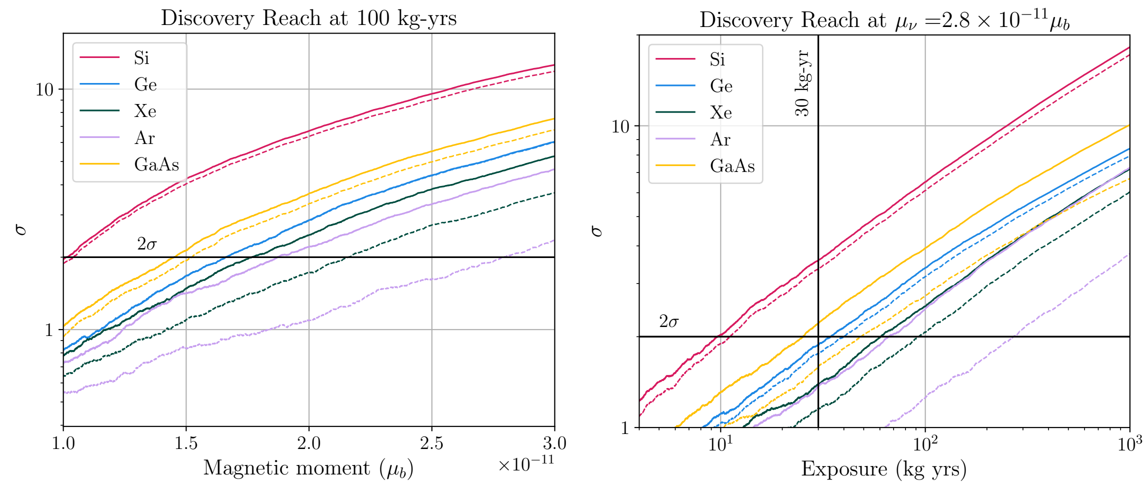

Figure 17. The discovery reach for the magnetic moment as a function of the value of the magnetic moment (left) and exposure (right). Solid lines are derived using all charge bins, dashed are using $n_e = 2$ in the semiconductors (Si, Ge, GaAs) and $n_e \geq 4$ in Xe and Ar.

additional constraints, color coded by whether the constraint depends on couplings to electrons (blue), both electrons and nuclei (grey), or either (red). A priori, the astrophysical constraints which arise from stellar cooling measurements dominate the parameter space of interest.

Additionally, there is a choice of parameters ϵ, g_{B-L} such that the gauge contribution exactly cancels with the kinetic mixing of the new vector boson with the photon, which provides an interesting case where the new vector directly couples only to neutrons and neutrinos and couplings to electrons are loop-suppressed.[2] This loop-suppression relaxes several of the astrophysical constraints, specifically the ones that rely on the electron-coupling, while preserving the direct-detection constraints. The sensitivities to nuclear couplings plotted in Figs. 6 and 7 will change modestly in such a model. The cancellation eliminates the couplings to protons which reduces

[2]However, such a choice presents both a fine-tuning problem and a stability problem under renormalization group evolution (see *e.g.* discussion in [294]).

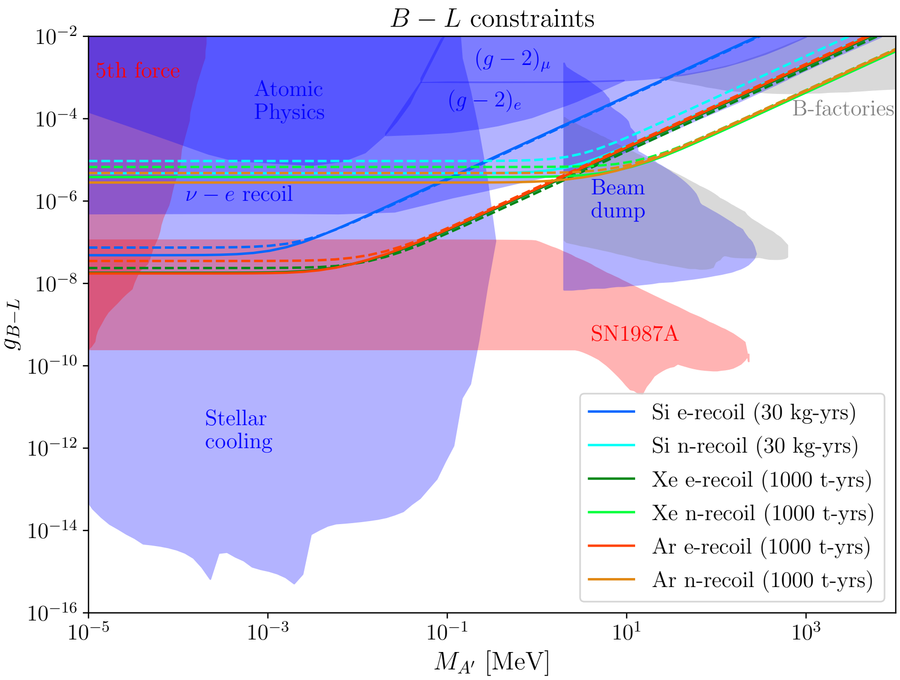

Figure 18. Constraints on gauged $B - L$ from terrestrial and astrophysical sources. Blue regions are sensitive to electron couplings, grey regions require both couplings and red regions are sensitive if the A' couples to either. SN1987A is dominated by neutrino pair coalescence and is therefor relevant regardless of electron and quark couplings [199] as are fifth force searches [48, 164]. The anomalous magnetic moment [140], atomic physics [127], and stellar cooling [385, 290] constraints require leptonic couplings. A stellar cooling bound can also be produced without an electron coupling by ν radiation, but this process is subdominant. The beam dump constraints [156, 128] can be divided into two categories: proton and electron beams. Both look for e^+e^- final states, but the former (grey) requires both electron and baryon couplings while the latter (blue) requires only electron couplings. The B-factories [175] constraint relies on both electron and quark couplings. The $\nu - e$ constraint [175] uses combined results of GEMMA [133], Borexino [106], Texono [207], and CHARM-II [152]. The blue (cyan) lines represent the projected sensitivity of silicon using electron (nuclear) recoils and line styles the same as Fig. 6. Similarly, green (lime) lines represent the electron (nuclear) detection channels in xenon and dark (light) orange for argon. For noble elements, the line style matches Fig. 7

the effective coupling Eq. (2.11) by a factor of $A/(A-Z)$, thereby reducing the sensitivity to nuclear scattering. In contrast, the sensitivities to electron-scattering will be greatly reduced as the interactions are cancelled at tree-level and the mediator becomes leptophobic. This alleviates the constraints (shown in blue and gray in Fig. 18) arising from stellar cooling, beam-dump experiments, $\nu - e$ recoils, and $(g-2)$. However, the constraints coming from fifth force experiments [127, 48, 164] and SN1987a [199, 208, 385] still apply as these rely on the coupling to nucleons. Chameleon effects are another proposed way to evade or weaken astrophysical constraints [239].

In addition to $U(1)_{B-L}$, a vector model can be mapped to $U(1)_{L_\mu - L_\tau}$ or the kinetic mixing of heavy sterile neutrinos. The latter can be tuned in such a way that the heavy neutrinos only produce recoils at arbitrarily low energy to evade constraints from existing detectors even with a much larger coupling. Low-threshold detectors provide an excellent way to study such a model.

Constraining scalar-mediated interactions of neutrinos is relevant as such models can influence neutrino oscillations in matter by modifying the effective mass matrix [110]. This effect is independent of the neutrino energy, unlike the vector or axial vector cases which modify the matter potential. Since the scalar interactions change the effective mass matrix, they change the CP phase and can lead to fake CP violation [266].

Axial vector currents would evade the next generation of long baseline neutrino oscillation experiments which will be able to place strong constraints on vector currents due to their influence on the matter potential [359]. This makes the improvement seen in Figs. 12 and 13 more important.

Note that we have not provided an exhaustive list of UV complete theories, as the set of simplified NSI models discussed in this paper are common to a large set of theories.

Acknowledgments

We thank Haidar Esseili, Guillermo Fernandez-Moroni, and Youssef Sarkis Mobarak for many useful discussions, as well as Roni Harnik, Joachim Kopp, and Pedro Machado for comments on the manuscript. This work was supported in part by NSF CAREER grant PHY-1944826.

Semiconductors: $Y(E_R)$

		E_c [eV]	Transition ($E_c < E_R < E_b$)	High energy model
silicon ($E_b = 600$ eV)	high	20	$4.49 \times 10^{-3} \times (E_R - E_c)^{0.486}$	
	fiducial	60	Sarkis et al.	Sarkis et al.
	low	200	$1.33 \times 10^{-2} \times (E_R - E_c)^{0.335}$	
germanium ($E_b = 100$ eV)	high	5	$7.06 \times 10^{-2} \times (E_R - E_c)^{0.195}$	
	fiducial	10	Sarkis et al.	Sarkis et al.
	low	20	$8.35 \times 10^{-2} \times (E_R - E_c)^{0.164}$	
gallium ($E_b = 254$ eV)	high	15	$0.183 \times (1 - e^{(E_R-E_c)/71.9)}$	
	fiducial	40	$0.182 \times (1 - e^{(E_R-E_c)/61.5})$	Lindhard
	low	90	$0.180 \times (1 - e^{(E_R-E_c)/42.7})$	
arsenic ($E_b = 254$ eV)	high	15	$0.180 \times (1 - e^{(E_R-E_c)/71.9})$	
	fiducial	40	$0.179 \times (1 - e^{(E_R-E_c)/61.5})$	Lindhard
	low	90	$0.177 \times (1 - e^{(E_R-E_c)/42.7})$	

Noble Liquids: $n_e(E_R)$

xenon ($E_b = 667$ eV)	high	10	$7.61 \times 10^{-4} \times (E_R - E_c)^{1.29}$	
	fiducial	50	$1.36 \times 10^{-3} \times (E_R - E_c)^{1.21}$	NEST
	low	200	$1.16 \times 10^{-2} \times (E_R - E_c)^{0.914}$	
argon ($E_b = 300$ eV)	high	10	$1.57 \times 10^{-6} \times (E_R - E_c)^{2.31}$	
	fiducial	50	$5.70 \times 10^{-6} \times (E_R - E_c)^{2.12}$	NEST
	low	200	$1.16 \times 10^{-4} \times (E_R - E_c)^{1.66}$	

Table 3. Yield functions for semiconductors ($E_e = E_R \times Y(E_R)$) and noble liquids ($n_e(E_R)$). Yields are zero below the cut-off (E_c) and match the high-energy model above the branching energy E_b. The high-energy models are given by Sarkis et al. [396, 395], Lindhard [344], and NEST [422]

CHAPTER III

HUNTING NONSTANDARD NEUTRINO INTERACTIONS AND LEPTOQUARKS IN DARK MATTER EXPERIMENTS

This work is co-authored with Volodymyr Takhistov and Tien-Tien Yu and is published in the Journal of Cosmology and Astroparticle Physics [404].

In this chapter, we continue the discussion of neutrino non-standard interactions now shifting to align with the conventional definition of NSI in the literature. Since the discovery of neutrino oscillations [259], a multitude of experiments have confirmed and further developed the SM picture of neutrino interactions and 3-flavor oscillations [441]. With neutrino physics entering the precision era in a broad, world-wide program including a variety of upcoming major next generation experiments such as DUNE and Hyper-Kamiokande, significant attention is being devoted to probing new neutrino physics. Sizable novel NSI can readily appear (see e.g. [1] for review) in broad classes of motivated models, such as those based on SM extensions by an additional $U(1)$ gauge symmetry and new mediators (e.g. [237]). These NSI will be observable in the previously mentioned upcoming neutrino experiments.

Along with precision tests of SM parameters, observations of CEνNS, such as data from COHERENT, allow for a unique probe of neutrino NSI and related theoretical models [126, 400, 360, 342, 273, 315, 211, 238, 92, 151, 148, 204, 121, 171, 243, 210]. Upcoming next generation DM experiments will have sensitivity to CEνNS that allows for unique opportunities to test novel neutrino interactions in complementary ways to dedicated neutrino experiments. Studies already initiated exploration of the reach of DM detectors to neutrino NSI [292, 174] mediated by novel scalar, pseudoscalar, vector, and axial-vector particles. Limits on solar neutrino NSI from observations of previous DM experiments have also been explored,[1] such as from LUX experiment data [147].

In this work, we expand on previous studies and demonstrate the power of DM experiments to probe neutrino NSI. In the case of heavy scalar mediators, the effective interaction becomes a dimension six operator which can either be the familiar NSI modeled after the SM vector-interaction ($\bar{\nu}\gamma^\alpha P_L \nu \bar{q}\gamma_\alpha P_L q$), which is a vector NSI, or a scalar NSI ($\bar{\nu}\nu\bar{q}q$). Our analysis advances the results in the literature in several important ways. While SM interactions of atmospheric neutrinos have been explored in DM experiments [371], we study for the first time their potential NSI effects. Furthermore, we explore first constraints on leptoquarks (LQs) and associated theories that can lead to sizable solar and atmospheric neutrino NSI effects in DM experiments, and for the first time use LZ data to set constraints on LQs. We discuss the complementarity of LQ searches in DM experiments and other venues, especially colliders, and connect them with models aiming to address flavor physics observations [83, 333, 241], $(g-2)_\mu$, and neutrino mass generation [221, 448, 100]. Our analyses are complementary to studies of NSI in DM experiments associated with light mediators, such as Ref. [340, 351, 292, 206, 174] or Ref. [405], the latter of which demonstrated that low-threshold ($\sim$ eV) DM detectors are sensitive to light ($\sim$ keV - MeV) mediators where the low energy limit provides an enhancement of the recoil rate.

The chapter is organized as follows. In the Sec. 3.1, we describe the neutrino flux, its flavor composition, and its signal in DM detectors. In Sec. 3.2 we show the effects of neutrino NSIs and the effective theories that produce such interactions. In

[1] Neutrino NSI can also be readily probed through electron scattering in DM experiments, which has been recently exploited in attempt to address excess in the XENON1T experiment data [161]. However, in this work we focus solely on CEνNS interactions.

Sec. 3.3 we discuss the details of a UV completion of the effective models as LQs including effects on neutrino masses, $(g-2)_\mu$, and neutrino oscillations. In Sec. 3.4 we demonstrate the ability of DM detectors to observe the effective models described in Sec. 3.2, calculate constraints from the LZ experiment, and project the discovery reach of future DM detectors based on xenon, argon, and lead.

3.1 Standard Model Neutrino Scattering

3.1.1 Interaction rates and CEνNS. In DM experiments, the recoil rate of neutrinos as a function of the nuclear recoil energy depends on both the physics of the scattering process encapsulated in the cross-section, neutrino energy and flux, as well as the properties of the detector such as target material, size, efficiency, energy threshold, and energy resolution. The general differential recoil rate is given by

$$\frac{dR}{dE'_R} = N_T \int_{E_\nu^{\min}} \frac{d\sigma}{dE'_R}\frac{dN_\nu}{dE_\nu} dE_\nu \ , \tag{3.1}$$

where dN_ν/dE_ν is the neutrino flux, N_T is the number of target nuclei per unit mass (ton) of detector material, $d\sigma/dE'_R$ is process cross-section and for SM CEνNS it is given by Eq. (3.5). Here, primed energies represent the scattering energy of the interaction while the unprimed energies are those actually measured by the detector. The effects of new physics on the interactions will be explored in Sec. 3.2. From kinematics, the minimum required neutrino energy to induce a recoil energy E'_R of a nucleus with mass m_N is

$$E_\nu^{\min} = \frac{1}{2}\left(E'_R + \sqrt{E'^2_R + 2E'_R m_N}\right) \ . \tag{3.2}$$

We incorporate the detection efficiency and energy resolution of the detector by integrating over E'_R convoluted with the efficiency and a Gaussian function representing uncertainty

$$\frac{dR}{dE_R} = \int_0^\infty \frac{dR}{dE'_R}\frac{\eta(E'_R)}{\zeta(E'_R)\sqrt{2\pi}} e^{-\frac{(E_R-E'_R)^2}{2\zeta^2(E'_R)}} dE'_R \, , \tag{3.3}$$

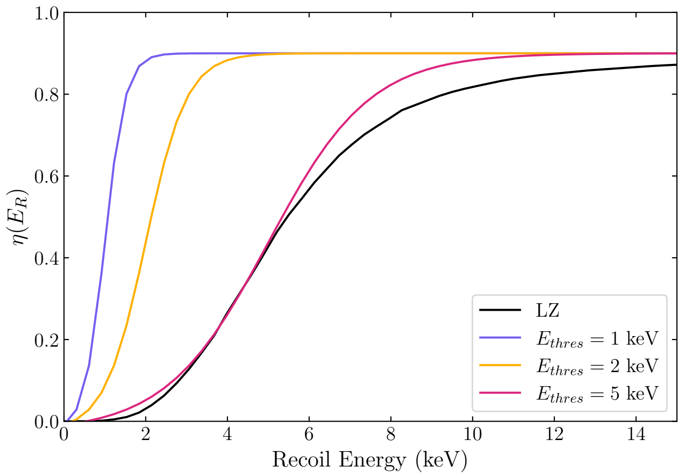

Figure 19. Efficiency models for 1, 2, and 5 keV thresholds compared to LZ experiment data analysis [4]. The sensitivity of DM detectors to NSI is strongly dependent on their energy threshold (e.g. [405]). We consider the 2 keV threshold model to be an optimistic efficiency for such near future detectors.

where for $\eta(E'_R)$ we will consider data-driven efficiency function of Eq. (3.4) and $\zeta(E'_R)$ is the energy resolution that we conservatively assume to be $\mathcal{O}(10)\%$ for all energies of interest.[2]

Focusing on the data analysis from LZ experiment as a characteristic target [4], we model the detection efficiency with a hyperbolic tangent as

$$\eta(E) = \frac{\eta_0}{1+\zeta}\left(\tanh \xi \left(\frac{E}{E_{\rm th}} - 1\right) + \zeta\right) \ , \tag{3.4}$$

where η_0 is the maximum efficiency at high energy, ξ sets the rate of the efficiency rise, $E_{\rm th}$ is the threshold energy, and ζ enforces that the efficiency vanishes at zero recoil energy. We fix $\xi = 2$, which requires $\zeta \approx 0.964$. To approximately match the LZ efficiency, we use $\eta_0 = 0.9$ such that the only remaining parameter is $E_{\rm th}$, which we vary between 1 and 5 keV. We display the efficiency for a selection of threshold energies in Fig. 19.

[2]Our analysis can be readily adapted for other efficiency and resolution functions.

Neutrinos that do not possess sufficient energy to discriminate individual nuclear constituents interact with the whole target nucleus via CEνNS mediated by the weak neutral current [247, 223]. For low momentum transfer $|q|$ satisfying $1/|q| \gg R$, where R is the nuclear radius, the target nucleons interact in phase. CEνNS is particularly relevant for neutrino sources with $E_\nu < 50$ MeV, above which other interactions become significant (see e.g. [244] for review). Within the SM, CEνNS interactions are given by

$$\frac{d\sigma_N}{dE_R}\bigg|_{SM} = \frac{G_F^2}{4\pi} F^2(E_R) Q_v^2 m_N \left(1 - \frac{m_N E_R}{2E_\nu^2}\right) , \tag{3.5}$$

where G_F is the Fermi constant, $Q_v = N - Z(1 - 4s_w^2)$ is the weak nuclear charge, N is the number of neutrons, Z is the number of protons, and s_w is the sine of the Weinberg angle. For the atomic mass number $A = N + Z$ and $m_n = 931$ MeV, the nucleus mass is $m_N \approx Am_n$. Here, we employ the Helm nuclear form factor [336, 295]

$$F^2(E_R) = \left[\frac{3j_1(qR_{\text{eff}})}{qR_{\text{eff}}}\right]^2 e^{-(qs)^2} , \tag{3.6}$$

where j_1 denotes spherical Bessel function, $q = \sqrt{2m_N E_R}$ is the transferred 3-momentum, $R_{\text{eff}} = \sqrt{(1.23A^{1/3} - 0.6)^2 + 7\pi^2 r_0^2/3 - 5s^2}$ is the effective nuclear radius, $s = 0.9$ fm is the skin thickness and $r_0 = 0.52$ fm is fit numerically from muon scattering data. With $s_w^2 = 0.232$ [441] CEνNS interactions scale as $\sim N^2$, signifying sizable enhancement of interaction rates for heavy target materials such xenon, argon, or lead.

3.1.2 Neutrino sources. A variety of neutrino sources can contribute to irreducible background (*i.e.* giving rise to "neutrino floor/fog") in direct DM detection experiments, including solar, reactor, geo-, diffusive supernovae background (DSNB) as well as atmospheric neutrinos. For reference, we consider benchmark detector located at SNOLab in Sudbury, Canada that is among likely sites to host next generation DM experiments.[3]

The integrated fluxes for various neutrino components and their uncertainties (rounded to percent level) are listed in Table 4. Contributions from atmospheric, reactor and geo-neutrinos will depend on the location of the experiment. Depending on the experimental energy threshold for nuclear recoil energy E_r, only fluxes resulting in neutrinos with maximum energy $E_\nu^{\rm max} > E_\nu^{\rm min}$, where $E_\nu^{\rm min}$ is given by Eq. (3.2), will contribute. In Table 4 we display the minimum required energy thresholds in xenon-based and argon-based DM experiments[4] to detect a particular neutrino source flux. We display the combined solar, DSNB and atmospheric neutrino flux contributions in Fig. 20, along with shaded bands depicting their respective uncertainties.

The keV-level threshold recoils in representative xenon-based experiment require that $E_\nu^{\rm min} \gtrsim \mathcal{O}(\text{few}\times\text{MeV})$, such that solar (hep and ^{8}B) background contributions dominate in the region of interest for non-standard neutrino interactions. We include the subdominant atmospheric neutrinos as they are useful in specific UV complete NSI models. A representative figure for scalar-mediated non-standard neutrino interactions are displayed in Fig. **??**, further discussed below in Sec. 3.2.

Solar neutrinos: The majority of neutrinos reaching the Earth's surface are produced in nuclear fusion processes in the Sun (for review see e.g. [293, 118]). The flux and energy spectrum of solar neutrinos depends on the specific nuclear reaction chain step that produces them. The vast majority of Sun's energy, nearly 99%, originates from proton-proton (pp) chain reactions, producing pp, hep, pep, ^{7}Be, ^{8}B

[3]The SNOLab experimental site is located at 46°28'19" N, 81°11'12" W with a 6010 meter water equivalent depth.

[4]Considering dominant isotopes, we take $A(Z) = 130$ (54) for xenon and $A(Z) = 40(18)$ for argon.

Neutrino Contribution	Total Flux [$\mathrm{cm}^{-2}\ \mathrm{s}^{-1}$]	$E_\nu^{\max}$ [MeV]	$E_{\mathrm{th}}^{\mathrm{Xe}}$ ($E_{\mathrm{th}}^{\mathrm{Ar}}$) [keV]
Solar (ν_e, pp)	$5.98(1 \pm 0.01) \times 10^{10}$	0.42	$2.99(9.81) \times 10^{-3}$
Solar (ν_e, pep)	$1.44(1 \pm 0.01) \times 10^{8}$	1.45	$3.42(11.2) \times 10^{-2}$
Solar (ν_e, hep)	$7.98(1 \pm 0.30) \times 10^{3}$	18.77	5.74(18.9)
Solar (ν_e, ^{7}Be)	$4.93(1 \pm 0.06) \times 10^{9}$	0.39	$1.20(3.96) \times 10^{-2}$
Solar (ν_e, ^{8}B)	$5.46(1 \pm 0.12) \times 10^{6}$	16.80	4.58(15.1)
Solar (ν_e, ^{13}N)	$2.78(1 \pm 0.15) \times 10^{8}$	1.20	$2.33(7.65) \times 10^{-2}$
Solar (ν_e, ^{15}O)	$2.05(1 \pm 0.17) \times 10^{8}$	1.73	0.0486(0.160)
Solar (ν_e, ^{17}F)	$5.29(1 \pm 0.20) \times 10^{6}$	1.74	0.0492(0.161)
Atm. (ν_e)[1]	$1.27(1 \pm 0.50) \times 10^{1}$	944	$1.47(5.00) \times 10^{4}$
Atm. ($\overline{\nu}_e$)	$1.17(1 \pm 0.50) \times 10^{1}$	944	$1.47(5.00) \times 10^{4}$
Atm. (ν_μ)	$2.46(1 \pm 0.50) \times 10^{1}$	944	$1.47(5.00) \times 10^{4}$
Atm. ($\overline{\nu}_\mu$)	$2.45(1 \pm 0.50) \times 10^{1}$	944	$1.47(5.00) \times 10^{4}$
DSNB (ν_e)[2]	$4.55(1 \pm 0.50) \times 10^{1}$	36.90	22.1(72.7)
DSNB ($\overline{\nu}_e$)	$2.73(1 \pm 0.50) \times 10^{1}$	57.01	52.8(174)
DSNB (ν_x)[3]	$1.75(1 \pm 0.50) \times 10^{1}$	81.91	109(359)
Reactor ($\overline{\nu}_e$, ^{235}U)[4]	$1.88(1 \pm 0.08) \times 10^{5}$	10.00	1.62(5.33)
Geo. ($\overline{\nu}_e$, ^{40}K)	$2.19(1 \pm 0.17) \times 10^{7}$	1.32	$2.83(9.29) \times 10^{-2}$
Geo. ($\overline{\nu}_e$, ^{238}U)	$4.90(1 \pm 0.20) \times 10^{6}$	3.99	0.259(0.849)
Geo. ($\overline{\nu}_e$, ^{232}Th)	$4.55(1 \pm 0.26) \times 10^{6}$	2.26	$8.29(27.2) \times 10^{-2}$

[1] The cut-off of Fluka analysis.
[2] Fermi-Dirac spectrum with neutrino temperature of $T_\nu = 3, 5, 8$ MeV for ν_e, $\overline{\nu}_e$, ν_x, respectively.
[3] ν_x is the total contribution from all other neutrinos and antineutrinos.
[4] Only the most dominant element is considered.

Table 4. Neutrino flux components that contribute to the coherent neutrino scattering background in direct detection experiments at the SNOLab location. Solar fluxes are from B16-GS98 [434], atmospheric from FLUKA [129], DSNB from a theoretical average [301], nuclear from the combined result from multiple nearby reactors [268], and Geo. from a global Earth model, incorporating several theoretical models.

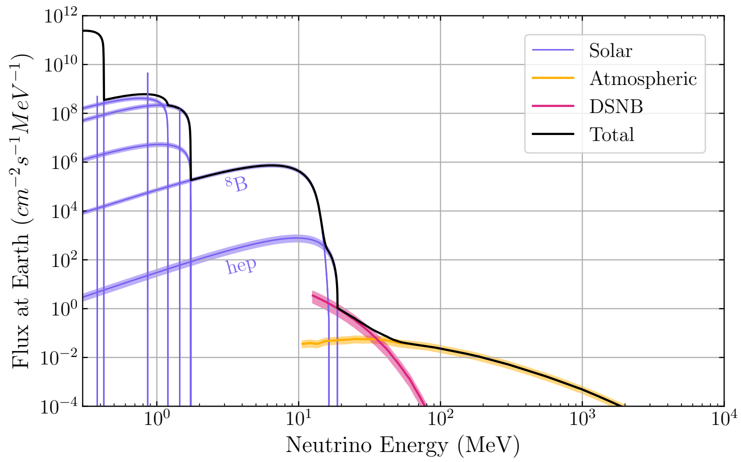

Figure 20. Neutrino flux contributions including solar, atmospheric, and DSNB components and their respective uncertainties on the surface of the Earth considering SNOLab detector location. See text and Table 4 for additional details.

neutrinos. The remaining $\sim 1\%$ of Sun's energy originates from Carbon-Nitrogen-Oxygen (CNO) cycle, producing ^{13}N, ^{15}O, ^{17}F neutrinos.

For $E_\nu \lesssim 20$ MeV energies, solar neutrinos dominate background for direct DM detection experiments. In this work we employ solar neutrino fluxes of high metallicity solar model B16-GS98 [434], favored by recent Borexino neutrino observation data analysis [84]. The dominant neutrino background contribution for a range of parameters stems from ^{8}B neutrinos.

DSNB: For neutrino energies around 20 MeV $\lesssim E_\nu \lesssim$ 50 MeV DSNB significantly contributes to neutrino background fluxes [132]. Around 99% of the gravitational binding energy is released in the form of neutrinos in core-collapsing supernova, resulting in $\sim 10^{58}$ neutrinos emitted yielding about $\sim 10^{53}$ ergs in energy. The DSNB denotes combined contributions of neutrinos originating from all the historic core-collapse supernovae events. The DSNB flux is formed from convolution of the redshift-dependent core-collapse supernovae rate, which is found from initial stellar mass function and star formation rate, as well as emitted core-collapse neutrino spectrum.

Approximating the emitted neutrino spectra as thermal, we consider DSNB neutrinos characterized by temperature T_ν averaged for each species over theoretical models in Ref. [301]. Significant efforts are underway by neutrino experiments, especially Super-Kamiokande [38], to detect the DSNB in the near future.

Atmospheric neutrinos: For $E_\nu \gtrsim 50$ MeV, neutrino contributions become dominated by neutrinos produced from cosmic ray collisions with nuclei in the atmosphere (see e.g. [261] for review). Such interactions produce copious amounts of $\pi^\pm$ and $K^\pm$ mesons that predominantly decay to $\mu^+ + \nu_\mu$ and $\mu^- + \bar{\nu}_\mu$, followed by muon decay to electrons and pairs of neutrinos resulting in a ν_μ and $\bar{\nu}_\mu$ flux twice that of ν_e and $\bar{\nu}_e$. The atmospheric neutrino flux carries an $\mathcal{O}(30\%)$ theoretical uncertainty, which we take to be 50% conservatively, due to the uncertainty in the cosmic ray flux and its propagation in the magnetic fields of the Earth and solar system. In addition to this uncertainty, the flux varies significantly though predictably with the position of the detector and the phase in the solar cycle [451].

Neutrino Oscillations: As shown in Table 4, solar neutrinos are produced as electron neutrinos. Since these neutrinos have a much longer baseline than those in reactor experiments, neutrino oscillations result in a significant fraction of neutrinos reaching the detector with μ- or τ-components, allowing experiments to constrain interactions of second and third generation neutrinos.

Neutrino oscillations in matter are further complicated by the Mikheyev–Smirnov–Wolfenstein (MSW) effects [440]. The matter potential $V_{\rm MSW} = \sqrt{2} G_F n_e {\rm diag}(1, 0, 0)$, where n_e is the electron number density, modifies the neutrino oscillation Hamiltonian as

$$\mathcal{H}_{\rm matter} = E_\nu + \frac{M M^\dagger}{2 E_\nu} + V_{\rm MSW} \ . \tag{3.7}$$

Vector NSI contribute to the matter potential analogously to MSW effects [257]. Scalar NSI contribute a new mass-like term, which has inverse neutrino energy dependence and hence suppressed at higher neutrino energies [267]. We consider these effects and include in oscillation analysis as discussed in Appendix B.3. Throughout, we assume normal neutrino mass ordering.

3.2 Nonstandard Neutrino Interactions

There are several formalisms to incorporate general interactions of neutrinos (see e.g. [215]). One system of simplified models which has gained popularity generates NSI by introducing new mediators which couple to neutrinos and normal fermions as outlined in Ref. [174], also employed in e.g. Ref. [345, 405]. categorizes interactions by the Lorentz structure of the mediator such that interactions are defined as scalar, pseudoscalar, vector, axial vector, and tensor (SPVAT). Specifically, we focus on scalar mediators with masses above ~ 1 TeV, which allows us to map our general interactions to effective four-Fermi interactions at low energies which are recognizable in the conventional language of NSI [215].

In this work, we will consider either flavor independent couplings of a generalized scalar interaction, or what is often called a "minimal coupling" scenario, in which all couplings are zero except the one of interest that couples a particular flavor of neutrino with a specific quark. The latter is typically more useful in mapping to UV complete models, and example of which we show in Sec. 3.3. For this case although the form of the cross-section is flavor-independent, the fluxes vary as discussed in Sec. 3.1. This means that for a comprehensive treatment of a scalar coupled to multiple flavors one would need to calculate the scattering of each flavor independently and combine the signals. Additionally, we are primarily interested in couplings to first generation quarks as this is where DM experiments are sensitive as we discuss in Sec. 3.4. In

Sec. 3.2.1 we provide the expressions for scalar NSI and in Sec. 3.2.2, we do the same for vector NSI.

3.2.1 Scalar NSI. The effective Lagrangian for scalar NSI with Dirac neutrinos is given by [267]

$$\mathcal{L}_{sNSI} \supset G_F \sum_{q,\alpha,\beta} \varepsilon_{\alpha\beta}^{qS} \bar{\nu}_\alpha \nu_\beta \bar{q} q \,, \tag{3.8}$$

where the interaction is a dimension six operator suppressed by two powers of a large mass scale. The indices q run over the quark flavors, while α, β run over the lepton flavors. In this work, we will consider flavor-conserving interactions, $\alpha = \beta = \ell$. Scalar NSI cannot be converted to conventional vector-like NSI by Fierz transformations since they arise from a neutral scalar mediator [111]. On the other hand, as we will discuss in Sec. 3.3, a charged (colored) scalar produces a conventional vector NSI after Fierz transformations.

The scalar NSI effective vertex gives rise to an additional contribution to the CEνNS cross-section:

$$\left.\frac{d\sigma}{dE_R}\right|_S = \frac{F^2(E_R) G_F^2 \varepsilon_{q\ell}^2 q_S^2 E_R m_N^2}{4\pi E_\nu^2} \,, \tag{3.9}$$

where E_R is the energy of the recoiling quark, m_N is the nuclear mass, and q_S is the effective scalar charge of the nucleus. In the flavor/generation independent case, we have $q_S \approx 14A + 1.1Z$ [174]. A sample of the differential recoil rate, both from the SM and NSI is shown in Fig. 21.

3.2.2 Vector NSI. The effective Lagrangian for a vector NSI is

$$\mathcal{L}_{NSI} = -2\sqrt{2} G_F \sum_{q,\alpha,\beta} \varepsilon_{\alpha\beta}^{qP} \left(\bar{\nu}_\alpha \gamma^\mu P_L \nu_\beta\right) \left(\bar{q} \gamma_\mu P q\right) \;, \tag{3.10}$$

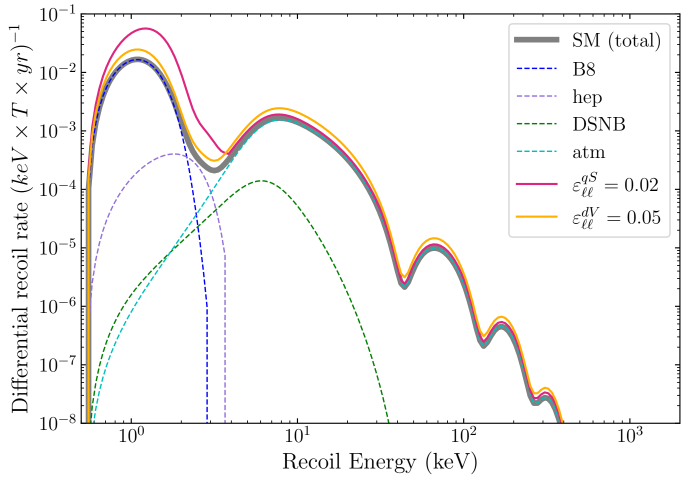

Figure 21. Recoil rates in a xenon detector with a 5 keV threshold for SM interactions of neutrinos (dashed lines), with B8, hep, DSNB, and atmospheric neutrino sources, and the total (thick grey line) as well as the total including a scalar NSI (magenta) for $\varepsilon_{\ell\ell}^{qS} = 0.02$ for all q and ℓ.

where $P = P_L, P_R$ are the projection operators. As with the neutral scalar, we assume flavor-conserving NSI, that is, $\alpha = \beta = \ell$. Similarly, we assume the interaction conserves quark flavor. Vector NSIs can be parameterized in terms of vector ($\varepsilon_{\ell\ell}^{qV} = \varepsilon_{\ell\ell}^{qL} + \varepsilon_{\ell\ell}^{qR}$) and axial ($\varepsilon_{\ell\ell}^{qA} = \varepsilon_{\ell\ell}^{qL} - \varepsilon_{\ell\ell}^{qR}$) components.

In the case of CEνNS, the vector component of the interaction gets enhanced by the size of the nucleus while the axial component is proportional to the nuclear spin. This results in a $1/A$ suppression of the axial component relative to the vector part. As in [126], we drop the axial component and consider only the vector component of the interaction. The scattering cross-section for vector NSI is given by

$$\left.\frac{d\sigma}{dE_R}\right|_{NSI} = \frac{F^2(E_R) G_F^2 Q_{NSI}^2 m_N}{2\pi E_\nu^2}\left(2E_\nu^2 - m_N E_R\right) \ . \tag{3.11}$$

In Eq. (3.11), Q_{NSI} is the change in the effective nuclear coupling induced by the NSI and given by

$$Q_{NSI}^2 = \left[Q_{SM} + \left(2\varepsilon_{\ell\ell}^{uV} + \varepsilon_{\ell\ell}^{dV}\right) Z + \left(\varepsilon_{\ell\ell}^{uV} + 2\varepsilon_{\ell\ell}^{dV}\right) N\right]^2 - Q_{SM}^2 \tag{3.12}$$

for a nucleus with Z protons and N neutrons. θ_W is the Weinberg angle and $Q_{SM} = \left[\left(1/2 - 2\sin^2(\theta_W)\right) Z - N/2\right]$ is the SM contribution to the neutrino-nuclear coupling. In general, since the $\varepsilon_{\ell\ell}^{qV}$ parameters can be positive or negative, there exists parameter space for a given detector material where the up and down couplings cancel and the NSI does not change the scattering rate.

In what follows, we will study two cases which we call "flavor universal" and "minimal" NSI, where "flavor universal" means $\varepsilon_{ee} = \varepsilon_{\mu\mu} = \varepsilon_{\tau\tau}$. In the scalar NSI case, this extends to the quark sector as well, that is $\varepsilon_{\ell\ell}^{uS} = \varepsilon_{\ell\ell}^{dS}$. In the vector NSI case, we note it is impossible for a singlet scalar to have both $\varepsilon_{\ell\ell}^{dV}$ and $\varepsilon_{\ell\ell}^{uV}$ while conserving electric charge, so in the case of vector NSI, "flavor universal" refers only to lepton flavors. "Minimal" NSI means $\varepsilon_{\ell\ell}^{qV} \neq 0$ for only one flavor of ℓ and q.

3.3 Case Study: Scalar Leptoquarks

We will demonstrate how models of leptoquarks (LQs), which interact with baryons and leptons, provide an example application of our formalism. LQs are theoretically well-motivated and naturally arise in the context of Grand Unification theories such as $SU(5)$ [269] and $SU(10)$ [258, 270], as well as the Pati-Salam models that unify quark and leptons [376]. Further, they can manifest in R-parity violating models of supersymmetry [288, 123].

LQs have been recently connected to possible observational anomalies in semi-leptonic B decays [81, 3, 83, 333]. In addition, scalar LQs have been posed as solutions to the neutrino mass problem [221, 100] (see Appendix. B.1 for an example). If the LQ couples to muons, it provides a contribution to the anomalous magnetic moment at one loop order and may be part of the explanation for the anomalous magnetic moment of the muon $(g-2)_\mu$ [448, 220, 241, 271].

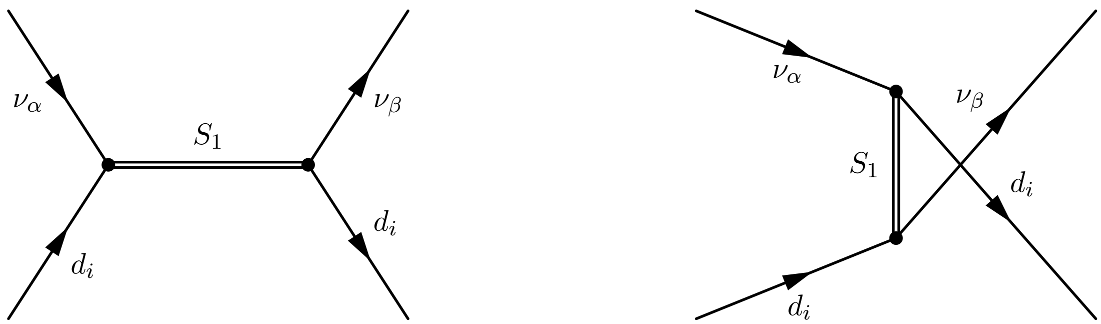

Figure 22. Neutrino-quark scattering mediated by the S_1 scalar leptoquark.

Here, we consider LQs in the large coupling regime, which are of interest for observations and provide a heavy scalar that couples to both quarks and neutrinos [399, 219]. To map the LQ models to the NSIs discussed above, we note that because the mediator carries lepton and quark quantum numbers, the interactions proceed via s and u-channel diagrams rather than the t-channel of uncharged scalar interactions (see Fig. 22). Once the massive fields are integrated out, a Fierz transformation leads to an effective four-fermion vertex identical to the vector NSI Sec. 3.2.2. We derive the vector NSI parameters in Appendix B.2.

3.3.1 The S_1 leptoquark. We will focus on scalar LQs as the simplest realization of neutrino NSIs. As a concrete realization, we consider the $S_1 = (\bar{3}, 1, 1/3)$ leptoquark, where parenthesis represent transformation under SM $(SU(3), SU(2), U(1))$ symmetries. The additional relevant Lagrangian terms due to S_1 are [99, 113, 114]:

$$\mathcal{L}_{S_1} \supset -m_{S_1}^2 |S_1|^2 + (\lambda_L^{i\ell} S_1 \bar{Q}_i^c \epsilon L_\ell + \lambda_R^{i\ell} S_1^* \bar{u}_R^i \bar{\ell}_R + h.c.)\,, \tag{3.13}$$

where $Q_i = (u_L, d_L)_i$ and $L_\ell = (\nu_{\ell L}, \ell_L)$ are the left-handed quark and lepton doublets respectively, ℓ is the lepton flavor, ϵ is the Levi-Civita tensor, and i is the quark generation index. From expansion of the $SU(2)$-doublets in Eq. (3.13), we note that the same Yukawa interaction that couples charged leptons to up-type quarks will couple neutrinos to down-type quarks. Thus, by constraining neutrino scattering, we also place constraints on the charged lepton S_1 couplings. Throughout, we do not consider possible effects of diquark terms, which could lead to nucleon decay. Such terms can be readily restricted by additional symmetries, however detailed model implementation is beyond the scope of the present work.

As stressed in Refs. [216, 399], without a model-independent reason dictating a flavor pattern of LQ couplings all nine quark-lepton generation pairings are possible. Strong constraints exist on the first generation couplings, λ^{qe}, particularly from atomic parity violating experiments [390, 113, 82, 399]. Here, we shall focus on LQ couplings to the μ and τ flavored leptons. For simplicity, we will also assume the LQ couples only to one-generation (sometimes called the "minimal leptoquark" [399]), either μ or τ leptons.[5]

The interactions of S_1 LQ can lead to distinct phenomenological consequences. Through the coupling to μ-sector the S_1 LQ can directly contribute to the magnetic moment of the muon. For $m_{S_1} \gg m_t$ the resulting contribution to $a_\mu = (g-2)_\mu/2$ is [130]

$$a_\mu^{S_1} = \sum_i \frac{m_\mu m_{u_i}}{4\pi^2 m_{S_1}^2} \left(\ln m_{S_1}^2/m_{u_i}^2 - 7/4\right) \Re(\lambda_R^{*i2}\lambda_L^{i2}) - \frac{m_\mu^2}{32\pi^2 m_{S_1}^2} \left(\sum_i |\lambda_R^{i2}|^2 + \sum_i |\lambda_L^{i2}|^2 \right) , \tag{3.14}$$

which is dominated by the term proportional to the up-type quark masses. In a LQ model where the charm and top quarks have the same coupling as the up-quark, we can estimate a favored region in the LQ mass vs. up-type Yukawa plane that alleviates the $(g-2)_\mu$ anomaly. This region is indicated with a grey band in Fig. 31.

[5]The flavor-changing constraints in this case are much weaker and couplings to both μ and τ may be simultaneously allowed as long as one coupling is marginally smaller than the other [449].

In the case that the coupling to charm and top quarks vanishes or $\lambda_R \ll \lambda_L$, the second term dominates and exacerbates the anomaly.

Since we are interested in coupling to protons and neutrons, we restrict ourselves to couplings to first generation of SM quarks. We are considering neutrino-nuclear scattering in or near the elastic regime, so the parton distribution functions (PDFs) are dominated by the first generation quarks.[6] Thus, we consider scalar S_1 LQ with couplings $\lambda^{d\ell}$, where $\ell = \mu, \tau$.

With these assumptions and for an $\mathcal{O}$(TeV) LQ, we can integrate our the LQ field, perform a Fierz transformation, and map the resulting dimension six operator back to the NSI parameters in eq. (3.10) as

$$\varepsilon^{dV}_{\ell\ell,S_1} = \frac{-|\lambda^{d\ell}_L|^2}{4\sqrt{2}G_F m^2_{S_1}} \,. \tag{3.15}$$

We provide details on this calculation in Appendix B.2. Note the interactions only involve down-type quarks, which is accounted for by a change in the effective charge Q_{S_1}.

$$Q_{S_1} = Z\left(\frac{1}{2} - 2\sin^2(\theta_W) + \varepsilon^{dV}_{\ell\ell,S_1}\right) + N\left(-\frac{1}{2} + 2\varepsilon^{dV}_{\ell\ell,S_1}\right)\,, \tag{3.16}$$

Lastly, we are considering the "minimal LQ" model in which the S_1 couples to a single flavor of neutrinos, such that the neutrino-nuclear scattering signal only involves a single neutrino-flavor. Note that this is contrast to SM CEνNS, which involve all flavors.

[6]This neglects the "sea quarks" which provide trace amounts of anti-quarks of the first generation as well as (even fewer) strange quarks and anti-quarks. In principle, these sea quarks provide an effective charge allowing detection of NSIs coupled to strange quarks or, as in the case of the $\tilde{R}_2$ LQ (defined in Appendix B.1), NSIs which only couple neutrinos to anti-quarks (or quarks to anti-neutrinos), though the PDF suppression is such that neutrino scattering is not a competitive means to set bounds.

3.4 Discovery Reach of Dark Matter Detectors

We are interested in calculating the potential of a DM direct detection experiment to uncover signals of neutrino NSIs, with the SM CEνNS as our effective background. In the following analysis, we will present our results in terms of the general NSI parameters $\varepsilon_{\ell\ell}^{qS}$ and in terms of the LQ model parameters, $\lambda_{S_1}^{d\ell}, m_{S_1}$, from the previous section. For generality, we will consider that we are dominated by statistics and do not focus on making predictions in the context of more detector-specific systematic backgrounds, such as radioactive decay in or near the detector, or any other instrumental noise. Neutrino oscillation effects are present for both scalar and vector NSIs, though as we discuss in Appendix B.3, these effects are minimal for the NSI parameters we consider and are not included in the following analysis. We also do not consider the presence of a DM signal in this analysis, although Ref. [147] studied the effect of NSIs on the neutrino fog.

3.4.1 Statistical analysis. Since we have reduced the NSI cross-section to one free parameter, $\varepsilon_{\ell\ell}^{qS}$, we use a likelihood ratio method to project the significance of simulated data. This follows the method used for the magnetic moment calculation in Ref. [405], which was also dependent on only one parameter. We take as our likelihood function

$$\mathcal{L}(\varepsilon, \vec{\phi}) = \frac{e^{-\Sigma_{j=1}^{n_\nu}(\eta_{\varepsilon,j}+\eta_{SM,j})}}{N!} \times \prod_{j=1}^{n_\nu} \mathcal{L}(\phi_j) \times \prod_{i=1}^{N} \left(\sum_{j=1}^{n_\nu} (\eta_{\varepsilon,j} f_{\varepsilon,j}(E_i) + \eta_j f_{SM,j}(E_i)) \right) , \tag{3.17}$$

where we have dropped the labels on $\varepsilon = \varepsilon_{\ell\ell}^{qS}$ for simplicity, n_ν label the neutrino fluxes and N labels the energy bins. Here, $\vec{\phi}$ are nuisance parameters normalizing the neutrino flux channels. They are allowed to fluctuate weighted by Gaussian distribution,

$$\mathcal{L}(\phi_j) = \frac{1}{\sigma_j\sqrt{2\pi}} e^{-\frac{1}{2}\left(\frac{\phi_j-\phi_{0,j}}{\phi_j}\right)^2}, \tag{3.18}$$

where the width of their uncertainties, σ_j is given in Table 4. The functions $f_{\varepsilon,j}(E_i)$ and $f_{SM,j}(E_i)$ are the distribution functions (*i.e.* the normalized rates) for the number of events in the i-th energy bin from the j-th neutrino flux from NSI (ε) or SM scattering. $\eta_{\varepsilon,j}$ and $\eta_{SM,j}$ are the number of events predicted from the NSI or SM in each channel (j) based on the nuisance parameters. The latter depends only on the normalization of the neutrino flux components while the former depends on both the flux normalization and the NSI parameter (ε). The product over i runs over the number of events in the simulated data.

For a particular data set, we maximize the likelihood with $\varepsilon = 0$ as our null hypothesis and $|\varepsilon| > 0$ for NSI signals. If the null likelihood is greater than the signal likelihood, we assign the significance $\sigma = 0$. If $\mathcal{L}(\varepsilon \neq 0)/\mathcal{L}(\varepsilon = 0) \equiv \lambda > 1$, we have a test statistic $t = 2\log(\lambda)$ and significance $\sigma = \sqrt{t}$. This analysis is run on 600 of sets of pseudo-data generated by Poisson fluctuating the expected rates for a given $\varepsilon_{\ell\ell}^{qS}$ and exposure. The average of these data sets is then used for the projections in Sec. 3.4.2.

3.4.2 Results. In this section, we present the results of the likelihood procedure described in the previous section. We show the 3σ and 5σ contours for ε in the exposure-ε plane in Fig. 23, for a flavor universal scalar ($\varepsilon_{\ell\ell}^{qS}$, upper left) and a minimal scalar ($\varepsilon_{\ell\ell}^{dS}$, upper right) while the equivalent contours for vector NSI are shown in the lower panels. The yellow curves show the reach using the efficiency from the LZ experiment [4]. Improving the detector efficiency can lead to a significantly stronger reach, and we see that lowering the detector threshold from $E_{\rm th} = 2$ keV to 1 keV improves the reach on ε by about a factor of few. Since $P_{e\to\tau} > P_{e\to\mu}$ when averaged over the solar neutrino spectrum, there will be ~ 3 ν_τ for every 2 ν_μ, thus we expect τ constraints to be stronger by a factor $\sim \sqrt{3/2}$. This is confirmed by the results in Fig. 23 where we also show the results of an analysis of only atmospheric neutrinos which are useful to constrain interactions with anti-neutrinos such as the $\tilde{R}_2$ LQ (see Appendix B.1). We further display how the results will improve as atmospheric neutrino flux uncertainty is further reduced, as far down as optimistic $\mathcal{O}(1\%)$-level.

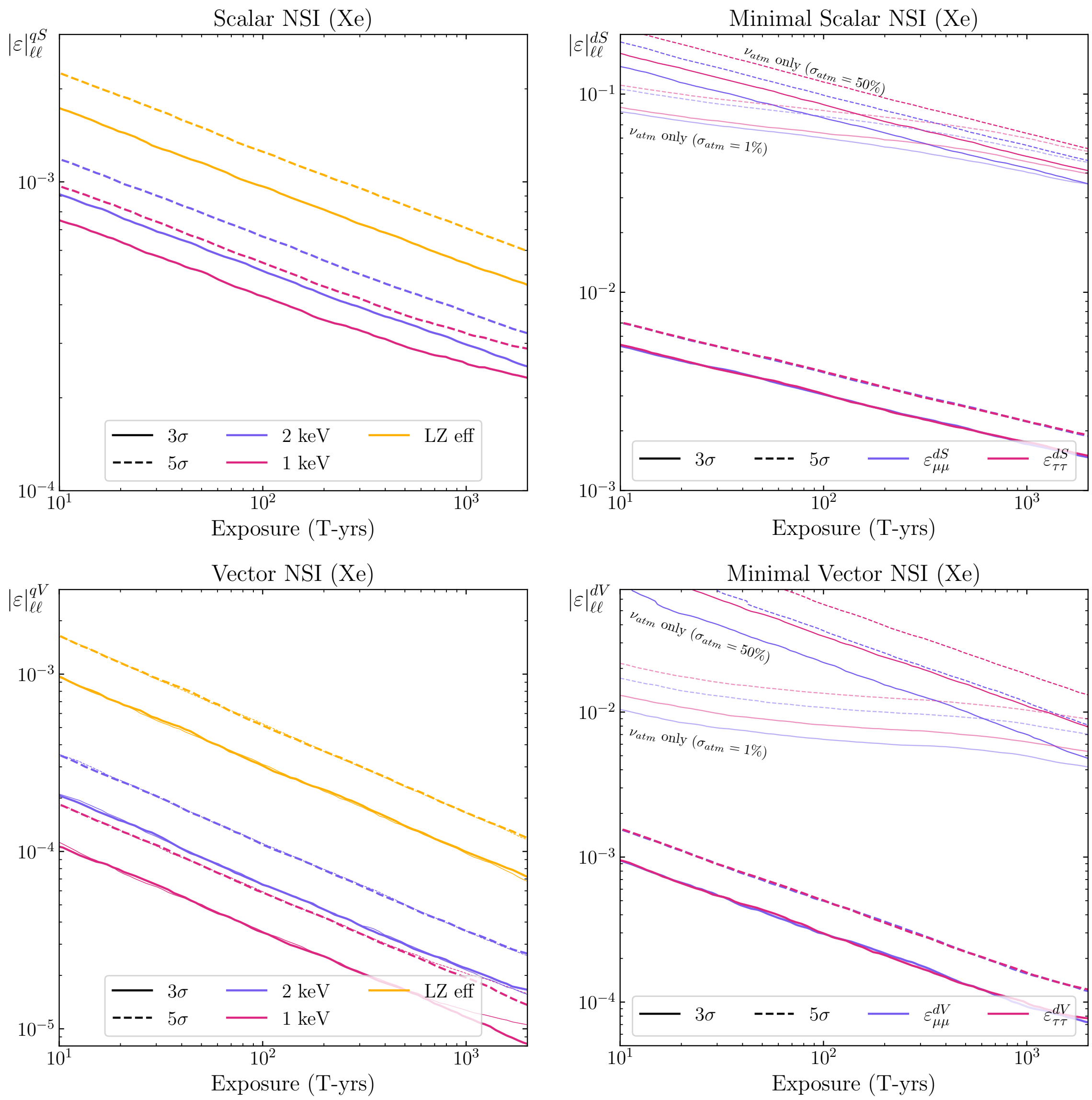

Figure 23. **Left:** 3σ (solid) and 5σ (dashed) discovery reach of a xenon detector for an NSI with universal couplings ($\varepsilon_{ee}^{dV} = \varepsilon_{\mu\mu}^{dV} = \varepsilon_{\tau\tau}^{dV}$) as a function of detector exposure, for a 1 keV (magenta) and 2 keV (purple) detector threshold as defined in Sec. 3.1.1. Also shown is the reach using the LZ efficiency and threshold (yellow). As expected, a lower threshold improves the discovery reach. **Right:** discovery reach of a xenon detector to NSIs coupling only the d quark to either ν_μ or ν_τ, assuming a 2 keV threshold. Thin lines indicate the sensitivity based only on atmospheric neutrinos. Fainter lines show the improvement to be gained from more precise measurement of the atmospheric neutrino flux with reduced uncertainties. Upper panels show results for scalar NSI while lower panels are vector NSI results. In the vector NSI panels, we present results for both $\varepsilon < 0$ ($\varepsilon > 0$) with the thick (thin) lines, and show that they are similar. The lower right panel maps to the S_1 LQ parameters in Fig. 31.

In addition to xenon, other DM experiments can also have enhanced sensitivity to CEνNS and related new physics. In general, the effective charge of the nucleus grows as the square of its mass, so for a given detector target mass, larger nuclei are expected to result in more events even though there are fewer target nuclei. This competes with the kinematic effects whereby higher intensity but lower energy neutrinos are often pushed below threshold in detectors with heavy nuclei.

In figures 24 and 25 we display the 3σ and 5σ discovery reach contours for the NSI parameter ε in the exposure-ε plane for argon and lead-based detectors. For estimating the sensitivity to scalar NSIs, while the details depend on the specific experimental configuration, we assume for simplicity the same threshold and efficiency parameters as for xenon-based detector. Note that argon does not see much improvement as the threshold falls below 5 keV (the differences seen above are statistical noise). Argon has a relatively light nucleus and the peak induced by boron-8 is at higher energy, so lowering the threshold does not increase the number events as efficiently until the oxygen-16 neutrinos have an effect (below ~ 0.5 keV). For the heavier lead nucleus, recoils induced by boron-8 neutrinos are partially cut by the threshold, so improving the threshold makes a much larger number of recoils accessible. The lower panels of figures 24 and 25 show the sensitivity to minimal couplings assuming the 2 keV threshold and efficiency.

Acknowledgments

We thank Pouya Asadi, Kaladi Babu, Bhupal Dev, Bhaskar Dutta, Motoi Endo, Danny Marfatia for helpful discussions. T.S. and T.-T.Y. were supported in part by NSF CAREER grant PHY-1944826. T.-T.Y. also thanks the CCPP at NYU for hospitality and support. V.T. was supported in part by the World Premier

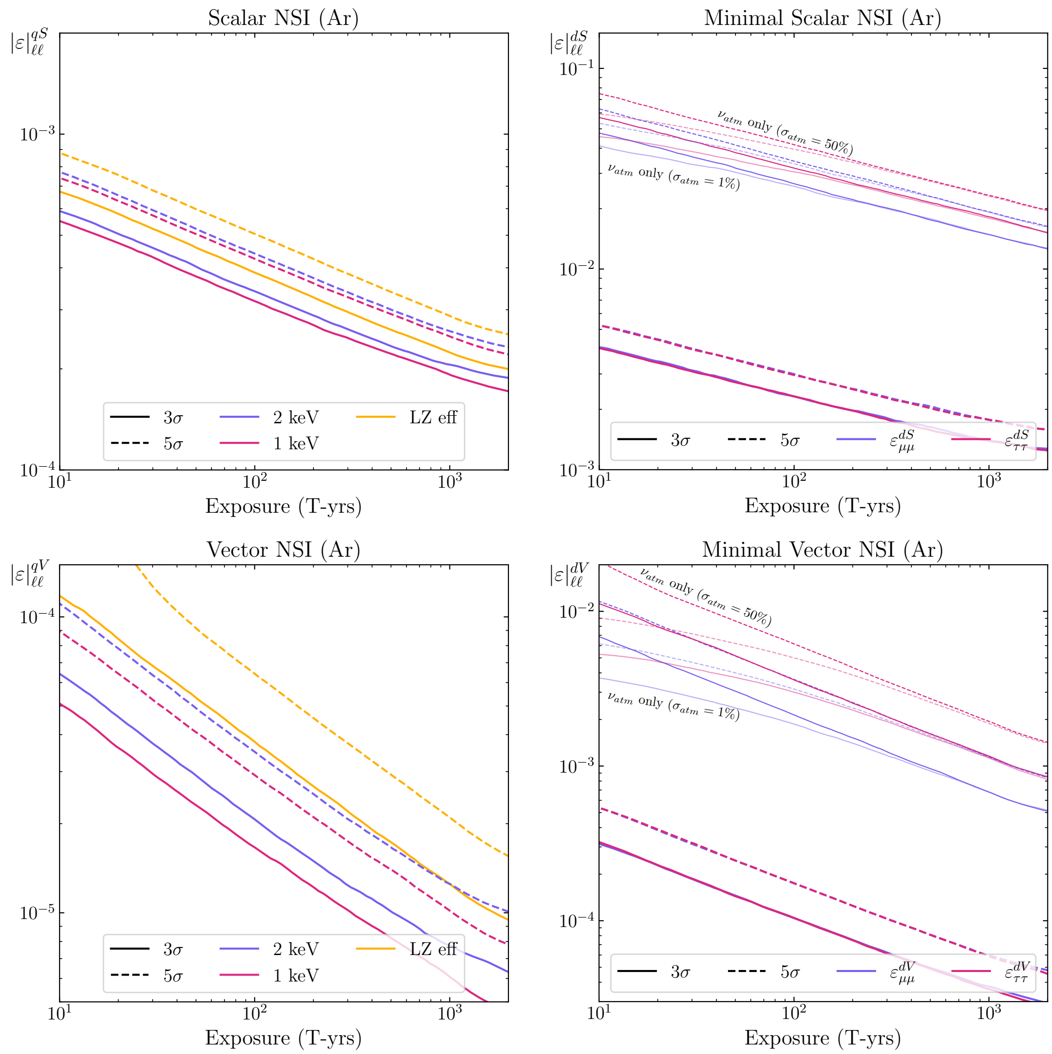

Figure 24. **Left:** 3σ (solid) and 5σ (dashed) discovery reach of an argon detector for a scalar (top) or vector (bottom) NSI with universal couplings as a function of detector exposure, for a 1 keV (magenta) and 2 keV (purple) detector threshold as defined in Sec. 3.1.1. As expected, a lower threshold improves the discovery reach. Due to its larger target mass, kinematics disfavors lead detectors despite the increased scattering rate. This is also responsible for the more dramatic improvement with detector threshold in lead. **Right:** discovery reach of an argon detector to scalar (top) or vector (bottom) NSIs coupling only the d quark to either ν_μ or ν_τ, assuming a 2 keV threshold. Thin lines indicate the sensitivity based only on atmospheric neutrinos. Fainter lines show the improvement to be gained from more precise measurement of the atmospheric neutrino flux.

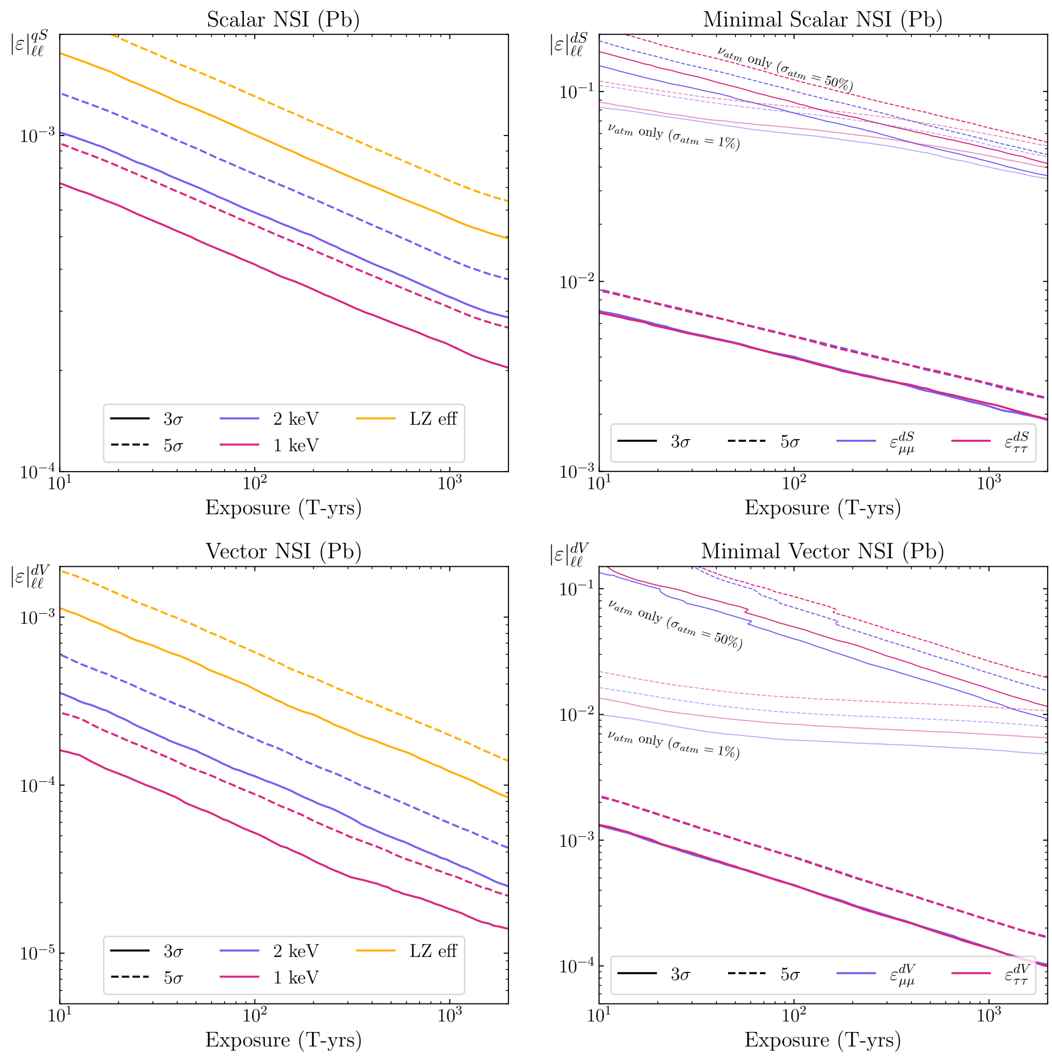

Figure 25. Same as Fig. 24, but for a lead detector. Note that due to its heavier nucleus, lead loses more sensitivity than argon or xenon at higher thresholds, and gains more from higher energy neutrinos such as the atmospheric flux.

International Research Center Initiative (WPI), MEXT, Japan and also by JSPS KAKENHI grant No. 23K13109.

CHAPTER IV

NEUTRINO WHISPERS FROM DARK STARS SEEDING SUPERMASSIVE BLACK HOLES

In this chapter we transition to a different source of astrophysical neutrinos. Rather than searching for hints of new physics from NSI which may be connected to the production of dark matter, we search directly for the products of DM annihilation. We do so in the context of a particular model of cosmology which is proposed as a general feature of WIMP dark matter. This work is co-authored with Volodymyr Takhistov and has been accepted for publication in the Astrophysical Journal Letters with a pre-print available here [403].

First stars powered by DM heating instead of fusion can appear in the early Universe from theories of new physics. These dark stars (DSs) can be significantly larger and cooler than early Population III stars, and could seed supermassive black holes (SMBHs). We show that neutrino emission from supermassive DSs provides a novel window into probing SMBH progenitors. We estimate first DS constraints using data from Super-Kamiokande and IceCube neutrino experiments, and consistent with James Webb Space Telescope observations. Upcoming neutrino telescopes offer distinct opportunities to further explore DS properties.

Dark Stars.– The first generation stars are thought to have played a pivotal role in the Universe, including shaping cosmic evolution, influencing reionization and chemical enrichment. These population III (Pop III) zero-metallicity stars are believed to have formed from the gravitational collapse of pristine gas left over after the Big Bang, within DM mini-halos of mass $\sim 10^5 - 10^7 M_\odot$ around redshifts $z \sim 20$ (e.g. [39, 169, 443]). Despite their significance, Pop III stars are yet to be observed, although candidates have been suggested [431, 439, 438].

Supermassive black holes (SMBHs) with masses ranging $\sim 10^6 - 10^9 M_\odot$ are ubiquitous at the centers of galaxies, powering quasars and active galactic nuclei (AGN). The origin of SMBHs at high redshifts remains a mystery, especially in light of recent observations by the James Webb Space Telescope (JWST) [353, 445, 217, 420] suggesting SMBH detections even at redshifts of up to $z \simeq 10.3$ [162]. Achieving the necessary rapid growth of such massive objects challenges Eddington-limited accretion and hierarchical mergers of stellar-mass black holes on relevant cosmological timescales (e.g. [433, 120]). While Pop III stars offer plausible candidates for forming lighter $\sim 10^2 - 10^3 M_\odot$ SMBH seeds, alternative scenarios such as direct collapse have also been suggested (see e.g. [436, 307] for review) and further investigation is necessary.

An intriguing distinct class of first stars, known as dark stars (DSs), powered by heating from DM constituting a small fraction of their mass instead of fusion, has been put forth and that could seed SMBHs [417, 249, 416]. DM heating can be a general byproduct of annihilation of weakly interacting massive particles (WIMPs) [417], but can also arise in contexts such as self-interacting DM [442]. During formation, the contraction of baryonic matter induces adiabatic contraction of DM, leading to high DM densities sufficient for efficient annihilation. The energy released from DM annihilation halts the collapse at low temperatures, preventing the onset of nuclear fusion. When the DM fuel is exhausted, the DS collapses into a black hole. Massive DSs seeding SMBHs could also explain paucity of intermediate-mass black holes [426]. Although detection of DS is challenging, their electromagnetic emission contributing to photon background has been considered [397, 354, 444]. Recently, it has been suggested that some high-redshift galaxy candidates observed by JWST could be spectroscopic manifestations of DSs [306].

In this work we investigate neutrino signatures originating from DSs and establish a new observational window into the progenitors of SMBHs. Going beyond previous limited considerations [397, 308], we show that DSs can produce detectable neutrino signals and we set constraints on DM annihilation using data from neutrino experiments. Furthermore, we show that our findings are consistent with observations from the JWST. Our study bridges key gaps between other directions, such as neutrino signatures [409, 410, 346, 365] from intermediate supermassive stars that might arise from star cluster collapse or primordial clouds in astrophysical SMBH formation paths.

Dark star population.– The DS population is expected to trace that of the first DM halos. The comoving number density distribution of DM halos based on a generalized halo mass function can be expressed as

$$\frac{dn_h}{dM_h} = \frac{\rho_m}{M_h}\sqrt{\frac{2A^2\beta}{\pi}}\Big(1+(\beta\nu^2)^{-p}\Big)e^{-\beta\nu^2/2}\frac{d\nu}{dM_h}\ , \tag{4.1}$$

where $\nu = \delta_c/D(z)\sigma(M_h)$ with $D(z) = \delta(a)/\delta(1)$ being the linear growth factor [303], $a = (1+z)^{-1}$ being the scale factor, and δ as defined in Ref. [173]. Here, $\delta_c = 1.68$ is the critical overdensity above which a spherically symmetric perturbation region will collapse to form virialized halo. $\rho_m = \rho_c\Omega_m(1+z)^3$ is the average mass density of the Universe scaled to critical density $\rho_c = 9\times10^{-30}$ g cm^{-3} at present by fraction $\Omega_m = 0.3$ [55]. In Eq. (4.1) parameters $(A,\beta,p) = (0.5,1,0)$ correspond to the Press-Schechter mass function [381], which we focus on throughout. We find similar results for the Sheth-Tormen [408] mass function, corresponding to $(A,\beta,p) = (0.322, 0.707, 0.3)$. The variance of the initial density fluctuation field $\sigma(M_h)$ is

$$\sigma^2(M_h) = \frac{1}{2\pi^2}\int W^2(kR_{M_h})P_\delta(k)k^2dk \tag{4.2}$$

where $W(x) = 3(\sin x - x\cos x)/x^3$ is a top-hat window function smoothing density fluctuation over scale $R_{M_h} = (3M_h/4\pi\rho_m)$. This is derived from the matter power spectrum $P_\delta(k) = A_s(k\ \mathrm{Mpc})^{n_s}T^2(k)$ where A_s is normalized by σ_8 [377] and $T(k)$ is transfer function fitted to cold DM model [124] with a spectral index $n_s = 0.965$ [55].

We model the DS formation rate to be proportional to the halo formation rate d^2n_h/dM_hdt up to a scaling f_{SMDS} that quantifies the fraction of DM halos hosting DSs. We do not consider the possible dependence of f_{SMDS} on halo mass and redshift and assume minimal delay between halo formation and the DS formation of initial mass $M_{\mathrm{DS},i} \simeq 5\ M_\odot$, which doesn't significantly affect our results unless these timescales are comparable to the DS lifetime. The DS growth proceeds by accretion, and we consider that halo mass does not appreciably changes during this period. We have confirmed that our DS luminosity as a function of mass matches numerically computed 1D stellar evolution of DS results of Ref. [389] within a factor of few, assuming a constant accretion rate of $\dot{M}_{\mathrm{DS}} = 10^{-9}M_h\ \mathrm{yr}^{-1}$ with DS mass following $M_{\mathrm{DS}}(t) = M_{\mathrm{DS},i} + \dot{M}_{\mathrm{DS}}t$.

The comoving number density of DSs surviving to a redshift z at a given cosmological time t in halos of mass M_h and age τ is given by

$$\frac{dn_{\mathrm{DS}}}{dM_h} = f_{\mathrm{SMDS}} \int_{z(t)}^{\infty} dz' \left|\frac{dt}{dz'}\right| \frac{d^2n_h}{dtdM_h}\left(M_h, z'(t-\tau)\right) \ , \tag{4.3}$$

where we consider $M_{\mathrm{DS}}^{\mathrm{lim}} = 10^{-2}M_h$ as the upper limit of DS mass. Here $dz/dt = (1+z)H(z)$ with the Hubble parameter for ΛCDM $H(z) \simeq H_0\sqrt{\Omega_m(1+z)^3 + \Omega_\Lambda}$, where $H_0 = 67.4$ km/s/Mpc is the Hubble constant at present, $\Omega_\Lambda = 0.7$ accounts for dark energy density and the radiation density of the Universe is neglected.

The total DS number n_{DS} can then be obtained by integrating Eq. (4.3) over the halos with DSs. For the lower limit we take $M_{h,\mathrm{min}} \sim 10^6\ M_\odot$ as the minimum mass where molecular hydrogen cooling causes protostellar clouds to collapse [305].

If lighter halos $M_h \sim 10^5\ M_\odot$ allow for DSs, this could significantly enhance their abundance (see Supplemental Material). However, we estimate that the lighter and less-luminous DSs would only contribute a factor ~ 2 enhancement to the total resulting neutrino flux. For the upper halo mass limit we take $M_{h,\max} \sim 10^9\ M_\odot$, but our results are not very sensitive this limit as such massive halos are rare at $z \gtrsim 15$.

The exact lifetimes and upper mass limits of DSs require further exploration. A large upper limit on DS mass being $\sim 5\%$ of the halo mass was considered in Ref. [305]. Recent high redshift SMBH observations appear to favor SMBH formation from $\sim 10^5\ M_\odot$ "heavy seeds" at $z \gtrsim 15$ [162]. Considering halos of mass $M_h > 10^6\ M_\odot$ as the supermassive DS hosts, the average halo mass is around $\sim 10^7\ M_\odot$. Typical DS masses of $\sim 10^5\ M_\odot$ can be achieved considering DSs grow to $\sim 1\%$ of host halo mass. Our results can be readily rescaled to account for different DS masses by appropriately considering the DM cross-section in Eq. (4.4). Smaller DSs are more challenging to detect with telescopes, with weakened constraints and allowing for higher abundance at lower redshifts.

Considering DS formation in mini-halos at redshifts $z \gtrsim 25$ and that they undergo collapse by $z \simeq 15$, as discussed below, the corresponding DS lifetime is $\mathcal{O}(10^8)$ yrs. Such DSs powered to luminosities of $\sim 10^{10}\ L_\odot$ will require fueling of $\sim 10^6\ M_\odot$ of DM, roughly percent-level of typical halo masses. DSs consuming heavier DM have smaller luminosities and can be expected to deplete host halos less significantly (see e.g. Ref. [252] discussion).

Dark star emission.– As baryonic matter undergoes protostellar collapse, it deepens the gravitational potential well at the center of a DM mini-halo of mass M_h. This alters the orbits of dissipation-less DM particles in accordance with the adiabatic invariant [157], $rM(r) = \text{const.}$, where $M(r)$ is the mass enclosed within radius r. As $M(r)$ increases due to baryonic inflow, r must decrease, leading to the adiabatic contraction of DM. This process concentrates DM at the center of the halo, where it can reach sufficiently high densities for efficient annihilation [417]. The energy released by DM annihilation heats the surrounding baryonic gas, stalling further collapse. The additional energy source in stellar evolution results in formation of a new DS category of early stars with much lower densities and temperatures.

We compute DS luminosity evolution considering an analytic polytropic model, as described in detail in Supplementary Materials. The resulting luminosity for DS of mass $M_{\rm DS}$ can be well fit by

$$L_{\rm DS} \simeq 2.1 \times 10^4 \left(\frac{M_{\rm DS}(t)}{M_\odot}\right)^{0.85} \left(\frac{\langle \sigma v \rangle}{10^{-26}~{\rm cm}^2/{\rm s}}\right)^{0.45} \times \left(\frac{m_\chi(1-f_\nu)}{100~{\rm GeV}}\right)^{-0.46} L_\odot~, \tag{4.4}$$

where reference $\langle \sigma v \rangle \simeq 10^{-26}{\rm cm}^3{\rm s}^{-1}$ is the thermally averaged DM annihilation cross-section as motivated by thermal relic abundance (e.g. [418]), f_ν is the fraction of the DM mass m_χ that is converted to neutrino energy. We find approximate agreement with results of Ref. [252].

The much lower temperatures of DSs, with $\lesssim$ few $\times\, 10^4$ K [389] at their surface, compared to Pop III stars result in lack of strong stellar winds. This facilitates persistent accretion of surrounding gas [253]. Depending on the mass of the host halo, DM concentration as well as baryonic accretion rates DSs can reach masses of $\sim 10^{6-7} M_\odot$ and luminosities of $\sim 10^{10} L_\odot$ [254]. In Fig. 26 we display the evolution of luminosities of DSs that grow to $\sim 10^6~M_\odot$ for different DM masses and annihilation channels, assuming $\dot{M}_{\rm DS} = 0.1 M_\odot~{\rm yr}^{-1}$ accretion rate in a $M_h = 10^8 M_\odot$ halo and

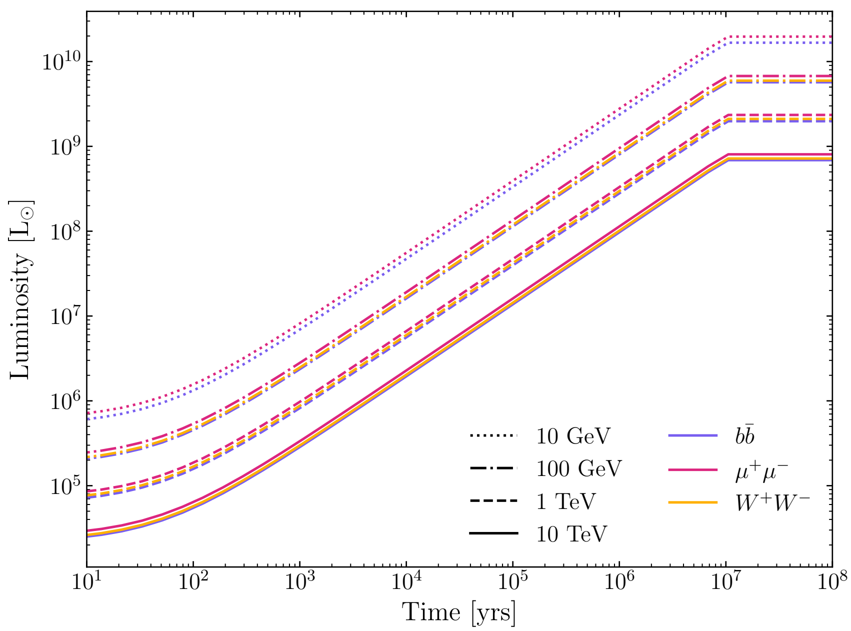

Figure 26. Evolution of DS luminosity for different DM masses and annihilation channels. We assume baryonic accretion rate of $0.1 M_\odot$ yr^{-1} in a $10^8 M_\odot$ halo until DS reaches a mass of $\sim 10^6 M_\odot$. We consider that baryonic accretion stalls when DS reaches approximately $\sim 1\%$ of the host halo mass, resulting in a plateau corresponding to DS mass and luminosity being approximately constant until DM annihilation becomes inefficient and DS collapses.

that DM fueling persists for extended period resulting in approximately constant DS mass and luminosity once the star reaches $M_{\rm DS} \sim 10^{-2} M_h$.

When DSs reach their maximal mass we consider efficient accretion to stall, leading to a phase of sustained stability. This persists until the surrounding DM in the host halo is sufficiently depleted, causing DM annihilation—the primary energy source of DSs—to become inefficient. At this stage, DSs collapse. High-mass DSs could collapse directly into black holes, though a brief intermediate phase of nuclear fusion is possible [254].

Supermassive black hole progenitors and JWST.– Supermassive DSs constitute intriguing possible early massive $\sim 10^{4-6} M_\odot$ seeds for SMBHs. We consider DS number densities consistent with distribution of SMBHs at galactic centers, one per $10^{10} M_\odot$ baryon mass object as can be found in some dwarf galaxies, analogous to the method of Ref. [365]. For this, we set $f_{\rm SMDS}$ in Eq. (4.3) such that number density of SMBH seeds is $n_{\rm SMBH}(z)/(1+z)^3 \sim \rho_B/10^{10} M_\odot$, where $n_{\rm SMBH}(z)$ is given by integrating Eq. (4.3) for contributing halos $M_h = 10^6$ to 10^9 $M_\odot$ and $\rho_B = \rho_c \Omega_b = 4 \times 10^{-31} {\rm g/cm}^3$ is the baryon density of the Universe with $\Omega_b = 0.0476$ [55]. We then evaluate $n_{\rm SMBH}(z)/(1+z)^3$ just before DS collapse, taking $z = 15$ for reference, and compare with $\rho_B/10^{10} M_\odot$ at present. We find $f_{\rm SMDS} \simeq 6 \times 10^{-3}$. This estimate is conservative as it does not account for such effects as mergers. To account for additional uncertainties, we consider $f_{\rm SMDS}$ in the range from 1% to 0.1%. Additional precision in $f_{\rm SMDS}$ evaluation can be obtained from detailed simulations of structure growth beyond our scope, including feedback effects [426].

Supermassive DSs could be directly detected by sensitive telescopes [305, 446, 306], providing an independent and complimentary probe. In particular, JWST's infrared sensitivity, ability to probe the high-redshift Universe and spectroscopic tools uniquely position it to search for DSs. Recently, three supermassive DS candidates at redshifts $z \sim 11-14$ have been claimed from JWST Advanced Deep Extragalactic Survey (JADES) data [306]. Ref. [305] used Hubble Space Telescope (HST) data to constrain DSs up surviving to redshift $z = 10$, and showed that JWST can efficiently detect supermassive DSs up to $z = 15$ for $M_{\rm DS} = 10^6\ M_\odot$.

DS parameters consistent with JWST observations can be identified from the number of supermassive DSs observable in JWST at a particular redshift expressed as

$$\begin{aligned} \frac{dN_{\rm obs}}{dz} = \frac{\theta^2}{4\pi} \int dM_{\rm DS} f_{\rm sur}(z, M_{\rm DS}) f_{\rm obs}(z, M_{\rm DS}) \\ \times \frac{dV_c}{dz} \frac{dn_{\rm DS}}{dM_h}(M_h, z(t-\tau)) \ , \end{aligned} \tag{4.5}$$

where $\theta^2 = 26.4$ arcmin^2 is the JWST coverage [388], $f_{\rm sur}$ and $f_{\rm obs}$ denote the DS fraction that survives to redshift z and the likelihood that JWST observes a DS of mass $M_{\rm DS}$ at redshift z respectively. Eq. (4.5) also includes the differential volume element dV_c/dz, with $V_c = (4\pi/3)D_M^3$ the comoving volume of the Universe where [317]

$$D_M = \left(\frac{2c}{H_0}\right) \frac{2 - \Omega_M(1-z) - (2-\Omega_M)\sqrt{1+z\Omega_M}}{\Omega_M^2(1+z)} \tag{4.6}$$

for a flat Universe without dark energy that is a good approximation at redshifts $z \gtrsim 10$ we consider. The total number of DSs observable with JWST is the integral of Eq. (4.5) over redshifts.

Here we consider $f_{\rm obs}(z > 15) = 0$ and survival model $f_{\rm sur}$ being a step-function at $z = 15$, resulting in conservative $N_{\rm obs} = 0$ DS candidates for all redshifts. This also maximizes possible DS neutrino flux consistent with JWST observations. In Supplemental Material we present a model of gradual DS collapse, showing that it can account for $N_{\rm obs} \geq 1$ JWST DS candidates.

Dark star neutrino signals.– Supermassive DSs shining at high luminosities can emit significant neutrino fluxes, contributing to a diffuse background analogous to the diffuse supernova neutrino background (DSNB) in the later Universe. Unlike the DSNB produced by transient events with neutrino energies determined by supernova temperatures, DSs emit neutrinos over prolonged time with neutrino energies determined by DM.

The electromagnetic comoving luminosity density of the total DS population as a function of redshift and integrated by DS age-distribution is

$$\begin{aligned} L_{\rm EM}(z) = & \int_0^{t(z)} d\tau \int_{M_{h,\rm min}}^{M_{h,\rm max}} dM_h L_{\rm DS}(M_h,\tau) \\ & \times f_{\rm sur}(z) \frac{d^2 n_{\rm DS}}{dM_h dt}(M_h, z(t-\tau)) \ , \end{aligned} \tag{4.7}$$

where evaluating $d^2 n_{\rm DS}/dM_h dt$ by differentiating Eq. (4.3) and evaluating at $z(t-\tau)$ gives the DS age τ distribution at cosmological time t formed in halos of mass M_h. Here, we do not include contributions from DM annihilation outside of DSs that is also enhanced by the adiabatic contraction, making our estimates conservative.

The resulting DS diffuse neutrino flux

$$\begin{aligned} \frac{d\phi}{dE_\nu} = & \int_{z_{\rm lim}}^{\infty} dz \Bigg[(1+z)\frac{dN}{dE_\nu}(E_\nu(1+z)) \\ & \times \left(\frac{f_\nu}{(1-f_\nu)\langle E_\nu\rangle} L_{\rm EM}(z)\right) \left|c\frac{dt}{dz}\right|\Bigg] \end{aligned} \tag{4.8}$$

where $\langle E_\nu \rangle$ is the average neutrino energy from DM annihilation and depends on considered channel (see Supplemental Material), dN/dE_ν is a neutrino emission spectrum from DM annihilation and spectrum factor $(1+z)$ accounts for compression of the energy scale. In Ref. [254] $f_\nu = 1/3$ was assumed. For DM annihilation channels we consider neutrino spectra computed by Ref. [188, 185], summarized in Supplemental Materials. Here, $f_\nu/(1-f_\nu)\langle E_\nu\rangle$ converts the electromagnetic luminosity to neutrino number flux. We integrate from a minimum redshift where

JWST becomes unable to observe the most massive DSs in our population $z_{\rm lim} = 15$. In the Supplemental Material we show that our generalized formalism for extended source emission can also account for fluxes like DSNB.

Acknowledgments. We thank Katherine Freese, Tracy Slatyer, Anna Suliga and Tien-Tien Yu for discussions. V.T. acknowledges support by the World Premier International Research Center Initiative (WPI), MEXT, Japan and JSPS KAKENHI grant No. 23K13109. This work was performed in part at the Aspen Center for Physics, which is supported by the National Science Foundation grant PHY-2210452.

CHAPTER V

CLASH OF THE TITANS: ULTRA-HIGH ENERGY KM3NET EVENT VERSUS ICECUBE DATA

Here we again consider a different category of astrophysical neutrino, in this case, and individual event observed in KM3NeT. While annihilating dark matter is capable of producing such an event, that is not the preferred context for this study. We instead focus on the phenomenology and statistics of such an observation while remaining agnostic on its implication for new physics. This work is co-authored with Shirley Li, Pedro Machado, and Daniel Naredo-Tuero and is under peer review for publication in Physical Review Letters with a pre-print available here [337].

KM3NeT has reported the detection of a remarkably high-energy through-going muon. Lighting up about a third of the detector, this muon likely originated from a neutrino exceeding 10 PeV in energy. The crucial question we need to answer is where this event comes from and what its source is. Intriguingly, IceCube has been operating with a much larger effective area for a considerably longer time, yet it has not reported neutrinos above 10 PeV. We quantify the tension between the KM3NeT event and the absence of similar high-energy events in IceCube. Through a detailed analysis, we determine the most likely neutrino energy to be in the range of $23 - 2400$ PeV. We find a 3.5σ tension between the two experiments, assuming the neutrino is from the diffuse isotropic neutrino flux. Alternatively, assuming the event is of cosmogenic origin and considering three representative models, this tension still falls within $3.1 - 3.6\sigma$. The least disfavored scenario is a steady or transient point source, though still leading to 2.9σ and 2.0σ tensions, respectively. The lack of observation of high-energy events in IceCube seriously challenges the explanation of this event coming from any known diffuse fluxes. Our results indicate the KM3NeT event is likely the first observation of a new astrophysical source.

5.1 Kilometer Scale Neutrino Telescopes

High-energy astrophysical neutrinos provide a unique means to observe the universe at distances and energies not easily accessible through electromagnetic radiation. Unlike photons or charged particles, neutrinos can travel vast distances across the universe without being absorbed or deflected, making them invaluable probes of astrophysical phenomena, particularly at identifying high-energy astrophysical sources.

The IceCube experiment has been a pioneer in the field of high-energy neutrino astronomy, observing neutrinos above the PeV scale [9, 8]. These observations have led to the discovery of an isotropic diffuse neutrino flux [21, 15, 23, 411, 26]. Additionally, point sources such as blazars have been identified as potential sources of high-energy neutrinos [22].

Moreover, several large-scale neutrino observatories are under construction or in development, such as KM3NeT in the Mediterranean Sea [50], Baikal-GVD in Lake Baikal [109], the Pacific Ocean Neutrino Experiment (P-ONE) in the Pacific Ocean [60], and the planned IceCube-Gen2 [16]. The synergy among these detectors, which employ different detection techniques and cover complementary regions of the sky, will improve our ability to detect astrophysical neutrinos and identify sources [68].

Recently, the KM3NeT collaboration reported a remarkable event: a through-going muon that triggered 3,672 photomultiplier tubes (PMTs), roughly a third of the detector [190, 69]. The collaboration inferred the energy of the neutrino that produced this muon to be between 72 – 2600 PeV, making it the highest-energy neutrino event ever confirmed.

Although this observation is extraordinary, it raises important questions, such as the origin of this neutrino and its production mechanism [53, 52, 366, 370, 236, 226]. Given IceCube's longer exposure time and larger effective area, one would expect it to have detected similar high-energy muons, which would help identify the source. However, no events exceeding 10 PeV have been reported by IceCube. This suggests a possible tension between the KM3NeT single-event observation and IceCube's lack of observation in more than ten years of data [54].

In this paper, we aim to examine potential sources for this KM3NeT event through compatibility tests of KM3NeT and IceCube data. We consider the diffuse flux observed by IceCube, cosmogenic neutrinos, and potential transient point sources. We evaluate the likelihood of each source by computing the tension between the KM3NeT detection and IceCube's non-observation given each flux assumption. Our analysis complements KM3NeT's test of the compatibility between their event and data from IceCube and Auger [54]. While our results are qualitatively similar to KM3NeT's, the differences in procedures lead to quantitatively distinct outcomes. We comment on these differences throughout this manuscript.

5.2 The KM3NeT event

Triggering a significant fraction of the detector's PMTs, the KM3NeT event is consistent with a through-going muon [190, 69]. The KM3NeT detector is still being constructed, and this event occurred during the ARCA21 phase, where 21 strings have been deployed, with an exposure of 288 days. The angular direction of the muon is well reconstructed, coming from 0.6° above the horizon. KM3NeT has estimated the muon energy to be 120 PeV, and the parent neutrino energy to be within 72 – 2600 PeV at 90% confidence level (CL). In addition, the collaboration reported the number of PMTs that were triggered by the through-going muon, $N_{\text{hit}} = 3672$, as

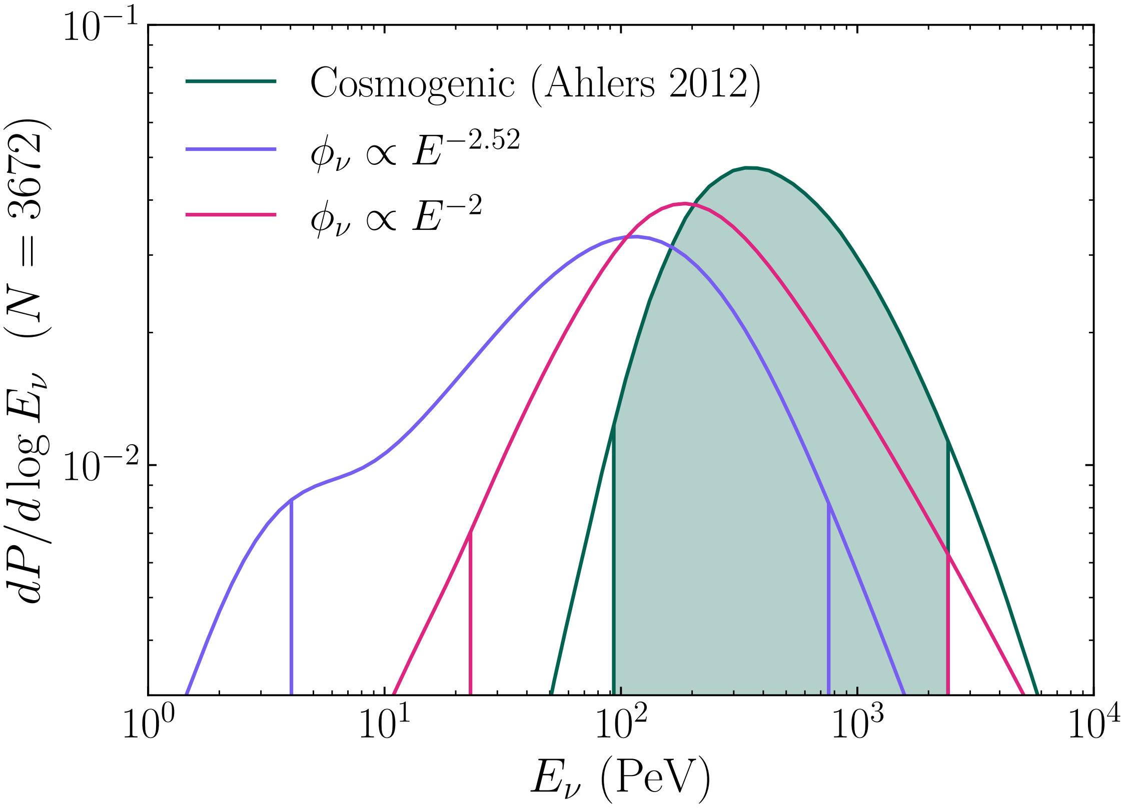

Figure 27. Inferred probability density of the neutrino energy of the KM3NeT event, given the 3,672 triggered PMTs, for three different underlying source flux assumptions.

well as Monte Carlo simulations of the number of PMTs triggered by 10, 100 and 1000 PeV through-going muons [190, 69].

Even though the collaboration reported the range of likely neutrino energy for the event, it did not report its probability density, which our analysis requires. Therefore, we first infer the probability density for the neutrino energy. Bayes theorem states that the probability of a neutrino energy given the number of triggered PMTs (hits) is

$$P(E_\nu|N_{\rm hit}) = \frac{1}{P(N_{\rm hit})} \int dE_\mu P(N_{\rm hit}|E_\mu)P(E_\mu|E_\nu)P(E_\nu), \tag{5.1}$$

where $P(E_\nu)$ is the prior on the neutrino energy and $P(E_\mu|E_\nu)$ is the probability that an interaction of neutrino with energy E_ν outside the detector leads to a muon entering the detector with energy E_μ. $P(N_{\rm hit}|E_\mu)$ is the probability of such a muon triggering $N_{\rm hit}$ PMTs in the detector. Note that the probability $P(E_\mu|E_\nu)$ depends on the effective area of the detector, for which our calculation matches well the official KM3NeT effective area, see App. D.1. This probability further depends on the neutrino charged-current interaction cross section, which we simulate using `MadGraph` [78]. The probability of a muon triggering $N_{\rm hit}$ PMTs, $P(N_{\rm hit}|E_\mu)$, depends on muon energy loss in water, simulated here with `PROPOSAL` [316], as well as the details of the detector, for which we adopt a simplified model to account Cherenkov light production, light propagation in water, and light detection. In addition, we set a prior that muons entering the detector need at least 1 PeV energy. For more details, see App. D.2.

Figure 27 shows the inferred neutrino energy of the event for three representative priors on the neutrino energy: a power-law flux $E_\nu^{-2.52}$, which represents the diffuse flux observed by IceCube [367]; a power-law flux E_ν^{-2}, which represents a generic source spectrum motivated by Fermi acceleration; and the cosmogenic neutrino flux from Ahlers *et al.* [66]. We also highlight the 90% interval and most likely neutrino energies, summarized in Table 5. We find excellent agreement when comparing our 90% confidence interval (CI) with KM3NeT's official 90% energy estimate for a E^{-2} power-law [69]. While the 90% interval has some dependence on the flux prior, we can see a robust preference for neutrino energies at or above the 100 PeV scale, possibly reaching EeV energies. This preference for ultrahigh neutrino energies raises an obvious question: Where does this event come from? Why hasn't IceCube observed similarly high-energy events?

Prior	Peak energy (PeV)	90% CI (PeV)
Power-law, ($\gamma = 2.52$)	120	$[4.0,\ 760]$
Power-law, ($\gamma = 2.0$)	190	$[23,\ 2400]$
Cosmogenic (Ahlers 2012)	335	$[93,\ 2400]$

Table 5. Most likely neutrino energies and 90% confidence intervals for the KM3NeT event assuming different underlying fluxes.

5.3 Compatibility between KM3NeT and IceCube data

The estimated compatibility between KM3NeT and IceCube data depends on the assumptions we adopt for the origin of the event. We will investigate three possibilities for the origin of this event: diffuse power-law, cosmogenic, and point source neutrino fluxes. For each assumption, the expected number of events triggering at least $N_{\rm hit}$ PMTs at KM3NeT can be calculated as

$$N_{\rm evt} = 4\pi T \int_0^\infty dE_\nu \int_{N_{\rm hit}}^\infty d\hat{N}_{\rm hit}\, P(\hat{N}_{\rm hit}|E_\nu) \left\langle \frac{d\phi}{dE_\nu} A_{\rm eff}(E_\nu) \right\rangle_\Omega , \tag{5.2}$$

where ϕ is the neutrino flux, $A_{\rm eff}$ is the effective area, angle brackets indicate an average over the solid angle, $T = 288$ days [69] is the exposure, and $P(N_{\rm hit}|E_\nu) = \int dE_\mu P(N_{\rm hit}|E_\mu) P(E_\mu|E_\nu)$ is the probability that $N_{\rm hit}$ PMTs are triggered by a muon originating from a neutrino with energy E_ν, as discussed in the previous section.

5.3.1 Power-law diffuse flux.

The diffuse flux of one flavor (muon neutrinos and antineutrinos) is well-characterized by a single power-law spectrum:

$$\frac{d\phi}{dE_\nu} = \phi_0 \left(\frac{E_\nu}{100\,\mathrm{TeV}} \right)^{-\gamma} \times 10^{-18}/\mathrm{GeV/cm^2/s/sr}\,, \tag{5.3}$$

where ϕ_0 is a dimensionless flux normalization and γ is the spectral index. This parametrization has successfully described the observed neutrino spectrum from tens of TeV to the PeV scale in IceCube [367].

In order to quantify the compatibility between KM3NeT and IceCube, we employ the likelihood

$$\mathcal{L}(\phi_0, \gamma) = \mathcal{L}_{\text{flux}}(\phi_0, \gamma) \cdot \mathcal{L}_{\text{evt}}(N_{\text{evt}}(\phi_0, \gamma))\,. \tag{5.4}$$

We account for IceCube's measurement of the high-energy neutrino flux with a Gaussian prior $\mathcal{L}_{\text{flux}}$ in ϕ_0 and γ. Although the flux parameters from IceCube differ slightly from different datasets, they are largely consistent with each other [367]. For our analysis, we take the results of the combined fit [367], which yields $\phi_0 = 1.83^{+0.13}_{-0.16}$ and $\gamma = 2.52 \pm 0.04$. The probability of observing one event at KM3NeT with $N_{\text{hit}} \geq 3672$, given the flux parameters, is encoded in the Poissonian term $\mathcal{L}_{\text{evt}} = N_{\text{evt}} e^{-N_{\text{evt}}}$, see Eq. (5.2). The posterior distribution is computed from the likelihood (5.4) assuming a flat prior on N_{evt}. We then quantify the tension by means of the usual Bayes factor between the KM3NeT observation and IceCube preference.

After marginalizing over the flux parameters, we find a 0.039% (3.5σ) tension between the ultra-high energy event observed in KM3NeT and the IceCube measurement of astrophysical neutrinos. If we take IceCube's power-law preference based on through-going events only [23], which allows slightly harder spectra, the tension is still 0.13% (3.2σ).

The tension found here is greater than the 1.9σ quoted by KM3NeT [54]. The reason for this discrepancy is twofold. Firstly, KM3NeT calculates the tension assuming that the probability for the neutrino energy is flat in the 90% CI. We account for the neutrino energy probability distribution, which penalizes lower energies where the tension would be smaller. Secondly, KM3NeT includes their non-observation of events outside the 90% CL energy interval. This increases the degrees-of-freedom while barely contributing to the test-statistic, due to strong analysis cuts.

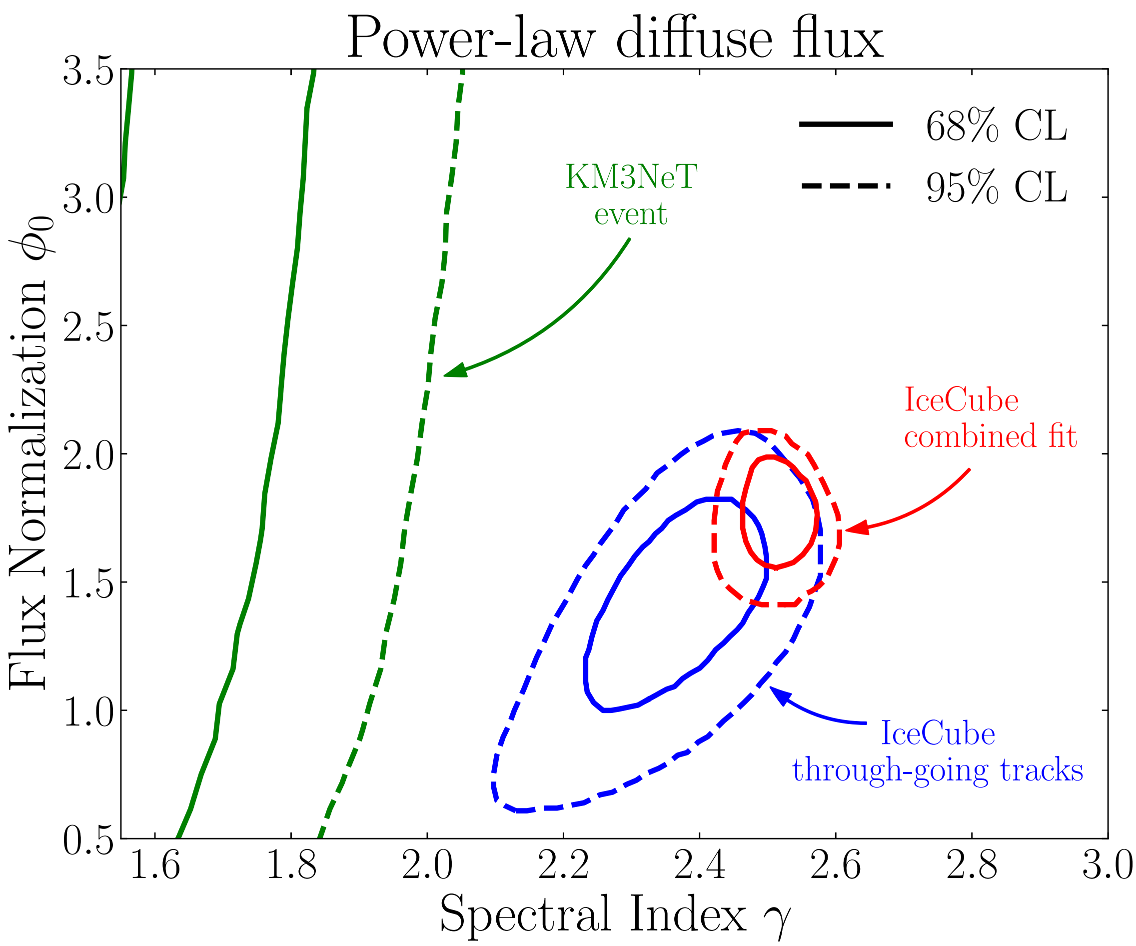

Figure 28. Preferred regions in the diffuse power-law spectrum flux normalization ϕ_0 and spectral index γ for the ultra-high energy KM3NeT event and IceCube data at 68% and 95% CL.

Consequently, this lowers the tension. If we follow KM3NeT's procedure, we confirm their 1.9σ result.

Another way to appreciate this tension is to examine the preferred regions for the power-law spectrum parameters given IceCube data and the ultra-high energy KM3NeT event in Fig. 28. Since it is obtained by fitting a single event while dropping the Gaussian prior on Eq. (5.4), the KM3NeT region exhibits a degeneracy between ϕ_0 and γ. For IceCube, we show the allowed regions for through-going events only and through-going plus shower events. The lack of overlap between IceCube and KM3NeT is the tension among these data. Given IceCube's nominal flux, KM3NeT should have expected 0.005 events between 72 – 2600 PeV during the exposure. Alternatively, given the normalization of the flux inferred from KM3NeT's event, assuming a spectral index of 2.52, IceCube should have expected 75 events in their diffuse search between 72 – 2600 PeV.

5.3.2 Cosmogenic flux. Given the extremely high energy of the event, it is reasonable to ask if this is the first detection of the long-awaited cosmogenic neutrinos. Cosmogenic neutrinos are produced when ultra high-energy cosmic rays interact with the cosmic microwave background [283, 447]. These neutrinos, which can reach EeV energies, have never been observed. We consider three benchmark scenarios for the cosmogenic flux, Ahlers 2010 [64], Ahlers 2012 [66], and van Vliet 2019 [430], as possible origins of the KM3NeT event. These scenarios have been previously studied by IceCube [28], which found p-values of 0.3%, 4.3%, and 26.8% for these models respectively based on the non-observation of a neutrino flux exceeding ~ 100 PeV. For each model, we calculate the probability of producing an event in KM3NeT that triggers at least 3672 PMTs, and subsequently combine this with the p-values provided by IceCube in Ref. [28].

Cosmogenic Model	Combined p-value
Ahlers2010 1EeV	3.3×10^{-4} (3.6σ)
Ahlers 2012	1.6×10^{-3} (3.1σ)
VanVliet2019	1.6×10^{-3} (3.1σ)

Table 6. Combined p-value of KM3NeT and IceCube, for distinct cosmogenic neutrino flux models.

We find p-values of 0.033%, 0.16%, 0.16% for Ahlers 2010, Ahlers 2012, and van Vliet 2019, respectively, revealing a robust tension between KM3NeT and IceCube data under these assumptions. The reason for the tension is fairly simple and it is depicted in Fig. 29, where we show IceCube and KM3NeT data, the flux predictions for each cosmogenic model, and the IceCube constraints on the power-law and cosmogenic fluxes. In a nutshell, Ahlers 2010 predicts 6.2×10^{-3} events in KM3NeT but it is disfavored by IceCube with a p-value of 0.3%. Using Ahlers 2012 yields 2.8×10^{-3} events in KM3NeT but its IceCube p-value is 4.3%. Finally, van Vliet 2019, with the highest IceCube p-value of 26.8%, only predicts 5.7×10^{-4} events in KM3NeT. Therefore, none of the benchmarks can readily accommodate the observed ultra-high-energy event without being in tension with IceCube's non-observation of neutrinos above 10 PeV. Even without taking IceCube data into account, none of the cosmogenic models considered here predict a sizable event rate in KM3NeT.

We note that the tension we report is more significant than KM3NeT's official numbers. In addition to the different treatment of the neutrino energy, this is due to the fact that we adopted IceCube's lastest constraint on cosmogenic flux [28], whereas KM3NeT used an older result in Ref. [14]. If we adopt the previous IceCube constraints on a cosmogenic neutrino flux, our tension decreases to about 2.5σ for Ahlers2010 1 EeV cosmogenic model, consistent with KM3NeT.

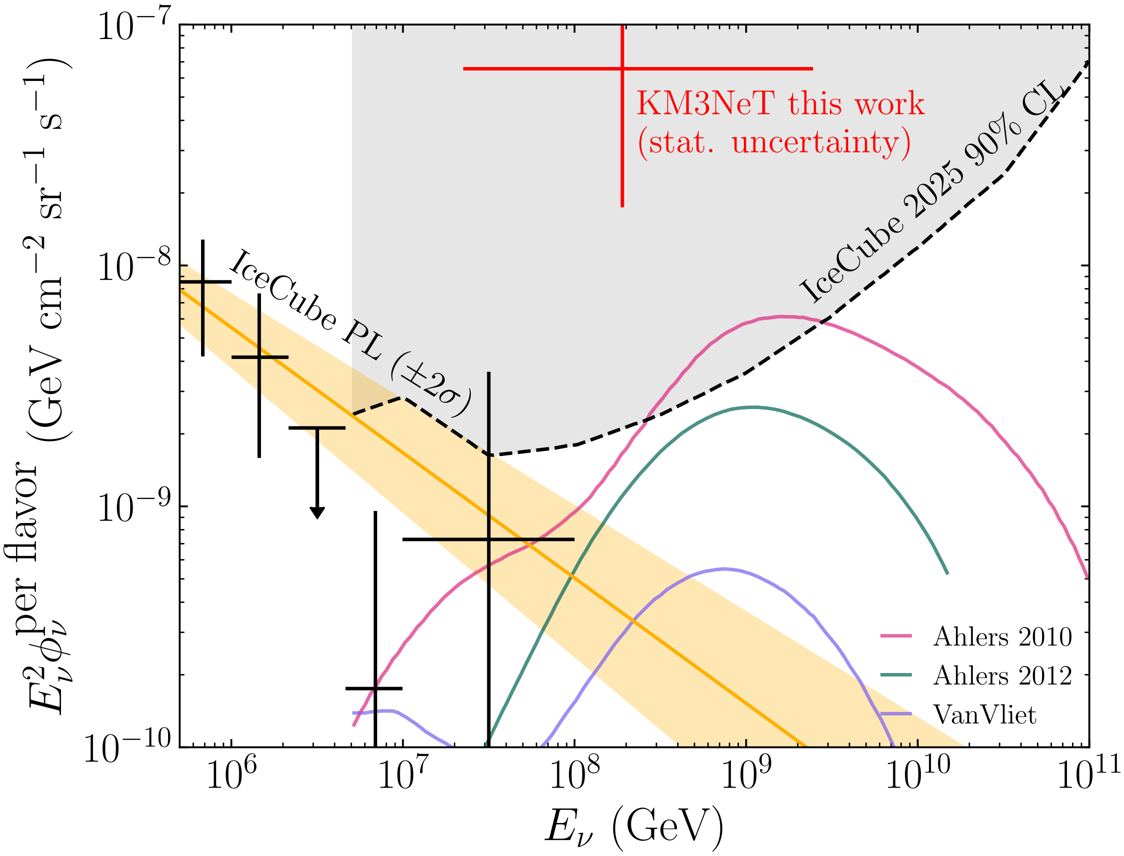

Figure 29. Predictions, measurements, and constraints on the high energy neutrino flux. The gold band shows the IceCube measurement of a single power-law flux, extrapolated to $E_\nu > 100$ PeV while the three colored curves represent a selection of cosmogenic neutrino models [64, 66, 430]. We show IceCube's segmented power-law data in black with error bars [367] and high energy constraints in gray [355]. In red we show a best fit segmented power-law flux from the event in KM3NeT in the 90% CI from a E_ν^{-2} power-law prior and 1σ error bars on the flux normalization.

5.3.3 Point Sources. The tensions discussed in the previous sections could potentially be alleviated if the event seen in KM3NeT originated from either a steady point source or a transient source that was in an unfavorable location for IceCube detection. At the high energies preferred by the KM3NeT event, absorption in the Earth strongly attenuates up-going neutrinos, making effective areas virtually null for sources below the detector horizon. Similarly, for down-going events, the smaller amount of target material above the detector not only reduces the interaction probability but also increases the cosmic ray background, which suppresses the effective area.

Therefore, a source location where KM3NeT has good sensitivity but IceCube has reduced sensitivity due to either Earth absorption or reduced interaction probability could help explain the apparent discrepancy between the detectors. Nevertheless, this is not the case here. Figure 30 depicts the IceCube sky coverage on KM3NeT local zenith and azimuth coordinates. The shaded gray region corresponds to a declination at IceCube of -15° where Earth matter would significantly absorb neutrinos above $E_\nu = 10$ PeV [20]. The dashed black line, on the other hand, corresponds to the IceCube horizon.

The event in KM3NeT, shown as a green dot in Fig. 30, was within 1° of the local horizon providing maximal sensitivity for KM3NeT. However, as shown in Fig. 30 the event's azimuthal angle of approximately 259.8° at KM3NeT (36° latitude) corresponds to roughly 8° above the horizon at IceCube –where IceCube maintains optimal sensitivity to ultra-high energy neutrinos.

Since the event originated from a zenith angle where IceCube has a larger effective area and has been recording data for about 10 times longer, a point source is unable to alleviate the tension between the two experiments. For a single event in KM3NeT,

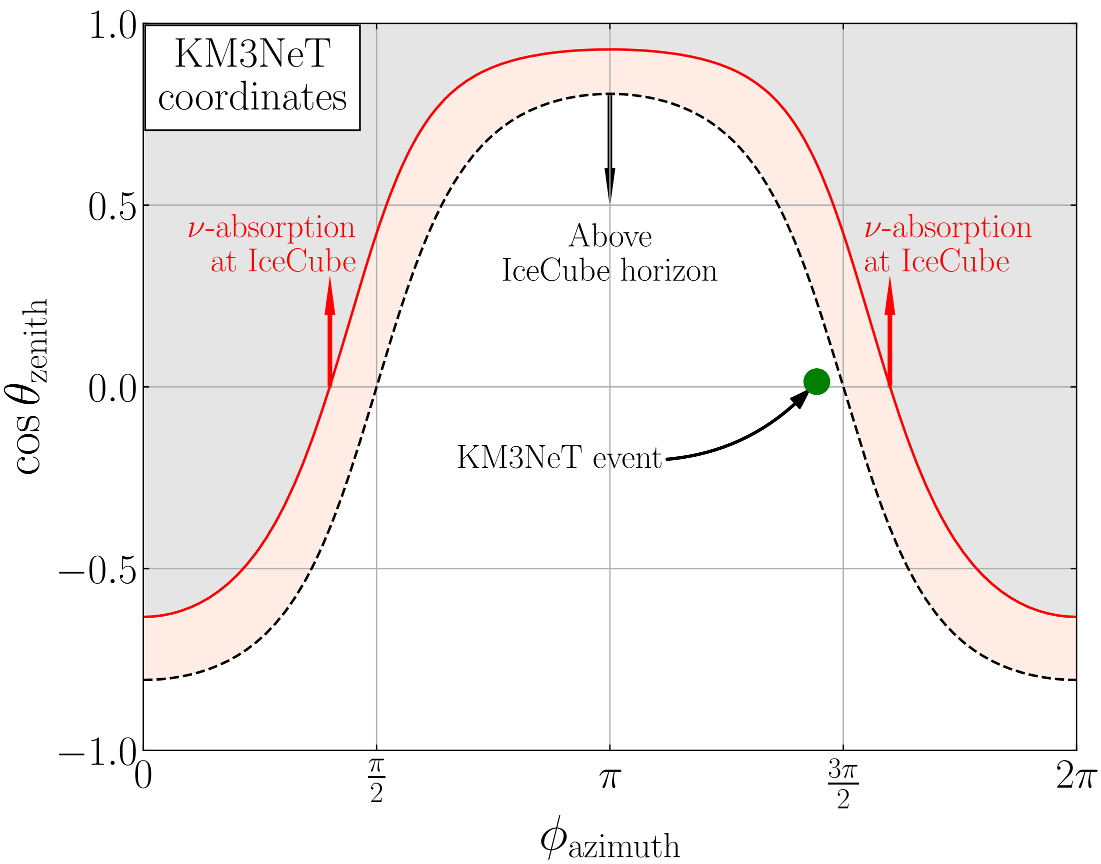

Figure 30. IceCube sky coverage on the KM3NeT local zenith and azimuth angles.

one would expect the number of events in IceCube to simply scale up as the ratio of effective areas times exposures, namely, $(A_{\rm eff}T)_{\rm IC}\,/\,(A_{\rm eff}T)_{\rm K}\sim 280$, where we have considered 10 years of IceCube and averaged the effective areas over the 90% CL energy interval when assuming a E_ν^{-2} power-law prior (see Table 5). Notice that, due to the Earth's rotation, KM3NeT's effective area should be averaged over the $\cos\theta_{\rm zenith}$ range spanned in a day. We find that $\cos\theta_{\rm zenith}\in[-0.87, 0.73]$, which implies that the day-averaged effective area is close to the sky-averaged effective area. Hence, we employ the latter in our statistical procedure. We consider a likelihood consisting of two Poissonian terms, which encode the probability of observing one event at KM3NeT and none at IceCube when $N_{\rm K}$ and $N_{\rm IC}$ are expected respectively.

$$\mathcal{L} = N_{\rm K}e^{-N_{\rm K}}\cdot e^{-N_{\rm IC}} \quad \text{with} \quad \frac{N_{\rm IC}}{N_{\rm K}} = \frac{(A_{\rm eff}T)_{\rm IC}}{(A_{\rm eff}T)_{\rm K}}\,, \tag{5.5}$$

We test, by means of a Bayes factor, this hypothesis against the scenario in which no events are seen in both experiments, assuming flat priors on $N_{\rm K}$ and $N_{\rm IC}$. This boils down to a 2.9σ tension. Similar results are obtained using a frequentist approach.

A last possibility would be a transient source whose neutrinos only started arriving at the Earth after KM3NeT started taking data. This would mitigate the tension by reducing IceCube's longer exposure. Nevertheless, the difference in effective areas still lead to a 2.0σ tension. We also note that mis-reconstruction of the azimuthal angle of this event could put it significantly above IceCube's horizon. In that case, due to large cosmic muon backgrounds, it would not be surprising that IceCube missed this transient source. However, as discussed in Ref. [69], 5.6° mis-reconstruction would be a 5σ deviation from KM3NeT's nominal systematic uncertainty on the direction of the event.

Acknowledgments

We thank John Beacom, Asher Berlin, Mattias Blennow, Mauricio Bustamante, Brian Clark, Enrique Fernandez-Martinez, Patrick Fox, Stefan Hoeche, Dan Hooper, Matheus Hostert, Joshua Isaacson, Tim Linden, Toni Mäkelä, Danny Marfatia, Nathan Whitehorn, and Bei Zhou for discussions. This manuscript has been authored by Fermi Forward Discovery Group, LLC under Contract No. 89243024CSC000002 with the U.S. Department of Energy, Office of Science, Office of High Energy Physics. The work of DNT is funded by the Spanish MIU through the National Program FPU (grant number FPU20/05333) and he has received support from the European Union's Horizon 2020 research and innovation programme under the Marie Skłodowska-Curie grant agreement No 860881-HIDDeN and No 101086085 - ASYMMETRY, and from the Spanish Research Agency (Agencia Estatal de Investigación) through the Grant IFT Centro de Excelencia Severo Ochoa No CEX2020-001007-S and Grant PID2022 137127NB-I00 funded by MCIN/AEI/10.13039/501100011033. TS is supported by the Dept. of Energy Office of Science Graduate Student Research (SCGSR) program administered by the Oak Ridge Institute for Science and Education (ORISE) for the DOE. ORISE is managed by ORAU under contract number DE-SC0014664.

Note added: After the publication of this manuscript, the KM3NeT results came out [69]. We have updated our effective areas accordingly and the distributions of triggered PMTs in D.2. Our conclusions remain unchanged. Moreover, Ref. [370] appeared, claiming that for a transient point source, the consistency between IceCube and KM3NeT is below the 90% CI. The main difference in our analyses is the statistical treatment in computing p-values. Reference [370] computes the 90% CI for both experimental observations, and due to the overlap of these two intervals, they conclude there is no tension at 90% CI. This procedure double counts the statistical error, artificially lowering the tension.

CHAPTER VI

CONCLUSION

6.1 Detection of Neutrino NSI with Solar Neutrinos in Low-Threshold Dark Matter Experiments

In Chapter 2, we showed that near-future low-threshold dark matter detectors, both semiconductor and noble liquid targets, have the potential to probe previously unconstrained parameter space for vector, scalar, and axial vector NSI simplified models; pseudoscalar models are more difficult to probe. The potential for vector mediators is especially promising with improvements to the electron (nuclear) coupling constraints of an order of magnitude for $M_V \lesssim 1(1000)$ keV in semiconductors and one (two) order of magnitude in noble liquid detectors at similar mediator masses. Axial vector models see a similar improvement except where detector nuclei have little or no spin (such as argon). In scalar models, semiconductors can roughly match the electron coupling constraints while improving upon the nuclear ones by an order of magnitude below $M_S \lesssim 1(1000)$ keV and noble liquids can improve constraints by an order of magnitude for electron and nuclear couplings. In contrast, there is little room for improvement with the pseudoscalar models; the noble liquid detectors can improve upon current constraints by a factor of a few but the semiconductor experiments are not competitive. In the event of a putative signal, one can perform an model-specific analysis in lines with the one discussed in Sec. 2.4.2. In addition to the simplified models, both semiconductors and noble liquids will be sensitive to a neutrino magnetic moment. A silicon (germanium) detector can match the current best bounds at 95%CL with an exposure of 10 (35) kg-yrs while xenon (argon) can do so with 60 (70) kg-yrs.

The sensitivity of Skipper-CCDs to reactor neutrinos was recently studied in [240], which provides a complementary analysis to the one performed in this work. Specifically, there are two key differences between reactor and solar neutrinos: the neutrino energies and the neutrino flavors probed. Although solar neutrinos are a lower intensity source, they are at higher energy than their reactor counterparts. The other difference is in the neutrino flavors detected. For a detector $\sim$ 10m from a reactor, all of the incident neutrinos will be electron neutrinos. In comparison, solar neutrinos are traveling much longer distances so a detector using solar neutrinos will be sensitive to the effects of neutrino oscillations and NSIs with any neutrino flavor. This broadens the set of UV theories such as $U(1)_{L_\mu - L_\tau}$ which map to these simplified models. Combining the results from reactor and solar neutrinos broadens the scope of analyses on NSIs.

In summary, we have demonstrated that current and near-future low-threshold DM direct detection experiments have tremendous potential to probe models of NSIs. The semiconductor experiments can improve the existing constraints on the neutrino magnetic moment and to measure the changes to the SM CEvNS rate while liquid xenon and argon detectors will be able to improve the measurement of potential electron couplings. We have shown that in noble liquid detectors, the improvements gained by lowering the threshold have a stronger effect at low masses compared to the order of magnitude increase in the exposure. A more robust statistical analysis could generally improve these constraints, but we leave that analysis to be performed on real data collected by future detectors. We have omitted the uncertainties associated with our choice of yield function to maintain plot legibility, but we include them in Appendix A.1 for a single exposure to demonstrate their importance. They dominate the uncertainty in these calculations and better measurement of them, specifically at low energies, is vital to validating constraints placed by such low-threshold DM detectors.

We have made use of the existing infrastructure of DM detectors to project constraints on NSIs because the signals produced by these NSIs, specifically in nuclear recoils, are very similar to DM recoils. A single event is indistinguishable, but by using the distribution of events a robust likelihood analysis, like the one used for the neutrino magnetic moment, can disentangle two BSM models such as a NSI and an ultralight DM particle. Additional information can be seen by the relative strengths of a signal in electron recoils or different materials such as argon's insensitivity to axial vector models. Such dedicated analyses are worthwhile undertakings that we leave for future work.

6.2 Nonstandard Neutrino Interactions and Leptoquarks in Dark Matter Experiments

In Chapter 3, we projected the sensitivity of larger scale, higher threshold dark matter experiments to neutrino NSI and realized these interactions in the form of a UV complete model of Leptoquarks. Results are presented in the main body of the chapter, but we reiterate the important conclusions here. We find that the discovery regions for general neutrino NSI of the experiments we consider are within the range of values allowed by IceCube ($-0.041 < \varepsilon_{\ell\ell}^{qV} < 0.042$) [30] and Super-Kamiokande ($-0.049 < \varepsilon_{\ell\ell}^{qV} < 0.049$) [362].

We also present our results in terms of the scalar LQ S_1 parameters, $\lambda^{d\ell}$ and m_{S_1}, in Fig. 31 for a few select detector exposures. Our work, for the first time, shows the constraints from the LZ experiment in black. In addition, we show constraints from the LHC searches looking for LQ pair production (PP) and Drell-Yan (DY) production using 36 fb^{-1} of data [413, 412]. As seen in Fig. 31, the DM direct detection

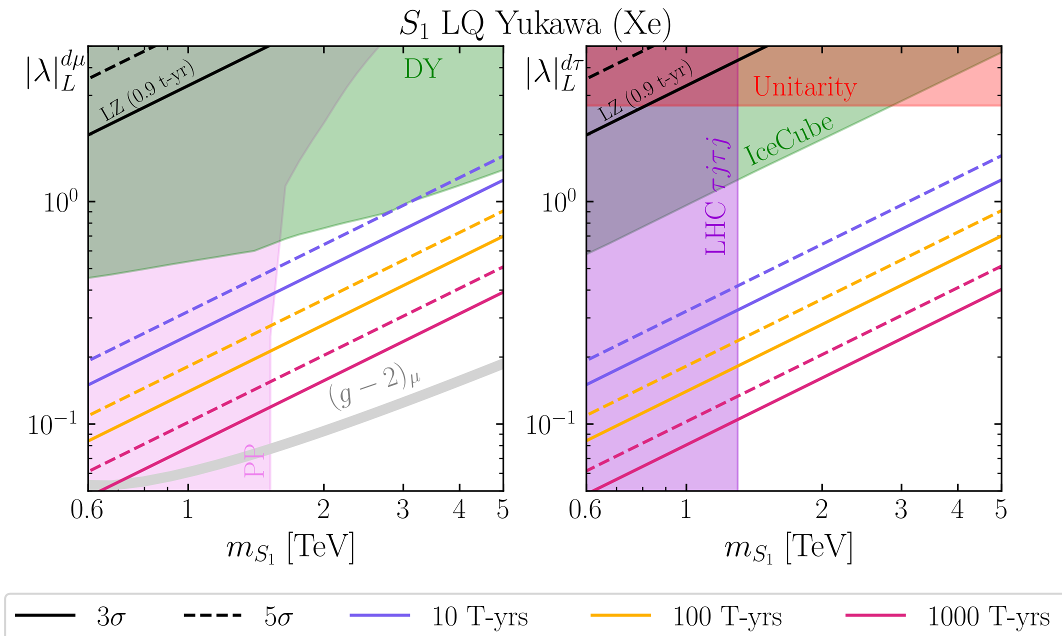

Figure 31. Projected constraints on the $\mu - d$ (left) and $\tau - d$ (right) Yukawas for a selections of exposures, mapped from sensitivity to a $\varepsilon_{\ell\ell}^{dV}$ minimal NSI in a xenon DM detector with a 2 keV threshold. Dashed (solid) lines represent 5σ and 3σ sensitivity reach. We set the first limits on LQs from preliminary LZ data with 0.9 ton-year exposure [7]. In the $d - \mu$ figure (left), the thick grey line indicates the preferred values to alleviate the $(g-2)_\mu$ anomaly for quark generation and chirality independent couplings. Pair production (PP) and Drell-Yan (DY) bounds on the muon coupling are from 36 fb^{-1} data from the LHC [413, 412]. In the $d - \tau$ figure (right), we show the LHC bounds on the tau coupling [192] which constrain $m_{LQ} > 1.3$ TeV. IceCube results are from resonance searches in atmospheric neutrino data [112]. At the highest masses, the LQ Yukawa coupling is only constrained by perturbative unitarity [77].

constraints are competitive with the LHC constraints for the $\lambda^{d\mu}$, but do not access the parameter region relevant for $(g-2)_\mu$ shown in gray. The DM direct detection constraints are significantly stronger than the LHC constraints for $\lambda^{d\tau}$, where the mass and short lifetime of the charged τ weaken the LHC constraints [399], and the IceCube constraints coming from atmospheric neutrinos [30]. For both scenarios, there are constraints from perturbative unitarity [77], which provide the strongest constraints on $\lambda^{d\tau}$ for $m_{S_1} \gtrsim 3$ TeV.

In Fig. 32, we translate our results into sensitivity projections for scalar LQ S_1 parameters, $\lambda_L^{q\ell}$ and m_{S_1}, as before. We find that a detector constructed from either material, argon or lead, and reaching multi-ton-year exposure can be sensitive and improve existing bounds on the S_1 LQ couplings.

Direct DM detection experiments constitute a central pillar in the search for DM and will continue to increase their exposures and lower thresholds and backgrounds. As we demonstrate, this will allow such experiments to constrain or reveal new physics in the space of neutrino interactions, complementary to conventional neutrino telescopes. We set new limits on LQs associated with scalar neutrino NSI using latest data of direct DM detection experiments, in particular LZ. We find that near-future DM detectors can probe parameter space of LQs that is out of reach of the LHC. We discuss how upcoming measurements improving uncertainties for atmospheric neutrino could probe LQ and NSI parameter space. The studied LQs are of particular interest for interpreting the observations of $(g-2)_\mu$ and explaining neutrino masses. Our analysis can be extended to variety of other models and similar methodology could also be applied to vector-like LQs, which may be associated with measurements and anomalies in flavor physics. Such a realization of massive scalar mediated NSIs provides a new benchmark for testing new physics beyond the SM at planned near-future experiments.

6.3 Neutrino Signals from Dark Stars Seeding Supermassive Black Holes

In Chapter 4 we departed from the detailed world of precision measurements of neutrino scattering to study neutrinos from much larger structures in the early universe. By considering the adiabatic contraction of DM with the first stars, we show that highly massive and luminous Dark Stars could produce neutrino signals which remain observable to the present day.

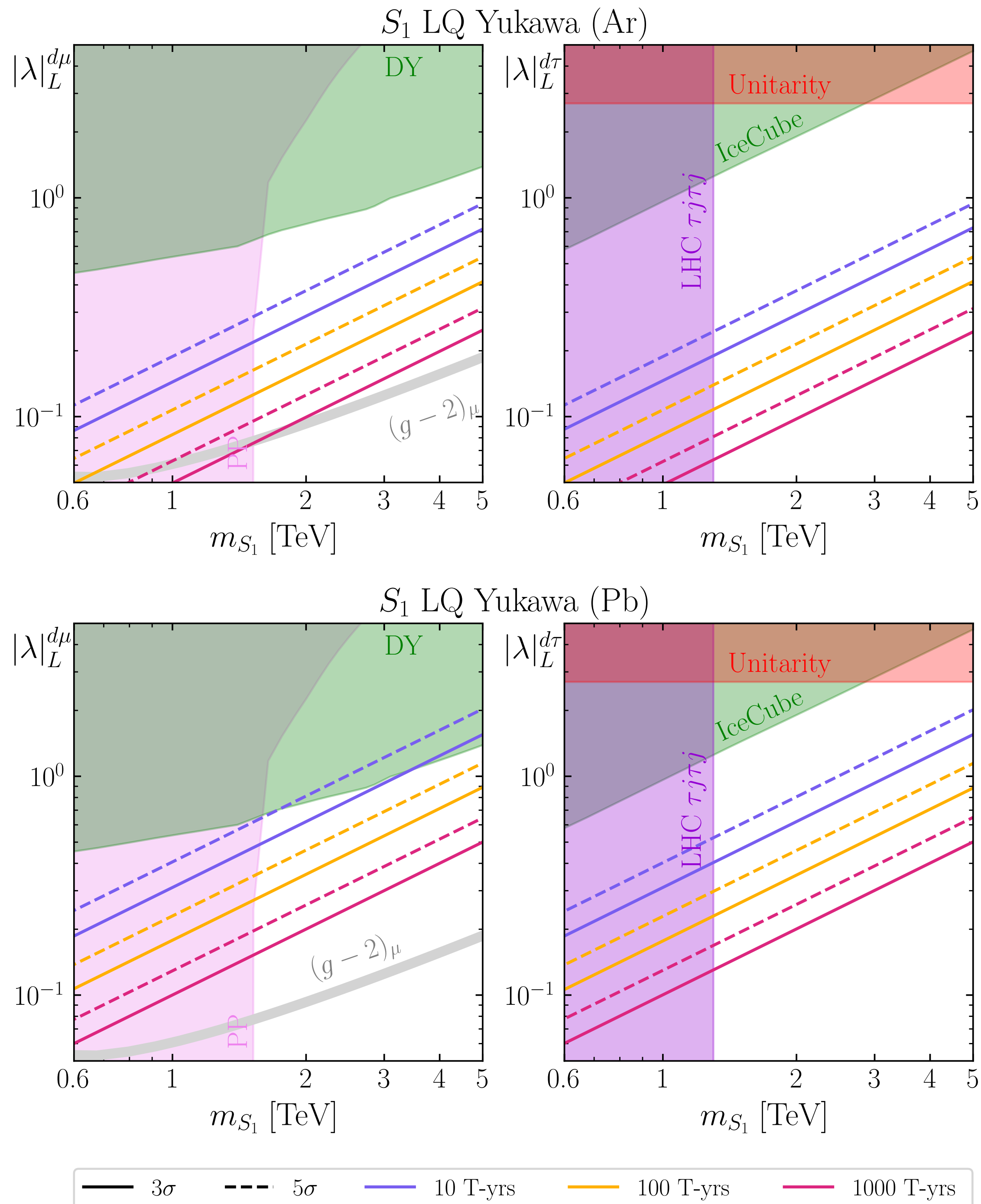

Figure 32. Same as Fig. 31, but for argon (top) and lead (bottom).

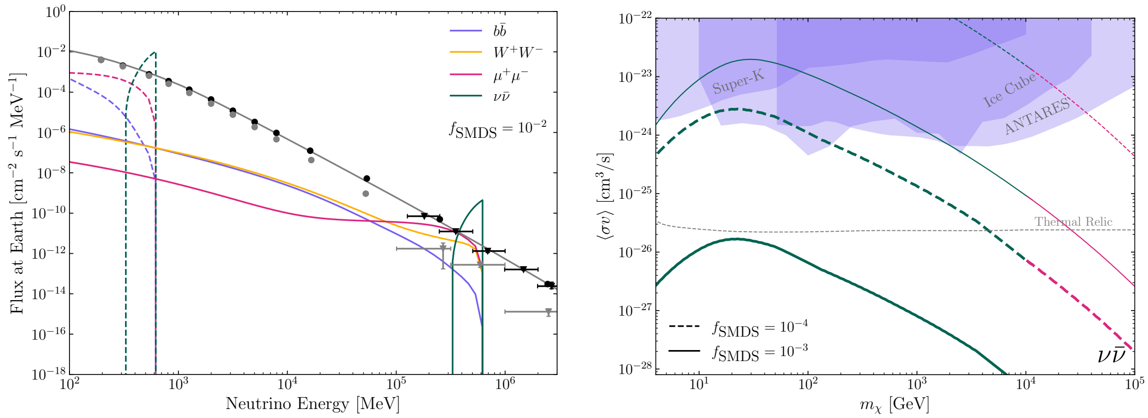

Figure 33. [Left] The neutrino flux from $10^6\ M_\odot$ supermassive DSs that can seed SMBHs for different DM annihilation channels considering DM mass $m_\chi = 10$ GeV (dashed line) and 10 TeV (solid line), for reference cross-section $\langle\sigma v\rangle = 3 \times 10^{-26}$. Measurements of atmospheric neutrino flux by Super-Kamiokande [387] (round marker) and IceCube [11, 12] (triangle marker) for electron neutrinos (grey) and muon neutrinos (black). Predicted combined muon and electron neutrino atmospheric flux from Ref. [297] (solid grey line) is also displayed. [Right] DM annihilation cross-sections for which the DS neutrino flux peak exceeds that of the atmospheric background for a selection of $f_{\rm SMSD}$ and $f_\nu = 1/3$. Line colors indicate where Super-Kamiokande (green) and IceCube (magenta) have leading sensitivity. Steep DS collapse model (thick lines) and gradual DS collapse model (thin lines), consistent with JWST candidate events, are shown. We assume DSs grow to 1% of their host halo mass in $M_h = 10^6 - 10^9\ M_\odot$ halos, to an upper mass limit of $M_{\rm DS} = 10^6 M_\odot$. Overlaid (shaded regions) are existing bounds from indirect DM detection searches in IceCube [25], Super-Kamiokande [37], and ANTARES [282]. The thermal relic DM annihilation cross-section [418] (gray dashed line) is displayed for reference.

In Fig. 33 we display resulting DS neutrino flux at present for different DM annihilation channels and masses computed with Eq. (4.8), together with atmospheric neutrino background. We focus on signals when $E_\nu \gtrsim 200$ MeV. At lower energies contributions from solar, DSNB and reactor neutrinos also appears.

The DS neutrino flux has cut-off energy spectrum within factor of few of $E_\nu \sim m_\chi/(z_{\rm lim} + 1) \sim m_\chi/16$, set by the DM mass and considered annihilation channel as well as redshift effects. Hence, such neutrino flux could be distinguished with atmospheric neutrino background including by spectral shape, depending on uncertainties. Further, at higher energies muon neutrinos dominate atmospheric flux [11], while the DS neutrino flux can contain all flavors. For lower DM masses we find Super-Kamiokande [387] data can place the strongest bounds, while data from IceCube [11, 12] for $m_\chi \gtrsim 10$ TeV.

In Fig. 33 (right panel) we show DM parameters for which neutrino flux peak from DSs is estimated to exceed the atmospheric neutrino background when DM annihilation has has $f_\nu = 1/3$ to $\nu\bar{\nu}$ for energies $E_\nu \gtrsim 200$ MeV following Super-Kamiokande [387] measurements, well fit by predictions [297], and at higher energies IceCube [11, 12] data. For reference, we overlay existing indirect detection constraints on DM annihilation. These estimated limits are seen to improve at higher DM masses due to different power law scaling between atmospheric flux and DS flux and at lower masses where the atmospheric flux flattens. Further, sensitivity at smaller DM masses increases also due to increased luminosity as seen from Eq. (4.4). These results can be further refined with detailed statistical analysis that we leave for future work. We estimated that a χ^2 analysis considering available data and uncertainties on detected neutrino energies (e.g. from Super-Kamiokande [387]) can be expected to yield results within $\sim 1-2$ orders of magnitudes of our present simplified treatment. At lighter masses the DS neutrino events become degenerate with those of DSNB, although with distinct spectra. At larger DM cross-sections, the electromagnetic emission from DSs is also enhanced and can affect other constraints. In the Supplementary Material we discuss DM annihilation to W^+W^-, $b\bar{b}$, and $\mu^+\mu^-$ and provide an equivalent figure.

Upcoming large scale neutrino telescopes such as the 187-kton water Cherenkov detector Hyper-Kamiokande [36], 40 kton liquid argon DUNE [40, 44] and 20 kton liquid scintillator JUNO [42] can probe DSs fueled by $\sim$GeV–TeV scale DM with enhanced sensitivity.

DSs provide compelling candidates for the first stars and potential seeds for SMBHs. Considering their neutrino emission and neutrino experiments, we estimated the first constraints on supermassive DSs and the DM interactions powering them from Super-Kamiokande and IceCube data, opening a novel window into SMBH progenitors. Our results are less sensitive to assumptions about DS populations and masses compared to direct searches such as with telescopes like JWST, offering a complementary approach to probing DSs at high redshifts. Our work paves the way for future probes of the nature of high redshift objects with upcoming neutrino telescopes including Hyper-Kamiokande, DUNE and JUNO as well as bridges fields of neutrino astronomy, DM physics, and early black hole formation.

6.4 Ultra-high energy KM3NeT event versus IceCube data

In the final chapter of this dissertation, we considered a single event, the highest energy neutrino ever recorded. While this event has been used by the KM3NeT collaboration to claim the discovery of a new cosmological source of neutrinos, we study the tension of such a flux with the non-observation of similar events in the much larger and older IceCube detector

We have shown that, if due to a neutrino interaction, this event would likely point to a neutrino with energies of hundreds of PeV. While this would be the highest energy neutrino observed to date, the lack of such high-energy events in IceCube's data set seems to point to an important tension between these experiments.

We have analyzed this potential tension under several assumptions for the origin of the KM3NeT event: power-law diffuse flux; cosmogenic origins; and point sources. Under any of these assumptions, the tension is found to be between 2.9σ and 3.6σ, corresponding to a p-values of 0.36% and 3.3×10^{-4}, respectively. Only a transient source would reduce this tension to 2.0σ, or 5.5%. The robust tension between this event and data from IceCube deepens the mystery of its origin. Given the small probability of this event to originate from the diffuse neutrino flux observed by IceCube, the KM3NeT event is very likely the first observation of a new astrophysical source.

The tension with IceCube data also carries broad implications for new physics beyond the standard model which might allow such an event to have gone unobserved in the larger, older experiment on the South Pole.

APPENDIX A

SUPPLEMENTAL MATERIAL FOR SOLAR NEUTRINOS IN LOW THRESHOLD DARK MATTER EXPERIMENTS

A.1 Yield Function Uncertainties

As noted in Sec. 2.5, the dominant source of uncertainty in these projected sensitivities in semiconductors (or the actual constraints placed by an experiment) is the yield function. Here we demonstrate these effects on the nuclear recoil sensitivities at a single exposure (1 kg-yr in semiconductors, 100 t-yrs in Xe and Ar) for both the 1 and $2e^-$ thresholds in semiconductors and 1 and $4e^-$ thresholds in the noble liquids. The sensitivity to electron recoils is only influenced by the change in the SM CEvNS rate thus is less sensitive to the yield function compared to the nuclear recoil case.

In Fig. A.34 we plot only the xenon rates, noting that argon exhibits a similar dependence on the yield function except in the axial vector case to which it is not sensitive. In Fig. A.35, we plot the uncertainty in silicon and germanium. We see that the ionization yield uncertainties have stronger effect for the lower threshold ($1e^-$), where they can change the projections by up to an order of magnitude in silicon.

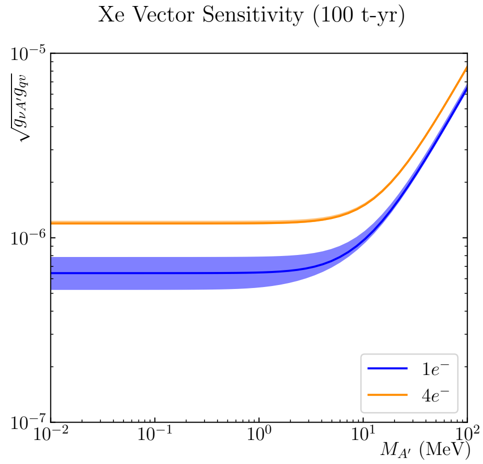

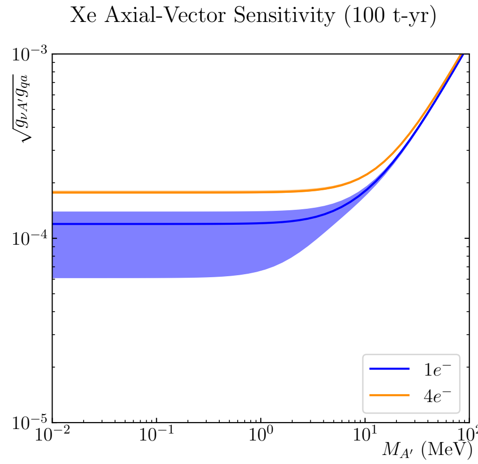

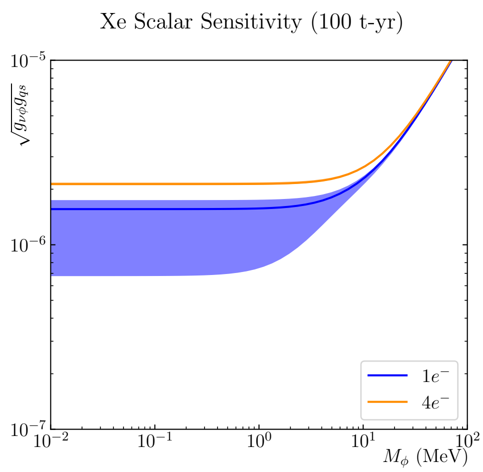

Figure A.34. In xenon and argon (not shown) the $1e^-$ threshold sensitivity is sensitive to the yield function, but the $4e^-$ case is not since $4e^-$ and higher events correspond to energies where the yield functions are well measured.

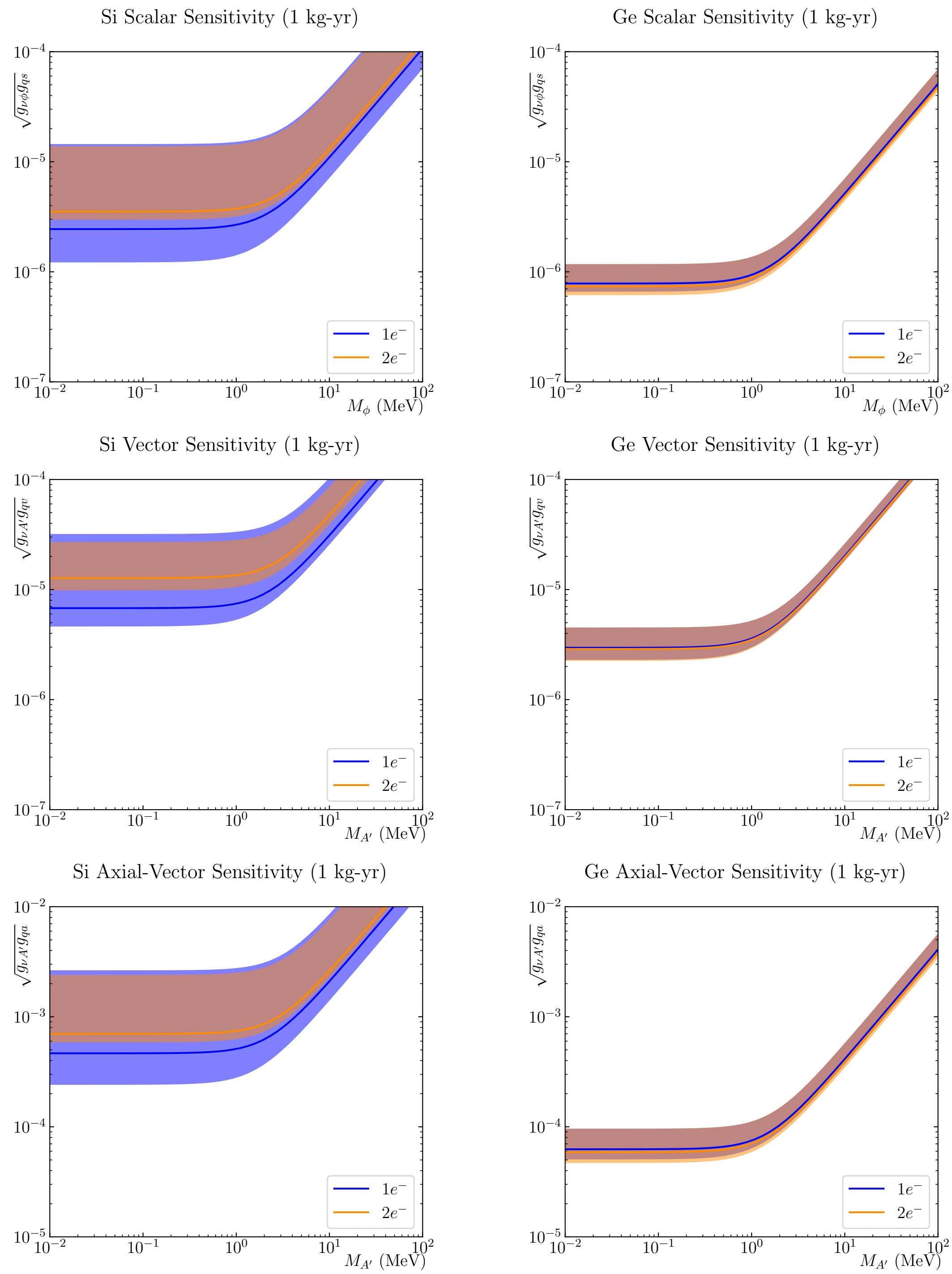

Figure A.35. Colored bands indicate the range of possible sensitivities to nuclear recoils contained within the choice of yield function between the red and blue lines in Fig. 3 for a 1 kg-yr semiconductor. Colors indicate the detector threshold.

APPENDIX B

SUPPLEMENTAL MATERIAL FOR LEPTOQUARKS IN DARK MATTER EXPERIMENTS

B.1 Model extension and neutrino mass

Following Ref. [113], we discuss a simple model extension of the S_1 LQ with a second scalar LQ, $\tilde{R}_2 = (3, 2, 1/6)$, that is an $SU(2)$ doublet $(R^{+2/3}, R^{-1/3})$, which can readily result in Majorana neutrino mass generation at one-loop level. The considered LQs can arise in a variety of theoretical frameworks, such as models of R-parity violating supersymmetry [288, 123]. The additional Lagrangian terms due to $\tilde{R}_2$ are

$$\mathcal{L}_{\tilde{R}_2} \supset (\tilde{\lambda}^{i\ell}\bar{d}^i_R\tilde{R}_2\varepsilon L_\ell + \mu H^\dagger \tilde{R}_2 S_1^* + h.c.) - m^2_{\tilde{R}_2}|\tilde{R}_2|^2 \,, \tag{B.1}$$

where the μ-term mixes S_1 and $\tilde{R}_2$ LQs and $H = (1, 2, 1/2)$ is the SM Higgs doublet.

At loop-level, S_1 and $\tilde{R}_2$ LQs generate neutrino mass, as displayed in Fig. B.1. Expanding the $SU(2)$ doublets, the necessary terms to generate neutrino NSI and masses are

$$\mathcal{L}_{S_1,\tilde{R}_2} \supset \tilde{\lambda}^{i\ell}\left(\nu_\ell \bar{d}_i R^{-1/3} - \ell \bar{d}_i R^{+2/3}\right) + \lambda_L^{i\ell}\left(\nu_\ell d_i - \ell \bar{u}_i^c\right) S_1 - \mu R^{-1/3} H^0 S_1^* + h.c. \tag{B.2}$$

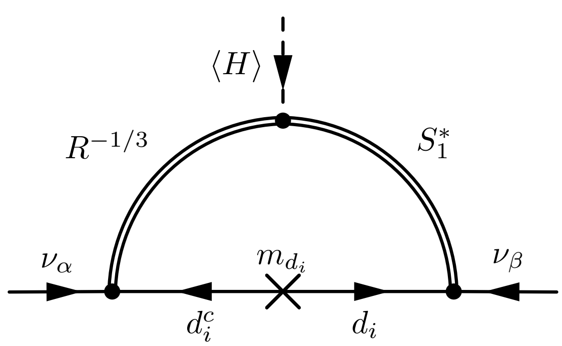

Figure B.1. One-loop neutrino mass generation in the $S_1 + \tilde{R}_2$ LQ model.

The mixing term implies the existence of a new LQ mass basis with eigenvalues

$$m_{1,2}^2 = \frac{1}{2}\left(m_{R^{+2/3}}^2 + m_{S_1}^2 \mp \sqrt{(m_{R^{-1/3}}^2 - m_{S_1}^2)^2 + 4\mu^2 v^2}\right) \tag{B.3}$$

and a mixing angle

$$\tan(2\theta) = \frac{-\sqrt{2}\mu v}{m_{S_1}^2 - m_{R^{-1/3}}^2}\ , \tag{B.4}$$

where v is the Higgs vev and $m_{R^{-1/3},S_1}$ include the bare masses and the mass induced by spontaneous symmetry breaking. The neutrino mass matrix is given by

$$M_\nu = \frac{3\sin(2\theta)}{32\pi^2}\log\left(\frac{m_1^2}{m_2^2}\right)(\tilde{\lambda} M_d \lambda_L^T + \lambda_L M_d \tilde{\lambda}^T) \tag{B.5}$$

where M_d is a diagonal matrix of down-type quark masses. In the case of a LQ coupled only to down-type quarks and leptons, Eq. (B.5) simplifies to

$$(M_\nu)^{\alpha\beta} = \frac{3\sin(2\theta)}{32\pi^2}\log\left(\frac{m_1^2}{m_2^2}\right) m_d \times (\lambda_L^{d\alpha}\tilde{\lambda}^{d\beta} + \tilde{\lambda}^{d\alpha}\lambda_L^{d\beta})\,, \tag{B.6}$$

and similarly for LQs coupled to only strange or bottom quarks with $m_d \to m_{s,b}$. In the specific cases we study, only one element of $\lambda_L^{d\alpha}$ is non-zero implying only the generation of a single neutrino mass. However, the $\tilde{R}_2$ coupling $\tilde{\lambda}^{d\alpha}$ may contribute a second element to the neutrino mass matrix, or as noted in 3.3.1, it is possible for both $\lambda_L^{d\mu}$ and $\lambda_L^{d\tau}$ to be non-zero.

We note that with a multitude of parameters determining the neutrino mass above, there is degeneracy in LQ coupling and mass parameter space. From cosmological observations, the sum of neutrino masses given by the eigenvalues of M_ν is constrained to $\sum m_\nu < 0.13$ eV by cosmic microwave background radiation (CMB) data from Planck and the Dark Energy Survey (DES) [32].

B.2 From leptoquarks to NSI

To map the S_1 LQ to the scalar NSI parameters, we need to find the expressions for $\varepsilon_{\ell\ell}^{dV}$ and q_S in terms of the LQ parameters. Expanding the $SU(2)_L$ doublets in eq.

(3.13) and explicitly writing the hermitian conjugate, we have

$$\mathcal{L}_{S_1} \supset -m_{S_1}^2 S_1^* S_1 + \lambda_L^{1\ell}\left(\bar{u}^c P_L \ell - \bar{d}^c P_L \nu_\ell\right) S_1 + \lambda_L^{*1\ell}\left(\bar{u}^c P_L \ell - \bar{d}^c P_L \nu_\ell\right)^\dagger S_1^* \tag{B.7}$$

Where we've specified $q = 1$ for the u and d quarks. Since we are considering massive scalars of $\mathcal{O}(\mathrm{TeV})$, we can integrate out the LQ using the equations of motion

$$\begin{aligned} \frac{\partial \mathcal{L}_{S_1}}{\partial S^*} &= -m_{S_1}^2 S_1 + \lambda_L^{*1\ell}\left(\bar{u}^c P_L \ell - \bar{d}^c P_L \nu_\ell\right)^\dagger = 0 \\ \frac{\partial \mathcal{L}_{S_1}}{\partial S} &= -m_{S_1}^2 S_1^* + \lambda_L^{1\ell}\left(\bar{u}^c P_L \ell - \bar{d}^c P_L \nu_\ell\right) = 0 \end{aligned} \tag{B.8}$$

and find

$$\mathcal{L}_{S_1} \supset \frac{|\lambda_L^{1\ell}|^2}{m_{S_1}^2}\left[(\bar{u}^c P_L \ell)(\bar{u}^c P_L \ell)^\dagger - (\bar{u}^c P_L \ell)(\bar{d}^c P_L \nu_\ell)^\dagger - (\bar{d}^c P_L \nu_\ell)(\bar{u}^c P_L \ell)^\dagger + (\bar{d}^c P_L \nu_\ell)(\bar{d}^c P_L \nu_\ell)^\dagger\right] \tag{B.9}$$

We now focus on the last term which introduces an effective four-Fermi interaction between d quarks and neutrinos.

$$\mathcal{L}_{S_1} \supset \frac{|\lambda_L^{1\ell}|^2}{m_{S_1}^2}(\bar{d}^c P_L \nu_\ell)(\nu_\ell^\dagger P_L (\bar{d}^c)^\dagger) = \frac{|\lambda_L^{1\ell}|^2}{m_{S_1}^2}(\bar{d}^c P_L \nu_\ell)(\bar{\nu}_\ell P_R d^c) \tag{B.10}$$

After a Fierz transformation [155], this becomes

$$\mathcal{L}_{S_1} \supset -\frac{|\lambda_L^{1\ell}|^2}{2m_{S_1}^2}(\bar{d}^c \gamma_\mu P_R d^c)(\bar{\nu}_\ell \gamma_\mu P_L \nu_\ell) \tag{B.11}$$

Now we evaluate the charge conjugation of the quarks and find

$$\mathcal{L}_{S_1} \supset \frac{|\lambda_L^{1\ell}|^2}{2m_{S_1}^2}(\bar{d} \gamma_\mu P_L d)(\bar{\nu}_\ell \gamma_\mu P_L \nu_\ell) \tag{B.12}$$

Finally, noting that we get no RH coupling and $\varepsilon_{\ell\ell}^{qV} = \varepsilon_{\ell\ell}^{qL} + \varepsilon_{\ell\ell}^{qR}$ we find that the S_1 LQ maps to Eq. (3.10) with

$$\varepsilon_{\ell\ell,S_1}^{dV} = \frac{-|\lambda_L^{d\ell}|^2}{4\sqrt{2} G_F m_{S_1}^2}\,. \tag{B.13}$$

We note that the NSI parameter resulting from an S_1 LQ is negative.

B.3 Neutrino oscillation effects

In Sec. 3.1 we briefly discussed the effects of neutrino oscillations. Here, we expand the discussion and consider neutrino oscillations with and without NSI effects in neutrino propagation through the Earth or Sun. To analyze neutrino propagation through Earth we use the NuCraft code [437], which is based on the PREM Earth reference model[1] [227], and include modifications for vector neutrino NSI [257, 276, 196] and scalar neutrino NSI [267]. For solar neutrinos, full in-medium effects and NSI are already built into the SNuDD module [80] that we use to calculate the flavor dependence of the solar neutrinos when they reach Earth. In all cases we assume normal neutrino mass ordering.

In the case of vector NSI, the contributions to the matter potential result in the effective Hamiltonian

$$\mathcal{H}_{\text{vNSI,matter}} \simeq E_\nu + \frac{MM^\dagger}{2E_\nu} \pm (V_{\text{SI}} + V_{\text{NSI}})\,, \tag{B.14}$$

where the neutrino mass matrix M, SM matter potential V_{SI}, and the vector NSI matter potential contributions V_{NSI} are 3×3 matrices. The matter potential becomes significant only when the neutrino energy E_ν or matter density are sizable $2E_\nu V \gtrsim \Delta m^2_{ij}$ [267]. Flavor conserving NSI in the $\mu-\tau$ sector can be parameterized by a single parameter $\varepsilon_{\tau\tau} - \varepsilon_{\mu\mu}$ where $\varepsilon_{\ell\ell} = \sum_f Y_f \varepsilon^{fV}_{\ell\ell}$ is the sum of couplings to each fermion weighted by the fermion number density Y_f (relative to Y_e). In this parameterization, current experimental limits are $|\varepsilon_{\ell\ell}| \lesssim 0.04$ [30] in $\mu - \tau$ sector. Constraints on flavor violating NSI from oscillations are much stronger since they have a greater effect on oscillation probabilities, but we do not consider these NSI in this work.

In Fig. B.2 we display the oscillation probabilities for a characteristic vector NSI values we consider $|\varepsilon^{qV}_{\tau\tau}| \sim 10^{-2}$ along with the SM medium effects inside the Earth. For the SM effects, we find reasonable agreement with [35]. Note that effects of a coupling to up or down quarks are similar, since the NSI potential scales with Y_u and

[1]NuCraft was built for IceCube and thus considers a detector 2 km deep near the south pole. Slight deviations are noted with results for different geomagnetic locations including Kamioka in Japan and Sudbury in Canada

Y_d respectively. From Fig. B.2 we observe that at particular propagation directions with respect to zenith[2] and neutrino energies vector NSI $\varepsilon \sim 0.01$ can modify flavor oscillation by $\mathcal{O}(10\%)$. Here we do not consider detectors with directional sensitivity. Hence, integrating the atmospheric flux contributions over the field-of-view and including recoil kinematics and detector resolution further reduces the significance of the vector NSI on the signal in dark matter experiments. Further detailed study and consideration of detectors with directional sensitivity could leverage these effects to improve sensitivities to vector NSI, analysis of which we leave for future work.

The vector NSI effects are suppressed at lower neutrino energies and thus the NSI parameters we consider have negligible effect on solar neutrinos despite the increase in medium density. In Fig. B.3 we display oscillation probabilities for solar neutrinos as calculated using SNuDD package considering NSI of $\varepsilon = 0.1$, which is significantly larger than the parameters we consider in this work. Solar neutrino oscillations in vacuum are also considered, though are subdominant to the medium effects. We assume a constant Earth-Sun distance of 1.5×10^8 km. Qualitatively, we have found agreement of our considerations with discussion in Ref. [352].

In contrast to vector NSI, scalar NSI induce an effective correction to the neutrino mass matrix, which scales with the matter density and is suppressed by the neutrino energy. This leads to a neutrino oscillation probability that is sensitive to the matter density variations along the propagation baseline [267]. In the flavor basis, $M_{eff} = M + M_{\rm NSI}$ where M is the standard neutrino mass matrix and $M_{\rm NSI} = \sum_q n_q G_F \varepsilon_{\ell\ell}^{qS}$ where $\varepsilon_{\ell\ell}^{qS}$ is the scalar NSI parameter in Eq. (3.8) and n_q is the quark number density. We focus on flavor conserving NSIs, so $M_{\rm NSI}$ is diagonal in the flavor basis[3].

[2]Straight down propagation is at 180°.

[3]In general, $\varepsilon_{\alpha\beta}^{qS}$ are also possible.

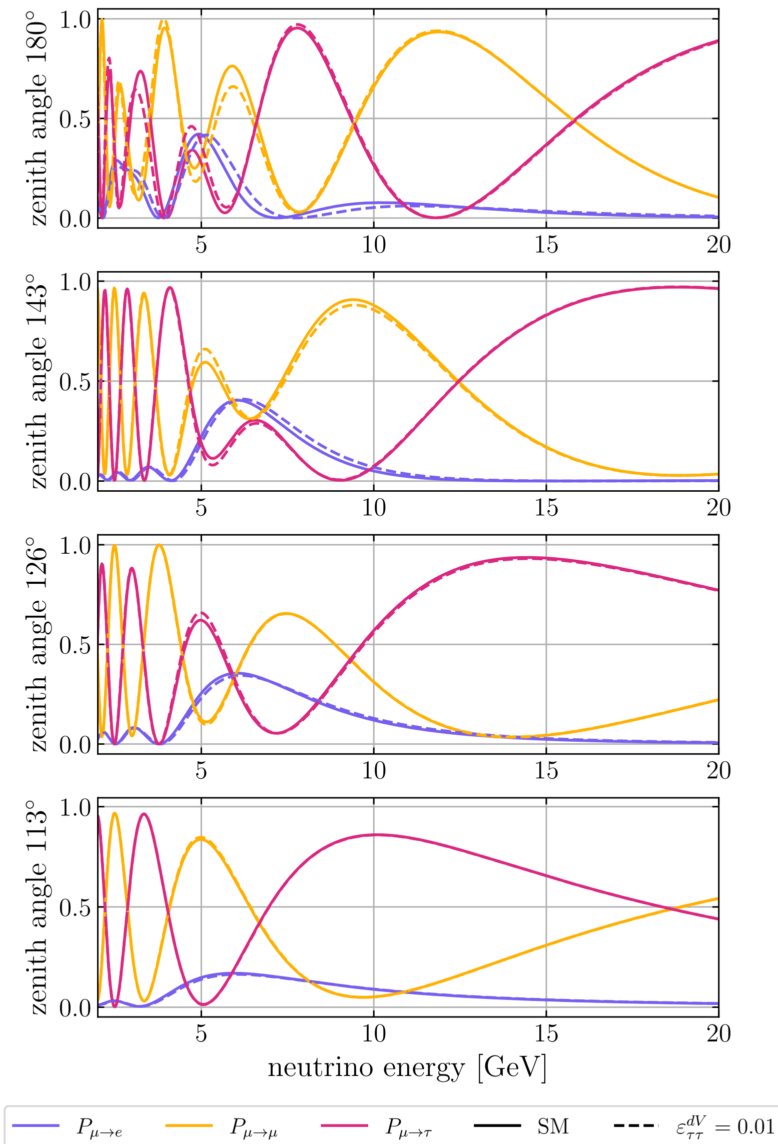

Figure B.2. Oscillation conversion probabilities of atmospheric neutrinos, calculated using the NuCraft code, with (dashed line) and without (solid line) vector NSI effects for distinct directions with respect to zenith.

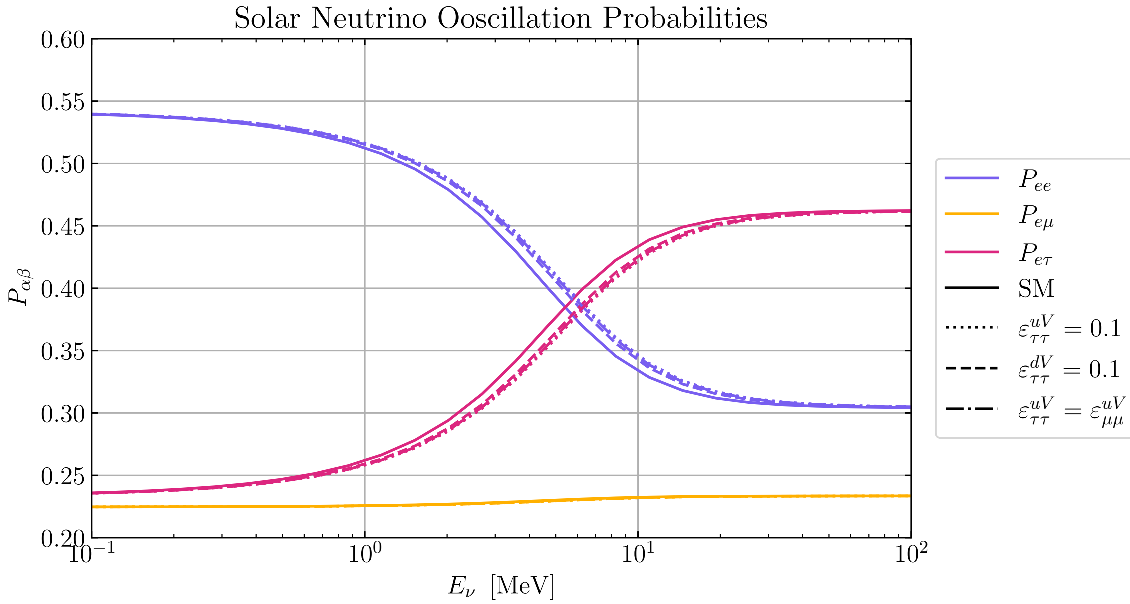

Figure B.3. Oscillation conversion probabilities of solar neutrinos, as calculated with the SNuDD module, for SM (solid line) and including vector NSI coupling of tau neutrinos to up quarks (dotted line), down quarks (dashed line), or both (dot-dashed line).

Transforming to the mass basis and rotating the phasing matrix into the NSI term, M_{eff} is given in Eq. (B.15) where $D_\nu = \mathrm{diag}(m_1, m_2, m_3)$[4] is the diagonal neutrino mass matrix, $\mathcal{U}$ is the PMNS matrix, and P is the diagonal rephasing matrix

$$M_{eff} = \mathcal{U} D_\nu \mathcal{U}^\dagger + P^\dagger M_{\mathrm{NSI}} P \ . \tag{B.15}$$

Following the notation of Ref. [267], we take $\sqrt{|\Delta m^2_{31}|}$ as a characteristic mass scale and parameterize the NSI mass contribution as

$$P^\dagger M_{\mathrm{NSI}} P = \delta M = \sqrt{|\Delta m^2_{31}|}(\eta)_{i,j} \tag{B.16}$$

where $(\eta)_{i,j}$ are matrix elements in the mass basis. For neutrinos propagating in matter with scalar NSI contributions, the effective Hamiltonian is

$$\mathcal{H}_{\mathrm{sNSI,matter}} = E_\nu + \frac{M_{eff} M^\dagger_{eff}}{2E_\nu} + V_{\mathrm{SI}} \ , \tag{B.17}$$

[4] $\mathrm{diag}(x, y, z)$ is defined as the 3×3 diagonal matrix with elements x, y, z on the diagonal.

where $V_{\rm SI}$ is the SM matter potential from charged-current interactions. For antineutrinos, $V_{\rm SI}$ changes sign. At the energies and couplings we consider in the analysis, SM vector interactions contribute significantly more strongly to neutrino oscillations than scalar NSI, such that the latter do not have appreciable effects in dark matter experiments.

APPENDIX C

SUPPLEMENTAL MATERIAL FOR DARK STARS

Here, we provide additional details of DS evolution, population, computation of resulting diffuse neutrino flux as well as comparison to indirect DM detection.

C.1 Dark Star Model and Evolution

We analytically investigate DS evolution by considering a polytrope model with hydrostatic and thermal equilibrium. This is expected to be in approximate agreement with detailed numerical evaluations of DS evolution with MESA 1D stellar evolution within a factor of few [389].

DSs are powered by DM heating instead of nuclear fusion in their cores and are of lower density and temperature than main sequence stars. With their equation of state typically dominated by non-relativistic gas pressure, DS stellar density profiles in early stages can be modeled as a polytrope with index $n = 3/2$ [250], describing systems supported primarily by thermal pressure with contributions from DM annihilation. In Ref. [416] later stages of DS evolution were modeled as $n = 3$ polytropes, considering dominance of radiation pressure. We confirmed that $n = 3$ polytropes result in larger DS volume and lower temperatures than their $n = 3/2$ counterparts, with resulting luminosity differing within a factor of few. Here, we use $n = 3/2$ throughout. The equation of state relating pressure P and density ρ is

$$P = K\rho^{1+1/n} \ , \tag{C.1}$$

where n is the polytrope index and constant K is set by the stellar boundary conditions. We focus on $n = 3/2$ polytrope description of DSs.

For mass M_r contained within a radius r

$$M_r = \int_0^r dr' 4\pi r'^2 \rho(r') \tag{C.2}$$

the hydrostatic equilibrium is

$$\frac{dP}{dr} = -\rho \frac{GM_r}{r^2} \ . \tag{C.3}$$

Combining with Eq. (C.1), this gives the well known Lane-Emden equation

$$\frac{1}{x^2}\frac{d}{dx}\left(x^2\frac{d\theta}{dx}\right) = -\theta^n \ , \tag{C.4}$$

in terms of the dimensionless variables $x = r/\alpha$, $\theta^n = \rho/\rho_c$ where $\alpha = (n+1)K/4\pi G\rho_c^{1-1/n}$ and ρ_c is the density at the center of the star. This is subject to the boundary conditions $\theta(0) = 1$, $d\theta/dx(0) = \theta'(0) = 0$, and $\theta(x_1) = 0$ where x_1 corresponds to the surface of the star. For $n = 3/2$, one finds $x_1 \simeq 3.65$. For a particular stellar radius R and mass M the constant K from Eq. (C.1) is determined by

$$K = \frac{1}{n}\left[\left(\frac{R}{x_1}\right)^{-1+3/n}\left(\frac{GM}{-x_1^2\theta'(x_1)}\right)^{1-1/n}(4\pi G)^{1/n}\right] \ . \tag{C.5}$$

Here, we use the density contrast $D_n = \rho_c/\bar{\rho}$, which evaluates to $D_{3/2} = 5.99$ for $n = 3/2$, in order to set ρ_c.

We can then compute the photosphere radius R_s. The temperature is governed by the equation of state as

$$P(r) = \frac{\rho k_B T(r)}{\bar{m}} + \frac{4}{3}\frac{\sigma_B}{c}T(r)^4 \ , \tag{C.6}$$

where σ_B the Stefan-Boltzmann constant, k_B is the Boltzmann constant, and $\bar{m} = m_u(2X + 3Y/4)^{-1} \simeq 0.588 m_u$ is the mean atomic weight in terms of mean atomic mass unit $m_u \simeq 0.931$ GeV with H and He mass fractions $X = 0.76$ and $Y = 0.24$, respectively, taken from Big Bang nucleosynthesis [47]. The resulting photosphere radius can be obtained by solving

$$P\kappa\left(\rho_{R_s}, T_{R_s}\right) = \frac{2}{3}g(R_s) \ , \tag{C.7}$$

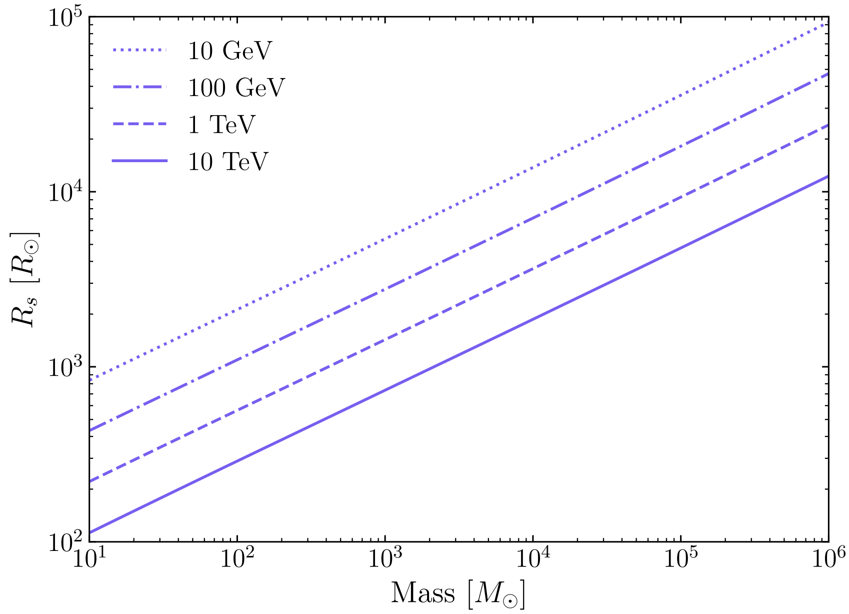

Figure C.1. DS photosphere radius for DM annihilation channel $\nu\bar{\nu}$ for different masses considering that the fraction of DM mass m_χ converted to neutrino energy is $f_\nu = 1/3$.

where κ is the opacity taken from numerically computed OPAL astrophysical opacity tables [304] and $g(r) = GM_r/r^2$ is the gravitational acceleration. Here, $\rho(r)$ is determined from the Lane-Emden equation (C.4), P from the polytrope equation (C.1), and T from the equation of state (C.6). The surface luminosity is then determined from the obtained photosphere radius and effective temperature considered to be $T(R_s)$

$$L_{\text{surf}} = 4\pi\sigma_B R_s^2 T(R_s)^4 \; . \tag{C.8}$$

We consider three distinct DS sources of energy playing a relevant role: (A) nuclear fusion, (B) gravitational energy and (C) DM heating via annihilation. Besides contributions from initial DM density, DM heating can benefit from the capture of additional DM from scattering with baryons in the star. We do not consider this contribution as it relies on additional assumptions about the DM-baryon interactions.

Once DM is depleted, the star contracts and transitions to hydrogen burning. Prior to this, DM contributions dominate due to the lower core densities and pressures that suppress nuclear fusion, and the efficiency of DM annihilation. As DM annihilation products are converted into heat and heating the star more efficiently than fusion, neutrinos escape [417]. Therefore, we have

$$L_{\rm tot} = L_{\rm fus} + L_{\rm grav} + L_{\rm DM} \simeq L_{\rm DM} \ . \tag{C.9}$$

The DM luminosity can be found from

$$L_{\rm DM} \simeq (1 - f_\nu) \int_0^R dr 4\pi r^2 \frac{\langle \sigma v \rangle \rho_\chi^2}{m_\chi} \ . \tag{C.10}$$

Note that eq. (C.10) is enhanced by a factor of two for Majorana particle DM. From Navarro-Frenk-White (NFW) DM profile [369] simulations, after adiabatic contraction the DM density at the outer edge of baryonic core is found to be [417]

$$\rho_\chi \simeq 1.7 \times 10^{11}\ {\rm GeV cm^{-3}} \Big(\frac{n_b}{10^{13}\ {\rm cm^{-3}}}\Big)^{0.81} \ , \tag{C.11}$$

where n_b is the baryon number density. We consider $n_b = 10^{13}$ cm^{-3} at the initial DS formation, as in Ref. [417]. We then iteratively solve the polytrope equations. As a DS evolves, n_b changes accordingly. Outside the core, the DM is found to scale with $r^{-1.9}$. We adopt this as the representative DM density.

In thermal equilibrium, the luminosity of Eq. (C.10) must balance the surface luminosity of Eq. (C.8), with

$$L_{\rm DM,eq.} = L_{\rm surf,eq} \ . \tag{C.12}$$

In Fig. C.1 we display the equilibrium radius as a function of time for DM annihilating to $\nu\bar{\nu}$ in a DS that reaches $10^6\ M_\odot$ after prolonged accretion at $\dot{M} = 0.1\ M_\odot\ {\rm yr}^{-1}$. To compute this, we first consider an initial DS radius value and find its photosphere radius. We then compare the surface and DM luminosities. After this, we iteratively adjust our initial radius as needed until Eq. (C.12) is satisfied. This procedure yields

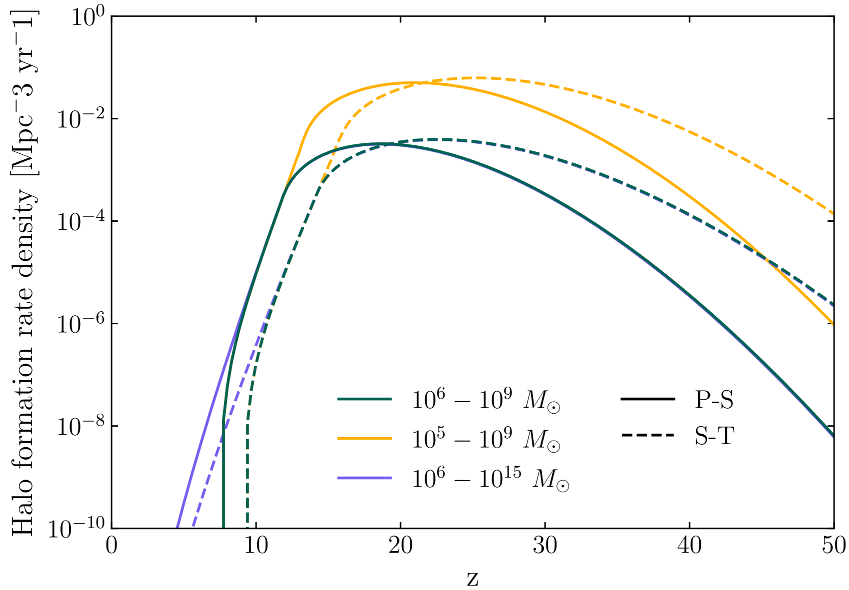

Figure C.2. Halo formation rate density $d^2n/dM_h dt$ integrated over halo mass range. Integrated halo formation rate density we consider as reference (green line), results extended to lighter halos (yellow line), results extended to more massive halos (lavender line) are shown. Press-Schechter (solid lines, P-S) and Sheth-Tormen (dashed lines, S-T) halo formation are indicated.

resulting DS luminosity and radius as well as temperature, density, and pressure profiles for a given DS mass and DM particle mass. We have verified that for other DM decay channels results are similar.

Incorporating numerical simulations, analysis of Ref. [252] revealed that centrophilic orbits [429], which repeatedly pass through the star, can sustain the DM fuel supply for $\gtrsim 1$ Gyr. This extended fueling allows to support supermassive DSs, with their masses reaching $\gtrsim 10^6\ M_\odot$ and luminosities of $10^9 - 10^{10}\ L_\odot$. In our study we also neglect the possibility of DM capture via scattering off baryons in DSs, which could extend their lifetime after the ambient DM density decreases. The effectiveness of this mechanism depends on the DM interactions with SM. The impact of DM capture on dark stars was initially studied in Ref. [255] and further refined in Ref. [254], where it was shown that stars fueled by captured DM are typically few times hotter and have radii smaller by an order of magnitude compared to those powered solely by adiabatic contraction.

Our results for supermassive DSs in Fig. 26 give luminosities that are approximately consistent with discussion of Ref. [389] indicating that luminosities obtained from polytropic model are expected to be suppressed by a factor of few compared to results from detailed stellar evolution simulations. We find that the DS luminosity can be well approximated by Eq. (4.4).

C.2 Dark Star Population and Collapse Rate

The halo density formation rate per halo mass $d^2n/dM_h dt$ can be obtained by differentiating Eq. (4.1) with respect to time. Integrated contributions over halo masses of the halo density formation rate in the total DS luminosity as described by Eq. (4.7) depend on the considered halo mass limits $M_{h,\min}$ and $M_{h,\max}$. In Fig. C.2 we illustrate the effect of different choices of the halo mass limits on the integral of $d^2n/dM_h dt$ with respect to M_h. Increasing $M_{h,\max}$ does not have an appreciable effect at $z_{\rm lim}$ since massive halos become increasingly rare at higher redshifts. On the other hand, decreasing $M_{h,\min}$ substantially increases the halo density formation rate due to larger contributing population of smaller halos. These lighter halos are less luminous and thus result in a smaller enhancement on the flux despite being numerous.

As discussed in the main text, DSs can potentially be detected by sensitive telescopes such as JWST. For $10^6\ M_\odot$ DSs, with luminosities of $10^{10}\ L_\odot$, we consider that JWST can observe all such objects that survive beyond $z = 15$. Three DS candidates have been identified considering JWST JADES survey [306], which initially covered approximately ~ 26.4 arcmin^2 [229, 388]. Since the identification of these candidates, the JADES survey has expanded its observational area to ~ 56 arcmin^2 [213]. We assume JWST can efficiently identify such DSs. Then,

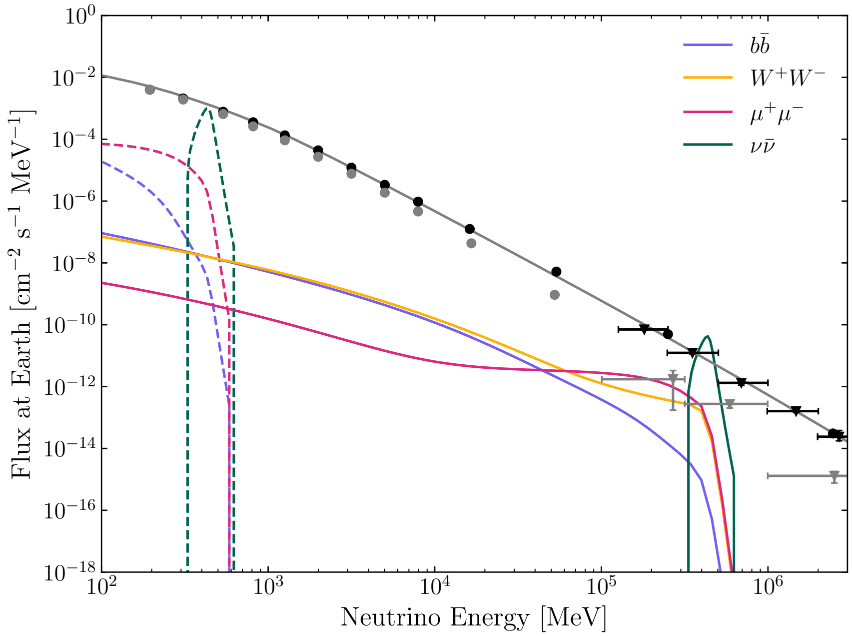

Figure C.3. Same as Fig. 33 considering gradual DS collapse model with $f_{\rm sur}$ given by Eq. (C.14).

to remain consistent with these observations, the majority of $\sim 10^6\ M_\odot$ DSs should collapse before $z = 15$.

In our analysis, we model DS collapse with a step function in redshift

$$f_{\rm sur} = 1 - \Theta(z - z_{\rm lim}) \tag{C.13}$$

where Θ is the Heaviside step function. We also consider a more gradual collapse scenario, with a DS survival fraction parameterized by

$$f_{\rm sur} = \frac{1}{2}\Big[1 + \tanh\left(z - z_0\right)\Big]\ , \tag{C.14}$$

where z_0 is a redshift parameter. In the framework of Eq. (C.14), a fraction of the population survives to later times. Observations by JWST allow to constrain the surviving DS fraction and combination $f_{\rm SMDS} f_{\rm sur}$. Choosing $f_{\rm SMDS} = 10^{-2}$ as a reference values, consideration of $z_0 \simeq 22$ allows for three candidate objects in the 26.4 arcmin^2 JADES field of view as claimed by analysis of Ref. [306]. Additional data from

JWST will expand the angular coverage θ^2. If no additional DS candidates are found, the resulting constraints on the population of luminous DSs will become more strict. Specifically, the bounds on the number of detectable DSs at high luminosities can be improved, with results scaling as $\propto N/\theta^2$ (see Eq. (4.5)). Our approach establishes a direct connection between DS diffuse neutrino emission and the DS candidates of JWST.

In Fig. C.3, we display the predicted DS neutrino flux considering gradual DS collapse with $f_{\rm sur}$ following Eq. (C.14) and compare with Fig. 33 based on step function rapid DS collapse model of Eq. (C.13). The gradual DS collapse model gives neutrino flux predictions suppressed by around an order of magnitude compared to the step-function model. This originates from constraints on the low-redshift tail of the DS population that also impact DS population at higher redshifts.

C.3 Generalized Diffuse Neutrino Flux

Our general formalism of Eq. (4.8), and considering Eq. (4.7) as the comoving luminosity density of population of sources, captures extended source emission with variety of source lifetimes. This can readily reduce to conventional formalism for transient sources [132]. In particular, we can consider the DSNB with evolving redshift-dependent core-collapse supernova rate $R_{\rm SN}(z)$.

Let us consider DS luminosity as a Dirac delta function

$$L_\delta = L_0 \delta(\tau) \ , \tag{C.15}$$

with $L_0 = \int d\tau L_{DS}(\tau)$ such that the total integrated DS luminosity is identical to that of prolonged emission. Note that Eq. (C.15) also implies all DS emission occurs at formation, with $\tau = 0$, allowing to neglect $f_{\rm sur}$. With this luminosity, Eq. (4.7)

Annihilation	m_χ = 10 GeV		m_χ =100 GeV		m_χ = 10 TeV		m_χ =100 TeV	
channel	f_ν	$\langle E_\nu \rangle$	f_ν	$\langle E_\nu \rangle$	f_ν	$\langle E_\nu \rangle$	f_ν	$\langle E_\nu \rangle$
$b\bar{b}$	0.47	0.224	0.45	0.944	0.45	4.19	0.45	19.8
$\mu^+\mu^-$	0.63	3.13	0.62	31.0	0.62	206	0.61	1113
W^+W^-	N/A	N/A	0.50	1.28	0.52	9.32	0.50	46.3
$\nu\bar{\nu}$	1/3	10	1/3	100	1/3	10^3	1/3	10^4

Table C.1. Fraction f_ν of DM mass m_χ emitted as neutrino energy different DM masses and annihilation channels. The $\nu\bar{\nu}$ channel only produces neutrinos and hence does not inherently allow powering DSs through heating when $f_\nu = 1$, and we consider $f_\nu \sim 1/3$. Energies are reported in GeV.

becomes

$$\begin{aligned} L_{\rm EM}(z) = & \int_0^{t(z)} d\tau \int_{M_{min}}^{M_{max}} dM_h L_0 \delta(\tau) \frac{d^2 n_{\rm DS}}{dM_h dt}\Big(z(t-\tau), M_h\Big) \\ = & \, L_0 \int_{M_{min}}^{M_{max}} dM_h \frac{d^2 n_{\rm DS}}{dM_h dt}\Big(z(t), M_h\Big) = L_0 R(z) \ . \end{aligned} \tag{C.16}$$

where in Eq. (C.16) we have identified $R(z)$ as the rate density of DS formation that is analogous to supernova rate $R_{\rm SN}(z)$ in computation of DSNB [132].

From this computation, our Eq. (4.8) becomes Eq. (C.17), where $L_0 f_\nu/(1 - f_\nu)\langle E_\nu \rangle$ is the number flux of neutrinos emitted per DS and spectrum dN/dE is normalized. Hence, $(dN/dE_\nu) L_0 f_\nu/(1-f_\nu)\langle E_\nu \rangle$ is the neutrino emission from a single DS analogous to the DSNB emission spectrum φ in Ref. [132] in units of neutrinos per unit energy. Under theses considerations, Eq. (C.17) can be matched with DSNB flux computation of Ref. [132]

$$\frac{d\phi}{dE_\nu} = \int dz \left[(1+z)\frac{dN}{dE_\nu}\Big(E_\nu(1+z)\Big)\frac{f_\nu/(1-f_\nu)}{\langle E_\nu \rangle} L_0\right] [R(z)] \left| c\frac{dt}{dz} \right| \ . \tag{C.17}$$

In Fig. C.4 we show the neutrino spectra dN/dE obtained from Ref. [188] and list a selection of neutrino fractions in Tab. C.1.

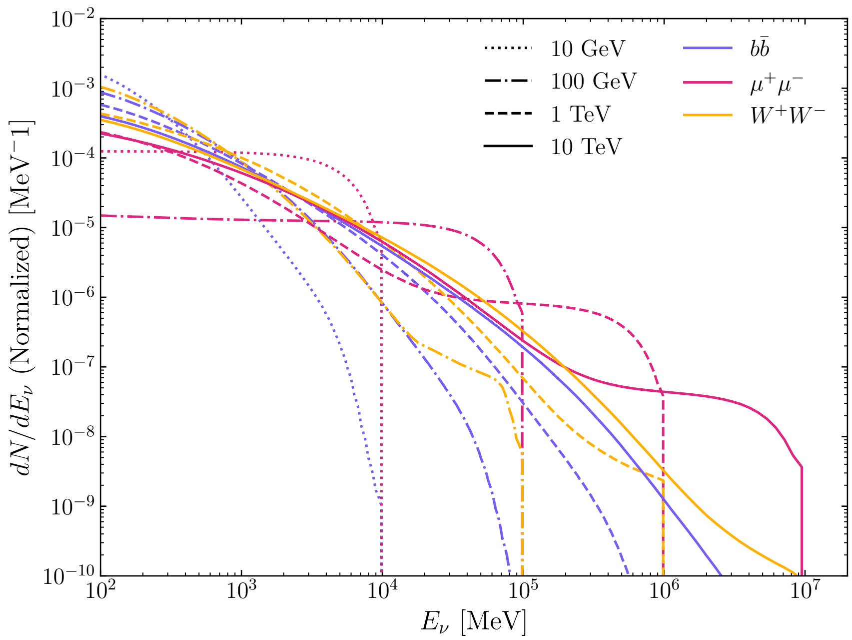

Figure C.4. Differential neutrino spectra normalized to one neutrino for a range of DM masses from $m_\chi = 10$ GeV to 10 TeV for different DM annihilation channels. Spectra are taken from Ref. [188, 185]

C.4 Comparison With Indirect Dark Matter Detection

DM annihilation can produce a range of observable signatures, including extragalactic diffuse gamma-ray background and the diffuse neutrino background. Here we examine how the emission from DSs associated with DM annihilation compares to signals in the context of indirect DM detection.

Since DM annihilation is follows $\propto \rho_{\rm DM}^2$ for DM density $\rho_{\rm DM}$, we define $f_{\rm DS}$ as the enhancement factor representing the overdensity of DM annihilation within DS compared to that in a typical galactic DM profile, which we assume follows the NFW [369] distribution

$$f_{\rm DS} = \frac{\int_0^{r_{\rm DS}} \rho_{\rm DS}^2(r) r^2 dr}{\int_0^{r_\Delta} \rho_h^2(r) r^2 dr} \ . \tag{C.18}$$

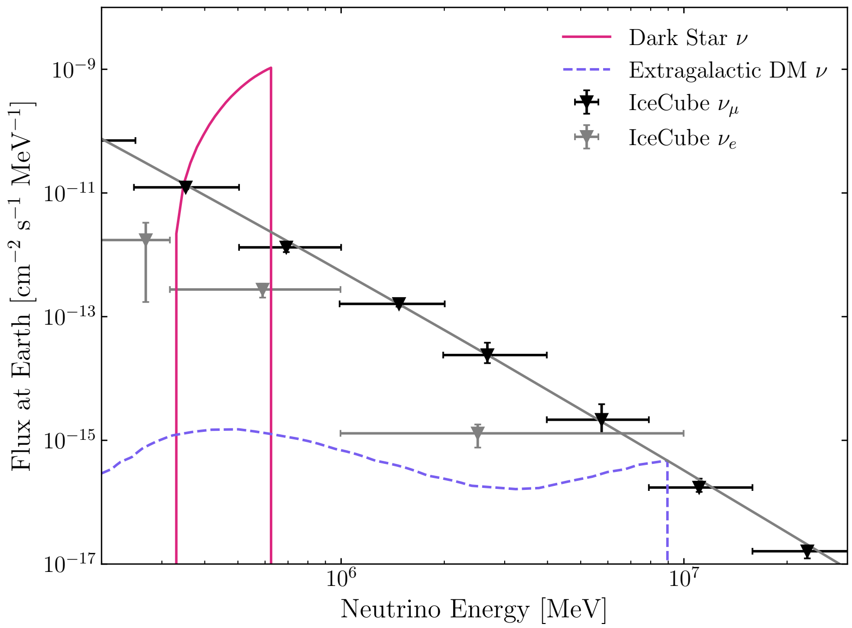

Figure C.5. Extragalactic neutrino flux from 10 TeV DM annihilating in dark stars (pink/solid) assuming DS reach 1% of their host halo mass which is in the range $M_h = 10^6 - 10^9\ M_\odot$ compared to the expected neutrino flux from conventional dark matter halos (purple/dashed) from [93].

Here, $\rho_{\rm DS}$ is the DS density profile, $r_{\rm DS}$ is the DS radius and $\rho_{\rm NFW}$ is the NFW profile density

$$\rho_h = \frac{4\rho_s}{(r/r_s)(1+r/r_s)^2} \tag{C.19}$$

where r_s is the characteristic radius and ρ_s is the characteristic density.

We consider r_Δ to denote the outer radius of the halo such that

$$M_h = \Delta\rho_c(z)\frac{4}{3}\pi r_\Delta^3\ , \tag{C.20}$$

where $\rho_c(z) \simeq \rho_c(\Omega_m(1+z)^3 + \Omega_\Lambda)$ is the critical density of the Universe with Ω_m and Ω_Λ denoting fractional contributions from matter and dark energy [55]. Hence, the density within r_Δ is Δ times the critical density of the Universe. Following Ref. [380], we consider overdensity threshold $\Delta = 200$. Then, the halo concentration is found from $c_\Delta = r_\Delta/r_s$. We employ $c_\Delta(M_h, z)$ parametrization of Ref. [347] obtained from the fit of all available data from the MultiDark/BigBolshoi simulations [380], and which enters as

$$\int_0^{r_\Delta} \rho_h^2(r) r^2 dr = \tilde{g}(c_\Delta) \frac{M_h \Delta \rho_c(z)}{12\pi} \tag{C.21}$$

where $\tilde{g}$ is given by

$$\tilde{g}(c_\Delta) = \frac{c_\Delta^3 [1 - (1 + c_\Delta)^{-3}]}{3[\ln(1 + c_\Delta) - c_\Delta/(1 + c_\Delta)]^2} \ . \tag{C.22}$$

Previously, analysis of DS gamma-ray background of Ref. [444] found that DM annihilation rate from DSs exceeds that of halos by enhancement of $f_{\rm DS} \sim 10^3$. They considered DS density profiles of Ref. [251] for $\sim 10 - 100 M_\odot$ DS forming in a $10^5 - 10^6\ M_\odot$ halo. Using of Ref. [251] we have computed similar $f_{\rm DS} \sim 10^3$ to that of Ref. [444]. Importantly, those profiles correspond to very early phase in DS formation when baryonic matter has only contracted to a hydrogen density of $\sim 10^{13}{\rm cm}^{-3}$.

However, as can be seen from Ref. [389] for the supermassive DSs we consider, the baryon densities reach nearly $\sim 10^{20}{\rm cm}^{-3}$. For an increase in density from $10^{13}{\rm cm}^{-3}$ to $10^{16}{\rm cm}^{-3}$, considering the DS and halo mass is the same and DS mass is only $M_{\rm DS} \sim 10^{-4} M_h$, the enhancement factor significantly increases to $f_{\rm DS} \sim 10^6$. For supermassive DSs we study, as DSs further evolve and grow to $\sim 1\%$ of the halo mass the enhancement factor increases to $f_{\rm DS} \sim 10^8$. For a $M_h = 10^8\ M_\odot$ halo we find $f_{\rm DS} = 4 \times 10^8$ for a DS of mass $M_{\rm DS} = 10^6$.

As we have demonstrated, supermassive DSs we explore benefit from greater enhancements $f_{\rm DS}$ compared to what was found in earlier studies (e.g. [444]) that focused on less concentrated smaller and earlier DSs that compose a less significant fraction of the host halo mass. We note that constraints from the extragalactic diffuse gamma-ray background have not been evaluated in such case in detail, which we leave for future work. We note that DS electromagnetic radiation has also been studied in the context of reionization [398, 397], however these analyses relied on a DS phases after DM depletion.

Besides electromagnetic diffuse emission, we can also compare DS emission with halo emission for DM annihilating to neutrinos. For comparison to the extragalactic neutrino flux from indirect DM detection, we are now interested in contributions from the entire halo population and compare to results of Ref. [93]. Noting that $f_{\rm DS}$ varies by only $\mathcal{O}(1)$ factors for halo masses in the range of 10^6 $M_\odot$ to 10^9 $M_\odot$, we assume a constant value $f_{\rm DS} \simeq 10^8$ for DSs that reach 1% of the halo mass. Since only massive halos in the range $10^6 - 10^9$ $M_\odot$ can host supermassive DSss, this enhancement is suppressed. Halos less than 10^6 $M_\odot$ are far more abundant and we find that they contribute $\sim 10^3$ times more to the extragalactic neutrino flux than the heavier portion of the halo population. Thus $f_{\rm DS} \sim 10^8$ enhances only portion of the total diffuse DS neutrino flux that is suppressed by a $\sim 10^{-3}$ due to subdominant contributions of large halos hosting DSs. From these approximate considerations, we expect supermassive DSs to enhance the neutrino flux compared to DM annihilation by a factor $\sim 10^5$. In Fig. C.5 we display our computational results, showing qualitative agreement with the estimates above and finding that the DS neutrino flux exceeds that of halos by around $\sim 10^6$.

C.5 Different Dark Matter Annihilation Channels

In the main text we focused on results for DM annihilating to $\nu\bar{\nu}$. In Fig. C.6 we provide results for DM annihilation to W^+W^-, $b\bar{b}$ and $\mu^+\mu^-$ channels. As in Fig. 33 of the main text, we show DM annihilation cross-sections for which neutrino emission from DSs in a fraction $f_{\rm SMDS}$ of halos exceeds the atmospheric background at energies $E_\nu \gtrsim 200$ MeV. The total energy radiated in neutrinos is primarily determined by DS luminosity, which only weakly depends on DM annihilation channel. The difference in these results stems from the different neutrino spectra, with softer spectra such as that of $b\bar{b}$ channel being more challenging to distinguish and identify than the peaked spectra such as from $\nu\bar{\nu}$ channel.

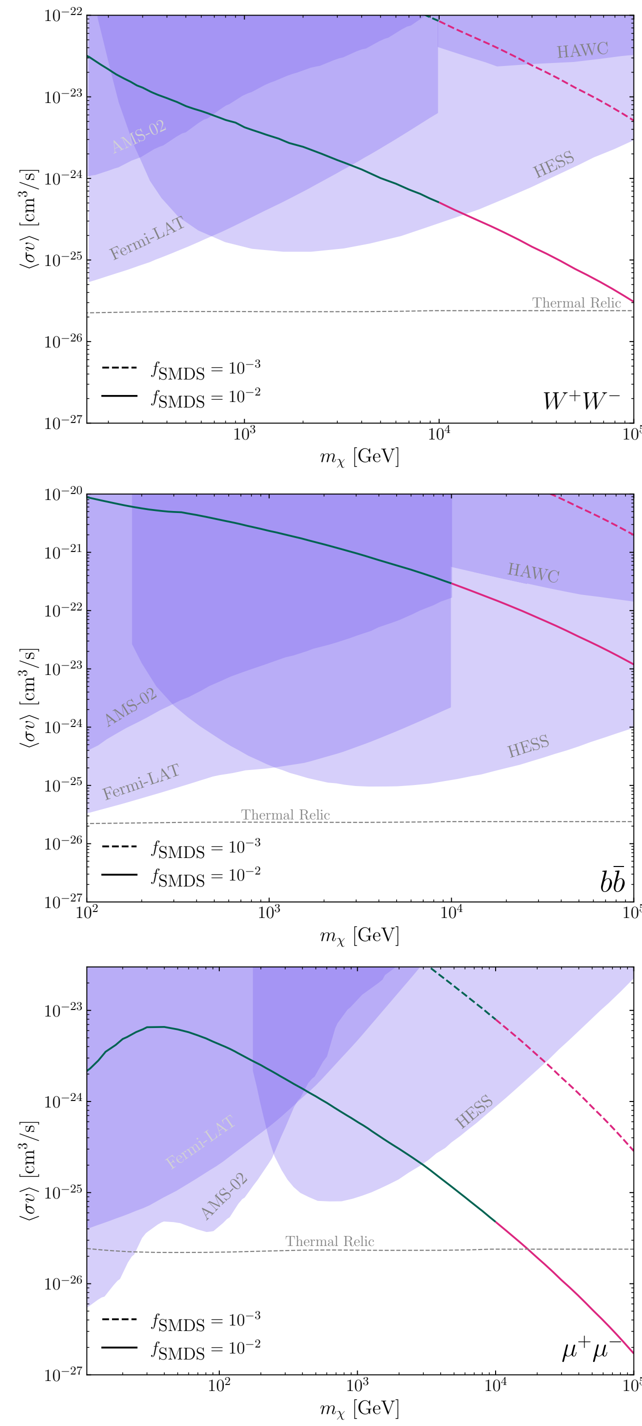

Figure C.6. Same as Fig. 33, but for DM annihilation to W^+W^- [Top], $b\bar{b}$ [Middle] and $\mu^+\mu^-$ [Bottom]. Existing bounds from indirect DM detection searches by HAWC [75], Fermi-LAT [45], AMS [61, 43] and HESS [33] are shown as shaded regions.

APPENDIX D

SUPPLEMENTAL MATERIAL FOR KM3NET AND ICECUBE

D.1 Effective area

The sensitivity of neutrino telescopes is typically quantified by the effective area, A_{eff}, which includes the propagation and scattering of neutrinos in the Earth. In the following, we reproduce A_{eff} from KM3NeT in order to extend it to higher neutrino energies.

By including propagation and scattering, the effective area captures all the ingredients to compute the neutrino event rate in an experiment. To be more precise, the expected rate of events is given by

$$\frac{dN(E_\nu)}{dE} = T \int d\Omega \, A_{\text{eff}}(E_\nu, \cos\theta) \, \Phi(E_\nu, \Omega), \tag{D.1}$$

where Ω is a solid angle, and Φ and E_ν are the neutrino flux and energy. Following the prescription in Ref. [262], we derive the effective area as

$$A_{\text{eff}}(E_\nu, \cos\theta) = \rho N_A V \sigma(E_\nu) e^{-\tau(E_\nu, \cos\theta)} \epsilon(E_\nu, \cos\theta), \tag{D.2}$$

where ρ is the density of the Earth near the detector, N_A is Avogadro's number, V is a volume, τ is the attenuation length of a neutrino with energy E_ν, arriving from a zenith angle θ, and ϵ captures the detector efficiency. We assume that for the high energies we are considering, the KM3NeT efficiency is unity, $\epsilon = 1$. We compute the attenuation of neutrinos in Earth from the neutrino cross section $\sigma(E_\nu)$ and using the PREM density profile [227]. For starting events, the volume V is the same as the detector volume. However, for through-going muons, V is more complicated as the effective volume is larger since muon neutrinos can interact outside the detector. This produces a muon which still propagates to the detector. We account for this effect following Ref. [262]. Although there is a dependence of the effective volume on the specific detector geometry, which translates into a $\cos\theta$ dependence to the effective area, this effect is much less significant than attenuation at PeV energies. For simplicity, we assume a spherical detector.

Figure D.1 shows the A_{eff} used throughout this work. IceCube data at 8° above the horizon (green) comes from Ref. [10]. Below 100 PeV, KM3NeT data at horizon (purple) can be found in Ref. [172] while at higher energies we use our own calculation of the effective area, matching the normalization to account for the simplifications made here.[1] We find the energy dependence of A_{eff} to match the KM3NeT curve well and, based on our calculation, we can extend the effective area to higher energies, and arbitrary zenith angles. For the all-sky averaged A_{eff} (gold) we use the result provided by the KM3NeT collaboration [69].

D.2 Neutrino and Muon Energy Reconstruction

As discussed in the main text, Bayes theorem states that the probability of a neutrino energy given the number of triggered PMTs (hits) is

$$P(E_\nu|N_{\text{hit}}) = \frac{1}{P(N_{\text{hit}})} \int dE_\mu P(N_{\text{hit}}|E_\mu) P(E_\mu|E_\nu) P(E_\nu), \tag{D.3}$$

where $P(E_\nu)$ is the prior on the neutrino energy, namely

$$P(E_\nu) = \frac{1}{\phi_\nu} \frac{d\phi_\nu}{dE_\nu}, \tag{D.4}$$

where ϕ_ν is the neutrino flux. $P(E_\mu|E_\nu)$ is the probability that a neutrino with energy E_ν interacts and produces a muon which has energy E_μ when entering the detector. This probability accounts for muon production from a neutrino with given energy, which is simulated with `MadGraph` [78].

[1] Using a spherical detector, our overall normalization is about a factor of 3 larger than KM3NeT official one at 100 PeV, which we consider to arise from the detector geometry.

More concretely,

$$P(E_\mu|E_\nu) = \frac{1}{\sigma(E_\nu)}\frac{d\tilde{\sigma}(E_\nu, E_\mu)}{dE_\mu}, \tag{D.5}$$

where $\sigma(E_\nu)$ is the neutrino cross section. The differential cross section for a neutrino with energy E_ν to produce a muon which reaches the detector with energy E_μ is given by [262]

$$\frac{d\tilde{\sigma}}{dE_\mu} = \frac{N_A}{\alpha(1 + E_\mu/E_{\rm crit})}\int_0^{1-E_\mu/E_\nu} dy' \int_0^1 dx \frac{d\sigma}{dx dy'}, \tag{D.6}$$

where $\alpha \simeq 2$ MeV/cm^2; $E_{\rm crit}$ is the critical energy, typically around 500 GeV; x is the Bjorken-x; and y' is the inelasticity parameter.

We then calculate the probability $P(N_{\rm hit}|E_\mu)$ that a muon arriving at the detector with energy E_μ triggers a certain number of PMTs $N_{\rm hit}$. We simulate muon energy loss in the detector with `PROPOSAL` [316, 73, 224] which records muon energy deposition through both continuous and radiative energy losses. We then map the muon energy loss to a number of triggered PMTs, $N_{\rm hit}$, in a simplified manner. We assume that light will be attenuated exponentially as a function of propagation distance in water. A PMT will trigger if the light intensity reaching it is above some threshold, which we take to be 8 GeV/cm^2. Varying this threshold does not lead to a large variation on $N_{\rm hit}$. This allows us to compute the fraction of detector volume which is above threshold and convert it to a number of triggered PMTs assuming they are uniformly distributed through the detector volume.

We find optimal values for light attenuation and PMT thresholds by matching the KM3NeT distributions for 10, 100, and 1000 PeV muons as shown in Fig. D.2. To model the tail of the $N_{\rm hit}$ distribution, we fit our histograms to a Fréchet distribution

$$P(x) = \frac{\alpha}{s}\left(\frac{x}{s}\right)^{-1-\alpha} e^{-(x/s)^{-\alpha}}, \tag{D.7}$$

where α sets the width and s the peak location. In Fig. D.2 we compare our distributions (dashed histograms) to KM3NeT's official ones (shaded histograms). For reference, the uncertainties on light propagation in water shift the KM3NeT distribution peaks by about 10% [190]. For the highest energy muons, we simulate the truncation of the triggered PMTs around 6,000 with a hyperbolic tangent function to match the KM3NeT result.

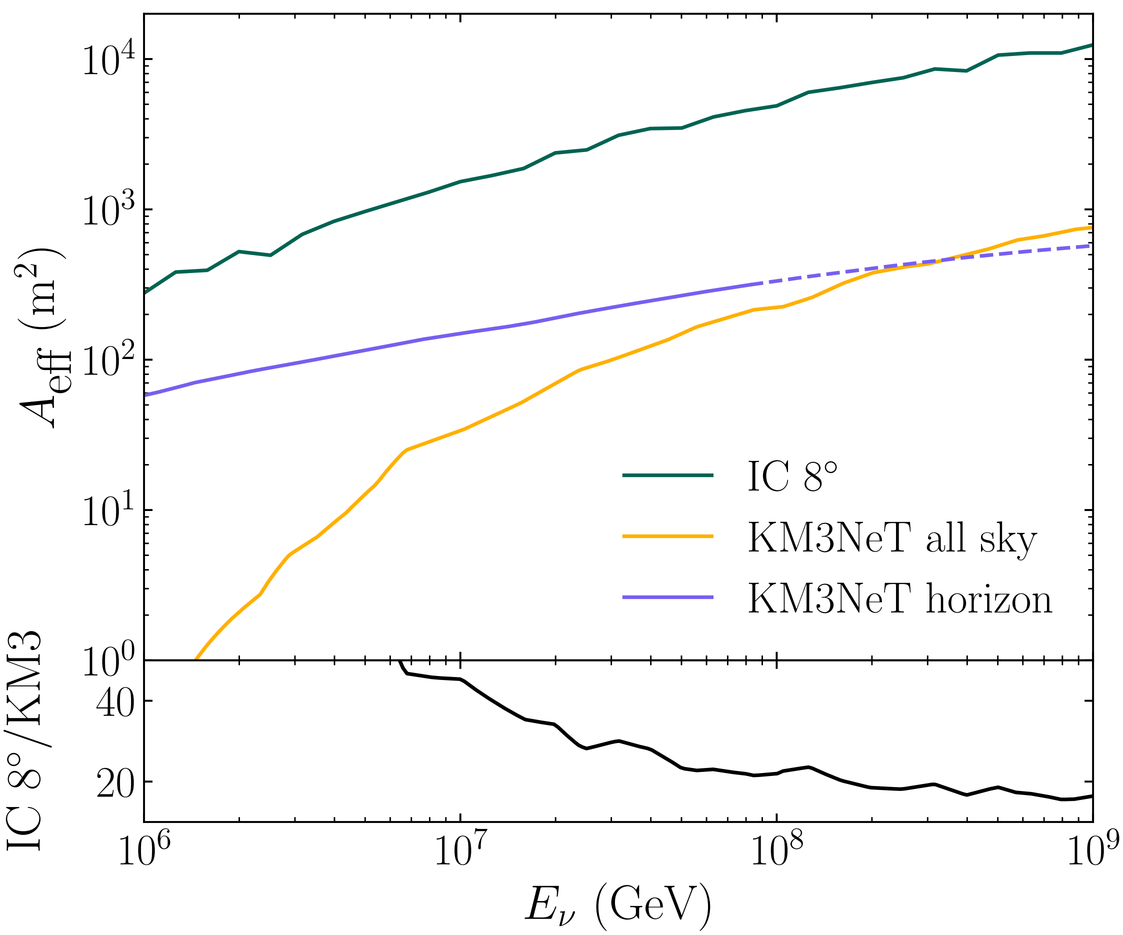

Figure D.1. Effective areas used in this work. We use the IceCube effective area 8° above the horizon [10] (green) in our discussion of point sources. For KM3NeT, below 100 PeV we used the one reported in Ref. [172] (purple solid), while above 100 PeV we extrapolate it by matching our own effective area calculation (purple dashed, see text for details). We take the all-sky averaged KM3NeT effective area (gold) from Ref. [69]. In the lower panel we plot the ratio of effective areas for IceCube 8° declination and KM3NeT all sky.

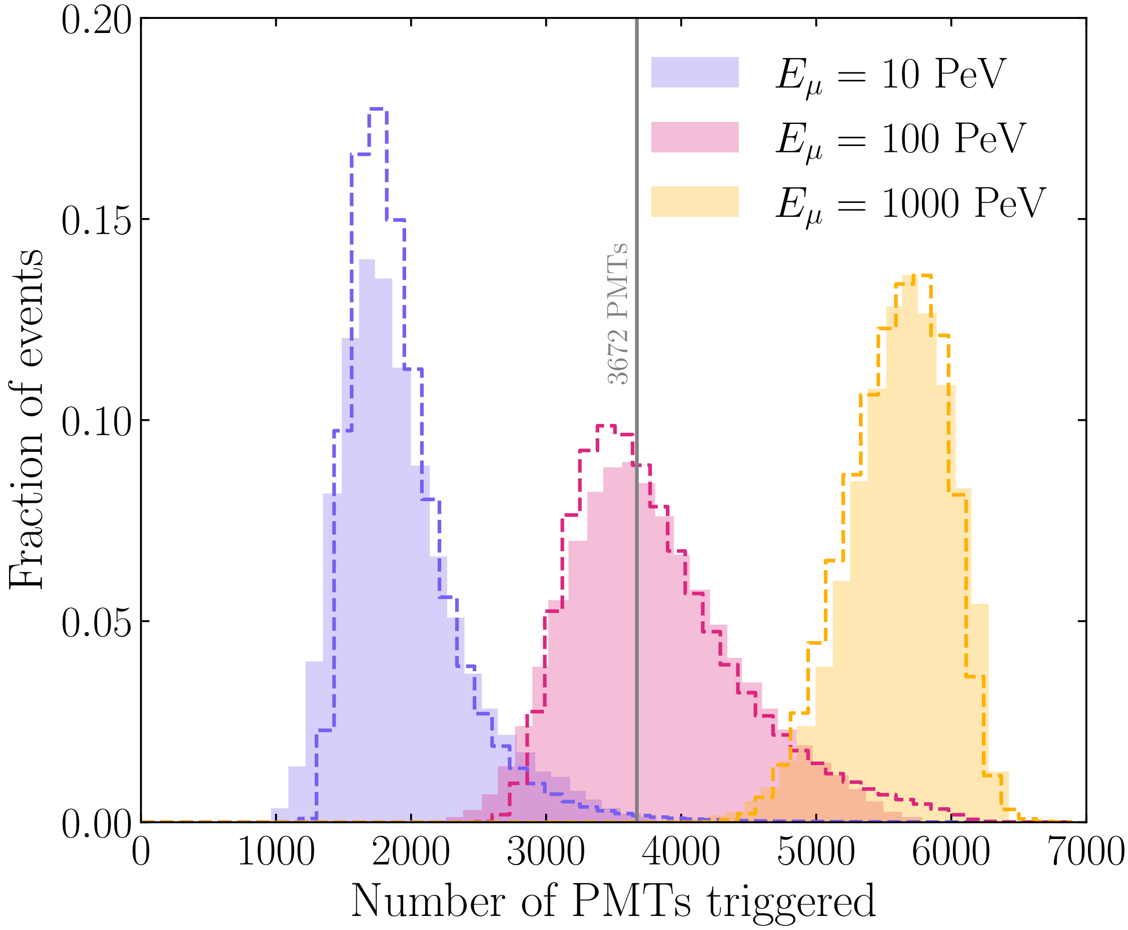

Figure D.2. The distributions derived in this work of the number of PMTs triggered for 10, 100, and 1000 PeV muons pass through KM3NeT as dashed histograms. The official results are also shown for comparison as shaded histograms [69]. The vertical line labeled "3,672 PMTs" indicates the number of triggered PMTs for the high energy event we are interested in.

REFERENCES CITED

[1] *Neutrino Non-Standard Interactions: A Status Report*, volume 2, 2019.

[2] Georges Aad et al. Observation of a new particle in the search for the Standard Model Higgs boson with the ATLAS detector at the LHC. *Phys. Lett. B*, 716:1–29, 2012.

[3] Roel Aaij et al. Test of lepton universality in beauty-quark decays. *Nature Phys.*, 18(3):277–282, 2022.

[4] J. Aalbers et al. First Dark Matter Search Results from the LUX-ZEPLIN (LZ) Experiment, 7 2022.

[5] J. Aalbers et al. First Dark Matter Search Results from the LUX-ZEPLIN (LZ) Experiment. *Phys. Rev. Lett.*, 131(4):041002, 2023.

[6] J. Aalbers et al. Dark Matter Search Results from 4.2 Tonne-Years of Exposure of the LUX-ZEPLIN (LZ) Experiment, 10 2024.

[7] J. Aalbers *et. al.* First dark matter search results from the lux-zeplin (lz) experiment, 2022.

[8] M. G. Aartsen et al. Evidence for High-Energy Extraterrestrial Neutrinos at the IceCube Detector. *Science*, 342:1242856, 2013.

[9] M. G. Aartsen et al. First observation of PeV-energy neutrinos with IceCube. *Phys. Rev. Lett.*, 111:021103, 2013.

[10] M. G. Aartsen et al. Searches for Extended and Point-like Neutrino Sources with Four Years of IceCube Data. *Astrophys. J.*, 796(2):109, 2014.

[11] M. G. Aartsen et al. Measurement of the Atmospheric ν_e Spectrum with IceCube. *Phys. Rev. D*, 91:122004, 2015.

[12] M. G. Aartsen et al. Observation and Characterization of a Cosmic Muon Neutrino Flux from the Northern Hemisphere using six years of IceCube data. *Astrophys. J.*, 833(1):3, 2016.

[13] M. G. Aartsen et al. Search for annihilating dark matter in the Sun with 3 years of IceCube data. *Eur. Phys. J. C*, 77(3):146, 2017. [Erratum: Eur.Phys.J.C 79, 214 (2019)].

[14] M. G. Aartsen et al. Differential limit on the extremely-high-energy cosmic neutrino flux in the presence of astrophysical background from nine years of IceCube data. *Phys. Rev. D*, 98(6):062003, 2018.

[15] M. G. Aartsen et al. Characteristics of the diffuse astrophysical electron and tau neutrino flux with six years of IceCube high energy cascade data. *Phys. Rev. Lett.*, 125(12):121104, 2020.

[16] M. G. Aartsen et al. IceCube-Gen2: the window to the extreme Universe. *J. Phys. G*, 48(6):060501, 2021.

[17] Kevork N. Abazajian, Nicolas Canac, Shunsaku Horiuchi, and Manoj Kaplinghat. Astrophysical and Dark Matter Interpretations of Extended Gamma-Ray Emission from the Galactic Center. *Phys. Rev. D*, 90(2):023526, 2014.

[18] Kevork N. Abazajian and Manoj Kaplinghat. Detection of a Gamma-Ray Source in the Galactic Center Consistent with Extended Emission from Dark Matter Annihilation and Concentrated Astrophysical Emission. *Phys. Rev. D*, 86:083511, 2012. [Erratum: Phys.Rev.D 87, 129902 (2013)].

[19] R. Abbasi et al. Multi-year search for dark matter annihilations in the Sun with the AMANDA-II and IceCube detectors. *Phys. Rev. D*, 85:042002, 2012.

[20] R. Abbasi et al. IceCube Data for Neutrino Point-Source Searches Years 2008-2018, 1 2021.

[21] R. Abbasi et al. The IceCube high-energy starting event sample: Description and flux characterization with 7.5 years of data. *Phys. Rev. D*, 104:022002, 2021.

[22] R. Abbasi et al. Evidence for neutrino emission from the nearby active galaxy NGC 1068. *Science*, 378(6619):538–543, 2022.

[23] R. Abbasi et al. Improved Characterization of the Astrophysical Muon–neutrino Flux with 9.5 Years of IceCube Data. *Astrophys. J.*, 928(1):50, 2022.

[24] R. Abbasi et al. Search for GeV-scale dark matter annihilation in the Sun with IceCube DeepCore. *Phys. Rev. D*, 105(6):062004, 2022.

[25] R. Abbasi et al. Search for neutrino lines from dark matter annihilation and decay with IceCube. *Phys. Rev. D*, 108(10):102004, 2023.

[26] R. Abbasi et al. Characterization of the astrophysical diffuse neutrino flux using starting track events in IceCube. *Phys. Rev. D*, 110(2):022001, 2024.

[27] R. Abbasi et al. Search for dark matter from the center of the Earth with ten years of IceCube data, 12 2024.

[28] R. Abbasi et al. A search for extremely-high-energy neutrinos and first constraints on the ultra-high-energy cosmic-ray proton fraction with IceCube, 2 2025.

[29] Rasha Abbasi et al. Indirect search for dark matter in the Galactic Centre with IceCube. In *37th International Cosmic Ray Conference*, 7 2021.

[30] R. Abbasi *et. al.* All-flavor constraints on nonstandard neutrino interactions and generalized matter potential with three years of icecube deepcore data. *Phys. Rev. D*, 104:072006, Oct 2021.

[31] B. P. Abbott et al. Multi-messenger Observations of a Binary Neutron Star Merger. *Astrophys. J. Lett.*, 848(2):L12, 2017.

[32] T. M. C. Abbott, M. Aguena, A. Alarcon, O. Alves, A. Amon, F. Andrade-Oliveira, J. Annis, B. Ansarinejad, S. Avila, D. Bacon, E. J. Baxter, K. Bechtol, M. R. Becker, B. A. Benson, G. M. Bernstein, E. Bertin, J. Blazek, L. E. Bleem, S. Bocquet, D. Brooks, E. Buckley-Geer, D. L. Burke, H. Camacho, A. Campos, J. E. Carlstrom, A. Carnero Rosell, M. Carrasco Kind, J. Carretero, R. Cawthon, C. Chang, C. L. Chang, R. Chen, A. Choi, R. Chown, C. Conselice, J. Cordero, M. Costanzi, T. Crawford, A. T. Crites, M. Crocce, L. N. da Costa, C. Davis, T. M. Davis, T. de Haan, J. De Vicente, J. DeRose, S. Desai, H. T. Diehl, M. A. Dobbs, S. Dodelson, P. Doel, C. Doux, A. Drlica-Wagner, K. Eckert, T. F. Eifler, F. Elsner, J. Elvin-Poole, S. Everett, W. Everett, X. Fang, I. Ferrero, A. Ferté, B. Flaugher, P. Fosalba, O. Friedrich, J. Frieman, J. García-Bellido, M. Gatti, E. M. George, T. Giannantonio, G. Giannini, D. Gruen, R. A. Gruendl, J. Gschwend, G. Gutierrez, N. W. Halverson, I. Harrison, K. Herner, S. R. Hinton, G. P. Holder, D. L. Hollowood, W. L. Holzapfel, K. Honscheid, J. D. Hrubes, H. Huang, E. M. Huff, D. Huterer, B. Jain, D. J. James, M. Jarvis, T. Jeltema, S. Kent, L. Knox, A. Kovacs, E. Krause, K. Kuehn, N. Kuropatkin, O. Lahav, A. T. Lee, P.-F. Leget, P. Lemos, A. R. Liddle, C. Lidman, D. Luong-Van, J. J. McMahon, N. MacCrann, M. March, J. L. Marshall, P. Martini, J. McCullough, P. Melchior, F. Menanteau, S. S. Meyer, R. Miquel, L. Mocanu, J. J. Mohr, R. Morgan, J. Muir, J. Myles, T. Natoli, A. Navarro-Alsina, R. C. Nichol, Y. Omori, S. Padin, S. Pandey, Y. Park, F. Paz-Chinchón, M. E. S. Pereira, A. Pieres, A. A. Plazas Malagón, A. Porredon, J. Prat, C. Pryke, M. Raveri, C. L. Reichardt, R. P. Rollins, A. K. Romer, A. Roodman, R. Rosenfeld, A. J. Ross, J. E. Ruhl, E. S. Rykoff, C. Sánchez, E. Sanchez, J. Sanchez, K. K. Schaffer, L. F. Secco, I. Sevilla-Noarbe, E. Sheldon, T. Shin, E. Shirokoff, M. Smith, Z. Staniszewski, A. A. Stark, E. Suchyta, M. E. C. Swanson, G. Tarle, C. To, M. A. Troxel, I. Tutusaus, T. N. Varga, J. D. Vieira, N. Weaverdyck, R. H. Wechsler, J. Weller, R. Williamson, W. L. K. Wu, B. Yanny, B. Yin, Y. Zhang, and J. Zuntz. Joint analysis of dark energy survey year 3 data and cmb lensing from spt and planck. iii. combined cosmological constraints. *Phys. Rev. D*, 107:023531, Jan 2023.

[33] H. Abdallah et al. Search for dark matter annihilations towards the inner Galactic halo from 10 years of observations with H.E.S.S. *Phys. Rev. Lett.*, 117(11):111301, 2016.

[34] K. Abe et al. Solar Neutrino Measurements in Super-Kamiokande-IV. *Phys. Rev. D*, 94(5):052010, 2016.

[35] K. Abe et al. Atmospheric neutrino oscillation analysis with external constraints in Super-Kamiokande I-IV. *Phys. Rev. D*, 97(7):072001, 2018.

[36] K. Abe et al. Hyper-Kamiokande Design Report, 5 2018.

[37] K. Abe et al. Indirect search for dark matter from the Galactic Center and halo with the Super-Kamiokande detector. *Phys. Rev. D*, 102(7):072002, 2020.

[38] K. Abe et al. Diffuse supernova neutrino background search at Super-Kamiokande. *Phys. Rev. D*, 104(12):122002, 2021.

[39] Tom Abel, Greg L. Bryan, and Michael L. Norman. The formation of the first star in the Universe. *Science*, 295:93, 2002.

[40] Babak Abi et al. Deep Underground Neutrino Experiment (DUNE), Far Detector Technical Design Report, Volume I Introduction to DUNE. *JINST*, 15(08):T08008, 2020.

[41] Babak Abi et al. Deep Underground Neutrino Experiment (DUNE), Far Detector Technical Design Report, Volume II: DUNE Physics, 2 2020.

[42] Angel Abusleme et al. JUNO physics and detector. *Prog. Part. Nucl. Phys.*, 123:103927, 2022.

[43] L. Accardo et al. High Statistics Measurement of the Positron Fraction in Primary Cosmic Rays of 0.5–500 GeV with the Alpha Magnetic Spectrometer on the International Space Station. *Phys. Rev. Lett.*, 113:121101, 2014.

[44] R. Acciarri et al. Long-Baseline Neutrino Facility (LBNF) and Deep Underground Neutrino Experiment (DUNE): Conceptual Design Report, Volume 2: The Physics Program for DUNE at LBNF, 12 2015.

[45] M. Ackermann et al. Searching for Dark Matter Annihilation from Milky Way Dwarf Spheroidal Galaxies with Six Years of Fermi Large Area Telescope Data. *Phys. Rev. Lett.*, 115(23):231301, 2015.

[46] Prakruth Adari et al. First Direct-Detection Results on Sub-GeV Dark Matter Using the SENSEI Detector at SNOLAB. *Phys. Rev. Lett.*, 134(1):011804, 2025.

[47] P. A. R. Ade et al. Planck 2015 results. XIII. Cosmological parameters. *Astron. Astrophys.*, 594:A13, 2016.

[48] E. G. Adelberger, B. R. Heckel, S. Hoedl, C. D. Hoyle, D. J. Kapner, and A. Upadhye. Particle-physics implications of a recent test of the gravitational inverse-square law. *Phys. Rev. Lett.*, 98:131104, 3 2007.

[49] Stephen L. Adler. Planet-bound dark matter and the internal heat of Uranus, Neptune, and hot-Jupiter exoplanets. *Phys. Lett. B*, 671:203–206, 2009.

[50] S. Adrian-Martinez et al. Letter of intent for KM3NeT 2.0. *J. Phys. G*, 43(8):084001, 2016.

[51] O. Adriani et al. Ten years of PAMELA in space. *Riv. Nuovo Cim.*, 40(10):473–522, 2017.

[52] O. Adriani et al. Characterising Candidate Blazar Counterparts of the Ultra-High-Energy Event KM3-230213A, 2 2025.

[53] O. Adriani et al. On the Potential Galactic Origin of the Ultra-High-Energy Event KM3-230213A, 2 2025.

[54] O. Adriani et al. The ultra-high-energy event KM3-230213A within the global neutrino landscape, 2 2025.

[55] N. Aghanim et al. Planck 2018 results. VI. Cosmological parameters. *Astron. Astrophys.*, 641:A6, 2020. [Erratum: Astron.Astrophys. 652, C4 (2021)].

[56] P. Agnes et al. Constraints on Sub-GeV Dark-Matter–Electron Scattering from the DarkSide-50 Experiment. *Phys. Rev. Lett.*, 121(11):111303, 2018.

[57] P. Agnes et al. Search for dark matter particle interactions with electron final states with DarkSide-50, 7 2022.

[58] R. Agnese et al. First Dark Matter Constraints from a SuperCDMS Single-Charge Sensitive Detector. *Phys. Rev. Lett.*, 121(5):051301, 2018. [Erratum: Phys.Rev.Lett. 122, 069901 (2019)].

[59] M. Agostini, K. Altenmüller, S. Appel, V. Atroshchenko, Z. Bagdasarian, D. Basilico, G. Bellini, J. Benziger, D. Bick, G. Bonfini, D. Bravo, B. Caccianiga, F. Calaprice, A. Caminata, S. Caprioli, M. Carlini, P. Cavalcante, A. Chepurnov, K. Choi, L. Collica, D. D'Angelo, S. Davini, A. Derbin, X. F. Ding, A. Di Ludovico, L. Di Noto, I. Drachnev, K. Fomenko, A. Formozov, D. Franco, F. Froborg, F. Gabriele, C. Galbiati, C. Ghiano, M. Giammarchi, A. Goretti, M. Gromov, D. Guffanti, C. Hagner, T. Houdy, E. Hungerford, Aldo Ianni, Andrea Ianni, A. Jany, D. Jeschke, V. Kobychev, D. Korablev, G. Korga, D. Kryn, M. Laubenstein, E. Litvinovich, F. Lombardi, P. Lombardi, L. Ludhova, G. Lukyanchenko, L. Lukyanchenko, I. Machulin, G. Manuzio, S. Marcocci, J. Martyn, E. Meroni, M. Meyer, L. Miramonti, M. Misiaszek, V. Muratova, B. Neumair, L. Oberauer, B. Opitz, V. Orekhov, F. Ortica, M. Pallavicini, L. Papp, Ö. Penek, N. Pilipenko, A. Pocar, A. Porcelli, G. Ranucci, A. Razeto, A. Re, M. Redchuk, A. Romani, R. Roncin, N. Rossi, S. Schönert, D. Semenov, M. Skorokhvatov, O. Smirnov, A. Sotnikov, L. F. F. Stokes, Y. Suvorov, R. Tartaglia, G. Testera, J. Thurn, M. Toropova, E. Unzhakov, A. Vishneva, R. B. Vogelaar, F. von Feilitzsch, H. Wang, S. Weinz, M. Wojcik, M. Wurm, Z. Yokley, O. Zaimidoroga, S. Zavatarelli, K. Zuber, and G. Zuzel. Limiting neutrino magnetic moments with borexino phase-ii solar neutrino data. *Phys. Rev. D*, 96:091103, 11 2017.

[60] Matteo Agostini et al. The Pacific Ocean Neutrino Experiment. *Nature Astron.*, 4(10):913–915, 2020.

[61] M. Aguilar et al. Electron and Positron Fluxes in Primary Cosmic Rays Measured with the Alpha Magnetic Spectrometer on the International Space Station. *Phys. Rev. Lett.*, 113:121102, 2014.

[62] A. Aguilar-Arevalo et al. Constraints on Light Dark Matter Particles Interacting with Electrons from DAMIC at SNOLAB. *Phys. Rev. Lett.*, 123(18):181802, 2019.

[63] Alexis Aguilar-Arevalo et al. Search for light mediators in the low-energy data of the CONNIE reactor neutrino experiment. *JHEP*, 04:054, 2020.

[64] M. Ahlers, L. A. Anchordoqui, M. C. Gonzalez-Garcia, F. Halzen, and S. Sarkar. GZK Neutrinos after the Fermi-LAT Diffuse Photon Flux Measurement. *Astropart. Phys.*, 34:106–115, 2010.

[65] M. Ahlers, H. Gies, J. Jaeckel, J. Redondo, and A. Ringwald. Laser experiments explore the hidden sector. *Phys. Rev. D*, 77:095001, 5 2008.

[66] Markus Ahlers and Francis Halzen. Minimal Cosmogenic Neutrinos. *Phys. Rev. D*, 86:083010, 2012.

[67] J. Ahrens et al. Icecube - the next generation neutrino telescope at the south pole. *Nucl. Phys. B Proc. Suppl.*, 118:388–395, 2003.

[68] S. Aiello et al. Astronomy potential of KM3NeT/ARCA, 2 2024.

[69] S. Aiello et al. Observation of an ultra-high-energy cosmic neutrino with KM3NeT. *Nature*, 638(8050):376–382, 2025.

[70] D. S. Akerib et al. Projected WIMP sensitivity of the LUX-ZEPLIN dark matter experiment. *Phys. Rev. D*, 101(5):052002, 2020.

[71] D. Akimov, J. B. Albert, P. An, C. Awe, P. S. Barbeau, B. Becker, V. Belov, A. Brown, A. Bolozdynya, B. Cabrera-Palmer, M. Cervantes, J. I. Collar, R. J. Cooper, R. L. Cooper, C. Cuesta, D. J. Dean, J. A. Detwiler, A. Eberhardt, Y. Efremenko, S. R. Elliott, E. M. Erkela, L. Fabris, M. Febbraro, N. E. Fields, W. Fox, Z. Fu, A. Galindo-Uribarri, M. P. Green, M. Hai, M. R. Heath, S. Hedges, D. Hornback, T. W. Hossbach, E. B. Iverson, L. J. Kaufman, S. Ki, S. R. Klein, A. Khromov, A. Konovalov, M. Kremer, A. Kumpan, C. Leadbetter, L. Li, W. Lu, K. Mann, D. M. Markoff, K. Miller, H. Moreno, P. E. Mueller, J. Newby, J. L. Orrell, C. T. Overman, D. S. Parno, S. Penttila, G. Perumpilly, H. Ray, J. Raybern, D. Reyna, G. C. Rich, D. Rimal, D. Rudik, K. Scholberg, B. J. Scholz, G. Sinev, W. M. Snow, V. Sosnovtsev, A. Shakirov, S. Suchyta, B. Suh, R. Tayloe, R. T. Thornton, I. Tolstukhin, J. Vanderwerp, R. L. Varner, C. J. Virtue, Z. Wan, J. Yoo, C.-H. Yu, A. Zawada, J. Zettlemoyer, A. M. Zderic, and COHERENT COLLABORATION. Observation of coherent elastic neutrino-nucleus scattering. *Science*, 357(6356):1123–1126, 9 2017. Publisher: American Association for the Advancement of Science.

[72] Kazunori Akiyama et al. First M87 Event Horizon Telescope Results. I. The Shadow of the Supermassive Black Hole. *Astrophys. J. Lett.*, 875:L1, 2019.

[73] Jean-Marco Alameddine, Mario Dunsch, Lars Bollmann, Tomasz Fuchs, Pascal Gutjahr, Jan-Hendrik Koehne, Claudio Kopper, Kai Krings, Chung-Yun Kuo, Thorben Menne, Maximilian Noethe, Alex Olivas, Wolfgang Rhode, Maximilian Sackel, Alexander Sandrock, Austin Schneider, Jan Soedingrekso, and Jacob van Santen. tudo-astroparticlephysics/proposal: Zenodo, March 2020.

[74] A. Albert et al. First HAWC Observations of the Sun Constrain Steady TeV Gamma-Ray Emission. *Phys. Rev. D*, 98(12):123011, 2018.

[75] A. Albert et al. An optimized search for dark matter in the galactic halo with HAWC. *JCAP*, 12:038, 2023.

[76] Rouzbeh Allahverdi, Yu Gao, Bradley Knockel, and Shashank Shalgar. Indirect Signals from Solar Dark Matter Annihilation to Long-lived Right-handed Neutrinos. *Phys. Rev. D*, 95(7):075001, 2017.

[77] Lukas Allwicher, Pere Arnan, Daniele Barducci, and Marco Nardecchia. Perturbative unitarity constraints on generic Yukawa interactions. *Journal of High Energy Physics*, 2021(10):129, October 2021.

[78] J. Alwall, R. Frederix, S. Frixione, V. Hirschi, F. Maltoni, O. Mattelaer, H. S. Shao, T. Stelzer, P. Torrielli, and M. Zaro. The automated computation of tree-level and next-to-leading order differential cross sections, and their matching to parton shower simulations. *JHEP*, 07:079, 2014.

[79] D. W. Amaral et al. Constraints on low-mass, relic dark matter candidates from a surface-operated SuperCDMS single-charge sensitive detector. *Phys. Rev. D*, 102(9):091101, 2020.

[80] Dorian W. P. Amaral, David Cerdeno, Andrew Cheek, and Patrick Foldenauer. A direct detection view of the neutrino NSI landscape. *JHEP*, 07:071, 2023.

[81] Yasmine Sara Amhis et al. Averages of b-hadron, c-hadron, and τ-lepton properties as of 2018. *Eur. Phys. J. C*, 81(3):226, 2021.

[82] D. Androić et al. Precision measurement of the weak charge of the proton. *Nature*, 557(7704):207–211, 2018.

[83] A. Angelescu, D. Bečirević, D. A. Faroughy, and O. Sumensari. Closing the window on single leptoquark solutions to the B-physics anomalies. *Journal of High Energy Physics*, 2018(10):183, October 2018.

[84] S. Appel et al. Improved Measurement of Solar Neutrinos from the Carbon-Nitrogen-Oxygen Cycle by Borexino and Its Implications for the Standard Solar Model. *Phys. Rev. Lett.*, 129(25):252701, 2022.

[85] E. Aprile et al. Light Dark Matter Search with Ionization Signals in XENON1T. *Phys. Rev. Lett.*, 123(25):251801, 2019.

[86] E. Aprile et al. Excess electronic recoil events in XENON1T. *Phys. Rev. D*, 102(7):072004, 2020.

[87] E. Aprile et al. Projected WIMP sensitivity of the XENONnT dark matter experiment. *JCAP*, 11:031, 2020.

[88] E. Aprile et al. First Dark Matter Search with Nuclear Recoils from the XENONnT Experiment. *Phys. Rev. Lett.*, 131(4):041003, 2023.

[89] E. Aprile et al. WIMP Dark Matter Search using a 3.1 tonne × year Exposure of the XENONnT Experiment. 2 2025.

[90] Elena Aprile et al. First Indication of Solar B8 Neutrinos via Coherent Elastic Neutrino-Nucleus Scattering with XENONnT. *Phys. Rev. Lett.*, 133(19):191002, 2024.

[91] Giorgio Arcadi, Maíra Dutra, Pradipta Ghosh, Manfred Lindner, Yann Mambrini, Mathias Pierre, Stefano Profumo, and Farinaldo S. Queiroz. The waning of the WIMP? A review of models, searches, and constraints. *Eur. Phys. J. C*, 78(3):203, 2018.

[92] Giorgio Arcadi, Manfred Lindner, Jessica Martins, and Farinaldo S. Queiroz. New physics probes: Atomic parity violation, polarized electron scattering and neutrino-nucleus coherent scattering. *Nucl. Phys. B*, 959:115158, 2020.

[93] Carlos A. Argüelles, Alejandro Diaz, Ali Kheirandish, Andrés Olivares-Del-Campo, Ibrahim Safa, and Aaron C. Vincent. Dark matter annihilation to neutrinos. *Rev. Mod. Phys.*, 93(3):035007, 2021.

[94] E Arik, S Aune, D Autiero, K Barth, A Belov, B Beltrán, S Borghi, G Bourlis, F.S Boydag, H Bräuninger, J.M Carmona, S Cebrián, S.A Cetin, J.I Collar, T Dafni, M Davenport, L. Di Lella, O.B Dogan, C Eleftheriadis, N Elias, G Fanourakis, E Ferrer-Ribas, H Fischer, P Friedrich, J Franz, J Galán, T Geralis, I Giomataris, S Gninenko, H Gómez, R Hartmann, M Hasinoff, F.H Heinsius, I Hikmet, D.H.H Hoffmann, I.G Irastorza, J Jacoby, K Jakovčić, D Kang, K Königsmann, R Kotthaus, M Krčmar, K Kousouris, M Kuster, B Lakić, C Lasseur, A Liolios, A Ljubičić, G Lutz, G Luzón, D Miller, J Morales, T Niinikoski, A Nordt, A Ortiz, T Papaevangelou, M.J Pivovaroff, A Placci, G Raffelt, H Riege, A Rodríguez, J Ruz, I Savvidis, Y Semertzidis, P Serpico, R Soufli, L Stewart, K. van Bibber, J Villar, J Vogel, L Walckiers, and K Zioutas. Probing eV-scale axions with CAST. *Journal of Cosmology and Astroparticle Physics*, 2009(02):008–008, 2 2009.

[95] D. Aristizabal Sierra, V. De Romeri, L. J. Flores, and D. K. Papoulias. Light vector mediators facing XENON1T data. *Phys. Lett. B*, 809:135681, 2020.

[96] D. Aristizabal Sierra, V. De Romeri, L. J. Flores, and D. K. Papoulias. Impact of COHERENT measurements, cross section uncertainties and new interactions on the neutrino floor. *JCAP*, 01(01):055, 2022.

[97] D. Aristizabal Sierra, Valentina De Romeri, and N. Rojas. COHERENT analysis of neutrino generalized interactions. *Phys. Rev. D*, 98:075018, 2018.

[98] D. Aristizabal Sierra, Bhaskar Dutta, Shu Liao, and Louis E. Strigari. Coherent elastic neutrino-nucleus scattering in multi-ton scale dark matter experiments: Classification of vector and scalar interactions new physics signals. *JHEP*, 12:124, 2019.

[99] D. Aristizabal Sierra, M. Hirsch, and S. G. Kovalenko. Leptoquarks: Neutrino masses and accelerator phenomenology. *Phys. Rev. D*, 77:055011, 2008.

[100] D. Aristizabal Sierra, M. Hirsch, and S. G. Kovalenko. Leptoquarks: Neutrino masses and related accelerator signals. *Phys. Rev. D*, 77:055011, Mar 2008.

[101] D. Aristizabal Sierra, N. Rojas, and M. H. G. Tytgat. Neutrino non-standard interactions and dark matter searches with multi-ton scale detectors. *JHEP*, 03:197, 2018.

[102] E. Armengaud et al. Searching for low-mass dark matter particles with a massive Ge bolometer operated above-ground. *Phys. Rev. D*, 99(8):082003, 2019.

[103] W. W. Armstrong et al. ATLAS: Technical proposal for a general-purpose p p experiment at the Large Hadron Collider at CERN, 12 1994.

[104] Q. Arnaud et al. First germanium-based constraints on sub-MeV Dark Matter with the EDELWEISS experiment. *Phys. Rev. Lett.*, 125(14):141301, 2020.

[105] I. Arnquist et al. First Constraints from DAMIC-M on Sub-GeV Dark-Matter Particles Interacting with Electrons. *Phys. Rev. Lett.*, 130(17):171003, 2023.

[106] C. Arpesella et al. Direct Measurement of the Be-7 Solar Neutrino Flux with 192 Days of Borexino Data. *Phys. Rev. Lett.*, 101:091302, 2008.

[107] Shoji Asai et al. Exploring the Quantum Universe: Pathways to Innovation and Discovery in Particle Physics, 12 2023.

[108] W. B. Atwood et al. The Large Area Telescope on the Fermi Gamma-ray Space Telescope Mission. *Astrophys. J.*, 697:1071–1102, 2009.

[109] A. D. Avrorin et al. Baikal-GVD: status and prospects. *EPJ Web Conf.*, 191:01006, 2018.

[110] K. S. Babu, Garv Chauhan, and P. S. Bhupal Dev. Neutrino nonstandard interactions via light scalars in the Earth, Sun, supernovae, and the early Universe. *Phys. Rev. D*, 101(9):095029, 2020.

[111] K. S. Babu, Garv Chauhan, and P. S. Bhupal Dev. Neutrino nonstandard interactions via light scalars in the earth, sun, supernovae, and the early universe. *Phys. Rev. D*, 101:095029, May 2020.

[112] K. S. Babu, P. S. Bhupal Dev, and Sudip Jana. Probing neutrino mass models through resonances at neutrino telescopes. *Int. J. Mod. Phys. A*, 37(11n12):2230003, 2022.

[113] K. S. Babu, P. S. Bhupal Dev, Sudip Jana, and Anil Thapa. Non-Standard Interactions in Radiative Neutrino Mass Models. *JHEP*, 03:006, 2020.

[114] K. S. Babu, P. S. Bhupal Dev, Sudip Jana, and Anil Thapa. Unified framework for b-anomalies, muon $g-2$ and neutrino masses. *JHEP*, 03:179, 2021.

[115] Howard Baer, Ki-Young Choi, Jihn E. Kim, and Leszek Roszkowski. Dark matter production in the early Universe: beyond the thermal WIMP paradigm. *Phys. Rept.*, 555:1–60, 2015.

[116] John N. Bahcall and Aldo M. Serenelli. How Do Uncertainties in the Surface Chemical Composition of the Sun Affect the Predicted Solar Neutrino Fluxes? *The Astrophysical Journal*, 626(1):530, June 2005. Publisher: IOP Publishing.

[117] John N. Bahcall, Aldo M. Serenelli, and Sarbani Basu. New Solar Opacities, Abundances, Helioseismology, and Neutrino Fluxes. *The Astrophysical Journal*, 621(1):L85, 1 2005. Publisher: IOP Publishing.

[118] John N. Bahcall, Aldo M. Serenelli, and Sarbani Basu. New solar opacities, abundances, helioseismology, and neutrino fluxes. *Astrophys. J. Lett.*, 621:L85–L88, 2005.

[119] E. A. Baltz and L. Bergstrom. Detection of leptonic dark matter. *Phys. Rev. D*, 67:043516, 2003.

[120] Eduardo Banados et al. An 800-million-solar-mass black hole in a significantly neutral Universe at redshift 7.5. *Nature*, 553(7689):473–476, 2018.

[121] Heerak Banerjee, Bhaskar Dutta, and Sourov Roy. Probing Lμ-Lτ models with CEνNS: A new look at the combined COHERENT CsI and Ar data. *Phys. Rev. D*, 104(1):015015, 2021.

[122] Liron Barak et al. SENSEI: Direct-Detection Results on sub-GeV Dark Matter from a New Skipper-CCD. *Phys. Rev. Lett.*, 125(17):171802, 2020.

[123] R. Barbier et al. R-parity violating supersymmetry. *Phys. Rept.*, 420:1–202, 2005.

[124] J. M. Bardeen, J. R. Bond, N. Kaiser, and A. S. Szalay. The Statistics of Peaks of Gaussian Random Fields. *APJ*, 304:15, May 1986.

[125] Basabendu Barman, Subhaditya Bhattacharya, Sudhakantha Girmohanta, and Sahabub Jahedi. Effective Leptophilic WIMPs at the e+e- collider. *JHEP*, 04:146, 2022.

[126] J. Barranco, O. G. Miranda, and T. I. Rashba. Probing new physics with coherent neutrino scattering off nuclei. *JHEP*, 12:021, 2005.

[127] D. F. Bartlett and Stefan Lögl. Limits on an electromagnetic fifth force. *Phys. Rev. Lett.*, 61:2285–2287, 11 1988.

[128] Brian Batell, Maxim Pospelov, and Adam Ritz. Exploring portals to a hidden sector through fixed targets. *Phys. Rev. D*, 80:095024, 11 2009.

[129] G. Battistoni, A. Ferrari, T. Montaruli, and P. R. Sala. The atmospheric neutrino flux below 100-MeV: The FLUKA results. *Astropart. Phys.*, 23:526–534, 2005.

[130] Martin Bauer and Matthias Neubert. Minimal leptoquark explanation for the $R_{D^{(*)}}$, R_K, and $(g-2)_\mu$ anomalies. *Phys. Rev. Lett.*, 116:141802, Apr 2016.

[131] Daniel Baxter, Itay M. Bloch, Mariano Cababie, Nuria Castello, Luke Chaplinsky, A. Chavarria, Juan Carlos D'Olivo, Rouven Essig, Juan Estrada, and Fernandez-Moroni. Status and plans for Oscura: A Multi-kilogram Skipper-CCD Array for Direct-Detection of Dark Matter. In *Instrumentation Frontier: Photon Detectors*, 8 2020.

[132] John F. Beacom. The Diffuse Supernova Neutrino Background. *Ann. Rev. Nucl. Part. Sci.*, 60:439–462, 2010.

[133] A. G. Beda, V. B. Brudanin, V. G. Egorov, D. V. Medvedev, V. S. Pogosov, E. A. Shevchik, M. V. Shirchenko, A. S. Starostin, and I. V. Zhitnikov. Gemma experiment: The results of neutrino magnetic moment search. *Physics of Particles and Nuclei Letters*, 10(2):139–143, 3 2013.

[134] A. G. Beda, V. B. Brudanin, V. G. Egorov, D. V. Medvedev, M. V. Shirchenko, and A. S. Starostin. Gemma experiment: Three years of the search for the neutrino magnetic moment. *Physics of Particles and Nuclei Letters*, 7(6):406–409, 11 2010.

[135] Nicole F. Bell, Giorgio Busoni, Maura E. Ramirez-Quezada, Sandra Robles, and Michael Virgato. Improved treatment of dark matter capture in white dwarfs. *JCAP*, 10:083, 2021.

[136] Nicole F. Bell, Giorgio Busoni, and Sandra Robles. Heating up Neutron Stars with Inelastic Dark Matter. *JCAP*, 09:018, 2018.

[137] Nicole F. Bell, Giorgio Busoni, and Sandra Robles. Capture of Leptophilic Dark Matter in Neutron Stars. *JCAP*, 06:054, 2019.

[138] Nicole F. Bell, Matthew J. Dolan, and Sandra Robles. Searching for dark matter in the Sun using Hyper-Kamiokande. *JCAP*, 11:004, 2021.

[139] G. Bellini, J. Benziger, D. Bick, S. Bonetti, G. Bonfini, M. Buizza Avanzini, B. Caccianiga, L. Cadonati, F. Calaprice, C. Carraro, P. Cavalcante, A. Chavarria, D. D'Angelo, S. Davini, A. Derbin, A. Etenko, K. Fomenko, D. Franco, C. Galbiati, S. Gazzana, C. Ghiano, M. Giammarchi, M. Goeger-Neff, A. Goretti, L. Grandi, E. Guardincerri, S. Hardy, Aldo Ianni, Andrea Ianni, V. Kobychev, D. Korablev, G. Korga, Y. Koshio, D. Kryn, M. Laubenstein, T. Lewke, E. Litvinovich, B. Loer, F. Lombardi, P. Lombardi, L. Ludhova, I. Machulin, S. Manecki, W. Maneschg, G. Manuzio, Q. Meindl, E. Meroni, L. Miramonti, M. Misiaszek, D. Montanari, P. Mosteiro, V. Muratova, L. Oberauer, M. Obolensky, F. Ortica, M. Pallavicini, L. Papp, C. Peña Garay, L. Perasso, S. Perasso, A. Pocar, R. S. Raghavan, G. Ranucci, A. Razeto, A. Re, A. Romani, A. Sabelnikov, R. Saldanha, C. Salvo, S. Schönert, H. Simgen, M. Skorokhvatov, O. Smirnov, A. Sotnikov, S. Sukhotin, Y. Suvorov, R. Tartaglia, G. Testera, D. Vignaud, R. B. Vogelaar, F. von Feilitzsch, J. Winter, M. Wojcik, A. Wright, M. Wurm, J. Xu, O. Zaimidoroga, S. Zavatarelli, and G. Zuzel. Precision measurement of the ^{7}Be solar neutrino interaction rate in borexino. *Phys. Rev. Lett.*, 107:141302, 9 2011.

[140] G. W. Bennett, B. Bousquet, H. N. Brown, G. Bunce, R. M. Carey, P. Cushman, G. T. Danby, P. T. Debevec, M. Deile, H. Deng, W. Deninger, S. K. Dhawan, V. P. Druzhinin, L. Duong, E. Efstathiadis, F. J. M. Farley, G. V. Fedotovich, S. Giron, F. E. Gray, D. Grigoriev, M. Grosse-Perdekamp, A. Grossmann, M. F. Hare, D. W. Hertzog, X. Huang, V. W. Hughes, M. Iwasaki, K. Jungmann, D. Kawall, M. Kawamura, B. I. Khazin, J. Kindem, F. Krienen, I. Kronkvist, A. Lam, R. Larsen, Y. Y. Lee, I. Logashenko, R. McNabb, W. Meng, J. Mi, J. P. Miller, Y. Mizumachi, W. M. Morse, D. Nikas, C. J. G. Onderwater, Y. Orlov, C. S. Özben, J. M. Paley, Q. Peng, C. C. Polly, J. Pretz, R. Prigl, G. zu Putlitz, T. Qian, S. I. Redin, O. Rind, B. L. Roberts, N. Ryskulov, S. Sedykh, Y. K. Semertzidis, P. Shagin, Yu. M. Shatunov, E. P. Sichtermann, E. Solodov, M. Sossong, A. Steinmetz, L. R. Sulak, C. Timmermans, A. Trofimov, D. Urner, P. von Walter, D. Warburton, D. Winn, A. Yamamoto, and D. Zimmerman. Final report of the e821 muon anomalous magnetic moment measurement at bnl. *Phys. Rev. D*, 73:072003, 4 2006.

[141] Asher Berlin, Joshua W. Foster, Dan Hooper, and Gordan Krnjaic. dSphobic Dark Matter, 4 2025.

[142] R. Bernabei et al. Investigating electron interacting dark matter. *Phys. Rev. D*, 77:023506, 2008.

[143] Nicolás Bernal, Justo Martín-Albo, and Sergio Palomares-Ruiz. A novel way of constraining WIMPs annihilations in the Sun: MeV neutrinos. *JCAP*, 08:011, 2013.

[144] Gianfranco Bertone, Marco Cirelli, Alessandro Strumia, and Marco Taoso. Gamma-ray and radio tests of the e+e- excess from DM annihilations. *JCAP*, 03:009, 2009.

[145] Gianfranco Bertone and Malcolm Fairbairn. Compact Stars as Dark Matter Probes. *Phys. Rev. D*, 77:043515, 2008.

[146] Gianfranco Bertone, Dan Hooper, and Joseph Silk. Particle dark matter: Evidence, candidates and constraints. *Phys. Rept.*, 405:279–390, 2005.

[147] Enrico Bertuzzo, Frank F. Deppisch, Suchita Kulkarni, Yuber F. Perez Gonzalez, and Renata Zukanovich Funchal. Dark Matter and Exotic Neutrino Interactions in Direct Detection Searches. *JHEP*, 04:073, 2017.

[148] Enrico Bertuzzo, Giovanni Grilli di Cortona, and Lucas Magno D. Ramos. Probing light vector mediators with coherent scattering at future facilities. *JHEP*, 06:075, 2022.

[149] Sulagna Bhattacharya, Andrew L. Miller, and Anupam Ray. Continuous gravitational waves: A new window to look for heavy nonannihilating dark matter. *Phys. Rev. D*, 110:043006, 2024.

[150] J. Billard, L. Strigari, and E. Figueroa-Feliciano. Implication of neutrino backgrounds on the reach of next generation dark matter direct detection experiments. *Phys. Rev. D*, 89(2):023524, 2014.

[151] Julien Billard, Joseph Johnston, and Bradley J. Kavanagh. Prospects for exploring New Physics in Coherent Elastic Neutrino-Nucleus Scattering. *JCAP*, 11:016, 2018.

[152] S. Bilmiş, I. Turan, T. M. Aliev, M. Deniz, L. Singh, and H. T. Wong. Constraints on dark photon from neutrino-electron scattering experiments. *Phys. Rev. D*, 92:033009, 8 2015.

[153] R. M. Bionta et al. Observation of a Neutrino Burst in Coincidence with Supernova SN 1987a in the Large Magellanic Cloud. *Phys. Rev. Lett.*, 58:1494, 1987.

[154] Ingolf Bischer and Werner Rodejohann. General neutrino interactions from an effective field theory perspective. *Nucl. Phys. B*, 947:114746, 2019.

[155] Ingolf Bischer, Werner Rodejohann, and Xun-Jie Xu. Loop-induced neutrino non-standard interactions. *Journal of High Energy Physics*, 2018(10):96, October 2018.

[156] James D. Bjorken, Rouven Essig, Philip Schuster, and Natalia Toro. New fixed-target experiments to search for dark gauge forces. *Phys. Rev. D*, 80:075018, 10 2009.

[157] G. R. Blumenthal, S. M. Faber, R. Flores, and J. R. Primack. Contraction of Dark Matter Galactic Halos Due to Baryonic Infall. *APJ*, 301:27, February 1986.

[158] C. Bœhm, D.G. Cerdeño, P.A.N. Machado, A. Olivares-Del Campo, and E. Reid. How high is the neutrino floor? *Journal of Cosmology and Astroparticle Physics*, 2019(01):043–043, 1 2019.

[159] Céline Bœhm, David G. Cerdeño, Malcolm Fairbairn, Pedro A. N. Machado, and Aaron C. Vincent. Light new physics in xenon1t. *Phys. Rev. D*, 102:115013, 12 2020.

[160] Celine Boehm, David G. Cerdeno, Malcolm Fairbairn, Pedro A. N. Machado, and Aaron C. Vincent. Light new physics in XENON1T. *Phys. Rev. D*, 102:115013, 2020.

[161] Celine Boehm, David G. Cerdeno, Malcolm Fairbairn, Pedro A. N. Machado, and Aaron C. Vincent. Light new physics in XENON1T. *Phys. Rev. D*, 102:115013, 2020.

[162] Akos Bogdan et al. Evidence for heavy-seed origin of early supermassive black holes from a $z \approx 10$ X-ray quasar. *Nature Astron.*, 8(1):126–133, 2024.

[163] Debasish Borah, Nayan Das, Sahabub Jahedi, and Bhavya Thacker. Collider and CMB complementarity of leptophilic dark matter with light Dirac neutrinos. *JHEP*, 01:074, 2025.

[164] M. Bordag, U. Mohideen, and V.M. Mostepanenko. New developments in the casimir effect. *Physics Reports*, 353(1):1–205, 2001.

[165] Debajit Bose, Tarak Nath Maity, and Tirtha Sankar Ray. Solar constraints on captured electrophilic dark matter. *Phys. Rev. D*, 105(12):123013, 2022.

[166] Debajit Bose, Rohan Pramanick, and Tirtha Sankar Ray. Neutrinos from captured dark matter in galactic stars, 5 2024.

[167] Joseph Bramante, Andrew Buchanan, Alan Goodman, and Eesha Lodhi. Terrestrial and Martian Heat Flow Limits on Dark Matter. *Phys. Rev. D*, 101(4):043001, 2020.

[168] Joseph Bramante, Jason Kumar, Gopolang Mohlabeng, Nirmal Raj, and Ningqiang Song. Light dark matter accumulating in planets: Nuclear scattering. *Phys. Rev. D*, 108(6):063022, 2023.

[169] Volker Bromm, Paolo S. Coppi, and Richard B. Larson. The formation of the first stars. I. The Primordial star forming cloud. *Astrophys. J.*, 564:23–51, 2002.

[170] Giorgio Busoni. Capture of Dark Matter in Neutron Stars. *Moscow Univ. Phys. Bull.*, 77(2):301–305, 2022.

[171] M. Cadeddu, N. Cargioli, F. Dordei, C. Giunti, Y. F. Li, E. Picciau, and Y. Y. Zhang. Constraints on light vector mediators through coherent elastic neutrino nucleus scattering data from COHERENT. *JHEP*, 01:116, 2021.

[172] B. Caiffi et al. Combined diffuse and point source search with km3net/arca and antares neutrino telescopes. Poster, 2024.

[173] Sean M. Carroll, William H. Press, and Edwin L. Turner. The cosmological constant. *Annual Review of Astronomy and Astrophysics*, 30:499–542, January 1992.

[174] David G. Cerdeño, Malcolm Fairbairn, Thomas Jubb, Pedro A. N. Machado, Aaron C. Vincent, and Céline Bœhm. Physics from solar neutrinos in dark matter direct detection experiments. *JHEP*, 05:118, 2016. [Erratum: JHEP 09, 048 (2016)].

[175] David G. Cerdeño, Malcolm Fairbairn, Thomas Jubb, Pedro A. N. Machado, Aaron C. Vincent, and Céline Bœhm. Physics from solar neutrinos in dark matter direct detection experiments. *Journal of High Energy Physics*, 2016(5):118, 5 2016.

[176] M. Cermeño and M. Angeles Pérez-García. Gamma rays from dark mediators in white dwarfs. *Phys. Rev. D*, 98(6):063002, 2018.

[177] Jae Hyeok Chang, Rouven Essig, and Samuel D. McDermott. Revisiting Supernova 1987A Constraints on Dark Photons. *JHEP*, 01:107, 2017.

[178] Bhavesh Chauhan and Subhendra Mohanty. Constraints on leptophilic light dark matter from internal heat flux of Earth. *Phys. Rev. D*, 94(3):035024, 2016.

[179] A. E. Chavarria et al. Measurement of the ionization produced by sub-keV silicon nuclear recoils in a CCD dark matter detector. *Phys. Rev. D*, 94(8):082007, 2016.

[180] Chuan-Ren Chen and Fuminobu Takahashi. Cosmic rays from Leptonic Dark Matter. *JCAP*, 02:004, 2009.

[181] Jiunn-Wei Chen, Hsin-Chang Chi, C.-P. Liu, and Chih-Pan Wu. Low-energy electronic recoil in xenon detectors by solar neutrinos. *Physics Letters B*, 774:656–661, 2017.

[182] Yu-Xuan Chen, Lei Zu, Zi-Qing Xia, Yue-Lin Sming Tsai, and Yi-Zhong Fan. Multi-frequency test of dark matter annihilation into long-lived particles in Sirius. *JCAP*, 08:036, 2023.

[183] Chen Cheng et al. Search for Light Dark Matter-Electron Scatterings in the PandaX-II Experiment. *Phys. Rev. Lett.*, 126(21):211803, 2021.

[184] Eung Jin Chun, Jong-Chul Park, and Stefano Scopel. Dirac gaugino as leptophilic dark matter. *JCAP*, 02:015, 2010.

[185] Paolo Ciafaloni, Denis Comelli, Antonio Riotto, Filippo Sala, Alessandro Strumia, and Alfredo Urbano. Weak corrections are relevant for dark matter indirect detection. *Journal of Cosmology and Astroparticle Physics*, 2011(03):019, 3 2011.

[186] Paolo Ciafaloni, Denis Comelli, Antonio Riotto, Filippo Sala, Alessandro Strumia, and Alfredo Urbano. Weak Corrections are Relevant for Dark Matter Indirect Detection. *JCAP*, 03:019, 2011.

[187] Marco Cirelli, Gennaro Corcella, Andi Hektor, Gert Hutsi, Mario Kadastik, Paolo Panci, Martti Raidal, Filippo Sala, and Alessandro Strumia. PPPC 4 DM ID: A Poor Particle Physicist Cookbook for Dark Matter Indirect Detection. *JCAP*, 03:051, 2011. [Erratum: JCAP 10, E01 (2012)].

[188] Marco Cirelli, Gennaro Corcella, Andi Hektor, Gert Hütsi, Mario Kadastik, Paolo Panci, Martti Raidal, Filippo Sala, and Alessandro Strumia. Pppc 4 dm id: a poor particle physicist cookbook for dark matter indirect detection. *Journal of Cosmology and Astroparticle Physics*, 2011(03):051, 3 2011.

[189] Marco Cirelli, Mario Kadastik, Martti Raidal, and Alessandro Strumia. Model-independent implications of the e+-, anti-proton cosmic ray spectra on properties of Dark Matter. *Nucl. Phys. B*, 813:1–21, 2009. [Addendum: Nucl.Phys.B 873, 530–533 (2013)].

[190] J Coelho. Latest results from km3net. In *XXXI International Conference on Neutrino Physics and Astrophysics*, 6 2024. on behalf of the KM3NeT Collaboration.

[191] Timothy Cohen and Kathryn M. Zurek. Leptophilic Dark Matter from the Lepton Asymmetry. *Phys. Rev. Lett.*, 104:101301, 2010.

[192] ATLAS Collaboration. Search for excited τ-leptons and leptoquarks in the final state with τ-leptons and jets in pp collisions at $\sqrt{s} = 13$ tev with the atlas detector, 2023.

[193] CONUS Collaboration, H. Bonet, A. Bonhomme, C. Buck, K. Fülber, J. Hakenmüller, G. Heusser, T. Hugle, M. Lindner, W. Maneschg, T. Rink, H. Strecker, and R. Wink. Novel constraints on neutrino physics beyond the standard model from the conus experiment, 2021.

[194] DARWIN Collaboration. DARWIN - a next-generation liquid xenon observatory for dark matter and neutrino physics. Ghent, Belgum, 7 2019.

[195] J. I. Collar, A. R. L. Kavner, and C. M. Lewis. Germanium response to sub-keV nuclear recoils: a multipronged experimental characterization. *Phys. Rev. D*, 103(12):122003, 2021.

[196] Pilar Coloma, Peter B. Denton, M. C. Gonzalez-Garcia, Michele Maltoni, and Thomas Schwetz. Curtailing the Dark Side in Non-Standard Neutrino Interactions. *JHEP*, 04:116, 2017.

[197] Jan Conrad, Luca Latronico, Francesco Longo, and Benoit Lott. Fermi Gamma-ray Space Telescope sees first light. *CERN Cour.*, 48N9:13–15, 2008.

[198] Michael Crisler, Rouven Essig, Juan Estrada, Guillermo Fernandez, Javier Tiffenberg, Miguel Sofo haro, Tomer Volansky, and Tien-Tien Yu. SENSEI: First Direct-Detection Constraints on sub-GeV Dark Matter from a Surface Run. *Phys. Rev. Lett.*, 121(6):061803, 2018.

[199] Djuna Croon, Gilly Elor, Rebecca K. Leane, and Samuel D. McDermott. Supernova Muons: New Constraints on Z' Bosons, Axions and ALPs. *Journal of High Energy Physics*, 2021(1):107, 1 2021.

[200] D.A. Cusano. Radiative recombination from gaas directly excited by electron beams. *Solid State Communications*, 2(11):353–358, 1964.

[201] Basudeb Dasgupta, Aritra Gupta, and Anupam Ray. Dark matter capture in celestial objects: Improved treatment of multiple scattering and updated constraints from white dwarfs. *JCAP*, 08:018, 2019.

[202] Tansu Daylan, Douglas P. Finkbeiner, Dan Hooper, Tim Linden, Stephen K. N. Portillo, Nicholas L. Rodd, and Tracy R. Slatyer. The Characterization of the Gamma-Ray Signal from the Central Milky Way: A Case for Annihilating Dark Matter. *Phys. Dark Univ.*, 12:1–23, 2016.

[203] André de Gouvêa and Kevin J. Kelly. Non-standard neutrino interactions at DUNE. *Nucl. Phys. B*, 908:318–335, 2016.

[204] Leon M. G. de la Vega, L. J. Flores, Newton Nath, and Eduardo Peinado. Complementarity between dark matter direct searches and CEνNS experiments in U(1)' models. *JHEP*, 09:146, 2021.

[205] M. Della Negra et al. CMS: The Compact Muon Solenoid: Letter of intent for a general purpose detector at the LHC, 10 1992.

[206] Patrick deNiverville, Maxim Pospelov, and Adam Ritz. Light new physics in coherent neutrino-nucleus scattering experiments. *Phys. Rev. D*, 92(9):095005, 2015.

[207] M. Deniz, S. T. Lin, V. Singh, J. Li, H. T. Wong, S. Bilmis, C. Y. Chang, H. M. Chang, W. C. Chang, C. P. Chen, M. H. Chou, K. J. Dong, J. M. Fang, C. H. Hu, G. C. Jon, W. S. Kuo, W. P. Lai, F. S. Lee, S. C. Lee, H. B. Li, H. Y. Liao, C. W. Lin, F. K. Lin, S. K. Lin, Y. Liu, J. F. Qiu, M. Serin, H. Y. Sheng, L. Singh, R. F. Su, W. S. Tong, J. J. Wang, P. L. Wang, S. C. Wu, S. W. Yang, C. X. Yu, Q. Yue, M. Zeyrek, D. X. Zhao, Z. Y. Zhou, Y. F. Zhu, and B. A. Zhuang. Measurement of $\overline{\nu}_{\rm e}$-electron scattering cross section with a csi(tl) scintillating crystal array at the kuo-sheng nuclear power reactor. *Phys. Rev. D*, 81:072001, 4 2010.

[208] James B. Dent, Francesc Ferrer, and Lawrence M. Krauss. Constraints on Light Hidden Sector Gauge Bosons from Supernova Cooling. 1 2012.

[209] Peter B. Denton, Yasaman Farzan, and Ian M. Shoemaker. A plan to rule out large non-standard neutrino interactions after coherent data, 2018.

[210] Peter B. Denton, Yasaman Farzan, and Ian M. Shoemaker. Testing large non-standard neutrino interactions with arbitrary mediator mass after COHERENT data. *JHEP*, 07:037, 2018.

[211] Peter B. Denton and Julia Gehrlein. A Statistical Analysis of the COHERENT Data and Applications to New Physics. *JHEP*, 04:266, 2021.

[212] S. Desai et al. Search for dark matter WIMPs using upward through-going muons in Super-Kamiokande. *Phys. Rev. D*, 70:083523, 2004. [Erratum: Phys.Rev.D 70, 109901 (2004)].

[213] Francesco D'Eugenio, Alex J. Cameron, Jan Scholtz, Stefano Carniani, Chris J. Willott, Emma Curtis-Lake, Andrew J. Bunker, Eleonora Parlanti, Roberto Maiolino, Christopher N. A. Willmer, Peter Jakobsen, Brant E. Robertson, Benjamin D. Johnson, Sandro Tacchella, Phillip A. Cargile, Tim Rawle, Santiago Arribas, Jacopo Chevallard, Mirko Curti, Eiichi Egami, Daniel J. Eisenstein, Nimisha Kumari, Tobias J. Looser, Marcia J. Rieke, Bruno Rodríguez Del Pino, Aayush Saxena, Hannah Übler, Giacomo Venturi, Joris Witstok, William M. Baker, Rachana Bhatawdekar, Nina Bonaventura, Kristan Boyett, Stéphane Charlot, A. Lola Danhaive, Kevin N. Hainline, Ryan Hausen, Jakob M. Helton, Xihan Ji, Zhiyuan Ji, Gareth C. Jones, Ignas Joudžbalis, Michael V. Maseda, Pablo G. Pérez-González, Michele Perna, Dávid Puskás, Irene Shivaei, Maddie S. Silcock, Charlotte Simmonds, Renske Smit, Fengwu Sun, Natalia C. Villanueva, Christina C. Williams, and Yongda Zhu. Jades data release 3 – nirspec/msa spectroscopy for 4,000 galaxies in the goods fields, 2024.

[214] Bhupal Dev, K. S. Babu, Peter Denton, Pedro Machado, Carlos A. Argüelles, Joshua L. Barrow, Sabya Sachi Chatterjee, Mu-Chun Chen, André de Gouvêa, Bhaskar Dutta, Dorival Gonçalves, Tao Han, Matheus Hostert, Sudip Jana, Kevin J. Kelly, Shirley Weishi Li, Ivan Martinez-Soler, Poonam Mehta, Irina Mocioiu, Yuber F. Perez-Gonzalez, Jordi Salvado, Ian Shoemaker, Michele Tammaro, Anil Thapa, Jessica Turner, and Xun-Jie Xu. Neutrino non-standard interactions: A status report. *SciPost Physics Proceedings*, (2):001, 12 2019.

[215] P. S. Bhupal Dev, K. S. Babu, Peter B. Denton, Pedro A. N. Machado, Carlos A. Argüelles, Joshua L. Barrow, Sabya Sachi Chatterjee, Mu-Chun Chen, André de Gouvêa, Bhaskar Dutta, Dorival Gonçalves, Tao Han, Matheus Hostert, Sudip Jana, Kevin J. Kelly, Shirley Weishi Li, Ivan Martinez-Soler, Poonam Mehta, Irina Mocioiu, Yuber F. Perez-Gonzalez, Jordi Salvado, Ian M. Shoemaker, Michele Tammaro, Anil Thapa, Jessica Turner, and Xun-Jie Xu. Neutrino non-standard interactions: A status report. *SciPost Phys. Proc.*, page 001, 2019.

[216] Bastian Diaz, Martin Schmaltz, and Yi-Ming Zhong. The leptoquark Hunter's guide: Pair production. *JHEP*, 10:097, 2017.

[217] Xuheng Ding, Masafusa Onoue, John D. Silverman, Yoshiki Matsuoka, Takuma Izumi, Michael A. Strauss, Knud Jahnke, Camryn L. Phillips, Junyao Li, Marta Volonteri, Zoltan Haiman, Irham Taufik Andika, Kentaro Aoki, Shunsuke Baba, Rebekka Bieri, Sarah E. I. Bosman, Connor Bottrell, Anna-Christina Eilers, Seiji Fujimoto, Melanie Habouzit, Masatoshi Imanishi, Kohei Inayoshi, Kazushi Iwasawa, Nobunari Kashikawa, Toshihiro Kawaguchi, Kotaro Kohno, Chien-Hsiu Lee, Alessandro Lupi, Jianwei Lyu, Tohru Nagao, Roderik Overzier, Jan-Torge Schindler, Malte Schramm, Kazuhiro Shimasaku, Yoshiki Toba, Benny Trakhtenbrot, Maxime Trebitsch, Tommaso Treu, Hideki Umehata, Bram P. Venemans, Marianne Vestergaard, Fabian Walter, Feige Wang, and Jinyi Yang. Detection of stellar light from quasar host galaxies at redshifts above 6. *Nature*, 621(7977):51–55, September 2023.

[218] Tadayoshi Doke, Akira Hitachi, Jun Kikuchi, Kimiaki Masuda, Hiroyuki Okada, and Eido Shibamura. Absolute scintillation yields in liquid argon and xenon for various particles. *Japanese Journal of Applied Physics*, 41(Part 1, No. 3A):1538–1545, 3 2002.

[219] I. Doršner, S. Fajfer, A. Greljo, J.F. Kamenik, and N. Košnik. Physics of leptoquarks in precision experiments and at particle colliders. *Physics Reports*, 641:1–68, 2016. Physics of leptoquarks in precision experiments and at particle colliders.

[220] Ilja Doršner, Svjetlana Fajfer, and Olcyr Sumensari. Muon g-2 and scalar leptoquark mixing. *Journal of High Energy Physics*, 2020(6):89, June 2020.

[221] Ilja Doršner, Svjetlana Fajfer, and Nejc Košnik. Leptoquark mechanism of neutrino masses within the grand unification framework. *Eur. Phys. J. C*, 77(6):417, 2017.

[222] Jeff A. Dror, Gilly Elor, Robert McGehee, and Tien-Tien Yu. Absorption of sub-MeV fermionic dark matter by electron targets. *Phys. Rev. D*, 103(3):035001, 2021. [Erratum: Phys.Rev.D 105, 119903 (2022)].

[223] A. Drukier and Leo Stodolsky. Principles and Applications of a Neutral Current Detector for Neutrino Physics and Astronomy. *Phys. Rev. D*, 30:2295, 1984.

[224] Mario Dunsch, Jan Soedingrekso, Alexander Sandrock, Max Meier, Thorben Menne, and Wolfgang Rhode. Recent improvements for the lepton propagator proposal. *Computer Physics Communications*, 242:132–144, 2019.

[225] Bhaskar Dutta, Sumit Ghosh, Kevin J. Kelly, Tianjun Li, Adrian Thompson, and Ankur Verma. Non-standard neutrino interactions mediated by a light scalar at DUNE. *JHEP*, 07:213, 2024.

[226] T. A. Dzhatdoev. The blazar PKS 0605-085 as the origin of the KM3-230213A ultra high energy neutrino event, 2 2025.

[227] A. M. Dziewonski and D. L. Anderson. Preliminary reference earth model. *Phys. Earth Planet. Interiors*, 25:297–356, 1981.

[228] EDELWEISS Collaboration, Q. Arnaud, E. Armengaud, C. Augier, A. Benoît, L. Bergé, J. Billard, A. Broniatowski, P. Camus, A. Cazes, M. Chapellier, F. Charlieux, M. De Jésus, L. Dumoulin, K. Eitel, E. Elkhoury, J.-B. Fillipini, D. Filosofov, J. Gascon, A. Giuliani, M. Gros, Y. Jin, A. Juillard, M. Kleifges, H. Lattaud, S. Marnieros, D. Misiak, X.-F. Navick, C. Nones, E. Olivieri, C. Oriol, P. Pari, B. Paul, D. Poda, S. Rozov, T. Salagnac, V. Sanglard, B. Siebenborn, L. Vagneron, M. Weber, E. Yakushev, and A. Zolotarova. First Germanium-Based Constraints on Sub-MeV Dark Matter with the EDELWEISS Experiment. *Physical Review Letters*, 125(14):141301, 10 2020. Publisher: American Physical Society.

[229] Daniel J. Eisenstein et al. Overview of the JWST Advanced Deep Extragalactic Survey (JADES). *arXiv e-prints*, page arXiv:2306.02465, June 2023.

[230] Rouven Essig, Marivi Fernandez-Serra, Jeremy Mardon, Adrian Soto, Tomer Volansky, and Tien-Tien Yu. Direct Detection of sub-GeV Dark Matter with Semiconductor Targets. *JHEP*, 05:046, 2016.

[231] Rouven Essig, Roni Harnik, Jared Kaplan, and Natalia Toro. Discovering new light states at neutrino experiments. *Phys. Rev. D*, 82:113008, 12 2010.

[232] Rouven Essig, Aaron Manalaysay, Jeremy Mardon, Peter Sorensen, and Tomer Volansky. First Direct Detection Limits on Sub-GeV Dark Matter from XENON10. *Physical Review Letters*, 109(2):021301, 10 2012. Publisher: American Physical Society.

[233] Rouven Essig, Jeremy Mardon, and Tomer Volansky. Direct Detection of Sub-GeV Dark Matter. *Phys. Rev. D*, 85:076007, 2012.

[234] Rouven Essig, Philip Schuster, and Natalia Toro. Probing dark forces and light hidden sectors at low-energy e^+e^- colliders. *Phys. Rev. D*, 80:015003, 7 2009.

[235] Rouven Essig, Mukul Sholapurkar, and Tien-Tien Yu. Solar neutrinos as a signal and background in direct-detection experiments searching for sub-GeV dark matter with electron recoils. *Physical Review D*, 97(9):095029, 5 2018. Publisher: American Physical Society.

[236] Ke Fang, Francis Halzen, and Dan Hooper. Cascaded Gamma-ray Emission Associated with the KM3NeT Ultra-High-Energy Event KM3-230213A, 2 2025.

[237] Yasaman Farzan and Julian Heeck. Neutrinophilic nonstandard interactions. *Phys. Rev. D*, 94(5):053010, 2016.

[238] Yasaman Farzan, Manfred Lindner, Werner Rodejohann, and Xun-Jie Xu. Probing neutrino coupling to a light scalar with coherent neutrino scattering. *JHEP*, 05:066, 2018.

[239] Baruch Feldman and Ann E Nelson. New regions for a chameleon to hide. *Journal of High Energy Physics*, 2006(08):002–002, 8 2006.

[240] G. Fernandez-Moroni, R. Harnik, P. A. N. Machado, I. Martinez-Soler, Y. F. Perez-Gonzalez, D. Rodrigues, and S. Rosauro-Alcaraz. The physics potential of a reactor neutrino experiment with Skipper-CCDs: Searching for new physics with light mediators. *arXiv:2108.07310 [hep-ex, physics:hep-ph]*, 8 2021. arXiv: 2108.07310.

[241] Pavel Fileviez Perez, Clara Murgui, and Alexis D. Plascencia. Leptoquarks and matter unification: Flavor anomalies and the muon g-2. *Phys. Rev. D*, 104(3):035041, 2021.

[242] D. J. Fixsen, E. S. Cheng, J. M. Gales, J. C. Mather, R. A. Shafer, and E. L. Wright. The cosmic microwave background spectrum from the FullCOBEFIRAS data set. *The Astrophysical Journal*, 473(2):576–587, 12 1996.

[243] L. J. Flores, Newton Nath, and Eduardo Peinado. Non-standard neutrino interactions in U(1)' model after COHERENT data. *JHEP*, 06:045, 2020.

[244] J. A. Formaggio and G. P. Zeller. From eV to EeV: Neutrino Cross Sections Across Energy Scales. *Rev. Mod. Phys.*, 84:1307–1341, 2012.

[245] Patrick J. Fox and Erich Poppitz. Leptophilic Dark Matter. *Phys. Rev. D*, 79:083528, 2009.

[246] Katarzyna Frankiewicz. *Indirect Search for Dark Matter with the Super-Kamiokande Detector*. PhD thesis, Warsaw, Inst. Nucl. Studies, 2018.

[247] Daniel Z. Freedman. Coherent Neutrino Nucleus Scattering as a Probe of the Weak Neutral Current. *Phys. Rev. D*, 9:1389–1392, 1974.

[248] Katherine Freese. Can Scalar Neutrinos Or Massive Dirac Neutrinos Be the Missing Mass? *Phys. Lett. B*, 167:295–300, 1986.

[249] Katherine Freese, Peter Bodenheimer, Douglas Spolyar, and Paolo Gondolo. Stellar Structure of Dark Stars: a first phase of Stellar Evolution due to Dark Matter Annihilation. *Astrophys. J. Lett.*, 685:L101–L112, 2008.

[250] Katherine Freese, Peter Bodenheimer, Douglas Spolyar, and Paolo Gondolo. Stellar structure of dark stars: A first phase of stellar evolution resulting from dark matter annihilation. *The Astrophysical Journal*, 685(2):L101, 9 2008.

[251] Katherine Freese, Paolo Gondolo, J. A. Sellwood, and Douglas Spolyar. Dark Matter Densities during the Formation of the First Stars and in Dark Stars. *Astrophys. J.*, 693:1563–1569, 2009.

[252] Katherine Freese, Cosmin Ilie, Douglas Spolyar, Monica Valluri, and Peter Bodenheimer. Supermassive dark stars: Detectable in jwst. *The Astrophysical Journal*, 716(2):1397, 6 2010.

[253] Katherine Freese, Tanja Rindler-Daller, Douglas Spolyar, and Monica Valluri. Dark Stars: A Review. *Rept. Prog. Phys.*, 79(6):066902, 2016.

[254] Katherine Freese, Tanja Rindler-Daller, Douglas Spolyar, and Monica Valluri. Dark stars: a review. *Reports on Progress in Physics*, 79(6):066902, may 2016.

[255] Katherine Freese, Douglas Spolyar, and Anthony Aguirre. Dark matter capture in the first stars: a power source and limit on stellar mass. *Journal of Cosmology and Astroparticle Physics*, 2008(11):014, nov 2008.

[256] George M. French and Marc Sher. Monoenergetic neutrinos from WIMP annihilation in Jupiter. *Phys. Rev. D*, 106(11):115037, 2022.

[257] Alexander Friedland, Cecilia Lunardini, and Carlos Pena-Garay. Solar neutrinos as probes of neutrino matter interactions. *Phys. Lett. B*, 594:347, 2004.

[258] Harald Fritzsch and Peter Minkowski. Unified Interactions of Leptons and Hadrons. *Annals Phys.*, 93:193–266, 1975.

[259] Y. Fukuda et al. Evidence for oscillation of atmospheric neutrinos. *Phys. Rev. Lett.*, 81:1562–1567, 1998.

[260] Y. Fukuda et al. The Super-Kamiokande detector. *Nucl. Instrum. Meth. A*, 501:418–462, 2003.

[261] T. K. Gaisser and M. Honda. Flux of atmospheric neutrinos. *Ann. Rev. Nucl. Part. Sci.*, 52:153–199, 2002.

[262] Thomas K. Gaisser, Ralph Engel, and Elisa Resconi. *Cosmic Rays and Particle Physics: 2nd Edition.* Cambridge University Press, 6 2016.

[263] C. Galbiati, C. Arpesella, H. O. Back, M. Balata, G. Bellini, J. Benziger, S. Bonetti, A. Brigatti, B. Caccianiga, L. Cadonati, F. Calaprice, C. Carraro, G. Cecchet, A. Chavarria, M. Chen, F. Dalnoki-Veress, D. D'Angelo, A. de Bari, A. de Bellefon, H. de Kerret, A. Derbin, M. Deutsch, A. di Credico, G. di Pietro, R. Eisenstein, F. Elisei, A. Etenko, R. Fernholz, K. Fomenko, R. Ford, D. Franco, B. Freudiger, F. Gatti, S. Gazzana, M. Giammarchi, D. Giugni, M. Goeger-Neff, T. Goldbrunner, A. Goretti, C. Grieb, C. Hagner, W. Hampel, E. Harding, S. Hardy, F. X. Hartman, T. Hertrich, G. Heusser, Aldo Ianni, Andrea Ianni, M. Joyce, J. Kiko, T. Kirsten, V. Kobychev, G. Korga, G. Korschinek, D. Kryn, V. Lagomarsino, P. Lamarche, M. Laubenstein, C. Lendvai, M. Leung, T. Lewke, E. Litvinovich, B. Loer, P. Lombardi, L. Ludhova, I. Machulin, S. Malvezzi, S. Manecki, J. Maneira, W. Maneschg, I. Manno, D. Manuzio, G. Manuzio, A. Martemianov, F. Masetti, U. Mazzucato, K. McCarty, D. McKinsey, Q. Meindl, E. Meroni, L. Miramonti, M. Misiaszek, D. Montanari, M. E. Monzani, V. Muratova, P. Musico, H. Neder, A. Nelson, L. Niedermeier, L. Oberauer, M. Obolensky, M. Orsini, F. Ortica, M. Pallavicini, L. Papp, S. Parmeggiano, L. Perasso, A. Pocar, R. S. Raghavan, G. Ranucci, W. Rau, A. Razeto, E. Resconi, P. Risso, A. Romani, D. Rountree, A. Sabelnikov, R. Saldanha, C. Salvo, D. Schimizzi, S. Schönert, T. Shutt, H. Simgen, M. Skorokhvatov, O. Smirnov, A. Sonnenschein, A. Sotnikov, S. Sukhotin, Y. Suvorov, R. Tartaglia, G. Testera, D. Vignaud, S. Vitale, R. B. Vogelaar, F. von Feilitzsch, R. von Hentig, T. von Hentig, M. Wojcik, M. Wurm, O. Zaimidoroga, S. Zavatarelli, and G. Zuzel. New results on solar neutrino fluxes from 192 days of Borexino data. *Journal of Physics: Conference Series*, 136(2):022001, November 2008. Publisher: IOP Publishing.

[264] Galileo Galilei. *Dialogue Concerning the Two Chief World Systems*. University of California Press, 1632 (1967).

[265] Raghuveer Garani and Sergio Palomares-Ruiz. Evaporation of dark matter from celestial bodies. *JCAP*, 05(05):042, 2022.

[266] Shao-Feng Ge and Stephen J. Parke. Scalar nonstandard interactions in neutrino oscillation. *Phys. Rev. Lett.*, 122:211801, 5 2019.

[267] Shao-Feng Ge and Stephen J. Parke. Scalar Nonstandard Interactions in Neutrino Oscillation. *Phys. Rev. Lett.*, 122(21):211801, 2019.

[268] Graciela B. Gelmini, Volodymyr Takhistov, and Samuel J. Witte. Casting a Wide Signal Net with Future Direct Dark Matter Detection Experiments. *JCAP*, 07:009, 2018. [Erratum: JCAP 02, E02 (2019)].

[269] H. Georgi and S. L. Glashow. Unity of All Elementary Particle Forces. *Phys. Rev. Lett.*, 32:438–441, 1974.

[270] Howard Georgi. The State of the Art—Gauge Theories. *AIP Conf. Proc.*, 23:575–582, 1975.

[271] Valerio Gherardi, David Marzocca, and Elena Venturini. Low-energy phenomenology of scalar leptoquarks at one-loop accuracy. *Journal of High Energy Physics*, 2021(1):138, January 2021.

[272] Graham K Giovanetti. Searching for dark matter with liquid argon. In *Cosmic Frontier: Dark Matter*, 8 2020.

[273] C. Giunti. General COHERENT constraints on neutrino nonstandard interactions. *Phys. Rev. D*, 101(3):035039, 2020.

[274] I. Goldman and S. Nussinov. Weakly Interacting Massive Particles and Neutron Stars. *Phys. Rev. D*, 40:3221–3230, 1989.

[275] Nicolas M. Gonzalez. Searches for primary photons and neutrinos with the Pierre Auger Observatory. In *58th Rencontres de Moriond on Very High Energy Phenomena in the Universe*, 1 2025.

[276] M. C. Gonzalez-Garcia and Michele Maltoni. Determination of matter potential from global analysis of neutrino oscillation data. *JHEP*, 09:152, 2013.

[277] M. C. Gonzalez-Garcia, Michele Maltoni, Yuber F. Perez-Gonzalez, and Renata Zukanovich Funchal. Neutrino Discovery Limit of Dark Matter Direct Detection Experiments in the Presence of Non-Standard Interactions. *JHEP*, 07:019, 2018.

[278] Andrew Gould. Resonant Enhancements in WIMP Capture by the Earth. *Astrophys. J.*, 321:571, 1987.

[279] Andrew Gould. WIMP Distribution in and Evaporation From the Sun. *Astrophys. J.*, 321:560, 1987.

[280] Andrew Gould. Direct and Indirect Capture of Wimps by the Earth. *Astrophys. J.*, 328:919–939, 1988.

[281] Andrew Gould, Joshua A. Frieman, and Katherine Freese. Probing the Earth With Wimps. *Phys. Rev. D*, 39:1029, 1989.

[282] S. R. Gozzini. Indirect dark matter searches with neutrinos from the Galactic Centre region with the ANTARES and KM3NeT telescopes. *JINST*, 16(09):C09006, 2021.

[283] Kenneth Greisen. End to the cosmic ray spectrum? *Phys. Rev. Lett.*, 16:748–750, 1966.

[284] Aman Gupta, Pooja Bhattacharjee, and Pratik Majumdar. Searching for dark matter annihilating into light-long-lived mediators from stars inside dwarf spheroidal galaxies, 1 2025.

[285] Aman Gupta, Debasish Majumdar, and Ashadul Halder. KM3NeT upper bounds of detection rates of solar neutrinos from annihilations of dark matter at the solar core. *Mod. Phys. Lett. A*, 37(35n36):2250233, 2022.

[286] Tolga Güver, Arif Emre Erkoca, Mary Hall Reno, and Ina Sarcevic. On the capture of dark matter by neutron stars. *JCAP*, 05:013, 2014.

[287] Naoyuki Haba, Yuji Kajiyama, Shigeki Matsumoto, Hiroshi Okada, and Koichi Yoshioka. Universally Leptophilic Dark Matter From Non-Abelian Discrete Symmetry. *Phys. Lett. B*, 695:476–481, 2011.

[288] Lawrence J. Hall and Mahiko Suzuki. Explicit R-Parity Breaking in Supersymmetric Models. *Nucl. Phys. B*, 231:419–444, 1984.

[289] Masayuki Harada. Review of diffuse sn neutrino background. In *Neutrino*, 2024.

[290] Edward Hardy and Robert Lasenby. Stellar cooling bounds on new light particles: plasma mixing effects. *Journal of High Energy Physics*, 2017(2):33, February 2017.

[291] Roni Harnik, Joachim Kopp, and Pedro A. N. Machado. Exploring ν signals in dark matter detectors. *Journal of Cosmology and Astroparticle Physics*, 2012(07):026–026, 7 2012. Publisher: IOP Publishing.

[292] Roni Harnik, Joachim Kopp, and Pedro A. N. Machado. Exploring nu Signals in Dark Matter Detectors. *JCAP*, 07:026, 2012.

[293] W. C. Haxton, R. G. Hamish Robertson, and Aldo M. Serenelli. Solar Neutrinos: Status and Prospects. *Ann. Rev. Astron. Astrophys.*, 51:21–61, 2013.

[294] Julian Heeck. Unbroken B–L symmetry. *Physics Letters B*, 739:256–262, 12 2014.

[295] Richard H. Helm. Inelastic and elastic scattering of 187-mev electrons from selected even-even nuclei. *Phys. Rev.*, 104:1466–1475, Dec 1956.

[296] K. Hirata et al. Observation of a Neutrino Burst from the Supernova SN 1987a. *Phys. Rev. Lett.*, 58:1490–1493, 1987.

[297] M. Honda, T. Kajita, K. Kasahara, and S. Midorikawa. Improvement of low energy atmospheric neutrino flux calculation using the JAM nuclear interaction model. *Phys. Rev. D*, 83:123001, 2011.

[298] M. Honda, M. Sajjad Athar, T. Kajita, K. Kasahara, and S. Midorikawa. Atmospheric neutrino flux calculation using the NRLMSISE-00 atmospheric model. *Phys. Rev. D*, 92(2):023004, 2015.

[299] Dan Hooper, Ilias Cholis, Tim Linden, Jennifer Siegal-Gaskins, and Tracy Slatyer. Pulsars Cannot Account for the Inner Galaxy's GeV Excess. *Phys. Rev. D*, 88:083009, 2013.

[300] Dan Hooper and Lisa Goodenough. Dark Matter Annihilation in The Galactic Center As Seen by the Fermi Gamma Ray Space Telescope. *Phys. Lett. B*, 697:412–428, 2011.

[301] Shunsaku Horiuchi, John F. Beacom, and Eli Dwek. The Diffuse Supernova Neutrino Background is detectable in Super-Kamiokande. *Phys. Rev. D*, 79:083013, 2009.

[302] Yu Huang, Viacheslav Chubakov, Fabio Mantovani, Roberta L. Rudnick, and William F. McDonough. A reference Earth model for the heat producing elements and associated geoneutrino flux. *arXiv e-prints*, page arXiv:1301.0365, January 2013.

[303] Dragan Huterer. Growth of cosmic structure. *The Astronomy and Astrophysics Review*, 31(1):2, 2023.

[304] Carlos A. Iglesias and Forrest J. Rogers. Updated Opal Opacities. *APJ*, 464:943, June 1996.

[305] Cosmin Ilie, Katherine Freese, Monica Valluri, Ilian T. Iliev, and Paul R. Shapiro. Observing supermassive dark stars with James Webb Space Telescope. *Monthly Notices of the Royal Astronomical Society*, 422(3):2164–2186, May 2012. _eprint: https://academic.oup.com/mnras/article-pdf/422/3/2164/18454337/mnras0422-2164.pdf.

[306] Cosmin Ilie, Jillian Paulin, and Katherine Freese. Supermassive Dark Star candidates seen by JWST. *Proc. Nat. Acad. Sci.*, 120(30):e2305762120, 2023.

[307] Kohei Inayoshi, Eli Visbal, and Zoltán Haiman. The Assembly of the First Massive Black Holes. *Ann. Rev. Astron. Astrophys.*, 58:27–97, 2020.

[308] Fabio Iocco. Dark Matter Capture and Annihilation on the First Stars: Preliminary Estimates. *Astrophys. J. Lett.*, 677:L1–L4, 2008.

[309] Hans-Thomas Janka. Explosion Mechanisms of Core-Collapse Supernovae. *Ann. Rev. Nucl. Part. Sci.*, 62:407–451, 2012.

[310] Isabelle John, Rebecca K. Leane, and Tim Linden. Dark Branches of Immortal Stars at the Galactic Center, 5 2024.

[311] Isabelle John and Tim Linden. Cosmic-Ray Positrons Strongly Constrain Leptophilic Dark Matter. *JCAP*, 12:007, 2021.

[312] Isabelle John and Tim Linden. Accurate inverse-Compton models strongly enhance leptophilic dark matter signals. *Phys. Rev. D*, 108(10):103022, 2023.

[313] Yuji Kajiyama, Shaaban Khalil, Hiroshi Okada, and Ernest Ma. Gauged B-L Leptogenesis, 3 2010.

[314] Marc Kamionkowski. Energetic neutrinos from heavy neutralino annihilation in the sun. *Phys. Rev. D*, 44:3021–3042, 1991.

[315] Amir N. Khan, Douglas W. McKay, and Werner Rodejohann. CP-violating and charged current neutrino nonstandard interactions in CEνNS. *Phys. Rev. D*, 104(1):015019, 2021.

[316] Jan-Hendrik Koehne, Katharina Frantzen, Martin Schmitz, Tomasz Fuchs, Wolfgang Rhode, Dmitry Chirkin, and J Becker Tjus. Proposal: A tool for propagation of charged leptons. *Computer Physics Communications*, 184(9):2070–2090, 2013.

[317] Edward W. Kolb. *The Early Universe*, volume 69. Taylor and Francis, 5 2019.

[318] E. Kolbe, K. Langanke, and P. Vogel. Estimates of weak and electromagnetic nuclear decay signatures for neutrino reactions in Super-Kamiokande. *Phys. Rev. D*, 66:013007, 2002.

[319] Joachim Kopp, Viviana Niro, Thomas Schwetz, and Jure Zupan. DAMA/LIBRA and leptonically interacting Dark Matter. *Phys. Rev. D*, 80:083502, 2009.

[320] Chris Kouvaris. WIMP Annihilation and Cooling of Neutron Stars. *Phys. Rev. D*, 77:023006, 2008.

[321] A. Kramida, Yu. Ralchenko, J. Reader, and and NIST ASD Team. NIST Atomic Spectra Database (ver. 5.12), [Online]. Available: `https://physics.nist.gov/asd` [2025, May 20]. National Institute of Standards and Technology, Gaithersburg, MD., 2024.

[322] Lawrence M. Krauss, Salah Nasri, and Mark Trodden. A Model for neutrino masses and dark matter. *Phys. Rev. D*, 67:085002, 2003.

[323] Lawrence M. Krauss, Mark Srednicki, and Frank Wilczek. Solar System Constraints and Signatures for Dark Matter Candidates. *Phys. Rev. D*, 33:2079–2083, 1986.

[324] Dhashin Krishna, Rinchen Sherpa, Akash Kumar Saha, Tarak Nath Maity, Ranjan Laha, and Nirmal Raj. ν limits from Super-Kamiokande on dark matter-electron scattering in the Sun, 3 2025.

[325] Rebecca K. Leane. Indirect Detection of Dark Matter in the Galaxy. In *3rd World Summit on Exploring the Dark Side of the Universe*, pages 203–228, 2020.

[326] Rebecca K. Leane and Tim Linden. First Analysis of Jupiter in Gamma Rays and a New Search for Dark Matter. *Phys. Rev. Lett.*, 131(7):071001, 2023.

[327] Rebecca K. Leane, Tim Linden, Payel Mukhopadhyay, and Natalia Toro. Celestial-Body Focused Dark Matter Annihilation Throughout the Galaxy. *Phys. Rev. D*, 103(7):075030, 2021.

[328] Rebecca K. Leane, Kenny C. Y. Ng, and John F. Beacom. Powerful Solar Signatures of Long-Lived Dark Mediators. *Phys. Rev. D*, 95(12):123016, 2017.

[329] Rebecca K. Leane and Tracy R. Slatyer. Revival of the Dark Matter Hypothesis for the Galactic Center Gamma-Ray Excess. *Phys. Rev. Lett.*, 123(24):241101, 2019.

[330] Rebecca K. Leane and Juri Smirnov. Exoplanets as Sub-GeV Dark Matter Detectors. *Phys. Rev. Lett.*, 126(16):161101, 2021.

[331] Rebecca K. Leane and Juri Smirnov. Floating dark matter in celestial bodies. *JCAP*, 10:057, 2023.

[332] Rebecca K. Leane and Joshua Tong. Optimal celestial bodies for dark matter detection. *JCAP*, 12:031, 2024.

[333] Hyun Min Lee. Leptoquark option for B-meson anomalies and leptonic signatures. *Phys. Rev. D*, 104(1):015007, 2021.

[334] Benjamin V. Lehmann. Higher multipoles of the cow, 4 2025.

[335] J. D. Lewin and P. F. Smith. Review of mathematics, numerical factors, and corrections for dark matter experiments based on elastic nuclear recoil. *Astroparticle Physics*, 6(1):87–112, 12 1996.

[336] J.D. Lewin and P.F. Smith. Review of mathematics, numerical factors, and corrections for dark matter experiments based on elastic nuclear recoil. *Astroparticle Physics*, 6(1):87–112, 1996.

[337] Shirley Weishi Li, Pedro Machado, Daniel Naredo-Tuero, and Thomas Schwemberger. Clash of the Titans: ultra-high energy KM3NeT event versus IceCube data, 2 2025.

[338] Shuaijie Li et al. Search for Light Dark Matter with Ionization Signals in the PandaX-4T Experiment. *Phys. Rev. Lett.*, 130(26):261001, 2023.

[339] Yu-Feng Li and Shuo-yu Xia. Constraining Light Mediators via Detection of Coherent Elastic Solar Neutrino Nucleus Scattering, 1 2022.

[340] Yu-Feng Li and Shuo yu Xia. Constraining light mediators via detection of coherent elastic solar neutrino nucleus scattering. *Nuclear Physics B*, 977:115737, 2022.

[341] Jiajun Liao and Danny Marfatia. Coherent constraints on nonstandard neutrino interactions. *Physics Letters B*, 775:54–57, 2017.

[342] Jiajun Liao and Danny Marfatia. COHERENT constraints on nonstandard neutrino interactions. *Phys. Lett. B*, 775:54–57, 2017.

[343] Qing Lin, Jialing Fei, Fei Gao, Jie Hu, Yuehuan Wei, Xiang Xiao, Hongwei Wang, and Kaixuan Ni. Scintillation and ionization responses of liquid xenon to low energy electronic and nuclear recoils at drift fields from 236 V/cm to 3.93 kV/cm. *Phys. Rev. D*, 92:032005, 8 2015.

[344] Jens Lindhard, V Nielsen, M Scharff, and PV Thomsen. Integral equations governing radiation effects. *Mat. Fys. Medd. Dan. Vid. Selsk*, 33(10):1–42, 1963.

[345] Manfred Lindner, Werner Rodejohann, and Xun-Jie Xu. Coherent neutrino-nucleus scattering and new neutrino interactions. *Journal of High Energy Physics*, 2017(3):97, March 2017.

[346] Felix Linke, Jose A. Font, Hans-Thomas Janka, Ewald Muller, and Philippos Papadopoulos. Spherical collapse of supermassive stars: Neutrino emission and gamma-ray bursts. *Astron. Astrophys.*, 376:568, 2001.

[347] Laura Lopez-Honorez, Olga Mena, Sergio Palomares-Ruiz, and Aaron C. Vincent. Constraints on dark matter annihilation from CMB observationsbefore Planck. *JCAP*, 07:046, 2013.

[348] Ernest Ma. Verifiable radiative seesaw mechanism of neutrino mass and dark matter. *Phys. Rev. D*, 73:077301, 2006.

[349] Tarak Nath Maity, Akash Kumar Saha, Sagnik Mondal, and Ranjan Laha. Neutrinos from the Sun can discover dark matter-electron scattering, 8 2023.

[350] Anirban Majumdar, D. K. Papoulias, and Rahul Srivastava. Dark Matter Detectors as a Novel Probe for Light New Physics, 12 2021.

[351] Anirban Majumdar, D. K. Papoulias, and Rahul Srivastava. Dark matter detectors as a novel probe for light new physics. *Phys. Rev. D*, 106:013001, Jul 2022.

[352] Michele Maltoni and Alexei Yu. Smirnov. Solar neutrinos and neutrino physics. *Eur. Phys. J. A*, 52(4):87, 2016.

[353] Jorryt Matthee et al. Little Red Dots: An Abundant Population of Faint Active Galactic Nuclei at z $\sim$ 5 Revealed by the EIGER and FRESCO JWST Surveys. *Astrophys. J.*, 963(2):129, 2024.

[354] A. Maurer, M. Raue, T. Kneiske, D. Horns, D. Elsasser, and P. H. Hauschildt. Dark matter powered stars: Constraints from the extragalactic background light. *Astrophys. J.*, 745:166, 2012.

[355] Maximilian Meier. Recent cosmogenic neutrino search results with IceCube and prospects with IceCube-Gen2. In *58th Rencontres de Moriond on Very High Energy Phenomena in the Universe*, 9 2024.

[356] Yue Meng et al. Dark Matter Search Results from the PandaX-4T Commissioning Run. *Phys. Rev. Lett.*, 127(26):261802, 2021.

[357] Piotr Mijakowski. Dark Matter Searches at Super-Kamiokande. *J. Phys. Conf. Ser.*, 1342(1):012075, 2020.

[358] L. Salvador Miranda, S. Basegmez du Pree, K. C. Y. Ng, A. Cheek, and C. Arina. Towards detecting super-GeV dark matter via annihilation to neutrinos. *JCAP*, 08:006, 2023.

[359] O G Miranda and H Nunokawa. Non standard neutrino interactions: current status and future prospects. *New Journal of Physics*, 17(9):095002, 9 2015.

[360] O. G. Miranda, D. K. Papoulias, G. Sanchez Garcia, O. Sanders, M. Tórtola, and J. W. F. Valle. Implications of the first detection of coherent elastic neutrino-nucleus scattering (CEvNS) with Liquid Argon. *JHEP*, 05:130, 2020. [Erratum: JHEP 01, 067 (2021)].

[361] Alessandro Mirizzi, Javier Redondo, and Günter Sigl. Microwave background constraints on mixing of photons with hidden photons. *Journal of Cosmology and Astroparticle Physics*, 2009(03):026–026, 3 2009.

[362] G. Mitsuka, K. Abe, Y. Hayato, T. Iida, M. Ikeda, J. Kameda, Y. Koshio, M. Miura, S. Moriyama, M. Nakahata, S. Nakayama, Y. Obayashi, H. Sekiya, M. Shiozawa, Y. Suzuki, A. Takeda, Y. Takenaga, Y. Takeuchi, K. Ueno, K. Ueshima, H. Watanabe, S. Yamada, S. Hazama, I. Higuchi, C. Ishihara, H. Kaji, T. Kajita, K. Kaneyuki, H. Nishino, K. Okumura, N. Tanimoto, F. Dufour, E. Kearns, M. Litos, J. L. Raaf, J. L. Stone, L. R. Sulak, M. Goldhaber, K. Bays, J. P. Cravens, W. R. Kropp, S. Mine, C. Regis, M. B. Smy, H. W. Sobel, M. R. Vagins, K. S. Ganezer, J. Hill, W. E. Keig, J. S. Jang, J. Y. Kim, I. T. Lim, J. Albert, K. Scholberg, C. W. Walter, R. Wendell, T. Ishizuka, S. Tasaka, J. G. Learned, S. Matsuno, Y. Watanabe, T. Hasegawa, T. Ishida, T. Ishii, T. Kobayashi, T. Nakadaira, K. Nakamura, K. Nishikawa, Y. Oyama, K. Sakashita, T. Sekiguchi, T. Tsukamoto, A. T. Suzuki, A. Minamino, T. Nakaya, M. Yokoyama, Y. Fukuda, Y. Itow, T. Tanaka, C. K. Jung, G. Lopez, C. McGrew, C. Yanagisawa, N. Tamura, Y. Idehara, M. Sakuda, Y. Kuno, M. Yoshida, S. B. Kim, B. S. Yang, H. Okazawa, Y. Choi, H. K. Seo, Y. Furuse, K. Nishijima, Y. Yokosawa, M. Koshiba, Y. Totsuka, S. Chen, J. Liu, Y. Heng, Z. Yang, H. Zhang, D. Kielczewska, K. Connolly, E. Thrane, and R. J. Wilkes. Study of nonstandard neutrino interactions with atmospheric neutrino data in super-kamiokande i and ii. *Phys. Rev. D*, 84:113008, Dec 2011.

[363] Youssef Sarkis Mobarak. Improved study of the ionization efficiency for nuclear recoils in si and ge at low energies. `https://indico.cern.ch/event/1075677/contributions/4556828/`, 2021. [Online; accessed 3-January-2022].

[364] B. Moore, S. Ghigna, F. Governato, G. Lake, Thomas R. Quinn, J. Stadel, and P. Tozzi. Dark matter substructure within galactic halos. *Astrophys. J. Lett.*, 524:L19–L22, 1999.

[365] Victor Munoz, Volodymyr Takhistov, Samuel J. Witte, and George M. Fuller. Exploring the origin of supermassive black holes with coherent neutrino scattering. *JCAP*, 11(11):020, 2021.

[366] Marco S. Muzio, Tianlu Yuan, and Lu Lu. Emergence of a neutrino flux above 5 PeV and implications for ultrahigh energy cosmic rays, 2 2025.

[367] Richard Naab, Erik Ganster, and Zelong Zhang. Measurement of the astrophysical diffuse neutrino flux in a combined fit of IceCube's high energy neutrino data. In *38th International Cosmic Ray Conference*, 7 2023.

[368] Julio F. Navarro, Carlos S. Frenk, and Simon D. M. White. The Structure of cold dark matter halos. *Astrophys. J.*, 462:563–575, 1996.

[369] Julio F. Navarro, Carlos S. Frenk, and Simon D. M. White. A Universal density profile from hierarchical clustering. *Astrophys. J.*, 490:493–508, 1997.

[370] Andrii Neronov, Foteini Oikonomou, and Dmitri Semikoz. Km3-230213a: An ultra-high energy neutrino from a year-long astrophysical transient, 2025.

[371] Jayden L. Newstead, Rafael F. Lang, and Louis E. Strigari. Atmospheric neutrinos in next-generation xenon and argon dark matter experiments. *Phys. Rev. D*, 104(11):115022, 2021.

[372] Thong T. Q. Nguyen, Tim Linden, Pierluca Carenza, and Axel Widmark. Super-kamiokande strongly constrains leptophilic dark matter capture in the sun, 2025.

[373] M. U. Nisa, J. F. Beacom, S. Y. BenZvi, R. K. Leane, T. Linden, K. C. Y. Ng, A. H. G. Peter, and B. Zhou. The Sun at GeV–TeV Energies: A New Laboratory for Astroparticle Physics, 3 2019.

[374] Ciaran A. J. O'Hare. New Definition of the Neutrino Floor for Direct Dark Matter Searches. *Phys. Rev. Lett.*, 127(25):251802, 2021.

[375] J. H. Oort. The force exerted by the stellar system in the direction perpendicular to the galactic plane and some related problems. *Bulletin of the Astronomical Institutes of the Netherlands*, 6:249, August 1932.

[376] Jogesh C. Pati and Abdus Salam. Lepton Number as the Fourth Color. *Phys. Rev. D*, 10:275–289, 1974. [Erratum: Phys.Rev.D 11, 703–703 (1975)].

[377] Elena Pierpaoli, Douglas Scott, and Martin J. White. Power spectrum normalization from the local abundance of rich clusters of galaxies. *Mon. Not. Roy. Astron. Soc.*, 325:77, 2001.

[378] Maxim Pospelov. Secluded u(1) below the weak scale. *Phys. Rev. D*, 80:095002, 11 2009.

[379] Maxim Pospelov and Anupam Ray. Neutrinos from Earth-bound dark matter annihilation. *JCAP*, 01:029, 2024.

[380] Francisco Prada, Anatoly A. Klypin, Antonio J. Cuesta, Juan E. Betancort-Rijo, and Joel Primack. Halo concentrations in the standard LCDM cosmology. *Mon. Not. Roy. Astron. Soc.*, 423:3018–3030, 2012.

[381] William H. Press and Paul Schechter. Formation of Galaxies and Clusters of Galaxies by Self-Similar Gravitational Condensation. *APJ*, 187:425–438, February 1974.

[382] William H. Press and David N. Spergel. Capture by the sun of a galactic population of weakly interacting massive particles. *Astrophys. J.*, 296:679–684, 1985.

[383] G. G. Raffelt. *Stars as laboratories for fundamental physics: The astrophysics of neutrinos, axions, and other weakly interacting particles*. University of Chicago Press, 5 1996.

[384] K. Ramanathan and N. Kurinsky. Ionization yield in silicon for eV-scale electron-recoil processes. *Phys. Rev. D*, 102(6):063026, 2020.

[385] Javier Redondo. Helioscope bounds on hidden sector photons. *Journal of Cosmology and Astroparticle Physics*, 2008(07):008, 7 2008.

[386] Simeon Reusch et al. Candidate Tidal Disruption Event AT2019fdr Coincident with a High-Energy Neutrino. *Phys. Rev. Lett.*, 128(22):221101, 2022.

[387] E. Richard et al. Measurements of the atmospheric neutrino flux by Super-Kamiokande: energy spectra, geomagnetic effects, and solar modulation. *Phys. Rev. D*, 94(5):052001, 2016.

[388] Marcia J. Rieke et al. JADES Initial Data Release for the Hubble Ultra Deep Field: Revealing the Faint Infrared Sky with Deep JWST NIRCam Imaging. *Astrophys. J. Suppl.*, 269(1):16, 2023.

[389] Tanja Rindler-Daller, Michael H. Montgomery, Katherine Freese, Donald E. Winget, and Bill Paxton. Dark Stars: Improved Models and First Pulsation Results. *Astrophys. J.*, 799(2):210, 2015.

[390] B. M. Roberts, V. A. Dzuba, and V. V. Flambaum. Parity and Time-Reversal Violation in Atomic Systems. *Ann. Rev. Nucl. Part. Sci.*, 65:63–86, 2015.

[391] Sandra Robles and Stephan A. Meighen-Berger. Extending the Dark Matter Reach of Water Cherenkov Detectors using Jupiter. 11 2024.

[392] Dario Rodrigues et al. Absolute measurement of the Fano factor using a Skipper-CCD. *Nucl. Instrum. Meth. A*, 1010:165511, 2021.

[393] R. K. Romani et al. Thermal detection of single e-h pairs in a biased silicon crystal detector. *Appl. Phys. Lett.*, 112(4):043501, 2018.

[394] Vera C. Rubin, W. Kent Ford, Jr., and Norbert Thonnard. Extended rotation curves of high-luminosity spiral galaxies. IV. Systematic dynamical properties, Sa through Sc. *Astrophys. J. Lett.*, 225:L107–L111, 1978.

[395] Y. Sarkis, A. Aguilar-Arevalo, and J. C. D'Olivo. A Study of the Ionization Efficiency for Nuclear Recoils in Pure Crystals. *Phys. At. Nucl.*, 84(4):590–594, 2021.

[396] Y. Sarkis, Alexis Aguilar-Arevalo, and Juan Carlos D'Olivo. Study of the ionization efficiency for nuclear recoils in pure crystals. *Phys. Rev. D*, 101:102001, 5 2020.

[397] Dominik R. G. Schleicher, Robi Banerjee, and Ralf S. Klessen. Dark stars: Implications and constraints from cosmic reionization and extragalactic background radiation. *Phys. Rev. D*, 79:043510, 2009.

[398] Dominik R. G. Schleicher, Robi Banerjee, and Ralf S. Klesser. Reionization - A probe for the stellar population and the physics of the early universe. *Phys. Rev. D*, 78:083005, 2008.

[399] Martin Schmaltz and Yi-Ming Zhong. The leptoquark Hunter's guide: large coupling. *JHEP*, 01:132, 2019.

[400] Kate Scholberg. Prospects for measuring coherent neutrino-nucleus elastic scattering at a stopped-pion neutrino source. *Phys. Rev. D*, 73:033005, 2006.

[401] B. J. Scholz, A. E. Chavarria, J. I. Collar, P. Privitera, and A. E. Robinson. Measurement of the low-energy quenching factor in germanium using an ^{88}Y/Be photoneutron source. *Phys. Rev. D*, 94(12):122003, 2016.

[402] Marc Schumann. Direct Detection of WIMP Dark Matter: Concepts and Status. *J. Phys. G*, 46(10):103003, 2019.

[403] Thomas Schwemberger and Volodymyr Takhistov. Neutrino Whispers from Dark Stars Seeding Supermassive Black Holes, 12 2024.

[404] Thomas Schwemberger, Volodymyr Takhistov, and Tien-Tien Yu. Hunting nonstandard neutrino interactions and leptoquarks in dark matter experiments. *JCAP*, 11:068, 2024.

[405] Thomas Schwemberger and Tien-Tien Yu. Detecting beyond the standard model interactions of solar neutrinos in low-threshold dark matter detectors. *Phys. Rev. D*, 106(1):015002, 2022.

[406] SENSEI Collaboration, Liron Barak, Itay M. Bloch, Mariano Cababie, Gustavo Cancelo, Luke Chaplinsky, Fernando Chierchie, Michael Crisler, Alex Drlica-Wagner, Rouven Essig, Juan Estrada, Erez Etzion, Guillermo Fernandez Moroni, Daniel Gift, Sravan Munagavalasa, Aviv Orly, Dario Rodrigues, Aman Singal, Miguel Sofo Haro, Leandro Stefanazzi, Javier Tiffenberg, Sho Uemura, Tomer Volansky, and Tien-Tien Yu. SENSEI: Direct-Detection Results on sub-GeV Dark Matter from a New Skipper CCD. *Physical Review Letters*, 125(17):171802, 10 2020. Publisher: American Physical Society.

[407] Davide Serini, Francesco Loparco, and Mario Nicola Mazziotta. Constraints on dark matter scattering with long-lived mediators using gamma-rays from the Sun. *PoS*, ICRC2019:544, 2020.

[408] Ravi K. Sheth and Giuseppe Tormen. Large scale bias and the peak background split. *Mon. Not. Roy. Astron. Soc.*, 308:119, 1999.

[409] Xiang-Dong Shi and George M. Fuller. Neutrinos and supermassive stars: Prospects for neutrino emission and detection. *Astrophys. J.*, 503:307, 1998.

[410] Xiang-Dong Shi, George M. Fuller, and Francis Halzen. Observing the birth of supermassive black holes with the 'ICECUBE' neutrino detector. *Phys. Rev. Lett.*, 81:5722–5725, 1998.

[411] Manuel Silva, Sarah Mancina, and Jesse Osborn. Measurement of the Cosmic Neutrino Flux from the Southern Sky using 10 years of IceCube Starting Track Events. *PoS*, ICRC2023:1008, 2023.

[412] Albert M Sirunyan et al. Search for high-mass resonances in dilepton final states in proton-proton collisions at $\sqrt{s} = 13$ TeV. *JHEP*, 06:120, 2018.

[413] Albert M Sirunyan et al. Search for pair production of second-generation leptoquarks at $\sqrt{s} = 13$ TeV. *Phys. Rev. D*, 99(3):032014, 2019.

[414] Tracy R. Slatyer. Indirect detection of dark matter. In *Theoretical Advanced Study Institute in Elementary Particle Physics: Anticipating the Next Discoveries in Particle Physics*, pages 297–353, 2018.

[415] D. N. Spergel et al. First year Wilkinson Microwave Anisotropy Probe (WMAP) observations: Determination of cosmological parameters. *Astrophys. J. Suppl.*, 148:175–194, 2003.

[416] Douglas Spolyar, Peter Bodenheimer, Katherine Freese, and Palo Gondolo. Dark Stars: a new look at the First Stars in the Universe. *Astrophys. J.*, 705:1031–1042, 2009.

[417] Douglas Spolyar, Katherine Freese, and Paolo Gondolo. Dark matter and the first stars: a new phase of stellar evolution. *Phys. Rev. Lett.*, 100:051101, 2008.

[418] Gary Steigman, Basudeb Dasgupta, and John F. Beacom. Precise relic wimp abundance and its impact on searches for dark matter annihilation. *Phys. Rev. D*, 86:023506, Jul 2012.

[419] Robert Stein et al. A tidal disruption event coincident with a high-energy neutrino. *Nature Astron.*, 5(5):510–518, 2021.

[420] Meredith A. Stone, Jianwei Lyu, George H. Rieke, Stacey Alberts, and Kevin N. Hainline. Undermassive Host Galaxies of Five z $\sim$ 6 Luminous Quasars Detected with JWST. *APJ*, 964(1):90, March 2024.

[421] Alessandro Strumia and Francesco Vissani. Precise quasielastic neutrino/nucleon cross-section. *Phys. Lett. B*, 564:42–54, 2003.

[422] M. Szydagis, N. Barry, K. Kazkaz, J. Mock, D. Stolp, M. Sweany, M. Tripathi, S. Uvarov, N. Walsh, and M. Woods. NEST: a comprehensive model for scintillation yield in liquid xenon. *Journal of Instrumentation*, 6(10):P10002–P10002, 10 2011. Publisher: IOP Publishing.

[423] M. Szydagis, G. A. Block, C. Farquhar, A. J. Flesher, E. S. Kozlova, C. Levy, E. A. Mangus, M. Mooney, J. Mueller, G. R. C. Rischbieter, and A. K. Schwartz. A Review of Basic Energy Reconstruction Techniques in Liquid Xenon and Argon Detectors for Dark Matter and Neutrino Physics Using NEST. *Instruments*, 5(1):13, 3 2021. arXiv: 2102.10209.

[424] M. Szydagis, A. Fyhrie, D. Thorngren, and M. Tripathi. Enhancement of NEST capabilities for simulating low-energy recoils in liquid xenon. *Journal of Instrumentation*, 8(10):C10003–C10003, 10 2013. Publisher: IOP Publishing.

[425] Volodymyr Takhistov. Review of Atmospheric Neutrino Results from Super-Kamiokande. *PoS*, ICHEP2020:181, 2021.

[426] Jonathan C. Tan, Jasbir Singh, Vieri Cammelli, Mahsa Sanati, Maya Petkova, Devesh Nandal, and Pierluigi Monaco. The origin of supermassive black holes from pop iii.1 seeds, 2024.

[427] J. Thomas and D. A. Imel. Recombination of electron-ion pairs in liquid argon and liquid xenon. *Physical Review A*, 36(2):614–616, 10 1987. Publisher: American Physical Society.

[428] Javier Tiffenberg, Miguel Sofo-Haro, Alex Drlica-Wagner, Rouven Essig, Yann Guardincerri, Steve Holland, Tomer Volansky, and Tien-Tien Yu. Single-electron and single-photon sensitivity with a silicon Skipper CCD. *Phys. Rev. Lett.*, 119(13):131802, 2017.

[429] Monica Valluri, Victor P. Debattista, Thomas Quinn, and Ben Moore. The orbital evolution induced by baryonic condensation in triaxial haloes. *Monthly Notices of the Royal Astronomical Society*, 403(1):525–544, March 2010. _eprint: https://academic.oup.com/mnras/article-pdf/403/1/525/3350458/mnras0403-0525.pdf.

[430] Arjen van Vliet, Rafael Alves Batista, and Jörg R. Hörandel. Determining the fraction of cosmic-ray protons at ultrahigh energies with cosmogenic neutrinos. *Phys. Rev. D*, 100(2):021302, 2019.

[431] E. Vanzella, M. Meneghetti, G. B. Caminha, M. Castellano, F. Calura, P. Rosati, C. Grillo, M. Dijkstra, M. Gronke, E. Sani, A. Mercurio, P. Tozzi, M. Nonino, S. Cristiani, M. Mignoli, L. Pentericci, R. Gilli, T. Treu, K. Caputi, G. Cupani, A. Fontana, A. Grazian, and I. Balestra. Candidate Population III stellar complex at z = 6.629 in the MUSE Deep Lensed Field. *Monthly Notices of the Royal Astronomical Society*, 494(1):L81–L85, May 2020.

[432] Viktor S Vavilov. Radiation ionization processes in germanium and silicon crystals. *Soviet Physics Uspekhi*, 4(5):761, 1962.

[433] B. P. Venemans, J. R. Findlay, W. J. Sutherland, G. De Rosa, R. G. McMahon, R. Simcoe, E. A. Gonzalez-Solares, K. Kuijken, and J. R. Lewis. Discovery of three z>6.5 quasars in the VISTA Kilo-degree Infrared Galaxy (VIKING) survey. *Astrophys. J.*, 779:24, 11 2013.

[434] Núria Vinyoles, Aldo M. Serenelli, Francesco L. Villante, Sarbani Basu, Johannes Bergström, M. C. Gonzalez-Garcia, Michele Maltoni, Carlos Peña Garay, and Ningqiang Song. A new Generation of Standard Solar Models. *Astrophys. J.*, 835(2):202, 2017.

[435] F. Vissani and G. Pagliaroli. The diffuse supernova neutrino background: expectations and uncertainties derived from sn1987a. *A&A*, 528:L1, 2011.

[436] Marta Volonteri. Formation of Supermassive Black Holes. *Astron. Astrophys. Rev.*, 18:279–315, 2010.

[437] Marius Wallraff and Christopher Wiebusch. Calculation of oscillation probabilities of atmospheric neutrinos using nuCraft. *Comput. Phys. Commun.*, 197:185–189, 2015.

[438] Xin Wang, Cheng Cheng, Junqiang Ge, Xiao-Lei Meng, Emanuele Daddi, Haojing Yan, Zhiyuan Ji, Yifei Jin, Tucker Jones, Matthew A. Malkan, Pablo Arrabal Haro, Gabriel Brammer, Masamune Oguri, Meicun Hou, and Shiwu Zhang. A Strong He II λ1640 Emitter with an Extremely Blue UV Spectral Slope at z = 8.16: Presence of Population III Stars? *Astrophysical Journal Letters*, 967(2):L42, June 2024.

[439] Brian Welch, Dan Coe, Jose M. Diego, Adi Zitrin, Erik Zackrisson, Paola Dimauro, Yolanda Jiménez-Teja, Patrick Kelly, Guillaume Mahler, Masamune Oguri, F. X. Timmes, Rogier Windhorst, Michael Florian, S. E. de Mink, Roberto J. Avila, Jay Anderson, Larry Bradley, Keren Sharon, Anton Vikaeus, Stephan McCandliss, Maruša Bradač, Jane Rigby, Brenda Frye, Sune Toft, Victoria Strait, Michele Trenti, Soniya Sharma, Felipe Andrade-Santos, and Tom Broadhurst. A highly magnified star at redshift 6.2. *Nature*, 603(7903):815–818, March 2022.

[440] L. Wolfenstein. Neutrino Oscillations in Matter. *Phys. Rev. D*, 17:2369–2374, 1978.

[441] R. L. Workman et al. Review of Particle Physics. *PTEP*, 2022:083C01, 2022.

[442] Youjia Wu, Sebastian Baum, Katherine Freese, Luca Visinelli, and Hai-Bo Yu. Dark stars powered by self-interacting dark matter. *Phys. Rev. D*, 106(4):043028, 2022.

[443] Naoki Yoshida, Kazuyuki Omukai, Lars Hernquist, and Tom Abel. Formation of Primordial Stars in a lambda-CDM Universe. *Astrophys. J.*, 652:6–25, 2006.

[444] Qiang Yuan, Bin Yue, Bing Zhang, and Xuelei Chen. Constraint on dark matter annihilation with dark star formation using Fermi extragalactic diffuse gamma-ray background data. *JCAP*, 04:020, 2011.

[445] Minghao Yue, Anna-Christina Eilers, Robert A. Simcoe, Ruari Mackenzie, Jorryt Matthee, Daichi Kashino, Rongmon Bordoloi, Simon J. Lilly, and Rohan P. Naidu. Eiger. v. characterizing the host galaxies of luminous quasars at z $\gtrsim$ 6. *The Astrophysical Journal*, 966(2):176, May 2024.

[446] Erik Zackrisson, Pat Scott, Claes-Erik Rydberg, Fabio Iocco, Bengt Edvardsson, Göran Östlin, Sofia Sivertsson, Adi Zitrin, Tom Broadhurst, and Paolo Gondolo. Finding High-redshift Dark Stars with the James Webb Space Telescope. *APJ*, 717(1):257–267, 7 2010.

[447] G. T. Zatsepin and V. A. Kuzmin. Upper limit of the spectrum of cosmic rays. *JETP Lett.*, 4:78–80, 1966.

[448] Di Zhang. Radiative neutrino masses, lepton flavor mixing and muon g-2 in a leptoquark model. *Journal of High Energy Physics*, 2021(7):69, July 2021.

[449] Di Zhang. Radiative neutrino masses, lepton flavor mixing and muon g $-$ 2 in a leptoquark model. *JHEP*, 07:069, 2021.

[450] Yi-Ming Zhong, Samuel D. McDermott, Ilias Cholis, and Patrick J. Fox. Testing the Sensitivity of the Galactic Center Excess to the Point Source Mask. *Phys. Rev. Lett.*, 124(23):231103, 2020.

[451] Yi Zhuang, Louis E. Strigari, and Rafael F. Lang. Time variation of the atmospheric neutrino flux at dark matter detectors. *Phys. Rev. D*, 105:043001, Feb 2022.

[452] F. Zwicky. Die Rotverschiebung von extragalaktischen Nebeln. *Helvetica Physica Acta*, 6:110–127, January 1933.